Advances in Civil Engineering

Advances and Frontiers in Geotechnical Engineering

Lead Guest Editor: Zhuo Chen
Guest Editors: Mukhiddin Juliev, Danqing Song, Junfeng Tang, Fei Luo, and Xiangang Jiang

Advances and Frontiers in Geotechnical Engineering

Advances in Civil Engineering

Advances and Frontiers in Geotechnical Engineering

Lead Guest Editor: Zhuo Chen
Guest Editors: Mukhiddin Juliev, Danqing Song, Junfeng Tang, Fei Luo, and Xiangang Jiang

Contents

The Effect of Length and Content of Fiber on Glass Fiber and Basalt Fiber-Reinforced Granite Residual Soil

Weijie Chen, Jin Zhao, Litao Fan, Jia Li, Bingxiang Yuan, Hongzhong Li, Guoping Jiang, Hanbo Li, and Tianying Chen

Research Article (9 pages), Article ID 7803002, Volume 2022 (2022)

Hindawi
Advances in Civil Engineering
Volume 2023, Article ID 9919441, 11 pages
https://doi.org/10.1155/2023/9919441

Research Article

Seepage Migration Process of Soluble Contaminants in Porous Medium considering Adsorption History

Wenya Cai,[1] Guoqiang Zhang,[2] Pengyuan Zhang,[2] Siyang Zhang,[1] Weixi Li,[1] Zeyang Meng,[3] and Shunli You[2]

[1]*Beijing Guodaotong Highway Design&Research Institute Co., Ltd, Beijing 100055, China*
[2]*Beijing Uni-Construction Group Co., Ltd, Beijing 101200, China*
[3]*School of Civil Engineering, Beijing Jiaotong University, Beijing 100044, China*

Correspondence should be addressed to Zeyang Meng; 19125832@bjtu.edu.cn and Shunli You; 304957266@qq.com

Received 28 September 2022; Revised 28 January 2023; Accepted 4 April 2023; Published 3 May 2023

Academic Editor: Jiang Xiangang

By embedding a nonlinear nonequilibrium adsorption model considering the adsorption history (i.e., Bai model), a governing equation for the three-dimensional model is extended, which discussed the influence of varying seepage velocity and injection concentration. Compared with the previous linear adsorption model, the concentration peak value of the nonlinear nonequilibrium adsorption history model is higher than that of the linear model, and the time to reach the peak concentration is slightly earlier. In the case of horizontal seepage water, a pollution point source tends to migrate along the direction of water flow and has less ability to diffuse in the vertical direction. Compared with the adsorption history model, the linear model has a stronger blocking ability for pollutant migration, and the longer the time, the greater the gap between the two models. The longer the decay period, the wider the spread of contaminants, and the longer it takes for them to migrate out of the model completely. The more significant the head difference, the larger the diffusion area of pollutants in the main seepage direction, but it has no promotion effect on the lateral diffusion. The pollutant concentration is higher than that of the point source case, and the diffusion range in each section is wider. The closer it is to the center of the pollution source, the weaker the dispersion effect on the diffusion of pollutants in the main seepage direction, and the pollutants will spread in the countercurrent direction, causing pollution upstream.

1. Introduction

The migration of pollutants in the soil is affected by many conditions, such as seepage velocity, dispersion conditions, soil adsorption capacity, chemical factors, and biological factors [1–3]. The adsorption mechanism of soil is complicated for its complex nature [4, 5], and it also has specific characteristics for desorption. Previous studies have shown that the adsorption capacity of porous media does not change after the initial adsorption [6–8], but in practice, the residue of pollutants in porous media will weaken its adsorption capacity [9–11]. Diverse soil conditions will result in complex adsorption-desorption processes, which in turn affect the migration of pollutants. To better investigate the migration law of pollutants in soil, a more realistic adsorption-desorption model is needed to support the theoretical research [12, 13], which is the basis for the development of pollutant purification technology [8, 14].

Kim et al. [15] studied the influence of hydraulic conditions on the adsorption properties of porous media through experiments. According to different chemical conditions, it was found that the magnitude of particle separation increased with the improvement of particle size. Hosseini et al. [16] developed as an economical and alternative adsorbent to treat dye wastewater, in which the magnetic chitosan nanocomposites possessed of excellent adsorptive property for the recycle of wastewater contaminated by dye. García-García et al. [17] studied the effect of temperature on particle aggregation dynamics under different pH values and ionic strengths. They found that the

particle coagulation rate decreases with the temperature increase when the environment is alkaline. Lake and Rowe [18] found through laboratory tests that the diffusion coefficient is related to the concentration of the pollution source. Cui et al. [19] explored the effects of particle sizes, particle concentrations, penetration velocities, and penetration directions on the dispersion and deposition mechanisms of suspended particles through cylindrical penetration tests. Porubcan and Xu [20] discussed the migration characteristics of colloidal particles with different particle sizes in the porous media of quartz sand mixed with different particle sizes through experiments. They found that when the proportion of fine sand in uneven quartz sand increased, the adsorption of colloidal particles increased. Mahmoodi et al. [21] investigated the hydration inhibitive ability of surfactants by various experiments, including zeta potential, XRD, FTIR, particle size, and SEM measures for a dye removal by the surfactant-modified montmorillonite.

Cui et al. [22] found that different metal ions have different migration characteristics through laboratory research. The difference is mainly reflected in the adsorption properties, resulting in apparent differences in the migration process of different metal ions. Cui et al. [23] considered that the attenuation of soil adsorption performance is affected by its adsorption historical and temperature effect and conducted a sensitivity analysis on relevant parameters [24]. Some researchers [9, 25, 26], based on the hydrodynamic dispersion coefficient and flow velocity under unstable conditions, established their pollutant transport equations in semi-infinite space concerning space-time changes and obtained the analytical solution under the action of the Gaussian pulse pollution source. Cui et al. [22] proposed a short-time pulse pollution source by studying pollution sources, established a pollutant migration model, and calculated the migration and deposition characteristics of pollutants in porous media. Leij et al. [27] studied the migration law of pollutants during equilibrium adsorption, established a semi-infinite equation, and obtained the analytical solution of a unidirectional stable seepage field through Laplace and Fourier transform. Dahaghi et al. [28] deduced a new mathematical model of pollutant migration, which considers the complex migration process of particles. Rowe and Bookeret [29] proposed a two-dimensional finite layer calculation method considering vertical and horizontal directions and obtained the migration law of layered soil under the condition of linear equilibrium adsorption.

Miracapillo and Ferroni [30] considered the nonuniform groundwater flow to simulate the migration process of nuclides in the geological repository. They discussed the influence of distribution coefficient and hydraulic gradient on pollutant migration, respectively. Trofa et al. [31] used the arbitrary Lagrange–Eulerian method for numerical analysis to solve the governing equation of pollutant transport and numerically simulated the two-dimensional migration of suspended particles at an infinite Reynolds number. Villone et al. [32] used the arbitrary Lagrange–Eulerian method to numerically analyze the model from a three-dimensional perspective and obtained the corresponding numerical analysis results. Mironenko and Pachepsky [33] considered the exchange process and biochemical reaction process of solutes in immobile and movable water and established a pollutant migration model under the condition of a one-dimensional semi-infinite soil column. Tiraferri et al. [1] first determined the functional relationship between particle filtration coefficient and pore water ions through the deposition test of particles in siliceous sand and then established the corresponding model.

To explore the transport mechanisms of pollutants under regular boundary conditions in three-dimensional spatial, based on the in-depth analysis of typical adsorption models, a nonlinear nonequilibrium adsorption model (i.e., Bai model) [2] considering the adsorption history is embedded to carry out the theoretical calculation of pollutant migration. Classified by pollution source diffusion, the three-dimensional point source model and three-dimensional volume source model were discussed, respectively. This research analyzed the pollution source changes and parameter changes and obtained pollutant migration characteristics under the corresponding model.

2. Theoretical Model

2.1. Governing Equations. The governing equation has been derived as [2, 25]

$$\frac{\partial(\theta C)}{\partial t} = \nabla \cdot (\theta \mathbf{D} \cdot \nabla C - uC) - \frac{\partial(\rho_b C_d)}{\partial t}, \tag{1}$$

where C is the concentration of pollutants in porous media (ML^{-3}), θ is the porosity of porous media, t is the time (T), $\mathbf{D}$ is the hydrodynamic dispersion coefficient (T^2T^{-1}), u is the average velocity of cross section (LT^{-1}), ρ_b is the volumetric dry density of porous media (ML^{-3}), and C_d is the concentration of adsorption (MM^{-1}).

Equation (1) refers to the amount of solute adsorbed by the porous medium per unit mass. In the governing equation, the expression of the dispersion term is $\nabla \cdot (\theta \mathbf{D} \cdot \nabla C)$. The mechanical dispersion coefficient tensor and the molecular diffusion coefficient tensor are combined into the hydrodynamic dispersion coefficient tensor, i.e.,

$$D_{ij} = (D_d)_{ij} + D^* \tau_{ij}, \tag{2}$$

where D_{ij} is the hydrodynamic dispersion coefficient tensor (L^2T^{-1}); $(D_d)_{ij}$ is the mechanical dispersion coefficient tensor (L^2T^{-1}); $D^*\tau_{ij}$, represents the molecular diffusion coefficient tensor (L^2T^{-1}), is the molecular diffusion coefficient scalar, τ_{ij} is the curvature tensor of porous media.

For three-dimensional cases, assume that the seepage direction of the fluid is horizontal, that is, $v_z = 0$, D can be obtained $D_{xz} = D_{zx} = 0$, $D_{yz} = D_{zy} = 0$, so the hydrodynamic dispersion coefficient matrix is

$$D_{ij} = \begin{bmatrix} D_{xx} & D_{yx} & 0 \\ D_{xy} & D_{yy} & 0 \\ 0 & 0 & D_{zz} \end{bmatrix}. \tag{3}$$

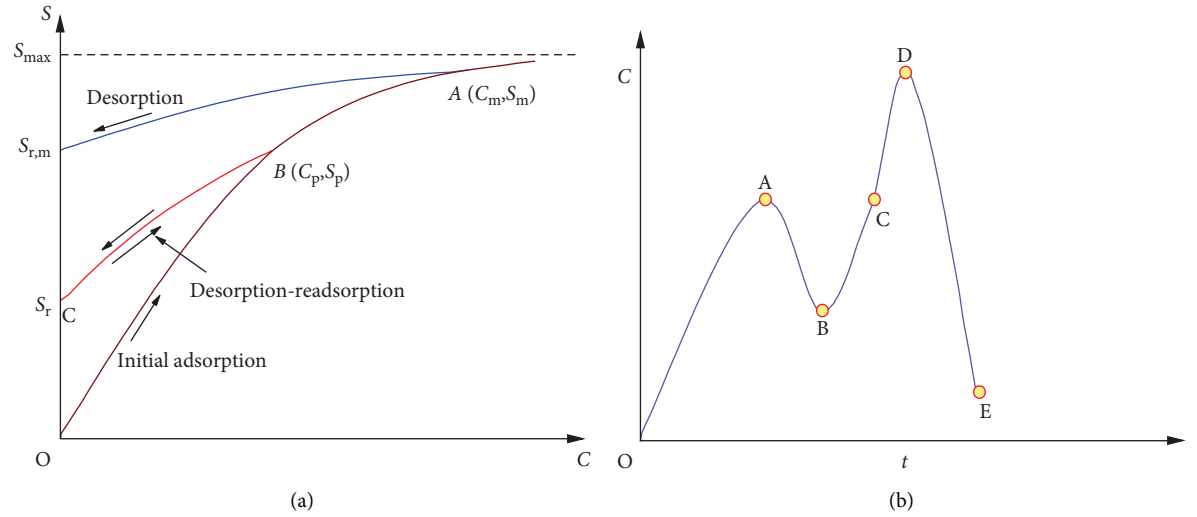

FIGURE 1: Schematic diagram of adsorption history model: (a) absorption-desorption process and (b) solution concentration variation of a point with time.

The expression of hydrodynamic dispersion coefficient tensor can be obtained when the main direction of seepage velocity in porous media [34–36] is consistent with the selected coordinates, and molecular diffusion is ignored

$$D_{ij} = \begin{bmatrix} \alpha_L v & 0 & 0 \\ 0 & \alpha_T v & 0 \\ 0 & 0 & \alpha_T v \end{bmatrix}, \tag{4}$$

where α_L is the longitudinal dispersion of porous media (L), and α_T is the transverse dispersion of porous media (L),

It is assumed that the velocity in the plane direction is mainly caused by pressure difference, and the velocity in the vertical direction is mainly caused by gravity [25]. The adsorption term of the governing equation represents the adsorption/desorption of pollutants in porous media [37], which has been discussed in previous literature [38, 39]. Actually, several important isothermal adsorption models such as Langmuir, Freundlich, and Dubinin–Radushkevich were reported previously, which was already applied to dye adsorption/desorption processes in environmental, biological, and chemical industries [40].

Combined with the famous adsorption history model proposed by Bai et al. [2, 3] (i.e., Bai model), we can get

$$\begin{aligned} &\frac{\partial C}{\partial t} = \nabla \bullet \left(\frac{\mathbf{D}}{R} \bullet \nabla C - \frac{\mathbf{v}}{R} C \right); R = \frac{\rho_b}{\theta} k_{NF} + 1, \\ &k_{NF} = \frac{\partial C_d}{\partial C} = \begin{cases} k_d \bullet e^{-\beta_1 c/c_l}, \text{ (initial ads orption)}, \\ k_r \bullet e^{-\beta_2 c/c_l}, \text{ (desorption process)}, \end{cases} \end{aligned} \tag{5}$$

where v is the rate of penetration (LT^{-1}), R is the retardation factor, k_d is the adsorption equilibrium coefficient (L^3M^{-1}), k_r is the desorption equilibrium coefficient (L^3M^{-1}), k_{NF} is the equilibrium coefficient (L^3M^{-1}), β_1 is the attenuation coefficient of initial adsorption (L^3M^{-1}), β_2 is the attenuation coefficient of desorption process (L^3M^{-1}), C_l is the characteristic concentration (MM^{-1}), and C_p is the maximum concentration before desorption (MM^{-1}).

When $\beta_1 = \beta_2 = 0$, it is a linear nonequilibrium adsorption process (Figure 1(a)). On the contrary, the adsorption history effect can be considered as a nonlinear nonequilibrium model.

In the past, the transport of pollution is generally characterized by the first-order attachment kinetics [25]. Here, a nonlinear attachment-detachment model with hysteresis is used. The attachment/desorption rate in equation (1) can be written as [2, 3]

$$\frac{\partial (C_d)}{\partial t} = \lambda \cdot (S - C_d), \tag{6}$$

where λ is the reaction rate (T^{-1}), and S is the equilibrium concentration (MM^{-1}).

The parameter λ denotes the mass conversion between moving and attached pollution under water flow and actually indicates the hysteretic effect of pollution attached onto the matrix. The determination method of some parameters was discussed in some previous references [26, 41], which is a very promising method for measuring migration parameters.

2.2. Model Characteristics and Numerical Calculation. Figure 1 shows that when the concentration in the solution increases (e.g., from point O to point B and further to point A), the adsorption rate decreases. There is a maximum adsorption concentration ($C_{d,\,max}$). When the concentration decreases from a certain point (e.g., point B), a desorption reaction occurs, and its magnitude is related to the maximum concentration of C_P. When adsorption occurs again due to the increment of solution concentration, the readsorption process is reversed along the desorption process (i.e., CB), and the readsorption capacity is weakened

Table 1: Model parameters.

Parameters	ρ_b g/cm^3	L cm	r cm	n	α_x cm	u_0 cm/s	K_d m^3/g	C_0 mol/L
Value	2.65	30	4.0	0.451	0.9	0.15	0.1	2

compared with the initial adsorption process (i.e., OB), indicating that the model is related to the adsorption history of porous media.

It is assumed that the concentration at a certain point in the pollution space changes with time, as shown in Figure 1(b). Then, in the stage OA, the pollutant concentration increases, and the porous medium undergoes an initial adsorption reaction. During stage AB, the concentration of pollutants decreases, and the porous medium undergoes a desorption reaction. In the later stage (e.g., stage BC), when the concentration increases again, the adsorption reaction occurs again, and the change path is opposite to that of the desorption reaction in stage AB. During the numerical calculation, it is necessary to record the concentration peak (i.e., deposition history) during the concentration change process. Of course, when the concentration is higher than point A in the CD stage, it continues along the initial adsorption process [41–43].

The coupling calculation is carried out using the physical field of "dilute matter transfer in porous media" and the mathematical field of "domain ordinary differential and differential algebraic equations" in COMSOL Multiphysics 5.4. Special solution settings complete the numerical model calculation. The time step algorithm uses the backward difference formula (BDF). According to existed literature [2, 3, 6, 24], the selected calculation parameters can be seen in Table 1.

3. Adsorption History Effect of Pollutant Migration under a Point Source

3.1. Model Establishment. Taking a point source case as an example, the influence of adsorption history on the pollutant migration process is analyzed. It is specified that the positive direction of water flow is the positive direction of x, and it is assumed that the model is a part of the semi-infinite soil layer. Therefore, the six surface boundaries of the cuboid model are set as the outflow boundary. The pollutants can flow freely from the boundary during the migration process. The pollution source will be set in the cuboid formation and vary according to schemes. To improve the calculation accuracy, the relative tolerance is set to 0.0001, the duration is from 0 to 200 d, and the time step is 1 d.

For convenience, the point source of the pollution source is set at the center of the plane, that is, the coordinates (25 m, 25 m). The concentration can be set to exponential attenuation, i.e.,

$$c = 10 \times e^{-(t/T)}, \tag{7}$$

where C is the concentration (in mol/l), and T represents the attenuation period of pollutants.

The initial value of concentration is set as 10 mol/l, and the attenuation period is assumed to be 100 d. The migration of point source pollutants in cuboid formation can be obtained by calculating the model (Figure 2). Figure 2 indicates that the diffusion trajectory of the point source is approximately a cone, which gradually expands outward from the pollution source. Here, we will explore the characteristics of the adsorption history model from the two perspectives of line and surface.

3.2. Case of a Line Segment. Take a line segment to analyze the concentration change, and the coordinates at both ends of the line segment are (0, 25, 15), (100, 25, 15). The change of concentration with time at this line segment is taken and compared with the previous linear model (Figure 3). From the concentration change of the nonlinear adsorption history model, the pollutant distribution range is 30 m–40 m at 20 d, and the concentration value is small. With the increase of time, the diffusion range of pollutants gradually expands, and the maximum concentration first increases and then decreases. Thus, in the early stage of pollutant (point source attenuation) migration, the peak concentration is higher, but the pollutant distribution range is smaller. The peak concentration will decrease when the pollutant distribution range increases. The concentration distribution of the nonlinear model is similar to that of the adsorption history model. However, the pollutants in the adsorption history model are more significant, and the gap becomes larger and more prominent with time. This shows that the adsorption capacity of the adsorption history model is weaker than that of the nonlinear nonequilibrium model.

Similarly, take another line segment in the model, and the coordinates at both ends of the line segment are (0, 25, 35), (100, 25, 35). The concentration value at this curve has decreased, which proves that the pollutant concentration at the bottom of the model is higher than that at the top under the action of gravity. From the perspective of concentration changes, the peak concentration changes less, and the concentration changes are more smoothly with time.

3.3. Changes of Pollutants at the Section. The $z = 10$, 30 m plane is intercepted to study the changes of concentration distribution with time. Compare the adsorption history model with the linear model, as shown in Figure 4. For the adsorption history model, at 30 d, the pollutant migrates to the cross section at $z = 10$ m. At 60 d, the pollutant propagation area has reached 1316.7 m^2, the propagation range in the x direction is 29.5 m–73.4 m, and the maximum concentration in the center is 0.01 mol/l. With increased time, the transmission area of pollutants gradually increases. Due to the attenuation of the pollution source, the propagation range moves with the seepage direction. In the case of continuous seepage, pollutants will eventually flow out of the model. Compared with the adsorption history model, the linear model has a more vital ability to block the migration of pollutants. For example, at 35 d, the pollutants diffuse to the cross section, and at 60 d, the pollutant propagation area reaches 1173.4 m^2, the propagation range in the x direction is

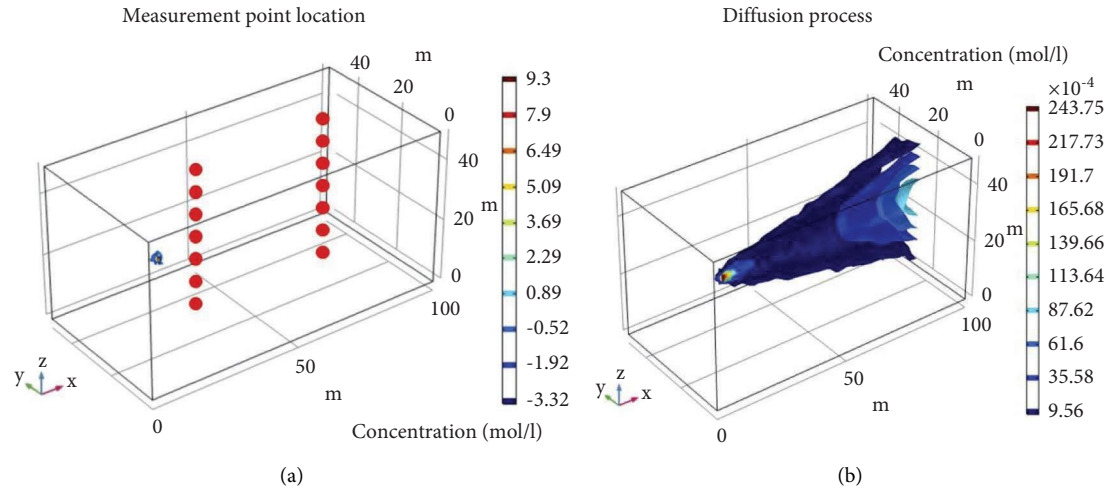

Figure 2: The diffusion trajectory of point source problem: (a) measurement point location and (b) diffusion process.

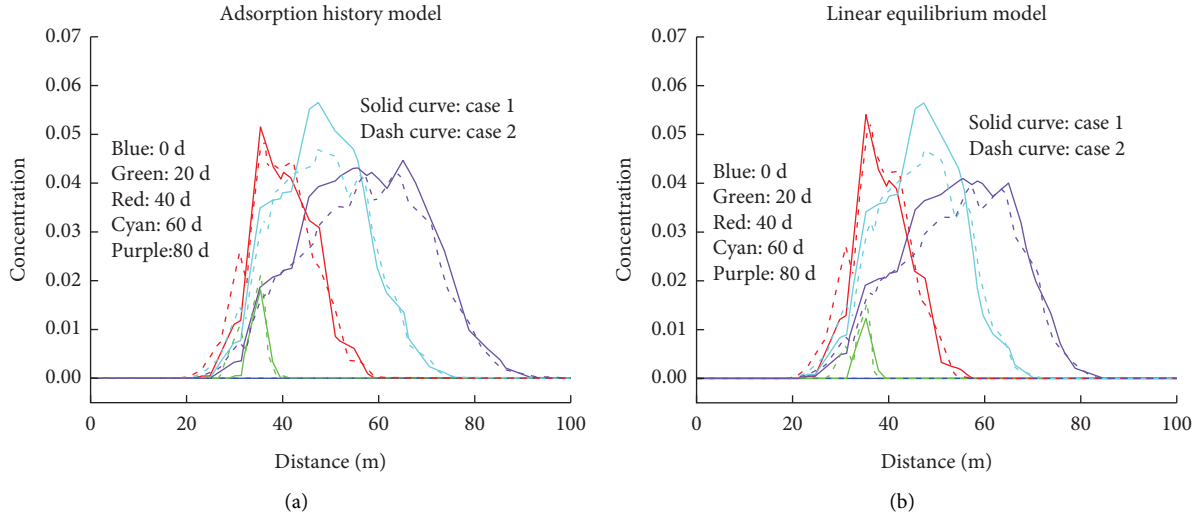

Figure 3: Concentration distribution on the x-axis calculated by (a) adsorption history model and (b) linear equilibrium model.

28.5 m–68.3 m, and the maximum concentration in the center is 0.01 mol/l. Compared with the adsorption history model, the pollutant propagation range in the linear model is more diminutive. For section $x = 30$ m, its fundamental law is similar to that of section $x = 10$ m.

3.4. Influence of Head Difference Change. The head difference mainly controls the seepage velocity for the porous geomaterials such as loose soil layer, soft rock, and fractured rock mass. Hence, the calculation scheme considered the effect of different seepage velocities (Figure 5). For example, comparing the distribution of pollutants in 60 days vertically, when the head difference is 10 m, the distribution range of pollutants is 1620.2 m^2. When the head difference is 25 m, the pollutant distribution range is 2759.8 m^2, and the concentration value basically remains unchanged. The head difference (seepage velocity) significantly impacts the migration of pollutants. The larger the head difference, the larger the pollutants migration and diffusion area. From the comparison result, the head difference only affects the pollutant migration in the seepage direction but has no significant impact on the horizontal diffusion. By horizontal comparison, the concentration value decreases with the increase of pollutant transmission area. It should be noted that the physical mechanisms can be attributed to the head difference and gravity.

4. Volume Pollution Source

The established geometric model is 800 m long, 400 m wide, and 400 m high, which is set as isotropic saturated porous media. The volume source pollutants are simplified as a sphere with a diameter of 20 m, and its central coordinates are 200 m, 200 m, 200 m, located in the middle of the stratigraphic model near the left.

Assuming that there is a pollutant leakage in all directions of the volume source, the boundary condition

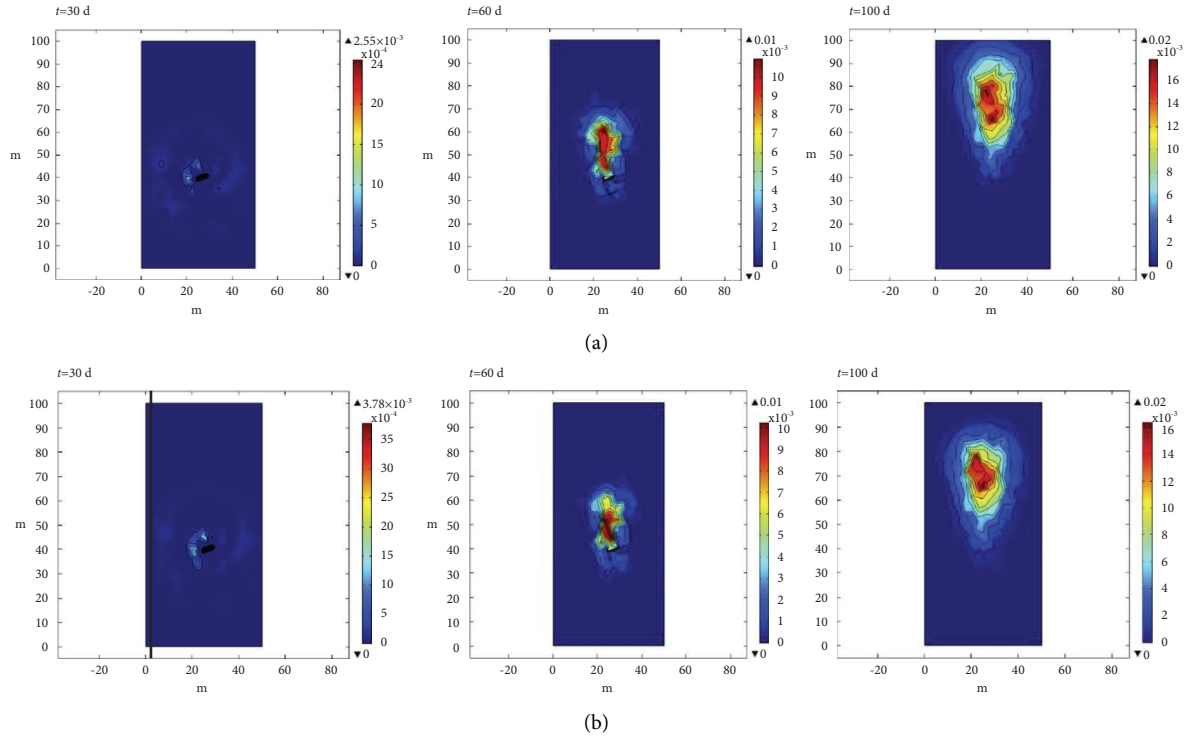

Figure 4: Concentration change in section $z = 10$ m at $t = 30$, 60, 100 d: (a) adsorption history model and (b) linear model.

setting and meshing are consistent with the point source model, and each side of the cuboid is set as the outflow boundary condition. The specific geometric modeling is shown in Figure 6. The spherical boundary is set as the concentration boundary condition. To reflect the concentration attenuation of pollutants, the concentration value is set as

$$c = 10 \times e^{-(t/3000d)}. \tag{8}$$

The concentration attenuation period is set as 3000 d. The diffusion trajectory of pollutants obtained by calculation is shown in Figure 6. The characteristic sections $z = 100$, 300 m are intercepted, and the variation of the concentration of each section with time is shown in Figure 7. The area of pollutants is greatly expanded compared with the point source model. The diffusion rate of pollutants is also significantly increased. For example, at $z = 200$ m, the pollutant area is 97729 m^2 at 300 d, the maximum concentration value is 7.41 mol/l, and the reverse migration distance of pollutants along the x-axis is 53 m. At 800 d, the pollutant area is 234920 m^2, the maximum concentration is 4.49 mol/l, and the reverse migration distance of pollutants along the x-axis is 70 m. This section is in the center of the volume source, with a larger diffusion area and higher concentration of pollutants. It is evident that although the diffusion area of this section is larger, the propagation distance becomes shorter. The closer to the center of the pollution source, the weaker the influence of dispersion on the diffusion of pollutants in the main seepage direction. Under the volume source model, pollutants can propagate in the reverse seepage direction, causing pollution upstream. Therefore, in the actual process of pollutant prevention and control, we should also pay attention to the pollution of the groundwater upstream.

The characteristic sections $y = 100$, 300 m are intercepted, and the variation of the concentration of each section with time is shown in Figure 8. The maximum concentration value at this section shows a trend of increasing first and then decreasing. The maximum concentration value will also decrease with the increase of pollutant area in the volume source model. For example, at $y = 100$ m, the pollutant area is 50605 m^2 at 300 d, and the maximum concentration value is 0.2 5 mol/l. At 600 d, the pollutant area is 161300 m^2, and the maximum concentration is 0.31 mol/l. At 800 d, the pollutant area is 211270 m^2, and the maximum concentration is 0.29 mol/l.

Comparing the two sections, it can be found that the changes of pollutants in the symmetrical sections on both sides of the center of the pollution source are the same. The diffusion of pollutants in the direction perpendicular to the main seepage is mainly affected by dispersion and is symmetrically distributed. The effect of countercurrent propagation of pollutants can be seen from the migration of pollutants in the section at $y = 300$ m.

The characteristic sections $x = 300$ m, 400 m are intercepted, and the variation of the concentration of each section with time is shown in Figure 9. In the direction perpendicular to the main seepage flow, the diffusion of pollutants is mainly affected by dispersion. The range and concentration of pollutants increase first and then decrease. Dispersion leads to the increase of pollutant area. However,

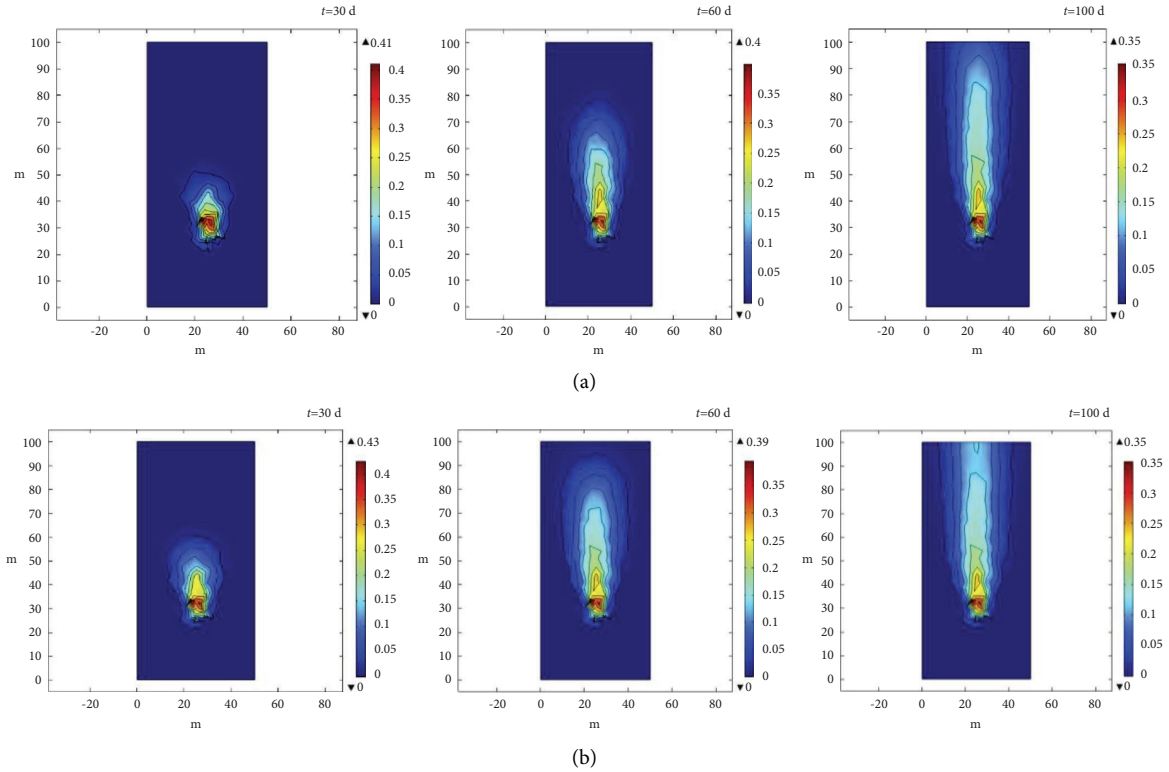

Figure 5: Influence of water head difference at $t = 30$, 60, 100 d: (a) $h = 15$ m and (b) $h = 25$ m.

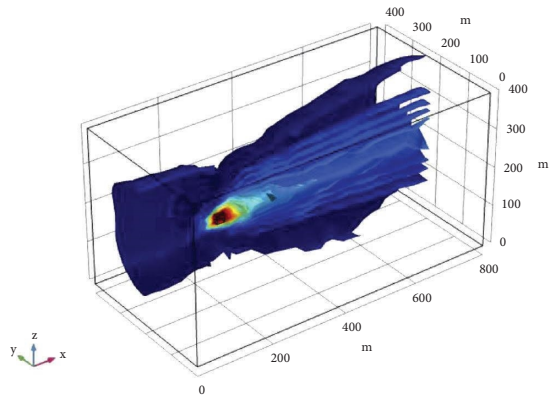

Figure 6: Volume pollutant source geometric model and diffusion trajectory.

because the seepage effect is stronger than the dispersion effect, the pollutant range and concentration value on the x section will decrease with the attenuation of the concentration of the pollution source. For example, at $x = 400$ m, the pollutant area is 7653 m^2 at 150 d, and the maximum concentration value is 0.05 mol/l. At 300 d, the pollutant area is 72047 m^2, and the maximum concentration is 1.18 mol/l. At 800 d, the pollutant area is 77171 m^2, and the maximum concentration is 1.28 mol/l. By comparison, the longer the section is from the pollution source, the later the pollutants appear, the faster the diffusion speed of pollutants, and the lower the concentration of pollutants. In the volume source model, the propagation of pollutants is still conical. The closer the pollution source, the smaller the propagation range, and the higher the concentration value. The farther away from the pollution source, the larger the propagation range, and the smaller the concentration value.

The three-dimensional nonlinear nonequilibrium adsorption model that takes into account the adsorption history can be used to reveal the diffusion law of pollutants under regular three-dimensional boundary conditions. That is, this model considers the probable increase or decrease of seepage velocity as well as pollutant concentration in practical engineering. The transport laws of pollution sources in three-dimensional spatial are also of interest in real pollution problems such as changes in the diffusion rate

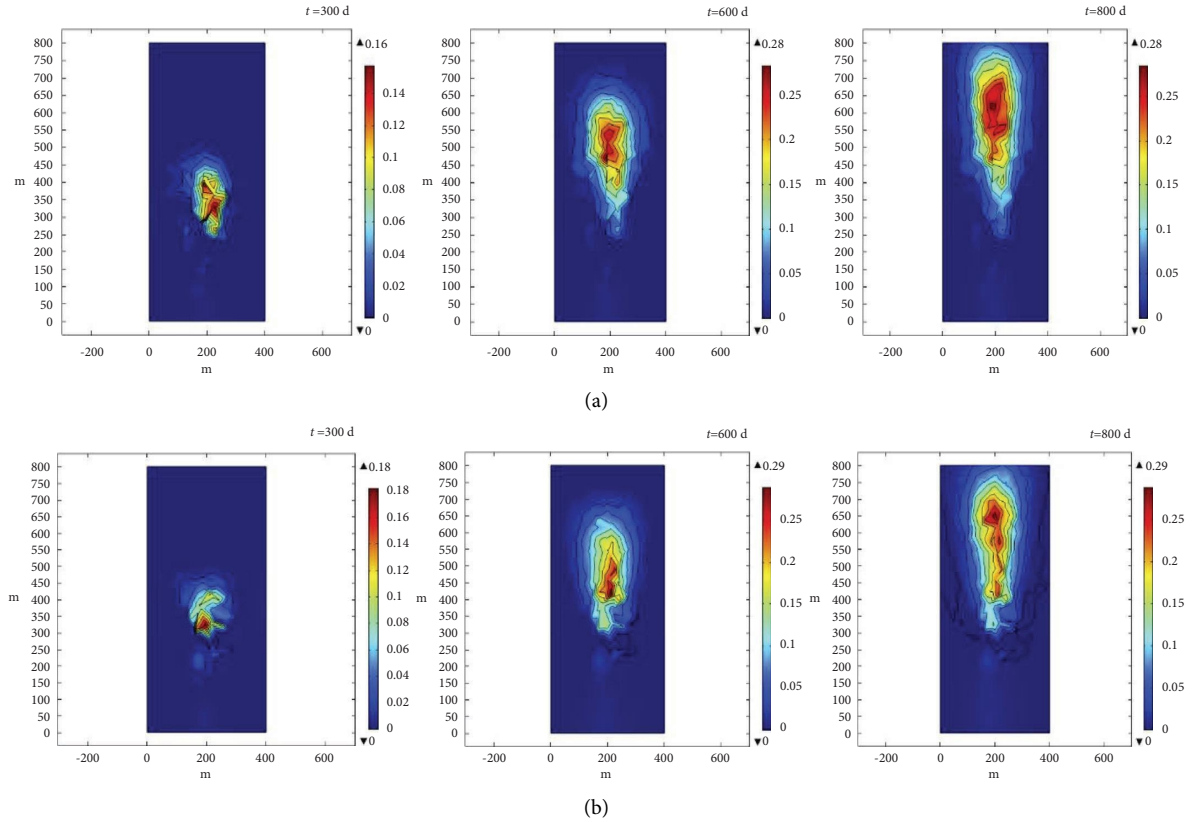

Figure 7: Analysis of pollutant migration characteristics in z-section at $t = 300$, 600, 800 d: (a) $z = 100$ m and (b) $z = 300$ m.

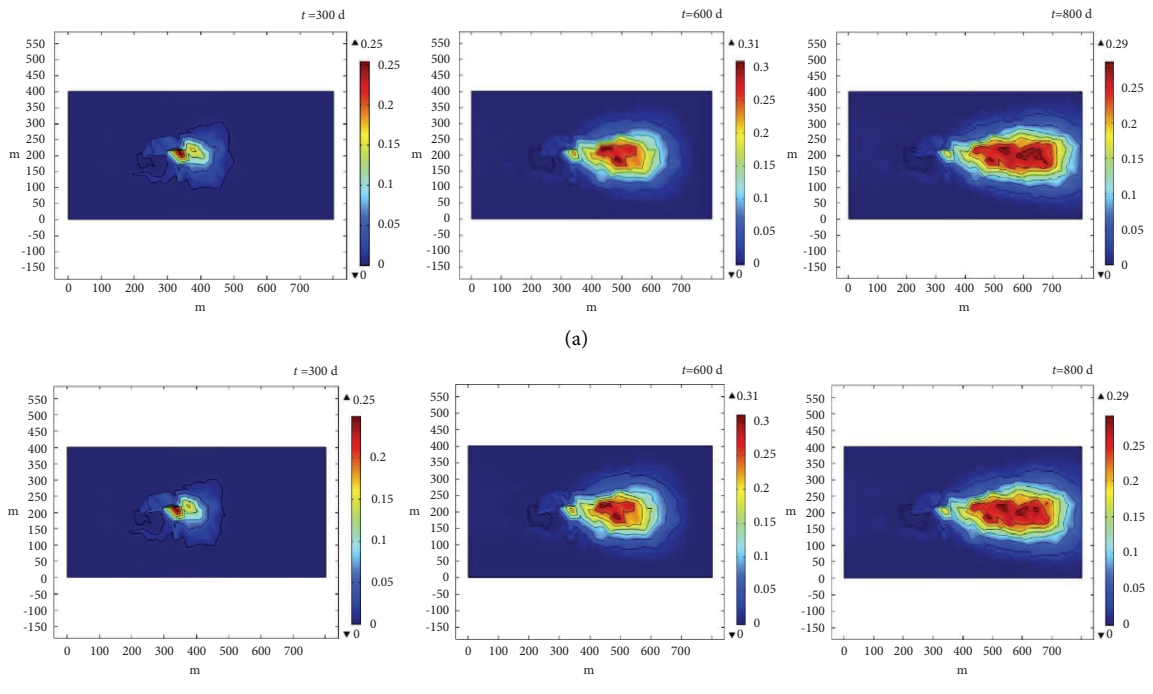

Figure 8: Analysis of pollutant migration characteristics in y-section at $t = 300$, 600, 800 d: (a) $y = 100$ m and (b) $y = 300$ m.

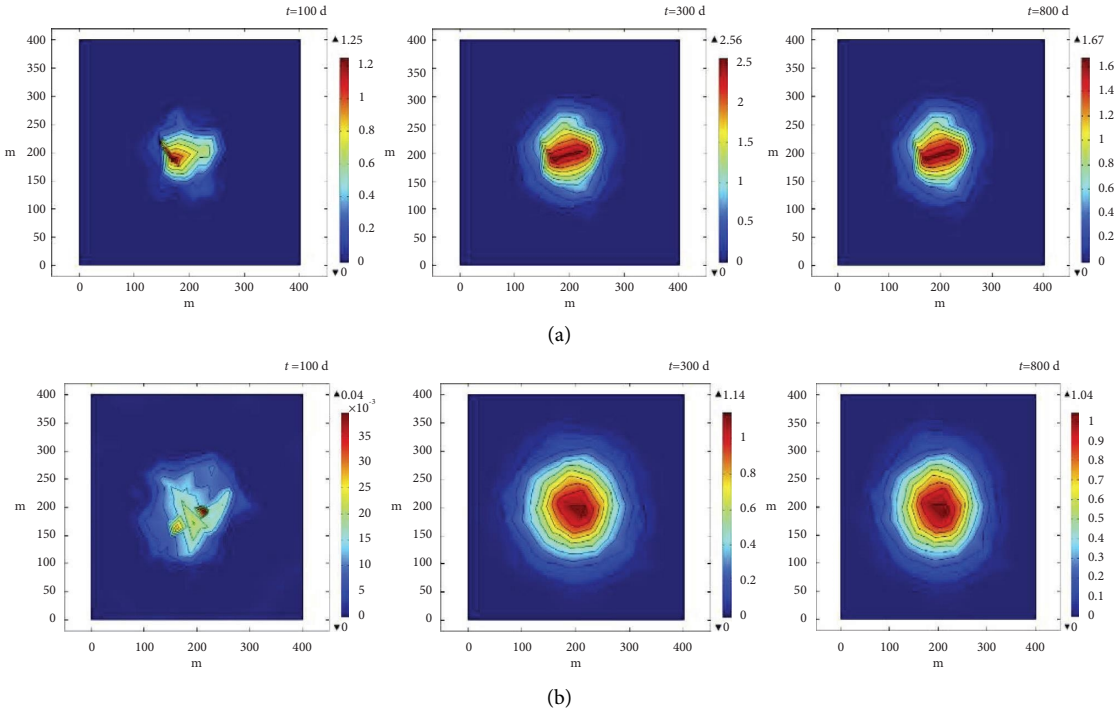

Figure 9: Analysis of pollutant migration characteristics in x-section at $t = 100$, 300, 800 d: (a) $x = 300$ m and (b) $x = 400$ m.

and concentration field of pollutants. The problem of pollutant diffusion under complex boundary conditions (e.g., the variation of seepage direction and gravity effect) should be discussed in the future.

5. Conclusions

A governing equation is obtained by embedding a nonlinear nonequilibrium adsorption model (i.e., Bai model) considering the adsorption history in the three-dimensional situation, which can be easily applied to solve practical engineering problems. The concentration peak of the nonlinear nonequilibrium adsorption history model is higher than that of the linear model, and the peak concentration appears slightly in advance. The pollution source tends to migrate horizontally along the water flow direction, and the diffusion capacity in the vertical direction is small. Due to the influence of gravity, the concentration changes at the symmetrical position of the vertical distance are different, and the bottom concentration is higher than the upper concentration.

In the early stage of pollutant migration, the peak concentration is high, but the distribution range of pollutants is small. When the distribution range of pollutants increases, the peak concentration will decrease. Compared with the adsorption history model, the linear model has a more vital ability to block the migration of pollutants. The longer the time, the more significant the gap between the two models. Close to the center of the pollution source, the gap between the two models increases. By changing the attenuation period of the pollution source, the longer the attenuation period is, the wider the diffusion range is, but the longer the time it takes for the pollutants to migrate out of the model entirely, and different sections have different regular distributions.

For the volume source model, the pollutant concentration is higher than that of the point source model, and the diffusion range of each section is more comprehensive. The closer to the center of the pollution source, the weaker the influence of dispersion on the diffusion of pollutants in the main seepage direction, and the pollutants will spread in the countercurrent direction, causing pollution upstream. The diffusion of pollutants in the direction perpendicular to the main seepage is mainly affected by dispersion and is symmetrically distributed.

Notations

C: Pollutant concentration in porous media
C_d: Adsorption concentration
C_l: Characteristic concentration
C_p: Maximum concentration before desorption
D: Hydrodynamic dispersion coefficient
k_d: Adsorption equilibrium coefficient
k_r: Desorption equilibrium coefficient
k_{NF}: Equilibrium coefficient
L: Length of soil column
r: Soil column radius
R: Retardation factor
t: Time
T: Pollutant attenuation period
u: Average velocity of cross section
v: Penetration rate
β_1: Attenuation coefficient of initial adsorption
β_2: Attenuation coefficient of desorption process
∇: Vector gradient operator

ρ_b: Volumetric dry density of porous media
$(D_d)_{ij}$: Mechanical dispersion coefficient tensor
$D^*\tau_{ij}$: Molecular diffusion coefficient tensor
τ_{ij}: Curvature tensor
α_L: Longitudinal dispersion of porous media
α_T: Transverse dispersion of porous media
α_x: Tortuosity degree
θ: Porous media porosity.

Data Availability

The data supporting the current study are available from the corresponding author upon request.

Conflicts of Interest

WC, SZ, and WL are employed by the Beijing Guodaotong Highway Design & Research institute Co., Ltd. GZ, PZ, and SY are employed by the Beijing Uni.-Construction Group Co., Ltd. The authors declare that they have no conflicts of interest.

Authors' Contributions

The main contribution of ZM in this paper is methodology, and the other authors (WC, GZ, PZ, SZ, WL, and SY) contributed to investigation and analysis.

Acknowledgments

This research was funded by the Beijing Natural Science Foundation (8222023).

References

[1] A. Tiraferri, T. Tosco, and R. Sethi, "Transport and retention of microparticles in packed sand columns at low and intermediate ionic strengths: experiments and mathematical modeling," *Environmental Earth Sciences*, vol. 63, no. 4, pp. 847–859, 2011.

[2] B. Bai, Q. Nie, H. Wu, and J. Hou, "The attachment-detachment mechanism of ionic/nanoscale/microscale substances on quartz sand in water," *Powder Technology*, vol. 394, pp. 1158–1168, 2021.

[3] B. Bai, S. Jiang, L. Liu, X. Li, and H. Wu, "The transport of silica powders and lead ions under unsteady flow and variable injection concentrations," *Powder Technology*, vol. 387, pp. 22–30, 2021.

[4] N. M. Mahmoodi, M. Ghezelbash, M. Shabanian, F. Aryanasab, and M. R. Saeb, "Efficient removal of cationic dyes from colored wastewaters by dithiocarbamate-functionalized graphene oxide nanosheets: from synthesis to detailed kinetics studies," *Journal of the Taiwan Institute of Chemical Engineers*, vol. 81, pp. 239–246, 2017.

[5] B. Bai, G. Yang, T. Li, and G. Yang, "A thermodynamic constitutive model with temperature effect based on particle rearrangement for geomaterials," *Mechanics of Materials*, vol. 139, Article ID 103180, 2019.

[6] B. Bai, F. Bai, C. Sun, Q. Nie, and S. Sun, "Adsorption mechanism of shell powders on heavy metal ions Pb^{2+}/Cd^{2+} and the purification efficiency for contaminated soils," *Frontiers of Earth Science*, vol. 10, Article ID 1071228, 2023.

[7] N. D. Ahfir, H. Q. Wang, A. Benamar, A. Alem, N. Massei, and J. P. Dupont, "Transport and deposition of suspended particles in saturated porous media: hydrodynamic effect," *Hydrogeology Journal*, vol. 15, no. 4, pp. 659–668, 2007.

[8] B. Bai, T. Xu, Q. Nie, and P. Li, "Temperature-driven migration of heavy metal Pb^{2+} along with moisture movement in unsaturated soils," *International Journal of Heat and Mass Transfer*, vol. 153, Article ID 119573, 2020.

[9] S. K. Yadav, A. Kumar, D. K. Jaiswal, and N. Kumar, "One-dimensional unsteady solute transport along unsteady flow through inhomogeneous medium," *Journal of Earth System Science*, vol. 120, no. 2, pp. 205–213, 2011.

[10] B. Bai, R. Zhou, G. Cai, W. Hu, and G. Yang, "Coupled thermo-hydro-mechanical mechanism in view of the soil particle rearrangement of granular thermodynamics," *Computers and Geotechnics*, vol. 137, no. 8, Article ID 104272, 2021.

[11] D. K. Jaiswal, A. Kumar, N. Kumar, and R. Yadav, "Analytical solutions for temporally and spatially dependent solute dispersion of pulse type input concentration in one-dimensional semi-infinite media," *Journal of Hydro-environment Research*, vol. 2, no. 4, pp. 254–263, 2009.

[12] X. Cui, Y. Fan, H. Wang, and S. Huang, "Ground environment characteristics during the operation of GWHP considering the particle deposition effect," *Energy and Buildings*, vol. 206, Article ID 109593, 2020.

[13] W. Hu, W. Cheng, S. Wen, and M. Mizanur Rahman, "Effects of chemical contamination on microscale structural characteristics of intact loess and resultant macroscale mechanical properties," *Catena*, vol. 203, Article ID 203105361, 2021.

[14] S. R. Mousavi, M. Asghari, and N. M. Mahmoodi, "Chitosan-wrapped multiwalled carbon nanotube as filler within PEBA thin film nanocomposite (TFN) membrane to improve dye removal," *Carbohydrate Polymers*, vol. 237, Article ID 116128, 2020.

[15] H. J. Kim, T. Phenrat, R. D. Tilton, and G. V. Lowry, "Effect of kaolinite, silica fines and pH on transport of polymer-modified zero valent iron nano-particles in heterogeneous porous media," *Journal of Colloid and Interface Science*, vol. 370, pp. 1–10, 2012.

[16] F. Hosseini, S. Sadighian, H. Hosseini-Monfared, and N. M. Mahmoodi, "Dye removal and kinetics of adsorption by magnetic chitosan nanoparticles," *Desalination and Water Treatment*, vol. 57, no. 51, pp. 24378–24386, 2016.

[17] S. García-García, S. Wold, and M. Jonsson, "Effects of temperature on the stability of colloidal montmorillonite particles at different pH and ionic strength," *Applied Clay Science*, vol. 43, no. 1, pp. 21–26, 2009.

[18] C. B. Lake and R. K. Rowe, "Diffusion of sodium and chloride through geosynthetic clay liners," *Geotextiles and Geomembranes*, vol. 18, no. 2-4, pp. 103–131, 2000.

[19] X. Cui, T. Wen, J. Li et al., "Migration and deposition characteristics of particles in sand layers with fluctuating water levels," *Water, Air, & Soil Pollution*, vol. 233, no. 139, pp. 1–14, 2022.

[20] A. A. Porubcan and S. Xu, "Colloid straining within saturated heterogeneous porous media," *Water Research*, vol. 45, no. 4, pp. 1796–1806, 2011.

[21] N. M. Mahmoodi, A. Taghizadeh, M. Taghizadeh, and M. Azimi Shahali Baglou, "Surface modified montmorillonite with cationic surfactants: preparation, characterization, and dye adsorption from aqueous solution," *Journal of Environmental Chemical Engineering*, vol. 7, no. 4, Article ID 103243, 2019.

[22] X. Cui, Y. Fan, H. Wang, and S. Huang, "Experimental investigation of suspended particles transport in porous medium under variable temperatures," *Hydrological Processes*, vol. 33, no. 7, pp. 1117–1126, 2019.

[23] X. Cui, D. Wu, H. Wang, S. Ding, and Y. Fan, "Pore features and seepage characteristics of natural gap graded sand with two size distributions," *Géotechnique*, pp. 1–12, 2022.

[24] B. Bai, R. Zhou, G. Yang, W. Zou, and W. Yuan, "The constitutive behavior and dissociation effect of hydrate-bearing sediment within a granular thermodynamic framework," *Ocean Engineering*, vol. 268, Article ID 113408, 2023.

[25] B. Bai, H. Li, T. Xu, and X. Chen, "Analytical solutions for contaminant transport in a semi-infinite porous medium using the source function method," *Computers and Geotechnics*, vol. 69, pp. 114–123, 2015.

[26] B. Bai, F. Long, D. Rao, and T. Xu, "The effect of temperature on the seepage transport of suspended particles in a porous medium," *Hydrological Processes*, vol. 31, no. 2, pp. 382–393, 2017.

[27] F. J. Leij, N. Toride, and M. T. van Genuchten, "Analytical solutions for non-equilibrium solute transport in three-dimensional porous media," *Journal of Hydrology*, vol. 151, no. 2–4, pp. 193–228, 1993.

[28] A. K. Dahaghi, V. Gholami, and J. Moghadasi, "A novel workflow to model permeability impairment through particle movement and deposition in porous media," *Transport in Porous Media*, vol. 86, no. 3, pp. 867–879, 2011.

[29] R. K. Rowe and J. R. Booker, "Modelling of two-dimensional contaminant migration in a layered and fractured zone beneath landfills," *Canadian Geotechnical Journal*, vol. 28, no. 3, pp. 338–352, 1991.

[30] C. Miracapillo and L. Ferroni, "Numerical simulation of radionuclides migration in the far field of a geological repository," *Energy Procedia*, vol. 82, 2015.

[31] M. Trofa, M. Vocciante, G. D'Avino, M. A. Hulsen, F. Greco, and P. L. Maffettone, "Numerical simulations of the competition between the effects of inertia and viscoelasticity on particle migration in Poiseuille flow," *Computers & Fluids*, vol. 107, pp. 214–223, 2015.

[32] M. M. Villone, F. Greco, M. A. Hulsen, and P. Maffettone, "Simulations of an elastic particle in Newtonian and viscoelastic fluids subjected to confined shear flow," *Journal of Non-newtonian Fluid Mechanics*, vol. 210, pp. 47–55, 2014.

[33] E. V. Mironenko and Y. A. Pachepsky, "Analytical solution for chemical transport with non-equilibrium mass transfer, adsorption and biological transformation," *Journal of Hydrology*, vol. 70, no. 1-4, pp. 167–175, 1984.

[34] Z. Xue, W. Cheng, L. Wang, and W. Hu, "Effects of bacterial inoculation and calcium source on microbial-induced carbonate precipitation for lead remediation," *Journal of Hazardous Materials*, vol. 426, Article ID 128090, 2022.

[35] W. Cheng, X. Bai, B. Sheil, G. Li, and F. Wang, "Identifying characteristics of pipejacking parameters to assess geological conditions using optimisation algorithm-based support vector machines," *Tunnelling and Underground Space Technology*, vol. 106, Article ID 103592, 2020.

[36] S. A. Hosseini, M. Vossoughi, N. M. Mahmoodi, and M. Sadrzadeh, "Clay-based electrospun nanofibrous membranes for colored wastewater treatment," *Applied Clay Science*, vol. 168, pp. 77–86, 2019.

[37] B. Hayati, N. M. Mahmoodi, and A. Maleki, "Dendrimer–titania nanocomposite: synthesis and dye-removal capacity," *Research on Chemical Intermediates*, vol. 41, no. 6, pp. 3743–3757, 2015.

[38] N. M. Mahmoodi, "Synthesis ofmagnetic carbon nanotube and photocatalytic dye degradation ability," *Environmental Monitoring and Assessment*, vol. 186, no. 9, pp. 5595–5604, 2014.

[39] N. M. Mahmoodi, B. Hayati, H. Bahrami, and M. Arami, "Dye adsorption and desorption properties of mentha pulegium in single and binary systems," *Journal of Applied Polymer Science*, vol. 122, no. 3, pp. 1489–1499, 2011.

[40] A. Almasian, N. M. Mahmoodi, and M. E. Olya, "Tectomer grafted nanofiber: synthesis, characterization and dye removal ability from multicomponent system," *Journal of Industrial and Engineering Chemistry*, vol. 32, pp. 85–98, 2015.

[41] B. Bai, Q. Nie, Y. Zhang, X. Wang, and W. Hu, "Cotransport of heavy metals and SiO_2 particles at different temperatures by seepage," *Journal of Hydrology*, vol. 597, Article ID 125771, 2021.

[42] W. Hu, W. Cheng, S. Wen, and K. Yuan, "Revealing the enhancement and degradation mechanisms affecting the performance of carbonate precipitation in EICP Process," *Frontiers in Bioengineering and Biotechnology*, vol. 9, Article ID 750258, 2021.

[43] B. Bai, B. Fan, X. Li, Q. Nie, X. Jia, and H. Wu, "The remediation efficiency of heavy metal pollutants in water by industrial red mud particle waste," *Environmental Technology & Innovation*, vol. 28, 2022.

Hindawi
Advances in Civil Engineering
Volume 2023, Article ID 9096839, 10 pages
https://doi.org/10.1155/2023/9096839

Research Article

Theoretical Study of a Design Method for Underexcavation in Building Rectification

Jun-Hua Xiao,[1,2] **Jian-Ping Sun**,[1,2] **Xin Zhang**,[1,2] **Zong-Bao Jiang**,[3] **and Dao-Tong Guo**[4]

[1]*School of Civil Engineering, Shandong Jianzhu University, Jinan 250101, China*
[2]*Key Laboratory of Building Structural Retrofitting and Underground Space Engineering (Shandong Jianzhu University), Ministry of Education, Jinan 250101, China*
[3]*Shandong Jianzhu University Engineering Appraisal and Strengthening Design Co., Ltd., Jinan 250014, China*
[4]*Shandong Jiangu Special Engineering Co., Ltd., Jinan 250014, China*

Correspondence should be addressed to Jun-Hua Xiao; 13606412056@163.com

Received 2 May 2022; Revised 20 June 2022; Accepted 5 April 2023; Published 20 April 2023

Academic Editor: Jiang Xiangang

For buildings with shallow foundations embedded in natural soil sediments, the underexcavation method is often used to correct building inclination. Relying on engineering experience and close field monitoring, rectification has been conducted successfully. However, theoretical studies are relatively scarce, resulting in an inadequately informed rectification design and procedure. Assuming the soil is an ideal elastic-plastic body, a simplified analysis was adopted to study the issue theoretically. First, the redistribution of the base contact pressure after building inclination was deduced. Second, according to the force balance between the total contact pressure of the base and the total stress on the horizontal plane at the excavation hole, the limit hole spacing at the critical state of building back tilt was obtained, which was also the preferable hole spacing for soil strip collapse. Third, because the amount of anticipated forced settlement at a certain section of soil excavation is equal to the volume of soil hole collapse, an accurate formula for the hole diameter was obtained. Combined with engineering experience, suggestions for the design procedure were proposed. Finally, two case histories were introduced to verify the correctness and practicability of the theoretical formula for hole spacing and diameter. These two key parameters provide a strong theoretical basis for building rectification in future engineering practice.

1. Introduction

In engineering practice, building inclination often occurs due to design error, severe settlement, or surrounding underground construction. For buildings with shallow foundations based on natural sediment layers or reinforced soil layers, underexcavation is the least intrusive and most economical method for building rectification [1–3]. The success of rectification and building safety heavily depend on close monitoring and dynamic construction. Theoretical guidance is urgently needed in construction design and correction. Based on the small hole expansion theory and Tresca yield criterion, a formula was reported to determine the radius of the plastic zone [4]. By submitting the Mohr–Coulomb failure criterion to an elastic solution of the stress around the hole for the plane strain problem, an analytical plastic zone around the excavation hole was obtained [5]. The finite element method was also introduced to further study the mechanism of building rectification [6, 7].

To directly observe soil deformations and obtain detailed data, several scale model tests were performed [8], and the test results indicated that the vertical stress decreased above the holes while increasing between the adjacent holes, showing the stress transfer law. Using the finite element method, Xiao et al. further described the continuous stress redistribution and displacement field [9] and the rectification mechanism was revealed.

Previous research has focused on the plastic zone and hole spacing. The consensus is that when the plastic zone bridges the soil strip between neighbouring holes, the strips

yield and produce plastic flow. At this moment, the building starts to tilt reversely. Although the finite element method can be used for inclination correction analysis, calculating a preferable hole spacing with a numerical simulation is excessively demanding for an engineer. Till to now, there is no applicable formula for the rectification design. Furthermore, there is a lack of research on the relations between the contact pressure and the redistributed stress between soil strips in the critical state of back tilt. The forced settlement of building rectification by underexcavation derives from the hole closure [3, 9], but few studies have focused on the quantitative relationship between the parameters of soil excavation and the expected base settlement.

A practical rectification design, given the expected correction target (forced settlement), is to determine the hole spacing, hole diameter, and plane layout of excavation holes under certain building load and subsoil conditions. By examining a number of rectification projects and studying case histories, the authors have comprehended the relationship between the design parameters and the rectification target. In this study, the subsoil is assumed to be an ideal elastic-plastic body. By using the simplified theoretical analysis, the two formulas for ultimate hole spacing and hole diameter are derived, which are the key parameters for a rectification design. The settlement can also be predicted by the underexcavation configuration.

In the next section, the redistribution of contact pressure is determined after the inclination of buildings. The third section presents the derivation of the preferable hole spacing and hole diameter. The fourth section describes the rectification design procedure. In the fifth section, two case histories are introduced to verify the design parameters. Finally, conclusions are offered in the last section.

2. Redistribution of Contact Pressure

When the building is inclined, the contact pressure is redistributed. For a building with a raft foundation, it is assumed that the total height of the building is H, the length of raft is L, and the width is B. The building tilt is often along the direction of width. The horizontal displacement of the building roof is ΔB, and the inclination of the building is i. When the building has a regular shape and uniform weight, it can be considered that the total structure load P of the building acts on the centroid. The horizontal eccentricity caused by inclination is e, as shown in Figure 1. The building inclination can be expressed as follows:

$$\mathrm{i} = \frac{\Delta \mathrm{B}}{\mathrm{H}} = \frac{\mathrm{e}}{(\mathrm{H}/2)}. \tag{1}$$

Solving for e, it can be expressed as

$$\mathrm{e} = \frac{\mathrm{Hi}}{2}. \tag{2}$$

Assuming that the subsoil is uniform, the redistributed contact pressure caused by building inclination can be calculated by

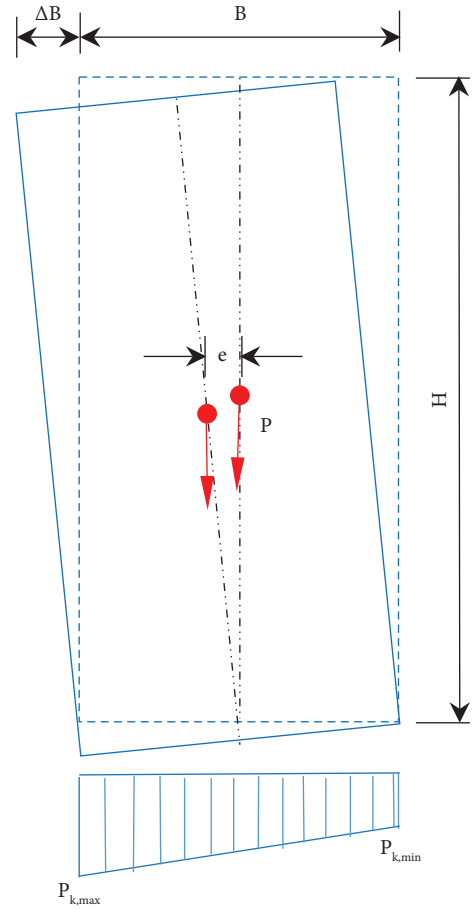

Figure 1: Analysis sketch for redistribution of contact pressure.

$$\left.\begin{matrix} \mathrm{p}_{\mathrm{k,\,max}} \\ \mathrm{p}_{\mathrm{k,\,min}} \end{matrix}\right\} = \frac{\mathrm{P}}{\mathrm{BL}}\left(1 \pm \frac{6\mathrm{e}}{\mathrm{B}}\right) = \frac{\mathrm{P}}{\mathrm{BL}}\left(1 \pm \frac{3\mathrm{Hi}}{\mathrm{B}}\right). \tag{3}$$

Taking $(H/B) = \beta$, the formula can be written as

$$\begin{matrix} \mathrm{p}_{\mathrm{k,\,max}} \\ \mathrm{p}_{\mathrm{k,\,min}} \end{matrix} = \frac{\mathrm{P}}{\mathrm{BL}}(1 \pm 3\beta \mathrm{i}). \tag{4}$$

Such a redistribution formula provides a basis for the rectification design in a more concise way. According to the "Code for Design of Building Foundation (GB50007-2011)" [10], the maximum inclination of buildings is controlled within 5%. Therefore, when the ratio of height to width $\beta \le 10$ and the building inclination $i \le 5‰$, the contact pressure changes within the range of ±15%.

3. Ultimate Hole Spacing and Hole Diameter

3.1. Ultimate Hole Spacing. When rectifying the inclined building, as the excavation proceeds, more holes are cut, the bearing area of the soil strips between the holes decreases gradually, and vertical stress is more transferred to the soil strips. Taking the subsoil as an ideal elastic-plastic body, when the vertical stress on the minimum section of the soil

strips increases to the ultimate soil bearing capacity, the soil strips will yield and collapse [3, 4]. The researchers simulated the plastic zone evolution. Under the conditions of a contact pressure of 90 kPa and an excavation hole spacing of 2.15 d, the maps of effective plastic strain are shown in Figure 2. For analysis details, we refer to document [9].

Marking contact pressure as p, it is close to or equal to the allowable bearing capacity of the subsoil when the raft area of a building foundation is determined. Therefore,

$$\mathrm{p} \approx \mathrm{f}_{ak} = \frac{p_u}{K}, \tag{5}$$

where p_u is the ultimate bearing capacity of the foundation that can be determined by property parameters or by unconfined compressive strength of the subsoil and K is the safety factor of the foundation bearing capacity.

Underexcavation is conducted from the less subsidence side of the building. Taking the cutting length as 1.0 m, when the hole spacing is l, hole diameter is d, and the total number of holes at the cutting section is n, the effective area for transferring vertical stress to deep is $n(l-d)$ at the cutting section. If the horizontal plane for small holes is to reach the crushing state, the vertical stress loading on the soil strip between the holes must reach the ultimate bearing capacity p_u of the subsoil, as shown in Figure 3. The excavation hole is generally within 1.0 m underneath the raft; therefore, the diffusion of contact pressure to the depth of the excavation hole can be ignored. According to the total vertical stress at the horizontal plane in the middle of the hole being equal to the total contact pressure under the raft, the following equilibrium formula is obtained:

$$nlp = n(l-d)p_u, \tag{6}$$

i.e., $nl(p_u/K) = n(l-d)p_u$

The ultimate hole spacing is

$$l = \frac{K}{K-1}d = \lambda d, \tag{7}$$

$$\lambda = \frac{K}{K-1}, \tag{8}$$

where λ is the multiple of hole spacing to diameter, depending on the safety reserve of the building foundation.

For an inclined building, its foundation bearing reserve is somewhat lower with a safety factor of 1.5~2.0, so the corresponding hole spacing is (2.0~3.0)d, which is consistent with the previous engineering experience.

3.2. Applicable Hole Diameter. The finite element method has been introduced to predict the building settlement [11–13]. However, the simulated settlement caused by underexcavation is often far less than the observed settlement in the engineering practice. Taking the soil elastic modulus as 15 MPa, when a pressure of 90 kPa is applied to the ground, the soil is excavated at a spacing of 4.3 d and the diameter of the excavation hole is 110 mm. The maximum ground settlement caused by underexcavation is approximately 1.5 mm according to the finite element calculation, as shown in Figure 4, whereas under the same excavation hole configuration, the excavation settlement in the project is approximately 20 mm. The reason is that the finite element method is applicable to continuous bodies, and the calculated deformation only represents those caused by stress redistribution. After the soil strips between the holes yield and collapse, the finite element method is no longer applicable for a broken discontinuous body. Nevertheless, hole collapse is the main source of forced foundation settlement for building rectification. This conclusion was also supported by Ovando–Shelley and Santoyo [3] and Xiao et al. [9]. Therefore, a simplified method is used to derive the hole diameter given the target settlement.

Ignoring the elastic deformation caused by stress redistribution from soil excavation, a section perpendicular to the soil cutting is taken for analysis. Assuming that the amount of forced settlement at this section is s, the multiple, i.e., λ of the hole spacing to diameter is determined by the above formula (8), the number of rows of soil excavation holes is m, and the number of holes in each row is n, as shown in Figure 5. If the settlement volume is equal to the amount of extraction soil, the equation is obtained as follows:

$$\text{ie, } snl = mn\frac{\pi d^2}{4}, \tag{9}$$

$$\text{ie, } sn\lambda d = mn\frac{\pi d^2}{4}. \tag{10}$$

The hole diameter is

$$d = \frac{4\lambda s}{m\pi}. \tag{11}$$

Forced settlement can also be predicted according to rectification design parameters as follows:

$$s = \frac{m\pi d}{4\lambda}. \tag{12}$$

It should be noted that the relationship between the diameter of the excavation hole and foundation settlement is derived under the condition of ignoring the raft stiffness. According to the theoretical calculation, the settlement along the cutting direction changes abruptly. Due to the stiffness of the raft and structure, the settlement along the cutting direction changes linearly with the maximum settlement at the cutting side. In engineering projects, when predicting the maximum settlement using the previous formula, a coefficient should be introduced to modify the difference between the theoretical value and site observations. According to the experience obtained from case histories, the coefficient is in the range of 1.0~3.0.

$$\mathrm{s}_{\max} = \eta\frac{\mathrm{m}\pi\mathrm{d}}{4\lambda}. \tag{13}$$

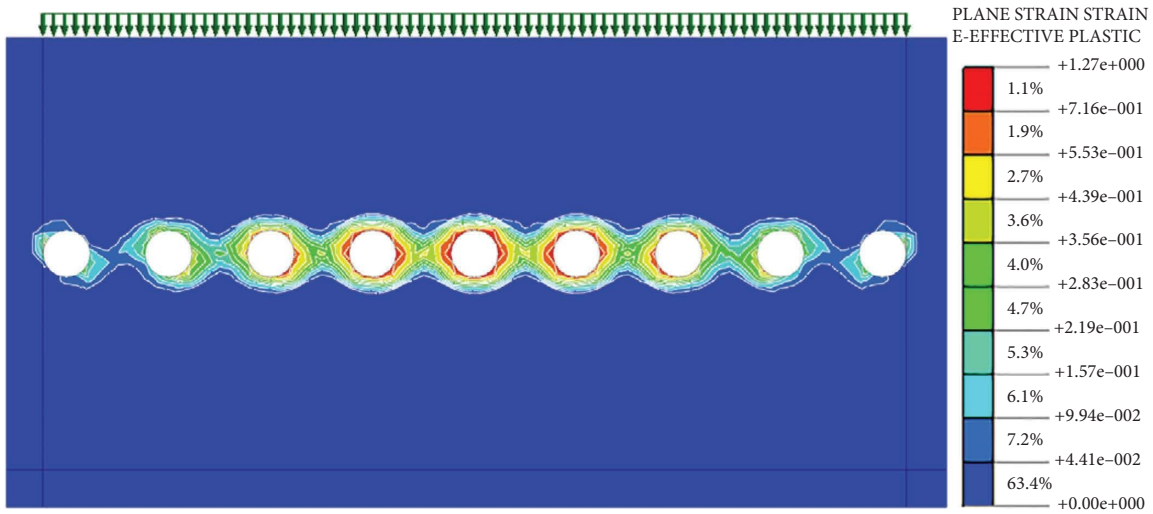

Figure 2: Maps of effective plastic strain of underexcavation.

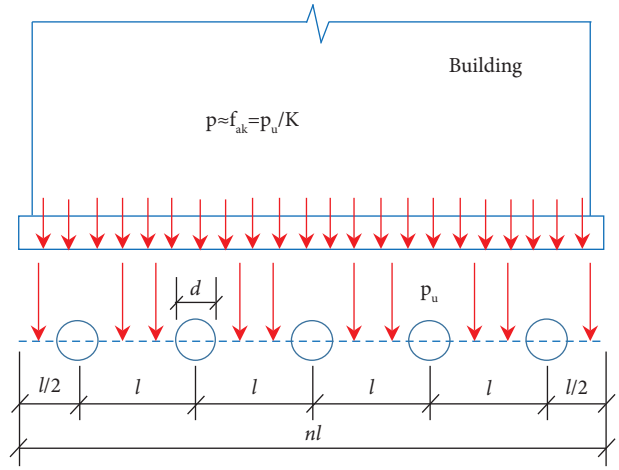

Figure 3: Analysis sketch for the ultimate spacing of holes.

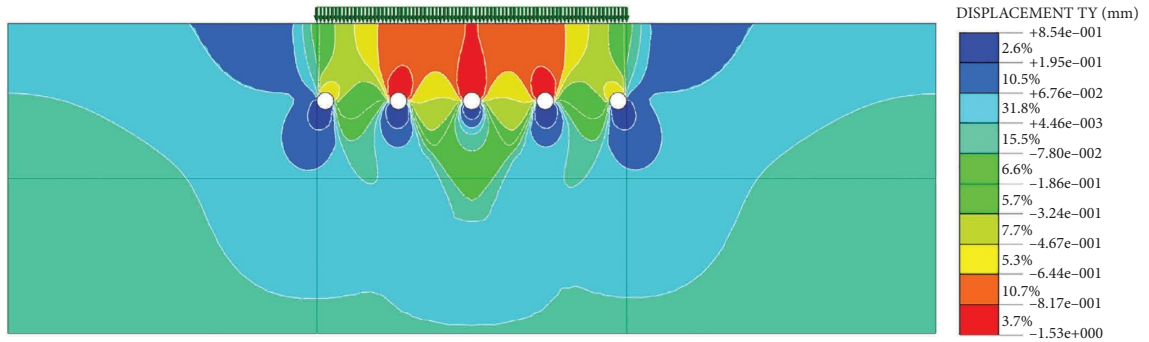

Figure 4: Simulated settlement after underexcavation.

4. Recommended Practical Design Steps

With two key parameters of hole spacing and diameter, combined with engineering experience, the design steps are recommended as follows:

Step 1. we calculate λ, the multiple of ultimate hole spacing to hole diameter. According to the ultimate bearing capacity of the foundation and contact pressure, the safety factor, K, is determined by formula (8). For a concise rectification design, the redistribution of contact pressure can be taken

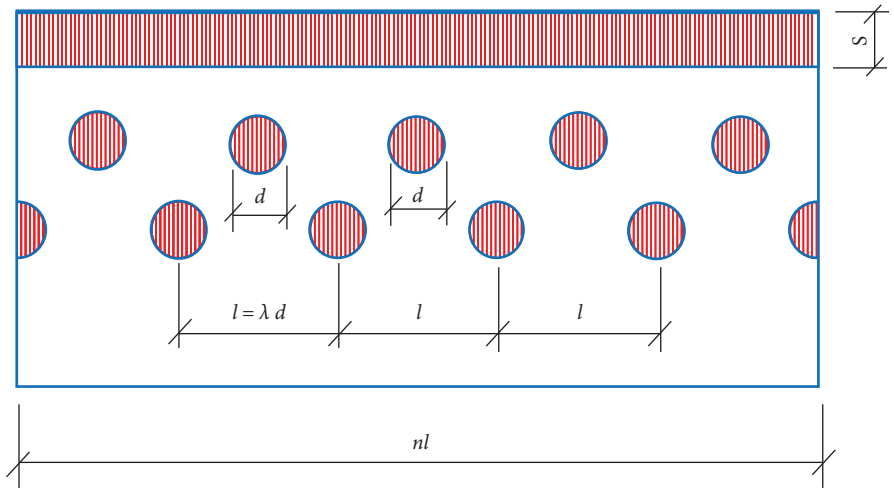

Figure 5: Analysis sketch for diameter of the digging hole.

into account. For the convenience of subsequent instructions, we take $\lambda = 3$.

Step 2. we determine the lengths of the excavation holes. For ordinary residential buildings within 16 m in building width, two drilling lengths can be appropriate for rectification. According to many years of experience in rectifying projects, the optimal maximum drilling length extends to the 3/4 of the dimensions in tilt direction [14], which not only facilitates the building back tilt but also avoids unnecessary settlement on the less subsidence side. The recommended hole lengths are 0.75 B and 0.5 B, as shown in Figure 6.

Step 3. we determine the hole diameter and the hole configuration. The target maximum forced settlement at the cutting side is s_{max}; when the foundation is completely rigid, the settlement at the centerline is $s_{max}/2$. Using formula (11), the corresponding diameter of the excavation hole is

$$\begin{aligned} d &= \frac{4\lambda}{m\pi} \bullet \frac{s_{max}}{2}. \\ &= \frac{6s_{max}}{m\pi}. \end{aligned} \tag{14}$$

When taking m = 1, we obtain

$$d = \frac{6s_{max}}{\pi}. \tag{15}$$

Assuming the expected maximum settlement $s_{max} = 60$ mm, we obtain $d \approx 115$ mm. According to the available bit type in the present market, a hole diameter of 110 mm is applicable. For the convenience of construction, the drilling diameters of the two types of holes with different lengths are taken as the same. It is recommended to take 2/3 of the total number of excavation holes with a length of 0.75 B and 1/3 of the total number with a length of 0.5 B to ensure that the theoretically calculated settlement area on the inclination correction profile is equal to the settlement area of the raft. The layout of the soil extraction holes is shown in Figure 6.

Step 4. we dynamically modify the rectification scheme. For each specific correction project, the building structure, foundation, subsoil, construction technology, and accompanying measures are different and the design scheme should be modified according to the site circumstances. For example, if the basement is surcharge loaded on site, the contact pressure increased. Correspondingly, the safety factor K of the soil strips is decreased. Based on $\lambda = K/(K-1)$, the critical hole spacing should be modified to be larger. For another example, water injection into an excavation hole helps decrease the shear parameters of cohesive subsoil, especially for those with a naturally low water content; as a result, the ultimate bearing capacity of the soil strip decreases. Therefore, when the measure of flushing water is adopted in the field, a larger hole spacing can crush the soil strip.

5. Verification by Case Histories

5.1. Case 1: An 11-Storey Building with a Frame Structure. A residential building in Jiangsu Province in China has a frame structure of 11 floors above ground and one floor underground [15]. The building is based on a beam-embedded raft of 450 mm in thickness. According to the geotechnical survey report, the bearing stratum underneath the raft is silt and silty clay, which have a characteristic bearing capacity (allowable bearing capacity in design) of 100 kPa. After completing the structure, it was found that the uneven settlement had occurred. Until building rectification, the inclination had reached 6%. The building is 52.8 m in east-west length and approximately 14.0 m in south-north width. A total of 76 excavation holes with three lengths were set at the building's north side, with a spacing of 600 to 800 mm; during onsite construction, 20 additional excavation holes were drilled due to difficulties in back tilting the building. The construction process was divided into three stages as follows:

Stage 1: preparation of underexcavation, including excavation of the working trench and dewatering to

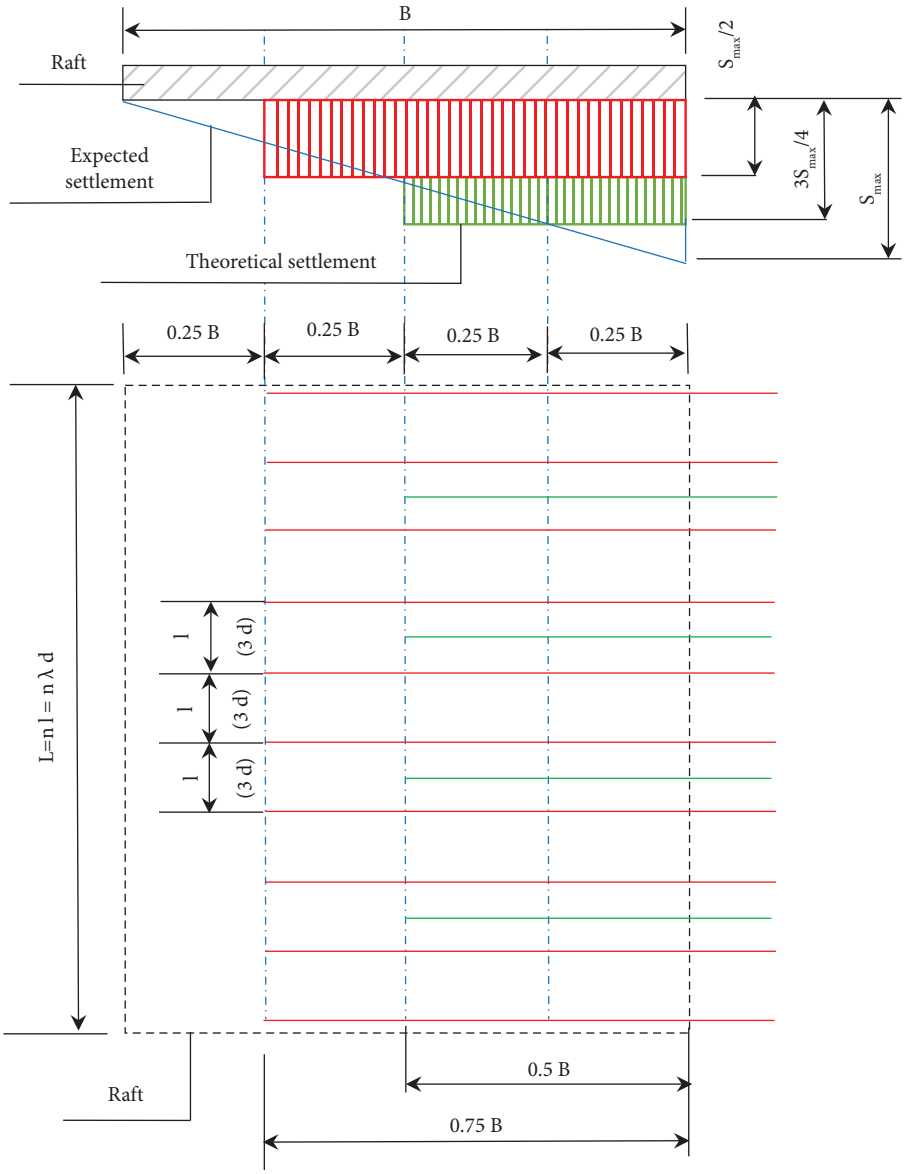

Figure 6: Sketch for rectification design.

lower the groundwater level below the working trench bottom

Stage 2: underexcavation for building rectification, during which the holes were cut uniformly and *symmetrically* along the building north side, with short holes first, then long holes, and finally supplementary holes

Stage 3: foundation reinforcement, including grouting to fill the not completely closed holes and *collapsed* loose soils upon accomplishment of correction and then driving 188 micropiles as settlement reducers

The construction photos are shown in Figure 7. The building exhibited relatively high rigidity during the back tilting process. The curves of settlement versus time of typical monitoring points are shown in Figure 8. To verify the theoretical formulas, only the settlement data in the excavation stage are investigated. Taking the monitoring data of 4 points in the building middle, the induced average settlement of M5 and M6 was 58 mm during the underexcavation stage, while the south monitoring of M15 and M16 presented slight uplift at the same time. The observations indicate that the building tilts back by rotating around a certain axis, showing relatively high rigidity.

5.1.1. Verification of the Hole Spacing. According to the allowable bearing capacity of the supporting subsoil given by the site investigation report, we take the ultimate bearing capacity p_u as two times the allowable value, 200 kPa. Considering the dead load and live load, the 12 floors of the building exert a contact pressure $p = 12 \times 15 = 180$ kPa. Because the building was not decorated and not occupied, the contact pressure was taken as 0.9 times the above

(a) (b)

Figure 7: Underexcavation of case 1. (a) The building. (b) Underexcavation field.

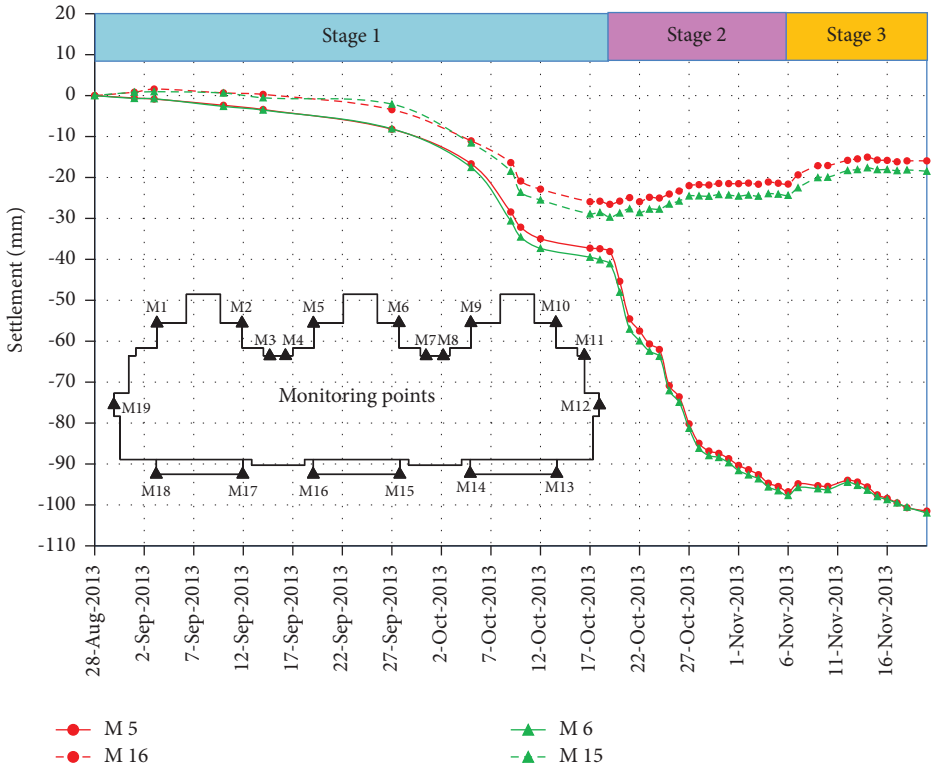

Figure 8: Settlement versus time of case 1.

estimated value, which is approximately 160 kPa. At the onset of rectification, the safety factor of the foundation soil is $K = (p_u/p) = (200/160) = 1.25$. Consequently, the ultimate hole spacing is $\lambda = (K/(k-1)) = 5$, i.e., hole spacing is $l = 5d$. The adopted hole diameter is 110 mm, and the theoretical spacing is 550 mm. Amazingly, the average hole spacing in the field is $l = (L/n) = (52800/(76+20)) = 550$mm, which agrees well with the theoretical calculation.

5.1.2. Verification of the Relationship between the Hole Diameter and Foundation Settlement. Using formula (12), the theoretical settlement is

$$s = \frac{m\pi d}{4\lambda} = \frac{1 \times 3.14 \times 110}{4 \times 5} = 17.27\text{mm}. \quad (16)$$

During the whole operational process of the building rectification and foundation reinforcement, the back

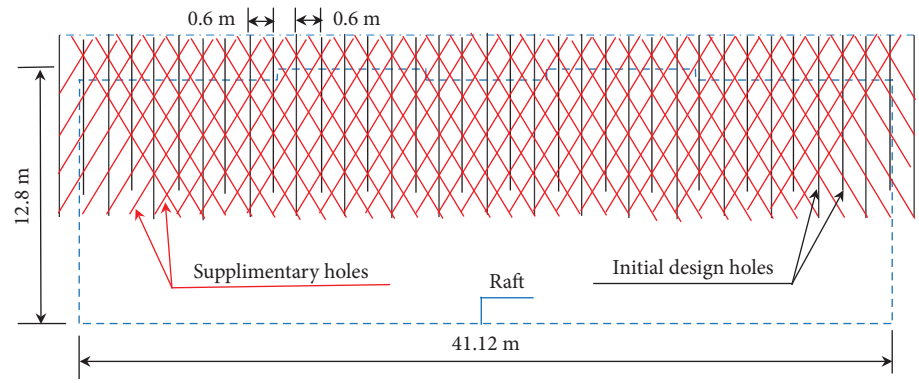

Figure 9: Hole configuration of case 2.

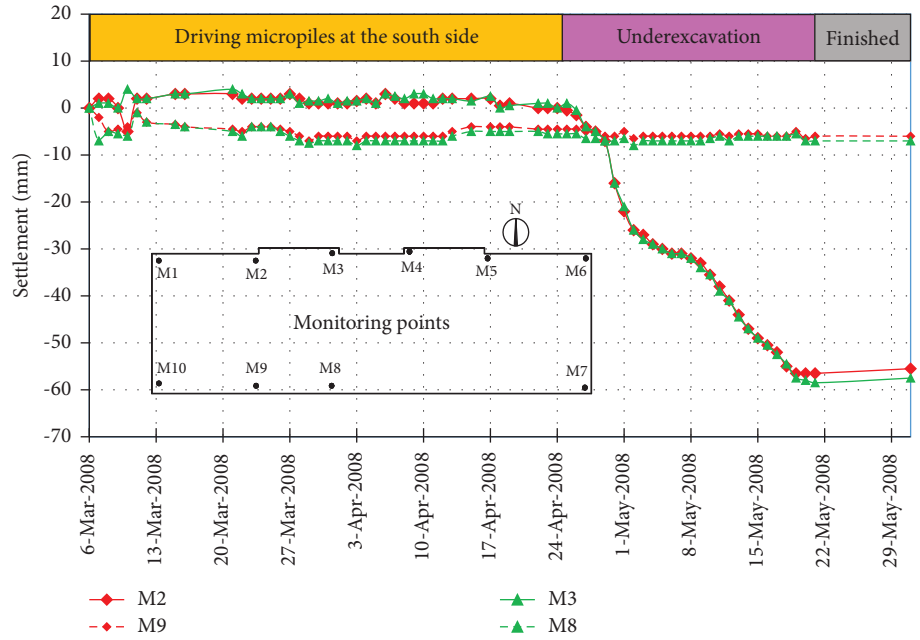

Figure 10: Settlement versus time of case 2.

inclination is 5.6%, perfectly achieving the target level of building rectification. During the underexcavation stage, the observed settlement is 58 mm, which is approximately 3.35 times the value of the theoretical calculation. Even considering $\eta = 3.0$, the observed settlement at the soil cutting side is still slightly larger. It is speculated that the following factors existed:

(1) Consolidation settlement continued to develop during underexcavation

(2) The foundation soil was soft, and the excavation of working trench released the lateral earth pressure. As a result, the soil creep deformation occurred, contributing to the north side settlement

(3) Dewatering caused additional stress in the subsoils, and additional settlement was induced

(4) Approximately one-quarter of the holes were repeatedly excavated, which brought more soil out the hole

5.2. Case 2: A 6-Storey Building with a Masonry Structure. A 6-storey masonry building in Shandong Province in China is 41.2 m in length and 12.8 m in width on plane [16]. The north side of the building is based on medium to stiff plastic silty clay, while the south side of the building is laid on a backfill and muddy soil layer. To solve this problem, a lime-soil cushion of 1.5 m in thickness was adopted above which a raft foundation was laid to strengthen the building stiffness. Nevertheless, half a year after the completion of the building, the measured inclination to the south reached 5.87‰. To correct the building, underexcavation beneath the lime-soil cushion was conducted.

5.2.1. Verification of the Hole Spacing. According to the geological survey report, the characteristic value f_{ak}, i.e., the allowable bearing capacity of silty clay is 150 kPa and the ultimate bearing capacity is 300 kPa. The building has 6 floors in total, and the estimated contact pressure, including lime-soil cushion weight, is $p = 15 \times 6 + 1.5 \times 18 = 117$ kPa.

Table 1: Comparison between the practical value and the calculated value.

Project	Case 1	Case 2
Floor	11F + 1F	6F
Design bearing capacity f_{ak} (kPa)	100	150
Adopted hole spacing (mm)	550	200
Theoretical hole spacing (mm)	550	180
Observed settlement (mm)	58	50
*Calculated settlement (mm)	17.27	47.45

Note. $^{*}\eta = 1.0$.

Therefore, the safety reserve of the foundation soil is $K = p_u/p = 300/117 = 2.56$; then, the multiple value of hole spacing to diameter in the limit state is $\lambda = K/(K - 1) = 1.64$. The ultimate hole spacing is $l = 1.64d$. With an applied hole diameter of 110 mm, the theoretical hole spacing should be 180 mm.

After the raft south edge was pinned by micropiles, soil extraction was conducted from the north side of the building. The excavation holes were spaced at 600 mm and extended to 7.0 m or 9.0 m in the tilt direction underneath the cushion. After the excavation was completed in accordance with the rectification design scheme, the back inclination of the building could not achieve the expected goal of less than an inclination of 2.0%. Therefore, supplementary holes with a length of 10.5 m were cut obliquely with the raft edge at a spacing of 600 mm. The conducted holes are shown in Figure 9. There are actually 3 excavation holes within each spacing of 600 mm, so the actual excavation hole spacing is 200 mm. This value is in good agreement with the theoretical calculation of 180 mm.

5.2.2. Verification of the Relationship between the Hole Diameter and Foundation Settlement. The actual multiple is

$$\lambda = \frac{200}{110} = 1.82. \tag{17}$$

Using formula (12), the theoretical settlement is

$$s = \frac{m\pi d}{4\lambda} = \frac{1 \times 3.14 \times 110}{4 \times 1.82} = 47.45\text{mm}. \tag{18}$$

The rectified settlement of the monitoring points is approximately 50 mm, as shown in Figure 10, which is close to the theoretical formula. The coefficient of settlement η is 1.05.

Two case histories verify the correctness and practicability of the theoretical formulas of ultimate hole spacing and adoptable hole diameter. In addition, design modification and dynamic construction are necessary for each building with a specific foundation. The comparison of these two typical case histories is shown in Table 1.

6. Conclusions

In the previous correction projects, the engineers had to rely on experience to design and conduct rectification. The success was severely dependent on close monitoring and holding on underexcavating. Through simplified theoretical analysis, the key parameters for inclination correction are deduced and its validity and practicability are verified by two case histories. The main conclusions are as follows:

(1) After the building is tilted, the base contact pressure is redistributed. Under the condition of uniform distribution of structural loads, a formula is proposed to calculate the stress redistribution according to the building incline. For a concise rectification design by underexcavation, the redistribution of contact pressure should be considered.

(2) Through simplified theoretical analysis, based on the total contact pressure underneath the raft being equal to the total pressure at the soil strips between excavation holes, the ultimate hole spacing is obtained. It is also the preferable hole spacing that facilitates the hole crushing. According to the volume of induced settlement being equal to the volume of soil extraction, the applicable hole spacing is obtained. Meanwhile, the induced settlement could be predicted by the determined parameters for underexcavation.

(3) The verification of case histories shows that the formulas are effective and applicable. These two formulas provide a solid theoretical basis for the design of rectification by underexcavation, but the design scheme needs to be modified according to the structure type, geotechnical conditions, and other extra measures for promoting settlement. During the process of building correction, close monitoring and dynamic modification are still essential.

(4) With the formulas presented in this study as a guide, the critical safety state and desired settlement can be controlled and the excavation time can be reduced. In this research, the ultimate crushing bearing capacity of soil strips between holes is not exactly the same as the ultimate bearing capacity of the foundation, which requires further study. When the maximum settlement at the excavation side of a building is predicted according to the parameters for underexcavation, the coefficient requires further accumulating empirical data.

Symbols

B: Raft width
L: Raft length
H: Total height of the building, including the underground part
ΔB: Horizontal displacement of the roof caused by building inclination
i: Inclination of building
e: Horizontal eccentricity caused by building inclination
β: Ratio of building height to width, $\beta = (H/B)$
P: Nominal combination of building load
p: Contact pressure of the shallow footing
$p_{k,\max}$: Maximum contact pressure

$p_{k,\min}$: Minimum contact pressure
s: Building settlement caused by underexcavation
$s_{\max}$: Maximum settlement at the cutting side
p_u: Ultimate bearing capacity of the foundation
f_{ak}: Allowable bearing capacity in foundation design
K: Safety factor of the foundation
λ: Multiple of hole spacing to diameter
d: Hole diameter
l: Hole spacing
m: Number of rows of excavation holes
n: Number of holes in the excavation section
η: Coefficient of settlement.

Data Availability

The data used to support the findings of this study are available from the corresponding author upon reasonable request.

Conflicts of Interest

The authors declare that they have no conflicts of interest.

Acknowledgments

This work was supported by the National Natural Science Foundation of China for Major Project (Grant no. 52038006) and by the Engineering Appraisal and Reinforcement Research Institute Co., Ltd. of Shandong Jianzhu University for School-Institute Cooperation Project (Grant no. H19233z).

References

[1] J. B. Burland, M. Jamiolkowski, and C. Viggiani, "Underexcavating the tower of Pisa: back to the future," *Geotechnical Engineering Journal of the SEAGS & AGSSEA*, vol. 46, no. 4, pp. 126–135, 2015.

[2] S. F. Fu and X. Rong, "Theoretical and application research on shallow digging method in CFG pile composite foundation of high-rise building," *Building Structure*, vol. 49, no. 8, pp. 123–129, 2019.

[3] E. Ovando-Shelley and E. Santoyo, "Underexcavation for leveling buildings in Mexico city: case of the metropolitan cathedral and the sagrario church," *Journal of Architectural Engineering*, vol. 7, no. 3, pp. 61–70, 2001.

[4] X. D. Xu, L. D. Jia, J. P. Sun, K. Z. Zhao, X. Zhang, and S. M. Li, "Design and practice of rectifying leaning building by digging-out soil and filling-in with water method," *Journal of Building Structures*, vol. 20, no. 5, pp. 59–65, 1999.

[5] Z. D. Deng, X. B. Zhang, and L. Wang, "Mechanism analysis and calculation method of horizontal soil landing rectifying method," *Journal of Civil Engineering and Management*, vol. 33, no. 5, pp. 38–43, 2016.

[6] J. Bai, D. Chan, and N. Morgenstern, "Numerical analysis of time-dependent behaviour for the leaning tower of Pisa," *Soils and Foundations*, vol. 48, no. 2, pp. 207–220, 2008.

[7] S. F. Fu, X. Rong, and Y. R. Li, "Finite element analysis of excavation unloading ditch method for rectification on less inclined side of high-rise building foundation," *Building Structure*, vol. 49, no. 8, pp. 130–135, 2019.

[8] H. Sun, "Experimental study on failure mechanism of under excavation method for building rectification," ME Dissertation, Shandong Jianzhu University, Jinan, China, 2019.

[9] J. H. Xiao, J. P. Sun, X. Zhang, and Q. X. Yue, "Mechanism of underexcavation and practical design method for building rectification," *SN Applied Sciences*, vol. 4, no. 4, pp. 103–115, 2022.

[10] *Ministry of Housing and Urban- Rural Development of the People's Republic of China*, "GB50007-2011: Code for design of building foundation", China Architecture & Building Press, Beijing, China, 2011.

[11] W. Q. Niu, X. B. Zhang, F. R. Wang, Q. Sun, M. Z. Hu, and G. Z. Wu, "Analysis and research on the rectifying and strengthening example of a Xining high-rise commercial and residential building and numerical calculation," *Building Structure*, vol. 48, no. s2, pp. 721–725, 2018.

[12] X. D. Song and Y. G. Liang, "Application and finite element analysis of converting foundation form in rectification engineering," *Construction Technology*, vol. 48, no. 18, pp. 99–102, 2019.

[13] X. N. Zhang, S. Y. Shi, M. Lu, and B. Liu, "Analysis of forced settlement rectification method of available brick-concrete structures in soft soil area," *Building Structure*, vol. 46, no. 8, pp. 88–94, 2016.

[14] Z. L. Shen and Z. Wang, *Rectification and Reinforcement Technology of Ancient Pagoda*, China Railway Publishing House, Beijing, China, 2011.

[15] F. Yang, "Analysis and applied research of rectifying technology for building by drawing out soil," ME Dissertation, Shandong Jianzhu University, Jinan, China, 2015.

[16] J. P. Sun, H. W. Wei, G. B. Shao, and Z. B. Jinag, "Affect analysis of reinforcement correction design and construction," *Sichuan Building Science*, vol. 36, no. 1, pp. 97–99, 2010.

Hindawi
Advances in Civil Engineering
Volume 2023, Article ID 2753641, 15 pages
https://doi.org/10.1155/2023/2753641

Research Article

Micro to Nanolevel Stabilization of Expansive Clay Using Agro-Wastes

Mehmood Munawar,[1] Ammad H. Khan,[1] Zia U. Rehman,[1] Abdur Rahim,[1] Mubashir Aziz,[2,3] Sultan Almuaythir,[4] Bothaina S. I. A. El Kheir,[5] and Farhan Haider[6]

[1]*Department of Transportation Engineering and Management, University of Engineering & Technology, Lahore 54890, Pakistan*
[2]*Department of Civil and Environmental Engineering, King Fahd University of Petroleum and Minerals, Dhahran 31261, Saudi Arabia*
[3]*Interdisciplinary Research Center for Construction and Building Materials, King Fahd University of Petroleum and Minerals, Dhahran 31261, Saudi Arabia*
[4]*Department of Civil Engineering, Prince Sattam Bin Abdul Aziz University, Alkharj 16273, Saudi Arabia*
[5]*Department of Architectural Engineering, Faculty of Engineering and Technology, Future University, Cairo 11835, Egypt*
[6]*Onstructive Pvt. Limited, Lahore 54792, Pakistan*

Correspondence should be addressed to Ammad H. Khan; chair-tem@uet.edu.pk

Received 10 November 2022; Revised 4 January 2023; Accepted 28 March 2023; Published 19 April 2023

Academic Editor: Jiang Xiangang

The circular economy encourages the production and consumption of sustainable embankment geomaterials and their blends utilizing recycled waste materials in roads, railway tracks, airfields, and underground structures. Geomaterials comprising high-plastic soft expansive clay pose excessive settlement during cyclic traffic/railway/airfield loading resulting in uneven geometry of overlying layers. This paper demonstrates multiobjective optimized improvement of expansive clay (C) geotechnical characteristics by cost-effective agro-wastes additives at microlevel (by 3% to 12% rice husk ash, i.e., RHA), nanolevel (by 0.6% to 1.5% rice husk derived green nano-SiO_2, i.e., NS), and synergistic micro to nanolevel (NS-RHA). The swell potential, resilient modulus (MR), initial elastic modulus (Es), unconfined compressive strength (UCT), and California bearing ratio (CBR) of C and its blends were determined. The chemical characterization of C and its blends were conducted through Fourier transform infrared spectroscopy (FTIR) and optical microscopic tests. The outcome of this study depicted that the cost ratio for the optimized composite, i.e., (1.2% NS-9% RHA)/(9% RHA) is 1.22 whereas stiffness ratio MR (NS-RHA)/MR(RHA) and Es (NS-RHA)/Es(RHA) and strength ratio UCT(NS-RHA)/UCT(RHA) and CBR(NS-RHA)/CBR(RHA) were found to be 2.0, 1.64, 2.17, and 2.82, respectively. FTIR revealed the chemical compatibility between C, RHA, & NS from durability perspective. Cost-stiffness results of this study can be applied by geotechnical experts to economize the green stabilization of C by use of agro-waste for sustainable development.

1. Introduction

Sustainable embankment materials are desired globally by geotechnical experts from durability, cost-effectiveness, and optimization perspectives for civil engineering infrastructures [1–10]. Urbanization around the world is going on fast-track [11] due to which the problematic soils sites are also in demand for soils improvement (stabilization).

All soils from A-1 to A-7 (AASHTO classification) can be used as subgrades in pavements. High plasticity expansive clays are one of the common problematic soils that need the stabilization before its usage as bearing or construction material under embankments. These expansive clays are sufficiently strong in dry condition but with increase of moisture, these soils loose strength drastically [12, 13]. Expansive clay subgrade of low bearing capacity is considered as a costly issue [14] for which stabilization is

a feasible solution to increase shear strength and to decrease water susceptibility [15]. Furthermore, the expansive clays as subgrade are prone to large settlements resulting in formation of uneven geometry around the embankment [16–18]. From geotechnical perspectives in pavements subgrades built with expansive clays, commonly the more important parameters of interest are resilient modulus (MR), elastic modulus (Es), unconfined compressive strength (UCT), and California bearing ratio (CBR) index. MR is used in pavement design to simulate dynamic haversine traffic loading. Es estimated from stress-strain curve of UCT can be used for conservative design of pavements, [19] and it can be evaluated from straight line drawn at stress-strain curve up to 50% of peak stress [20]. CBR is the vital parameter which is used in the estimation of pavement thicknesses.

Flexible pavement components such as wearing course, base course, and subbase course usually have enough elasticity and transmit the overpassing vehicle loads to the underneath layer of expansive clay subgrade for dissipation [12, 13].

Traditional microstabilizers most notably cement, lime, and fly ash are in frequent use worldwide to improve expansive clay for the last few decades [21–24]. The main drawback of cement and lime stabilization is the emission of harmful gases such as CO_2, SO_2, and NO_x in the environment which outweighs their beneficial effects [25–27]. These microstabilizers increase the pH of expansive clay up to 12 which creates environmental problems [17]. Fly ash (a coal combustion product) due to its high value of the pH reduces the nutrient access to plants when mixed with expansive clays, so the adoption of green additives for stabilization is trending amongst geotechnical and pavement engineers [28–30].

Environmental friendly microstabilizers derived from agro-wastes are rapidly replacing the traditional microstabilizers for expansive clays [18]. Straw, bagasse, and husk are popular form of agro-wastes used. The increase in the use of expansive clays with agro-waste microstabilizers reduces the expenditure on cement which is being used earlier in abundance [12, 13]. Husk derived from rice (RH) showed promising potential for microstabilization of expansive clayey soils. Furthermore, the ash of rice husk (RHA) also proved potential for expansive clay stabilization at microlevel. RH is abundantly available in rice producing countries all over the globe as waste product of rice milling process. The chemical analysis shows that the 35% cellulose, 35% hemicellulose, 20% lignin and 10–20% ash can be obtained from of rice husk on dry weight basis [31]. RHA can be used as green additives due to its high pozzolanic activity [32]. RHA is produced by the burning of rice husk at about 600°C in which high quantity of silica, low quantity of oxide and high specific surface is observed.

The common nanoparticles used with soils are aluminium oxide-Al_2O_3, titanium oxide-TiO_2, silicon oxide-SiO_2, carbon nanotubes etc. These nanoparticles can stabilize (nanostabilization) the structure of soil at nanoscale (100 nm). The use of nanoparticles takes significance from the aspect of interparticle space concept, i.e., voids between soil particles. The nanoparticles cause transformation of pore liquid to viscous gel resulting in enhancement of soil shear resistance. The nanostabilization of soil improves its structure, physical, and chemical properties due to filling of voids at nanolevel [18]. In addition, the nanostabilization causes enhancement of load bearing potential of soil [33]. Various earlier researches described the interparticle spaces and potential of making the expansive clay denser with nanosilica.

The stabilization of soil at the microscale (using RH/RHA/cement/lime/fly ash/) does not change the properties of parent material significantly. Because, microstabilizers normally reduces plasticity of soils and facilitate in pozzolanic action. Nanostabilization is very active and changes the interlayer structure of parent soil and enhances the density and intermolecular attractive forces ultimately causing the increase in stiffness (resilient and elastic moduli) of blend. These nanoparticles influence the microstructure, physical, chemical, and geotechnical properties. Furthermore, the use of nanoparticles imparts the pozzolanic action in the blends.

Cost-effective and eco-friendly extraction of nanosilica from RHA can be accomplished by chemical and combustion methods. Reference [18] presented the combined effect of microlevel (cement) and nanolevel (nanosilica) on marl clay and found that nanosilica was four times more effective compared with cement stabilized marl clay.

The individual effects of nano and microparticles are needed to be compared with combined effect of nano plus microsynergy of particles. Previous studies present details of improvement in strength and plasticity of soft expansive clays by use of RHA and nano-SiO_2 independently. There are rare studies on the effect of synergistic combination (green and cost-effective) of micro and nanolevel particles on the resilient modulus (MR), elastic modulus (Es), UCT, and CBR of expansive clay. Followings were the objectives of the study:

(i) Evaluation of optimal doses of micro, nano, and micronano agro-waste additives for the synergistic green stabilization of expansive clay

(ii) Determination of optimal ratios of MR, Es, UCT, and CBR for nano to microlevel stabilization and comparison with cost ratio for nano to micro-synergistic mixing of RHA and NS in expansive clay

(iii) Characterization of expansive clay and its blends with RHA and NS through Fourier transform infrared spectroscopy (FTIR) and optical microscopic tests

2. Materials and Methods

Expansive clay samples (C) were characterized in the laboratory by specific gravity, natural moisture content, gradation, Atterberg limits, engineering classification, shear strength, consolidation, and modified proctor compaction tests. All tests were carried out in accordance with the relevant ASTM standards. Characterization of such types of clay has been described by Lang et al. [25]. The rice husk was collected from rice mill near Lahore, Pakistan. The rice husk

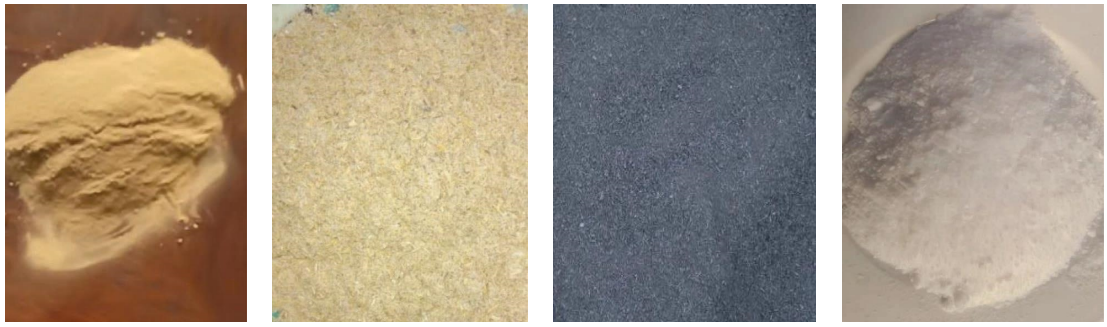

(a) (b) (c) (d)

Figure 1: Physical appearance of samples used (a) clay, (b) rice husk, (c) rice husk ash, and (d) nano-SiO_2.

was ground in 1000 rpm grinder for 4 minutes to prepare rice husk powder (RH). The particle sizes obtained ranged from 0.6 mm to 0.063 mm. The rice husk ash (RHA) was obtained by controlled burning of the RH at 600°C. RHA was characterized in the laboratory by the specific gravity, plasticity index, and loss-of-ignition tests. Commercially available nano-SiO_2 (NS) was procured. The properties of NS such as physical state, particle size, surface area, particles density, purity, and pH were determined in the laboratory.

Figure 1 shows the physical samples of clay, rice husk, rice husk ash, and nano-SiO_2 used.

RHA in the proportions of 3%, 6%, 9%, and 12% and NS in the proportions of 0.6%, 0.9%, 1.2%, and 1.5% were mixed in C to prepare samples for determination of swell potential, unconfined compressive strength (UCT), resilient modulus, and California bearing ratio (CBR). The proportion of RHA and NS was selected keeping in view the typical guideline range of these materials mixed with clay from previous studies [12–14, 32]. Tables 1–3 show the test matrix details used in experimentation.

C and its blends prepared with RHA and NS (Table 1) were subjected to evaluation of swell potential (ASTM D4546), unconfined compression (UCT) strength (ASTM D2166), resilient modulus (AASHTO T-307), and California bearing ratio (CBR) (ASTM D1883) tests. The length to diameter ratio of 2 was used in samples preparation. The strain rate of 1 mm/min in vertical axial direction was employed during UCT tests. The elastic modulus (Es) was derived from the initial portion of the stress-strain curves of UCT test. The peak stress, i.e., unconfined compressive strength (UCT), was also observed from the UCT stress-strain curves which depict the shear strength of the clay without any confining pressure. The resilient modulus (MR) test was performed on cyclic triaxial test machine. Cyclic haversine shaped load was applied for on each test specimen, and the last five cycles were selected for the measurement of load, horizontal deformation, and vertical deformation. In CBR tests, during saturation and shearing phases, a standard dead load of 10 lbs. was applied. The samples of C, C + RHA, C + NS, and C + RHA + NS prepared for UCT tests are shown in Figure 2.

Crystallographic structure of C and RHA was also evaluated by the X-ray diffraction (XRD) technique. The characteristics compositions of C, RH, RHA, NS, and C + RHA + NS (optimum blend) were also determined through the Fourier transform infrared (FTIR) spectroscopy and optical microscopy tests. The palettes of samples prepared for the FTIR tests are shown in Figure 3.

In order to compare the cost impact of different additives with clay, the stiffness to cost analysis was also carried out.

Table 1: Expansive clay plus rice husk ash composite tests matrix.

Sr	Label	Swell potential*	UCT*	Resilient modulus*	CBR*
1	C	X	X	X	X
2	C + 3%RHA	X	X	X	X
3	C + 6%RHA	X	X	X	X
4	C + 9%RHA	X	X	X	X
5	C + 12%RHA	X	X	X	X

Table 2: Expansive clay and nanosilica composite tests matrix.

Sr	Label	Swell potential*	UCT*	Resilient modulus*	CBR*
1	C + 0.6%NS	X	X	X	X
2	C + 0.9%NS	X	X	X	X
3	C + 1.2%NS	X	X	X	X
4	C + 1.5%NS	X	X	X	X

3. Results and Discussions

The geotechnical engineering characteristics of expansive clay are summarized in Table 4.

The C sample primarily comprised of fines, i.e., clay and silt in proportion of 73% and 23%, respectively. A fraction of 4% fine sand was also observed in the sample. The specific gravity of C was found 2.68 with plasticity index (PI) of 43%. The C was classified as medium to high-plastic clay (CH) in accordance with unified soil classification system (USCS). Such soils exhibit expansive nature, i.e., free swell potential 30% and swell pressure 232 kPa. The compression index of 0.44 was observed in C. The shear strength was found, i.e., cohesion of 61 kPa with friction angle of 100. The rice husk ash (RHA) and nanosilica characteristic properties are tabulated in Tables 5 and 6, respectively.

Table 3: Expansive clay, rice husk ash, and nanosilica composite tests matrix.

Sr	Label	Swell potential*	UCT*	Resilient modulus*	CBR*
1	C + 3%RHA + 0.6%NS	X	X	X	X
2	C + 3%RHA + 0.9%NS	X	X	X	X
3	C + 3%RHA + 1.2%NS	X	X	X	X
4	C + 3%RHA + 1.5%NS	X	X	X	X
5	C + 6%RHA + 0.6%NS	X	X	X	X
6	C + 6%RHA + 0.9%NS	X	X	X	X
7	C + 6%RHA + 1.2%NS	X	X	X	X
8	C + 6%RHA + 1.5%NS	X	X	X	X
9	C + 9%RHA + 0.6%NS	X	X	X	X
10	C + 9%RHA + 0.9%NS	X	X	X	X
11	C + 9%RHA + 1.2%NS	X	X	X	X
12	C + 9%RHA + 1.5%NS	X	X	X	X
13	C + 12%RHA + 0.6%NS	X	X	X	X
14	C + 12%RHA + 0.9%NS	X	X	X	X
15	C + 12%RHA + 1.2%NS	X	X	X	X
16	C + 12%RHA + 1.5%NS	X	X	X	X

*Average value of three replicates.

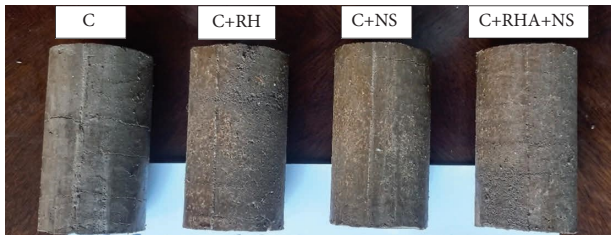

Figure 2: The UCT test samples of clay and its mixes.

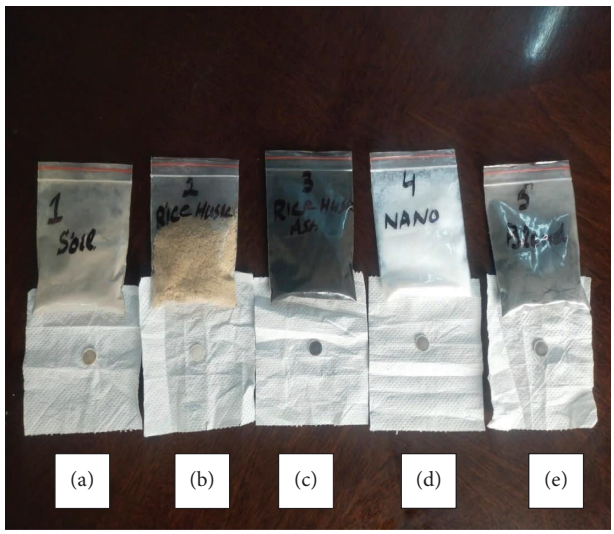

Figure 3: Palettes for the FTIR tests, i.e., (a) soil, (b) rice husk, (c) rice husk ash, (d) nanosilica, and (e) optimum blend of (a), (c), & (d).

The RHA exhibits dark grey color and nonplastic behavior with typical loss of ignition (LOI) value of 1%.

The nanosilica powder shows neutral behavior with an average particle density of 0.134 g/cm^2.

The effect of RHA and NS on free swell potential of clay is shown in Figure 4. It was observed that 3%, 6%, 9%, and 12%

Table 4: Summary of geotechnical engineering characteristics of expansive clay (C).

	Value^	Standard name
Constituent/property		
Specific gravity	2.68	ASTM D854
Natural moisture content (%)	22.5	ASTM D2216
Gradation/classification		
Sand (%)	4	ASTM D422
Silt (%)	23	ASTM D422
Clay (%)	73	ASTM D422
Atterberg limits		
LL-liquid limit (%)	91	ASTM D4318
PL-plastic limit (%)	49	ASTM D4318
PI-plasticity index (%)	43	ASTM D4318
SL-shrinkage limit (%)	39	ASTM D4318
USCS chart classification	CH	ASTM D2487
Cohesion (kPa)	61	ASTM 4767
Friction angle (degree)	10	ASTM 4767
Optimum moisture content (%)	24.3	ASTM D1557 ASTM D1557
Maximum dry density (g/cm^3)	1.74	ASTM 4546 ASTM4546
Free swell potential (%)	30	ASTM4546
Swell pressure (kPa)	232	ASTM4546
Compression index	0.44	

^Average value of three tests performed.

RHA caused 16%, 24%, 28%, and 32% decrease in swell potential of C. The C was also ameliorated with 0.6%, 0.9%, 1.2%, and 1.5% NS, which resulted in 24%, 40%, 44%, and 48% decrease in free swell potential. Moreover, the C was also blended with RHA plus NS composites. Synergistic composites of 3%, 6%, 9%, and 12% RHA with 0.6%, 0.9%, 1.2%, and 1.5% NS decreased the swell potential of C substantially as compared with the individual blends of C with RHA or NS as presented in Figure 4.

The optimal synergistic blend of 9% RHA plus 1.2% NS showed 72% decrease in free swell amongst studied proportions. The proportions blends showing the RHA and NS

Table 5: RHA properties.

Properties	Percentage, %
Specific gravity	1.64
Color	Dark grey
Plasticity index (%)^	Nonplastic
Loss-on-ignition (%)^	1

^Average value of three tests performed.

Table 6: Physical properties of nano-SiO_2.

Parameters	Values
Physical state	Powder
Apparent particle size (nm)^	27 to 36
Specific surface area (m^2/g)^	187
Particle density (g/cm^3)^	0.134
Purity (%)	98.7
pH^	7

^Average value of three tests performed.

beyond 9% RHA and 1.2% NS presented higher free swell values due to dispersive effects of stabilizers.

The C was blended with different proportions of RHA, and it was observed that 3%, 6%, 9%, and 12% RHA caused 1.36, 1.66, 2.3, and 1.92 times increase in unconfined compressive strength (UCT). The C was also ameliorated with 0.6%, 0.9%, 1.2%, and 1.5% NS, which resulted in increase of 1.62, 2.23, 2.87, and 43 times UCT. Moreover, the C was also mixed with RHA plus NS composites. Synergistic composites of 3%, 6%, 9%, and 12% RHA with 0.6%, 0.9%, 1.2%, and 1.5% NS increased the UCT of C substantially as compared with the individual blends of C with RHA or NS as presented in Figure 5.

The combined effect of RHA and NS enhanced the UCT from 53 kPa (clay) to 265 kPa, i.e., 5 times higher, by the addition of optimized contents of 9% RHA and 1.2% of NS.

The stress-strain curves of UCT in Figure 6 show that the stress with respect to strain enhances the linear portion with increase in RHA and NS. The C was blended with different proportions of RHA, and it was observed that 3%, 6%, 9%, and 12% RHA caused 1.07, 1.17, 1.44, and 1.24 times increase in elastic modulus (Es) of clay. The C was also mixed with 0.6%, 0.9%, 1.2%, and 1.5% NS which caused an increase of 1.15, 1.28, 1.8, and 1.33 times the Es of C. Moreover, the C was also ameliorated by synergistic composites of RHA plus NS. Composites of 3%, 6%, 9%, and 12% RHA with 0.6%, 0.9%, 1.2%, and 1.5% NS increased the Es of C substantially as compared with the individual blends of C with RHA or NS as presented in Figure 6.

The combined effect of RHA and NS enhanced the Es from 54 MPa (native clay) to 128 MPa, i.e., 2.37 times as compared with C, by the addition of optimized contents of 9% RHA and 1.2% of NS.

The effect of RHA and NS on resilient modulus (MR) of clay is shown in Figure 7. The C was blended with different proportions of RHA, and it was observed that 3%, 6%, 9%, and 12% RHA caused 1.14, 1.2, 1.39, and 1.28 times increase in MR. The C was also ameliorated with NS which resulted in increase of 1.26, 1.43, 1.8, and 1.67 times increase in MR. Moreover, the C was also mixed with RHA plus NS composites. Synergistic composites of 3%, 6%, 9%, and 12% RHA with 0.6%, 0.9%, 1.2%, and 1.5% NS increased the MR of C substantially as compared with the individual blends of C with RHA or NS as presented in Figure 7.

The optimal synergistic blend of 9% RHA plus 1.2% NS presented the highest resilient modulus value in the studied blends, i.e., 2.79 times as compared with C. The proportions blends showing the RHA and NS beyond 9% RHA and 1.2% NS presented lower MR values due to dispersive effects of stabilizers as an effect of excessive quantities of RHA and NS. Past studies like Lang et al. [25] show that the addition of 1.5% nano-SiO2 to native clay soil presents lower strengths due to dispersive effects of excessive nanoparticles.

Increase in maximum dry density (γ_{dmax}) and decrease in optimum moisture content (OMC) were observed because of addition of RHA and NS. The increase in γ_{dmax} was seen as 20.7%, 29%, and 47.5% at optimized blends of 9% RHA, 1.2% NS, and 9% RHA plus 1.2% NS blends, respectively. Similar trends were observed in the case of soaked CBR values.

The C was blended with different proportions of RHA, and it was observed that 3%, 6%, 9%, and 12% RHA caused 1.04, 1.15, 1.28, and 1.19 times increase in CBR as shown in Figure 8. The C was also ameliorated with NS which resulted in increase of 1.23, 1.60, 1.85, and 1.43 times CBR as compared with C. Moreover, the C was also mixed with RHA plus NS composites. Synergistic composites of 3%, 6%, 9%, and 12% RHA with 0.6%, 0.9%, 1.2%, and 1.5% NS increased the CBR of C substantially as compared with the individual blends of C with RHA or NS as presented in Figure 8.

The synergistic optimized blend of 9% RHA plus 1.2% NS showed highest increase in CBR, i.e., 3.62 times higher than C.

The data were validated by statistical analysis and found in good health with no outliers.

Tables 7 and 8 summarized the chemical composition of native clay (C) and rice husk ash (RHA) observed through X-ray fluorescence analysis.

Both C and RHA materials primarily comprised of silica with 48.6% and 78.2%, respectively. Aluminum oxide was observed at 14.7% in C and 3.7% in RHA. Ferric oxide was found 8.4% in C and 1.1% in RHA. Sodium oxide was 3.1% in C while in RHA, it was 0.6%. In C, the potassium oxide was 0.67% while in RHA, it was 2.4%. 4.3% magnesium oxide was present in C, and 0.9% in RHA. Calcium oxide was 12.3% in C sample and 1.5% in RHA sample. All major compounds chemical composition in C and RHA samples were found common; hence, good affinity between both materials after mixing in blends was observed.

Figure 9 shows the individual Fourier transform infrared spectroscopy (FTIR) profiling of C, RH, RHA, NS and synergistic optimized blend of C with 9% RHA plus 1.2% NS. The peak pickings labelled 1 to 12 in the FTIR test results (Figure 9) were analyzed [34], and details of bonds, i.e., single, double, triple, and foot prints in C, RHA, NS, and synergetic optimum blend are summarized in Table 9. The

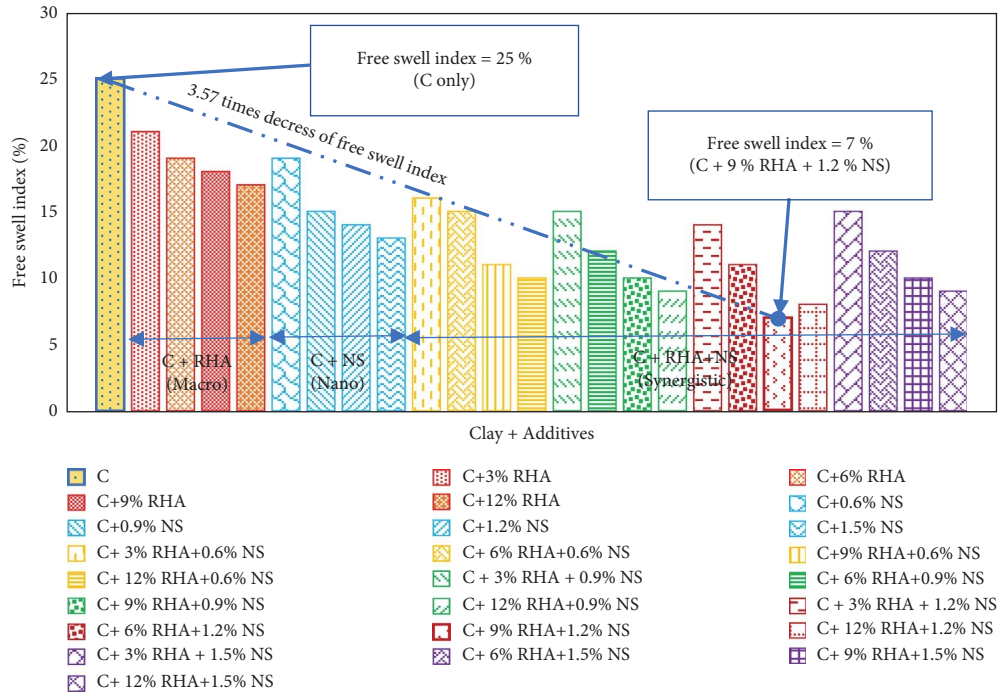

Figure 4: Free swell of clay and blends of clay plus RHA and NS synergistic.

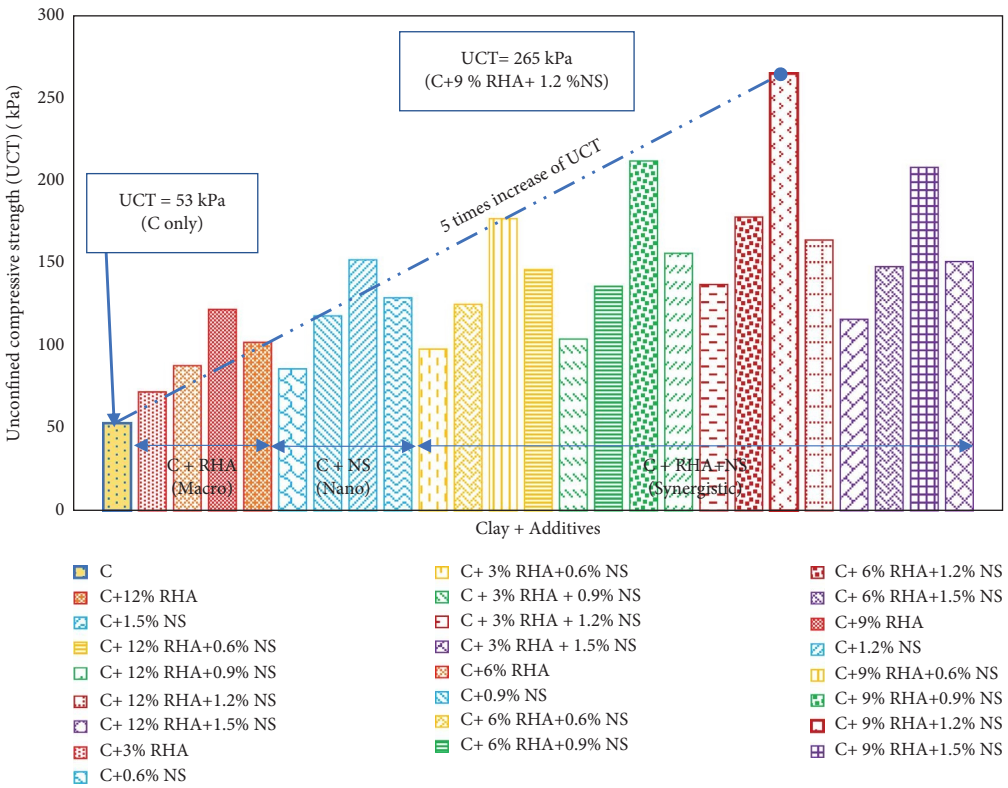

Figure 5: UCT of clay and blends of clay plus RHA and NS.

functional groups and their quantified frequencies were also determined for C, RHA, NS, and optimum blend [34].

The interpretation details of the FTIR results shown in Figure 9 and presented in Table 10 are explained as follows. In the range of 3650 and 3250 cm^{-1}, broad absorption bonds were observed in all samples showing the presence of hydrogen bond. Sharp bonds were observed round 3500 cm^{-1} regions in all samples illustrating the presence of oxygen

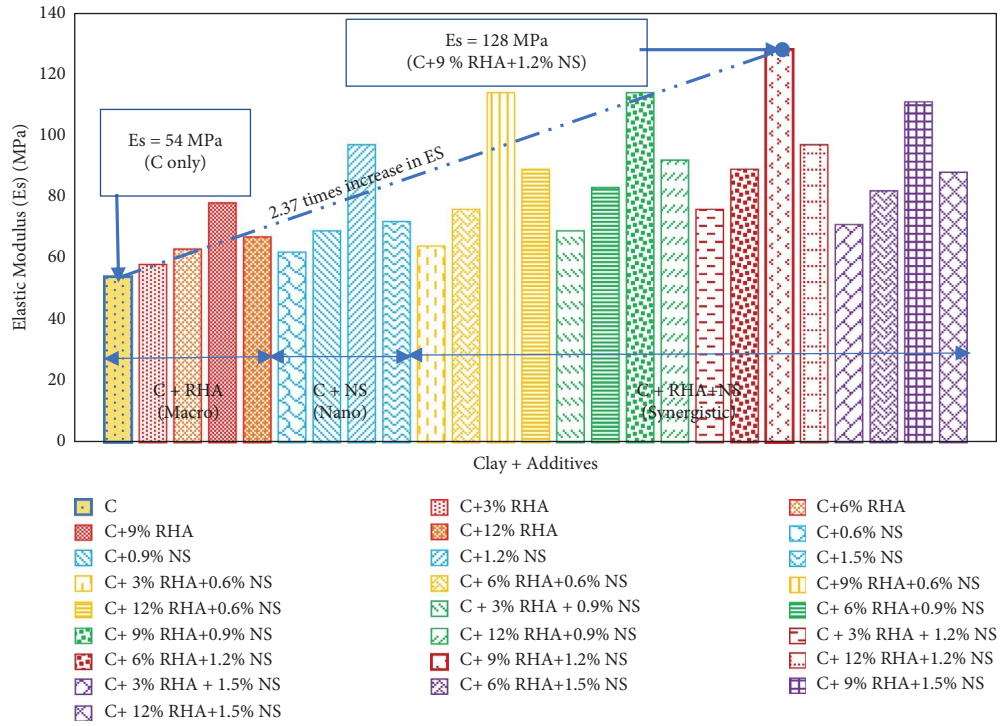

Figure 6: Es of clay and blends of clay plus RHA and NS.

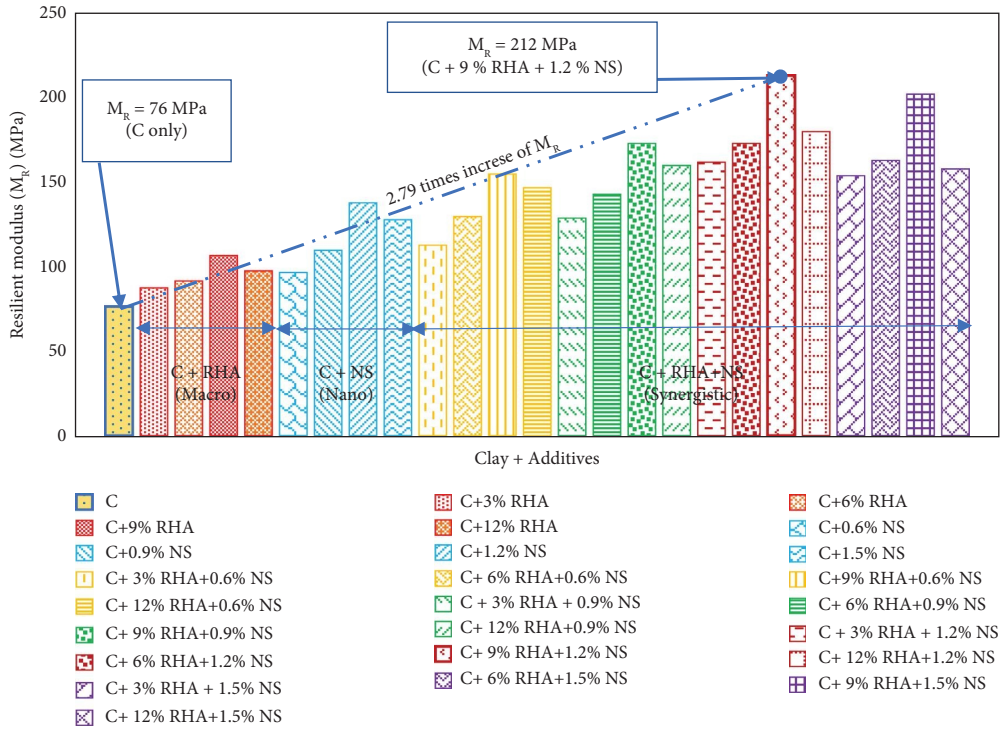

Figure 7: MR of clay and blends of clay plus RHA and NS.

related bonding. The peaks were observed in range of 3000 and 3200 cm^{-1} reflecting the presence of aromatic rings. Single bond of carbon (C-C) was observed in NS due to peak at 3000 cm^{-1}. No aldehyde peak was found in typical range of 2700 to 2800 cm^{-1}. No significant peaks were observed from 2000 to 2200 cm^{-1}, and hence, no carbon-carbon triple bond was observed in any samples. At about 1700 cm^{-1}, sharp peaks were observed in all samples demonstrating some carbonyl double bonds in the samples. At around 1600 cm^{-1}, peaks were observed in all samples informing the

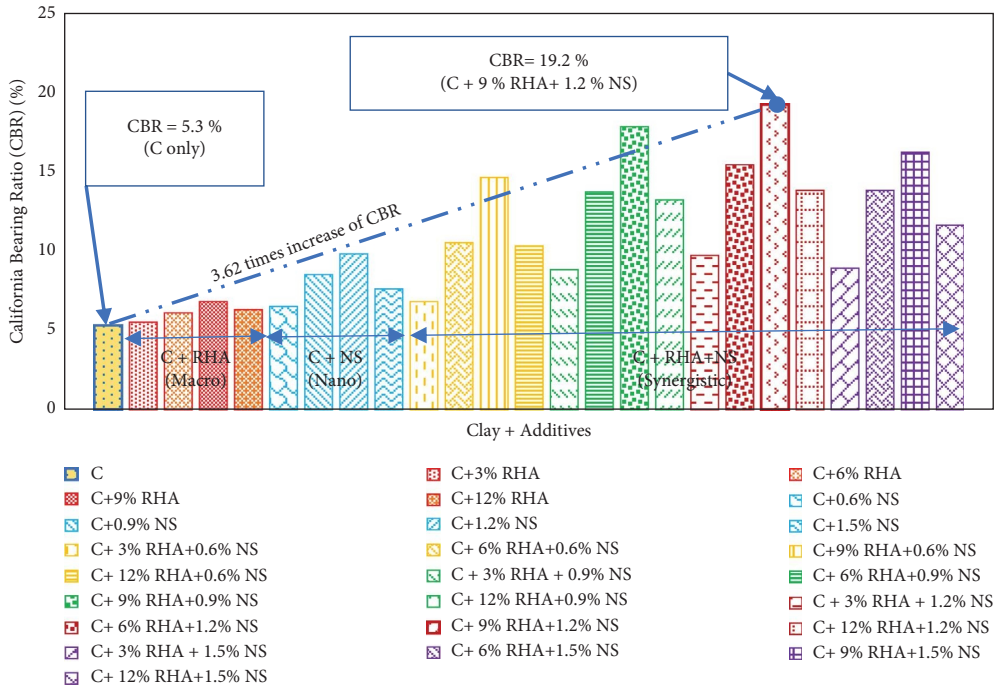

Figure 8: CBR of clay and blends of clay plus RHA and NS.

Table 7: Chemical composition of expansive clay (C) from X-ray (ASTM D5381) fluorescence analysis.

Constituents	Percentage, %
SiO_2-silica	48.6
Al_2O_3-aluminium oxide	14.7
Fe_2O_3- ferric oxide	8.4
MgO-magnesium oxide	4.3
CaO-calcium oxide	12.3
K_2O-potassium oxide	0.67
Na_2O-sodium oxide	3.1
Others	7.9

Table 8: Chemical composition of rice husk ash (RHA) from X-ray (ASTM D5381) fluorescence analysis.

Constituents	Percentage, %
SiO_2-silica	78.2
CaO-calcium oxide	1.5
Al_2O_3-aluminium oxide	3.7
Fe_2O_3-ferric oxide	1.1
Na_2O-sodium oxide	0.6
MgO-magnesium oxide	0.9
K_2O-potassium oxide	2.4
Others	11.6

presence of carbon-carbon double bond. At 1500 cm^{-1}, signals were observed showing the aromatic rings presence also in double bond region. Vinyl related compounds were also seen at about 1000 cm^{-1} in the finger print region. The similarity in peak trends was observed in all investigated materials showing comparable composition in spectrum and analysis regions (single bond, triple bond, double bond, and

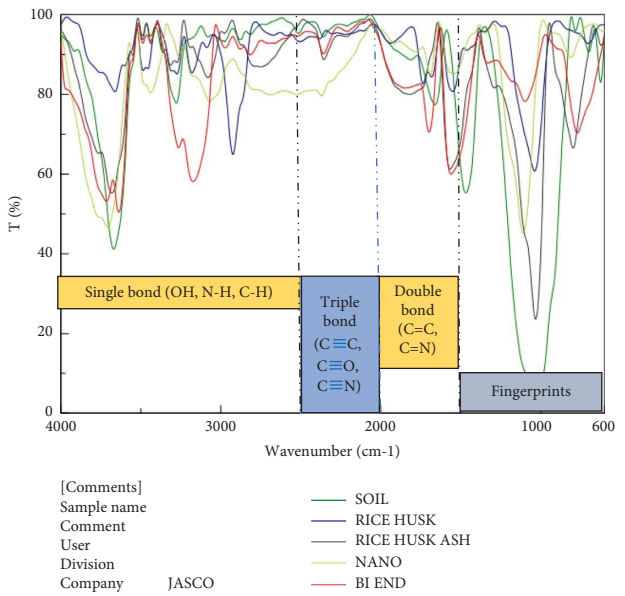

Figure 9: FTIR spectroscopy.

fingerprints). Out of all used materials and their combinations, i.e., C, RH, RHA, NS, and optimum blend, chemical compatibility was observed in FTIR spectroscopy except NS where single bond of carbon was observed in single bond analysis zone.

The optical microscopic images of C, RHA, NS, and C + RHA + NS optimal blend are presented in Figure 10. The optical images interpretation was carried out in accordance with guidelines of Pires et al. [36]. The results are summarized in Table 11. Pore size distribution (small, medium,

Table 9: The summary of FTIR tests analysis and wavenumber intensity and respective peak pickings.

Peak picking	1		2		3		4		5		6		7		8		9		10		11		12	
	W	T	W	T	W	T	W	T	W	T	W	T	W	T	W	T	W	T	W	T	W	T	W	T
C	3668	41	3278	77	2977	93	2358	94	1659	77	1467	55	1026	6	782	95	698	90	624	83	NA			
RHA	3681	55	3489	93	3437	92	3314	87	3080	84	2749	86	2355	88	1819	79	1566	61	1031	23	797	66	620	92
NS	3707	46	3549	89	3439	80	3262	89	3069	78	2370	79	1690	84	1538	85	1108	45	810	89	NA			
B	3715	53	3638	50	3487	92	3174	58	2814	98	2358	90	1697	70	1560	59	1098	78	771	70	NA			

W = wavenumber (cm^{-1}), T = transmittance (%).

Table 10: Interpretation of FTIR test results as per guidelines of Coates & Nandiyanto [34, 35].

Description	Spectrum	Analysis regions			
		Single bond (2500–4000 cm^{-1})	Triple bond (2000–2500 cm^{-1})	Double bond (1500–2000 cm^{-1})	Fingerprint (600–1500 cm^{-1})
C	Complex	(i)Hydrogen bond (ii)Oxygen related bonding (iii) Aromatic rings (iv) No aldehyde	(i) No carbon-carbon bond	(i) Carbonyl double bond (ii) Carbon-carbon double bond (iii) Aromatic rings	(i) Vinyl related compounds
RH	Complex	(i) Hydrogen bond (ii) Aromatic rings (iii) No aldehyde	(i) No carbon-carbon bond	(i) Carbonyl double bond (ii) Carbon-carbon double bond (iii) Aromatic rings	(i) Vinyl related compounds
RHA	Complex	(i) Hydrogen bond (ii) Oxygen related bonding (iii) Aromatic rings (iv) No aldehyde	(i) No carbon-carbon bond	(i) Carbonyl double bond (ii) Carbon-carbon double bond (iii) Aromatic rings	(i) Vinyl related compounds
NS	Complex	(i) Hydrogen bond (ii) Oxygen related bonding (iii) Aromatic rings (iv) No aldehyde (v) Single bond of carbon	(i) No carbon-carbon bond	(i) Carbonyl double bond (ii) Carbon-carbon double bond (iii) Aromatic rings	(i) Vinyl related compounds
C + 9%RHA + 1.2%NS blend	Complex	(i) Hydrogen bond (ii) Oxygen related bonding (iii) Aromatic rings	(i) No carbon-carbon bond	(i) Carbonyl double bond (ii) Carbon-carbon double bond (iii) Aromatic rings	(i) Vinyl related compounds

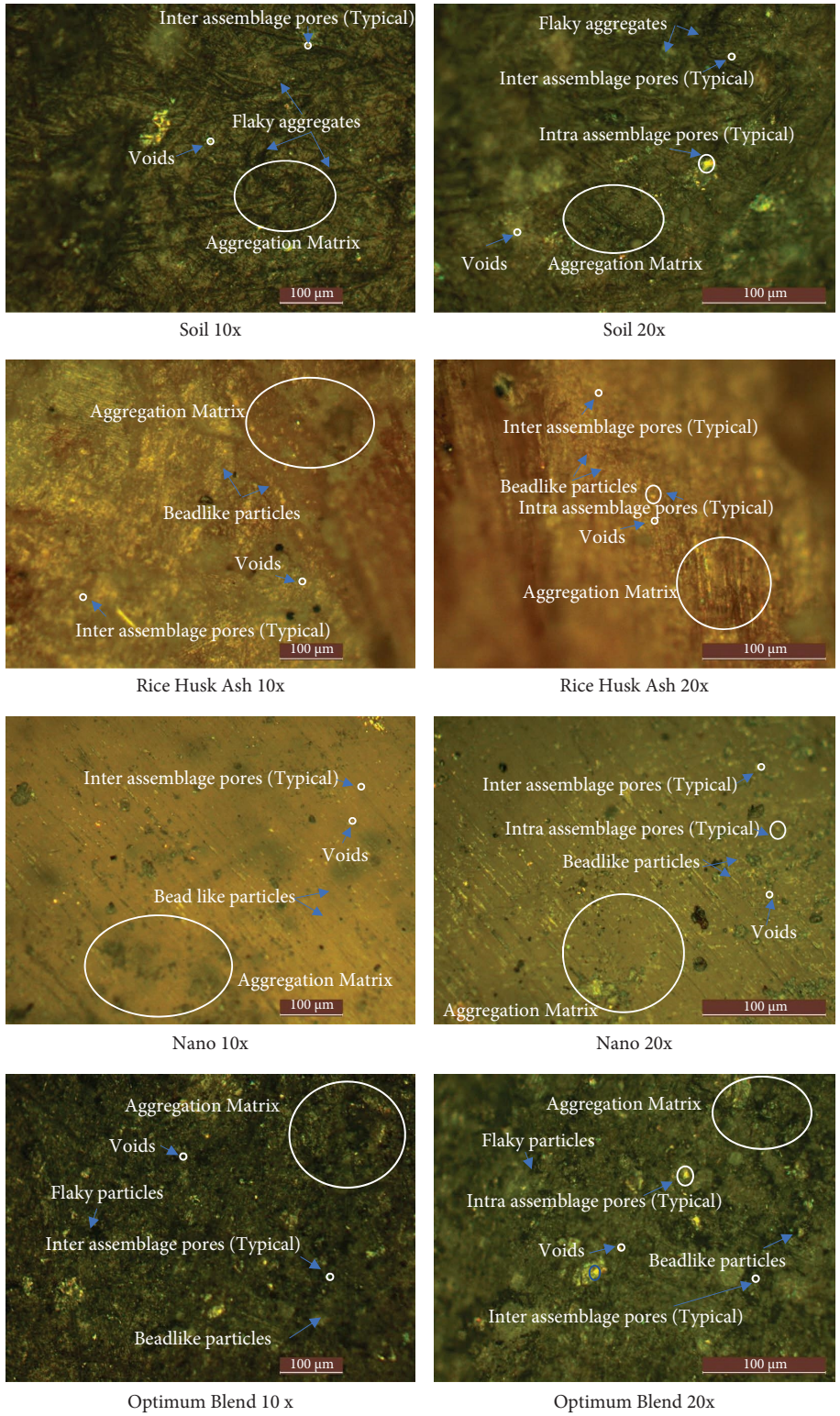

Figure 10: Optical microscopic images.

and large), irregularity (angular, flaky, and elongate), orientation (horizontal, circumferential, random), and macropore space and spatial distribution (bonded, intermediate, and elongated) were evaluated. Small to medium pore size distributions and voids were observed in the samples. In C and its optimal blend with RHA and NS, angular, flaky, and elongated fractions of irregularities were observed. The major orientation of RHA and NS being powders was observed circumferential/beadlike while C and its optimal blend exhibited a combination of circumferential/beadlike,

Table 11: Interpretation of optical image analysis results.

Description	Pore size distribution			Irregularity			Orientation			Space	Spatial distribution		
	Small	Medium	Large	Angular	Flaky	Elongated	Horizontal	Circumferential	Random	Macropore	Bonded	Intermediate	Elongated
C	—	X	—	X	X	X	X	X	X	X	X	X	X
RHA	X	X	—	—	—	—	—	X	—	X	X	—	—
NS	X	—	—	—	—	—	—	X	—	X	X	—	—
C + 9%RHA +1.2%NS	X	X	—	X	X	X	X	X	X	X	X	X	X

X denotes presence/yes.

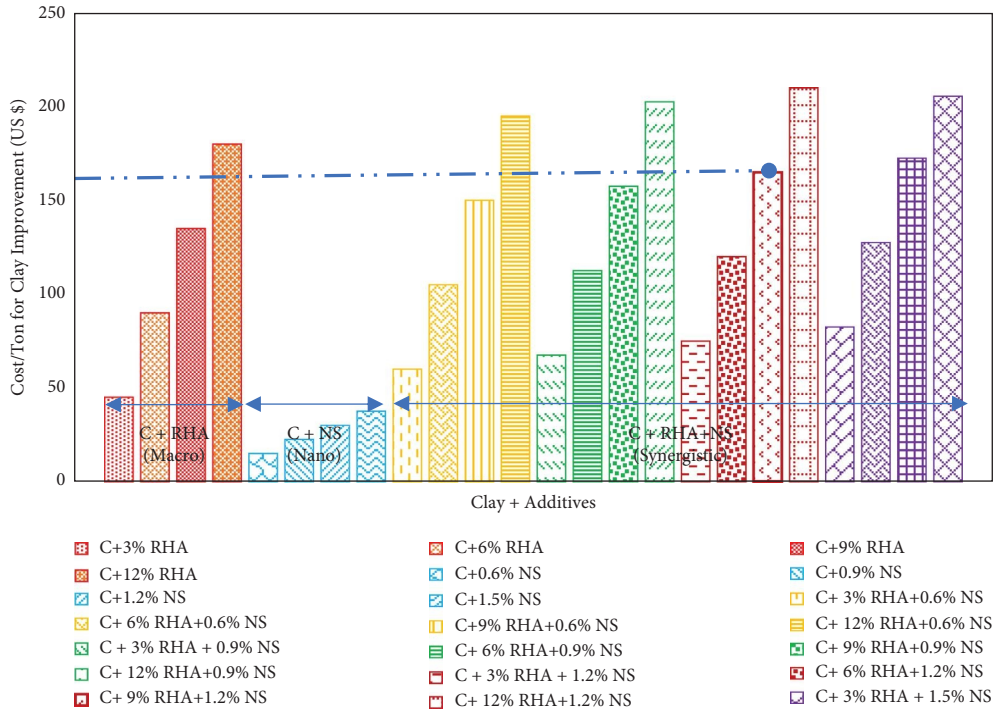

Figure 11: Cost versus stabilizer (RHA and NS) contents.

horizontal, and random orientations. Macropores can be seen in all samples marked as inter and intra-assemblage pores in Figure 10. The spatial distribution was observed in the form of aggregation matrix comprising of combination of bonded, intermediate, and elongated aggregates in C and its optimal blend. The RHA and NS, however, predominantly exhibited bonded spatial distribution.

The optical microscope analysis showed that clay stabilized with optimal dose of 1.2% of NS and 9% RHA exhibited optimum filling of pore spaces of native clay. Hence, the optimum values of density, stiffness, and strength parameters are validated.

The cost evaluation of microlevel stabilization (RHA) compared with nanolevel (NS) and micro plus nanolevel synergistic blends (C + RHA + NS) based on resultant optimal stiffness was carried out. The RHA and NS rates were used as \$1.5/kg and \$2.5/kg, respectively. In field, the cost of construction equipment, mixing, spreading, and compaction of both stabilizers, i.e., RHA and NS in expansive clay, is almost same. Hence, the cost analysis in this research only covered the cost of RHA and NS. The ratio of Cost(1.2%NS)/Cost(9%RHA) for individual stabilizers, i.e., NS and RHA, to achieve optimum stiffness and strength for treatment of one ton of clay, is \$30/\$135 = 0.22, whereas the optimal ratio for synergistic blend is Cost(1.2%NS–12%RHA)/Cost(12% RHA), i.e., \$165/\$135 = 1.22 which shows much higher enhancement in stiffness and strength of clay as the optimum ratios of MR (1.2%NS–9%RHA)/MR(9%RHA) = 2.0, Es (1.2%NS–9%RHA)/Es(9%RHA) = 1.64, UCT(1.2%NS-9% RHA)/UCT(9%RHA) = 2.17, and CBR(1.2%NS-9%RHA)/CBR(9%RHA) = 2.82. It was observed that the optimal blends of synergistic ratios show the RHA plus NS blends showing higher stiffness and strength ratios as compared with cost ratio of the corresponding blends. From Figures 5–8, it is observed that the ratio of MR (RHA-NS)/MR(RHA), Es (RHA-NS)/Es(RHA), UCT(RHA-NS)/UCT(RHA), and CBR(RHA-NS)/CBR(RHA) is 1.6, 1.3, 1.8, and 2.3 times higher than Cost(RHA-NS)/Cost(RHA), respectively, for optimal dose of 1.2% of NS plus 9% of microlevel RHA, validating the cost-effective solution for biocompatible stabilization of subgrade expansive clay.

It is observed from Figure 11 that for optimal blend of (1.2% NS + 9% RHA)/9% RHA, the ratio of cost for this blend is lower than the ratio of stiffness and strength parameters as presented in Figs. 5, 6, 7, 8. Beyond this optimal blend, the stiffness ratio decreases and the cost ratio increases making the blends uneconomical, e.g., 12% + 1.5% NS blend is uneconomical as it shows lower stiffness and strength ratios due to dispersive effects and higher cost ratio.

4. Conclusions

The purpose of this study was the sustainable stabilization of the high-plasticity expansive clay by green agro-waste additives at three levels, i.e., microlevel (by rice husk ash), nanolevel (by rice husk-derived nanosilica), and synergistic nano to microlevel (by blends of nanosilica and rice husk ash). FTIR, XRD, optical microscopic, and cost analysis were performed for each levels of stabilization for feasible blends evaluation to be used in amelioration of expansive clay. The following conclusions were addressed in this study:

(1) The optimal synergistic dose of micro to nanoparticles for stabilization of expansive clay was observed to be 1.2% of nanosilica (NS) and 9% of rice

husk ash (RHA) which resulted in improvement of resilient modulus (MR), elastic modulus (Es), unconfined compressive strength (UCT), and California bearing ratio (CBR) as 2.79, 2.37, 5.0, and 3.62 times, respectively, and free swell index was reduced up to 72% as compared with native expansive clay.

(2) The ratio of optimized contents for RHA, NS, and RHA-NS synergistic stabilization phases for MR, Es, UCT, and CBR are observed to be more than one, i.e., MR (RHA-NS)/MR(RHA), Es (RHA-NS)/Es(RHA), UCT (RHA-NS)/UCT(RHA), and CBR(RHA-NS)/CBR(RHA) as 2.0, 1.64, 2.17, and 2.82, respectively. Hence, it results in more sustainable stabilized mixes.

(3) The ratio of Cost(RHA-NS)/Cost(RHA) for optimal dose was evaluated as 1.22. The analysis also depicted that the ratio of MR (RHA-NS)/MR(RHA), Es (RHA-NS)/Es(RHA), UCT(RHA-NS)/UCT(RHA), and CBR(RHA-NS)/CBR(RHA) is 1.6, 1.3, 1.8, and 2.3 times higher than Cost(RHA-NS)/Cost(RHA), respectively, for optimal dose of 1.2% of rice husk-derived nanosilica plus 9% of microlevel rice husk ash, validating the cost-effective solution for biocompatible stabilization of subgrade expansive clay.

(4) The Fourier transform infrared spectroscopy (FTIR) revealed the chemical compatibility between C, RHA, & NS for possible future durability perspective. The optical microscope analysis showed that clay stabilized with optimal dose of 1.2% of NS and 9% RHA exhibited optimum filling of pore spaces of native clay. Hence, it validates the optimum values of density, stiffness, and strength parameters.

The study should be extended to explore the durability of the proposed blends. The optimization of the strength and durability is the function of C, RHA, and NS quantities of the blends.

Data Availability

The data supporting the current study are available from the corresponding author upon request.

Conflicts of Interest

The authors declare that they have no conflicts of interest.

Acknowledgments

This work was supported by the Higher Education Commission of Pakistan, NRPU 9631.

References

[1] A. H. Khan, Z. U. Rehman, and W. Abbass, "Prediction of post-yield strain from loading and unloading phases of pressuremeter, triaxial, and consolidation test curves for sustainable embankment design," *Sustainability*, vol. 14, p. 2535, 2022.

[2] W. Qamar, A. H. Khan, and Z. U. Rehman, "Sustainable application of wool-banana bio-composite waste material in geotechnical engineering for enhancement of elastoplastic strain and resilience of subgrade expansive clays," *Sustainability*, vol. 14, Article ID 13215, 2022.

[3] W. Chen, J. Zhao, L. Fan et al., "The effect of length and content of fiber on glass fiber and basalt fiber-reinforced granite residual soil," *Advances in Civil Engineering*, vol. 2022, no. 22, Article ID 7803002, 9 pages, 2022.

[4] Y. Liang, F. Zhang, M. Jing, and P. He, "Research on mechanical model of canal lining plates under the effect of frost heaving force," *Advances in Civil Engineering*, vol. 2022, no. 22, Article ID 8762382, 17 pages, 2022.

[5] W. Oueslati, C. Mejri, and A. B. H. Amara, "Impact of uniaxial mechanical perturbation on structural properties and smectite porosity features: ion exchanger efficiency and adsorption performance fate," *Advances in Civil Engineering*, vol. 2022, Article ID 4441705, 2022.

[6] D. Shewatatek, B. Tenaw, A. Yemiru, G. Belete, T. Tadesse, and T. Tolla, "Characteristics of sand at major quarrying areas around addis ababa," *Advances in Civil Engineering*, vol. 2022, Article ID 3198879, 9 pages, 2022.

[7] M. D. Bakare, R. R. Pai, S. Patel, and J. T. Shahu, "Environmental sustainability by bulk utilization of fly ash and GBFS as road subbase materials," *Journal of Hazardous, Toxic, and Radioactive Waste*, vol. 23, no. 4, 2019.

[8] B. A. Malik, P. Mandhaniya, and M. Y. Shah, "Experimental and numerical study on reinforcement of foundations using micropiles as a retrofitting measure," *Arabian Journal for Science and Engineering*, vol. 48, pp. 5335–5345, 2023.

[9] I. R. Sheikh, P. Mandhaniya, and M. Y. Shah, "A parametric study on pavement with geocell reinforced rock quarry waste base on dredged soil subgrade," *International Journal of Geosynthetics and Ground Engineering*, vol. 7, no. 2, p. 32, 2021.

[10] R. R. Pai, S. Patel, and M. D. Bakare, "Applicability of utilizing stabilized native soil as a subbase course in flexible pavement," *Indian Geotechnical Journal*, vol. 50, no. 2, pp. 289–299, 2020.

[11] E. A. Santos, C. T. D. S. Dutra, C. K. Chinelli, A. W. A. Hammad, A. N. Haddad, and C. A. P. Soares, "The main impacts of infrastructure works on public roads," *Infrastructure*, vol. 6, no. 9, p. 118, 2021.

[12] J. Karimiazar, M. Mahdad, and E. S. Teshnizi, "Assessing the geotechnical properties of soils treated with cement and nanosilica additives," *JOJ Science*, vol. 2, no. 3, pp. 56–59, 2020.

[13] J. Karimiazar, S. E. Teshnizi, and M. Mirzababaei, "California bearing ratio of a reactive clay treated with nano-additives and cement," *Journal of Materials in Civil Engineering*, vol. 34, no. 2, 2022.

[14] F. Buazar, "Impact of biocompatible nanosilica on green stabilization of subgrade soil," *Scientific Reports*, vol. 9, no. 1, 9 pages, Article ID 15147, 2019.

[15] K. Onyelowe, D. Bui Van, A. Eberemu et al., "Sorptivity, swelling, shrinkage, compression and durability of quarry dust treated soft soils for moisture bound pavement geotechnics," *Journal of Materials Research and Technology*, vol. 8, no. 4, pp. 3529–3538.

[16] A. Soltani, A. Taheri, M. Khatibi, and A. R. Estabragh, "Swelling potential of a stabilized expansive soil: a comparative experimental study," *Geotechnical & Geological Engineering*, vol. 35, no. 4, pp. 1717–1744, 2017.

[17] A. Ghorbani, H. Hasanzadehshooiili, M. Mohammadi et al., "Effect of selected nanospheres on the mechanical strength of

lime-stabilized high-plasticity clay soils," *Advances in Civil Engineering*, vol. 2019, Article ID 4257530, 11 pages, 2019.

[18] M. Mirzababaei, J. Karimiazar, E. Sharifi Teshnizi, R. Arjmandzadeh, and S. H. Bahmani, "Effect of nano-additives on the strength and durability characteristics of marl," *Minerals*, vol. 11, no. 10, p. 1119, 2021.

[19] J. E. Bowles, *Foundation Analysis and Design*, Wiley-Interscience, Hoboken, NJ, USA, 1996.

[20] R. D. Holtz, W. D. Kovacs, and T. C. Sheahan, *An Introduction to Geotechnical Engineering*, Prentice-Hall, Englewood Cliffs, NJ, USA, 2011.

[21] C. Olivier, A. Jean-Claude, and L. B. Tangi, "Microstructure and hydraulic conductivity of a compacted lime-treated soil," *Engineering Geology*, vol. 123, no. 3, pp. 187–193, 2011.

[22] B. Fatahi, T. M. Le, B. Fatahi, and H. Khabbaz, "Shrinkage properties of soft clay treated with cement and geofibers," *Geotechnical & Geological Engineering*, vol. 31, no. 5, pp. 1421–1435, 2013.

[23] S. M. S. Kazmi, S. Abbas, M. J. Munir, and A. Khitab, "Exploratory study on the effect of waste rice husk and sugarcane bagasse ashes in burnt clay bricks," *Journal of Building Engineering*, vol. 7, no. 9, pp. 372–378, 2016.

[24] J. Donrak, M. Hoy, and S. Horpibulsuk, "Environmental assessment of cement-stabilised lateritic soil/melamine debris for Thailand's pavement," *Environmental Geotechnique*, vol. 9, 2020.

[25] L. Lang, B. Chen, and N. Li, "Utilization of lime/carbide slag-activated ground granulated blast-furnace slag for dredged sludge stabilization," *Mineral Georesourse Geotechnology*, vol. 13, Article ID 1741050, 2020.

[26] K. Gu and B. Chen, "Research on the incorporation of untreated flue gas desulfurization gypsum into magnesium oxysulfate cement," *Journal of Cleaner Production*, vol. 271, Article ID 122497, 2020.

[27] L. Lang, B. Chen, and H. Duan, "Modification of nano-particles for the strength enhancing of cement-stabilized dredged sludge," *Journal of Rock Mechanics and Geotechnical Engineering*, vol. 13, no. 3, 2021.

[28] Y. Wang, P. Guo, and X. Li, "Behavior of fiber-reinforced and lime-stabilized clayey soil in triaxial tests," *Applied Sciences*, vol. 9, p. 900, 2019.

[29] S. G. F. P. Lemos, M. D. S. S Almeida, and N. C. Consoli, "Field and laboratory investigation of highly organic clay stabilized with portland cement," *Journal of Materials in Civil Engineering*, vol. 32, Article ID 04020063, 2020.

[30] H. Nasiri, N. Khayat, and M. Mirzababaei, "Simple yet quick stabilization of clay using a waste by-product," *Transportation Geotechnique*, vol. 28, Article ID 100531, 2021.

[31] B. S. Luh, *Rice: Production and Utilization*, AVI Publishing, CT, USA, 1980.

[32] J. Ma, Y. Su, and Y. Liu, "Strength and microfabric of expansive soil improved with rice husk ash and lime" Advances in Civil Engineering," vol. 2020, Article ID 9646205, 20 pages, 2020.

[33] O. Cuisinier, J. C. Auriol, T. Le Borgne, and D. Deneele, "Microstructure and hydraulic conductivity of a compacted lime-treated soil," *Engineering Geology*, vol. 123, no. 3, pp. 187–193, 2011.

[34] J. Coates, "Interpretation of infrar3d spoectra a practical approachEncyclopedia of analytical chemistry," *Infrared spectroscopy*, vol. 12, pp. 10815–10837, 2006.

[35] A. B. D. Nandiyanto, R. Oktiani, and R. Ragadhita, "How to read and interpret FTIR spectroscope of organic material," *Indonesian Journal of Science and Technology*, vol. 4, no. 1, pp. 97–118, 2019.

[36] L. F. Pires, F. S. Borges, S. Passoni, and A. Pereira, "Soil pore characterization using free software and a portable optical microscope," *Pedosphere*, vol. 23, no. 4, pp. 503–510, 2013.

Hindawi
Advances in Civil Engineering
Volume 2023, Article ID 5731841, 12 pages
https://doi.org/10.1155/2023/5731841

Research Article

Experimental Study on the Flexural Behavior of Connected Precast Concrete Square Piles

Zhongji Dong,[1] **Faning Dang**,[2] **and Jun Gao**[2]

[1]*Xi'an Engineering Investigation & Design Research Institute of China, National Nonferrous Metals Industry, Co., Ltd., Xi'an 710054, China*
[2]*State Key Laboratory of Eco-Hydraulics in Northwest Arid Region, Xi'an University of Technology, Xi'an 710048, China*

Correspondence should be addressed to Faning Dang; dangfn@163.com

Received 12 November 2022; Revised 1 February 2023; Accepted 27 March 2023; Published 19 April 2023

Academic Editor: Danqing Song

Part of deep foundation pit support engineering needs to select connected precast concrete square piles (CPCSPs). Under the premise that the quality of precast concrete square piles (PCSPs) meets engineering requirements, the quality of CPCSPs becomes the key factor to ensure the safety of foundation pit support structures. This paper puts forward a new connection technology of CPCSPs and carries out the flexural behavior experiment of unconnected precast concrete square piles (UPCSPs) and CPCSPs. The distribution of crack and strain on different surfaces of UPCSPs and CPCSPs are measured by carbon fiber composite strain sense optical cables, glass fiber composite strain sense optical cables, and fixed-point polyurethane strain sense optical cables. The anti-crack load, ultimate load, bending moment, and flexural deformation of UPCSPs and CPCSPs are measured. The experimental results of UPCSPs and CPCSPs are compared. The results show that the anti-crack strength of CPCSPs is greatly increased while the flexural deformation of CPCSPs is decreased before the occurrence of crack. With the development of crack (failure stage), the outside areas of hoop steel plate exhibit cracks. At this moment, the strength of CPCSPs is no longer controlled by the strength of middle areas. The ultimate strength of CPCSPs is basically equivalent to that of UPCSPs. The ultimate bending moment of CPCSPs is higher than its design value (about 66%~76%). The selection of CPCSPs in the design of foundation pit support has good reliability.

1. Introduction

The foundation pit support technologies in China mainly include cast-in place pile, prestress anchor, diaphragm wall, inner support, (composite) soil nail wall, and SMW construction method. According to incomplete data statistics, the above traditional support forms [1–5] are chosen by more than 95% of foundation pits. However, with the development of society and the progress of technology, the problems of high cost, large construction space, long construction period, high energy consumption, and serious environment pollution of traditional support forms have become increasingly prominent. Precast concrete piles are more and more widely used in foundation pit support engineering because of their advantages in short construction period, reliable construction quality, high environmental protection, and economic benefits [6–10]. Due to the limits of production molds, transportation conditions, and piling equipment, the length of precast concrete piles generally does not exceed 15 m. Only the connected piles can meet the requirements for the embedded depth of deep foundation pit support structures.

In recent years, the bearing capacity performances of precast concrete piles are researched deeply by engineering and academic circles, and abundant research results have been obtained. The connection method of bonded steel plate weld for PHC piles in standard atlas was improved by Li et al. [11]. It was found that the mechanical performance, construction technology, and weld quality of improved connection joint had significantly improved compared to standard connection joint. On this basis, a new PHC uplift pile with hold-hoop connection method was proposed by

Zhang et al. [12, 13], which could significantly improve the pullout capacity of piles. The new mechanic-connection method was developed by Qi et al. [14]. It was found that the compressive and tensile capacity of mechanic-connection bamboo joint piles were significantly better than those of common prestress piles. The flexural behavior test of prestress concrete hollow square piles was carried out by Liu et al. [15], and it was found that the ultimate bending moment of weld joints met the requirement of inspection value. At the same time, the axial tensile tests on the internal buckle mechanic-connection joint of prestress concrete hollow square uplift piles were carried out by Fan et al. [16]. The comprehensive detection ways and judgment of deflect of precast square concrete piles were proposed by Zhang [17]. An extensive evaluation of capacity interpretation criteria was presented for driven precast concrete (PC) piles under axial compression loading by Marcos et al. [18]. The tensile and flexural behaviors of prestressed concrete square pile connection joint with resilient clamping were studied by Wang et al. [19, 20]. The flexural performance of prestressed concrete solid square piles and resilient clamping connections were studied by Xu et al. [21]. The experimental results indicated that the head of rebar and end of plate were the weak parts of piles. The full-scale flexural behavior experiments on the connection joints of composite reinforcement concrete precast square piles were carried out by Xu et al. [22]. The experimental results showed that the ultimate anti-bending capacity of connection joint was greater than that of pile shaft. Several widely used connection methods for precast concrete piles from economic benefit, service life, and field workload were summarized and compared by Ptuhina et al. [23]. The influence of topographic and geological conditions was considered by Song et al. [24–30].

At present, the research of connected piles is focus on the tensile and compressive strength of pile joints. There is little research on the flexural behavior of pile joints. The research work that has been carried out is either the small size or low bending performance of test specimens. As the precast concrete pile of foundation pit support, the main force condition is anti-bending. The technology requirements of connected piles are far higher than those of compression piles and tension piles. Therefore, it has an important engineering application value for foundation pit support to carry out the research on connection technologies and flexural behaviors of precast concrete piles. In this paper, a new connection technology for precast concrete square piles (PCSPs) is proposed. The tensile and compressive loads are transferred by plate groove weld, and the flexural loads are transferred by hoop steel plate. That is, the connection technology of hoop steel plate after welding plate groove is chosen to solve the complex force problems when PCSPs are used for foundation pit support. The relationships between flexural loads and displacement, ultimate load, and failure mode are researched by the flexural behavior test of full-scale CPCSPs and UPCSPs. The research results will provide an important theoretical basis for the design and application of CPCSPs.

2. Connection Technology of Anti-Bending Pile

In order to solve the complex force problems of tension, compression, and bending when PCSPs are used for foundation pit support, the connection technology of hoop steel plate after welding plate groove is chosen. Firstly, the bevel of plate groove is chamfered to 8 : 20 before welding, so as to increase the contact area of weld spot. Secondly, the hoop steel plate is made into two symmetrical "L" parts. The side length of pile section is 500 mm and 600 mm, respectively, and the length of hoop steel plate is 1000 mm and 1200 mm, respectively. After a layer of adhesive steel structural glue is evenly applied on the inner side of hoop steel plate, the hoop steel plate is firmly fixed at the connection joint of PCSPs with clamps. Finally, the hoop steel plate is firmly welded by groove weld technology.

The section size at the connection joint of PCSPs with side length of 500 mm is 480×480 mm, and the specification of hoop steel plate is $480 \times 480 \times 8$ mm. The section size at the connection joint of PCSPs with side length of 600 mm is 580×580 mm, and the specification of hoop steel plate is $580 \times 580 \times 8$ mm. The PCSP with side length of 600 mm is taken as an example, and the connection technology parameters of PCSPs are shown in Figures 1 and 2.

3. Flexural Test Scheme of Precast Concrete Square Connection Pile

The research on the tensile and compressive properties of CPCSPs is relatively mature. In this paper, the flexural behavior of CPCSPs is researched. The test includes two groups of PCSPs with different side lengths, and each group includes three CPCSPs and one UPCSP. Among them, Nos. 5-1, 5-2, 5-3, 6-1, 6-2, and 6-3 are CPCSPs, and 5A and 6A are UPCSPs. The lengths of piles are 7.0 m. The connection locations are located at the middle of PCSPs. The concrete strength of 6 CPCSPs is 43.7~54.7 MPa, and the average concrete strength is 49.08 MPa. The main parameters of CPCSPs and UPCSPs are shown in Table 1.

3.1. Load Device and Measurement Device of Test. The distribution beam, hydraulic jack, and manual oil pump are used for loading during test. The oil pressure gauge with accuracy of 0.4 level is used to measure pressure. The load device of test is shown in Figure 3. The digital dial indicators are used to measure the deflection of PCSPs and erected at the connection joint of PCSPs, with both sides of PCSPs with 0.8 m and 1.6 m away from connection joint, which are shown in Figure 4. The carbon fiber composite strain sense optical cables and glass fiber composite strain sense optical cables are used to measure the strain crack of piles. The fixed-point polyurethane strain sense optical cables are used to measure the crack of piles. The sense optical cables are, respectively, arranged on the top, upper and lower of front, and upper of back of piles, which are shown in Figure 5. The purpose that authors choose three different strain sense optical cables is to ensure the reliability of experimental

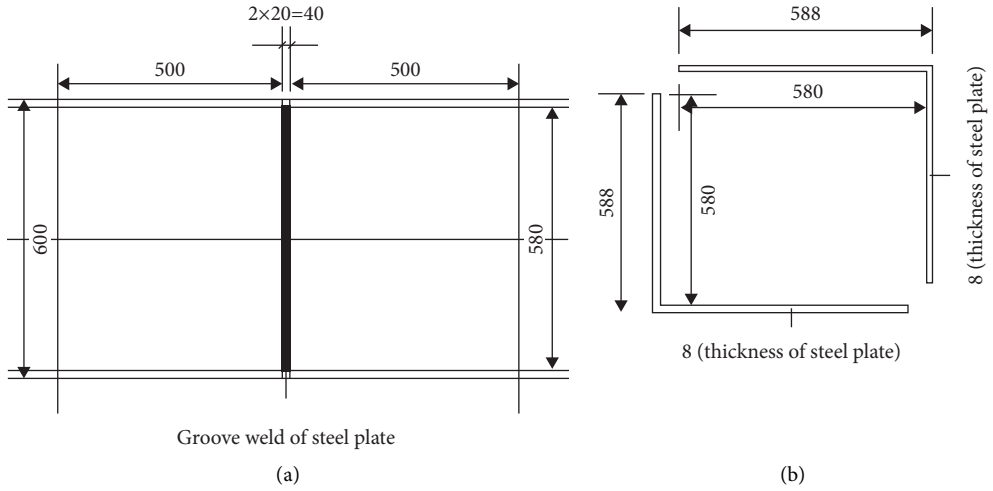

Figure 1: Schematic diagram of pile connection technology (unit: mm). (a) Connection location of pile. (b) Hoop steel plate.

Figure 2: Scene diagram of precast concrete square pile. (a) Precast concrete square pile. (b) Precast concrete square connection pile.

results. The main performances of measure instrument are shown in Table 2.

3.2. Load Method. Preload is loaded to eliminate virtual contact strain before test. The load increases from zero to 80% of estimated anti-crack bending moment according to the load with 20% of estimated anti-crack bending moment. The duration of each load level is 3 minutes. Then, the load increases from 80% to 100% of estimated anti-crack bending moment according to the load with 10% of estimated anti-crack bending moment. The duration of each load level is 3 minutes. During the test, observe whether there are cracks and record the distribution and development of cracks. If there is no crack at the load with 100% of estimated anti-crack bending moment, the load continues increasing until cracks appear according to the load with 10% of estimated anti-crack bending moment. The duration of each load level is 3 minutes. Then, the load continues increasing to the ultimate state of PCSPs according to the load with 10% of estimated anti-crack bending moment. The duration of each load level is 3 minutes. Observe and record all data.

3.3. Anti-Crack Load and Ultimate Load. It is considered to be the limit state of PCSPs when any of the following conditions occur. The crack width of piles reaches 1.5 mm. The tensile rebar is broken. The location of weld is broken or detached. The concrete in compression zone is failure. The load cannot increase or remain stable.

The anti-crack load is determined by following ways. When the crack occurs at the first time during loading, the previous load level is taken as the anti-crack load. When the crack occurs at the first time within the required duration of load level, the average value of the current load level and previous load level is taken as the anti-crack load. When the crack occurs at the first time after the required duration of load, the current load level is taken as the anti-crack load.

The ultimate load is determined by following ways. When the ultimate state is reached during loading, the previous load level is taken as the ultimate load. When the ultimate state is reached within the required duration of load level, the average value of the current load level and previous load level is taken as the ultimate load. When the ultimate state is reached after the required duration of load, the current load is taken as the ultimate load.

Before the test, the state of PCSPs is checked. All PCSPs are complete without crack. During the test, each PCSP is loaded to the ultimate state. The test results are as follows.

4. Test Results and Analysis

4.1. Distribution Law of Crack. During the test, each PCSP shows cracks. 5-1 and 5A are taken as examples to illustrate the distribution law of cracks in CPCSP and UPCSP, which are shown in Figures 6 and 7.

Figure 6 shows the crack distribution sketch of 5A and 5-1 under the last load level. Most cracks of piles are similar to the inversive splay, which is consistent with the stress state of

Table 1: Main parameters of precast concrete square pile.

Number of pile	Side length (mm)	Pile length (mm)	Pile shaft reinforcement	End plate	Concrete strength grade of pile shaft
5A 5-1 5-2 5-3	500	7	The main reinforcement is 12Φ12.6. The stirrup is Φ6.5. The distance between stirrups within 1.0 m at both ends of pile is 50 mm, and the rest of space is 75 mm.	480 × 480 × 20 mm (Q235 ordinary hot-rolled steel plate)	C40
6A 6-1 6-2 6-3	600	7	The main reinforcement is 20Φ12.6. The stirrup is Φ6.5. The distance between stirrups within 1.0 m at both ends of pile is 50 mm, and the rest of space is 75 mm.	580 × 580 × 20 mm (Q235 ordinary hot-rolled steel plate)	C40

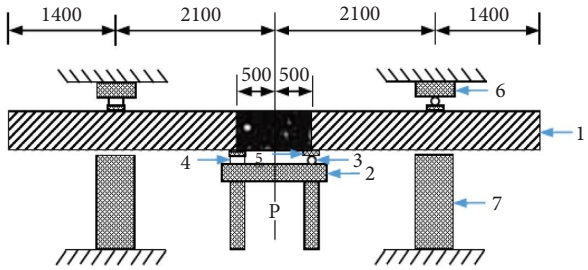

Figure 3: Schematic diagram of load equipment, where 1 is the CPCSP; 2 is the distribution beam; 3 is the rolling hinge support; 4 is the fixed hinge support; 5 is the bottom plate; 6 is the reaction pier after loading; and 7 is the protection pier before loading.

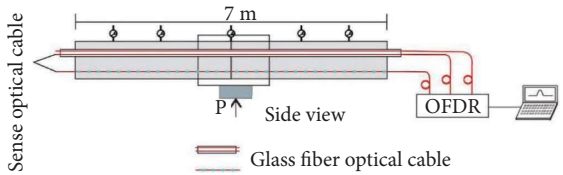

Figure 4: Layout of optical cable on the surface of CPCSP.

Table 2: Main performance of measurement instrument.

Name	Type	Range	Degree of accuracy
Digital dial indicator	MFX-50	50 mm	0.01 mm
Carbon fiber composite strain sense optical cable	NZS-DSS-C09(CF)	$\pm 15000\,\mu_\varepsilon$	$1\,\mu_\varepsilon$
Glass fiber composite strain sense optical cable	NZS-DSS-C09(GF)	$\pm 15000\,\mu_\varepsilon$	$1\,\mu_\varepsilon$
Fixed-point polyurethane strain sense optical cable	NZS-DSS-C08	$\pm 15000\,\mu_\varepsilon$	$1\,\mu_\varepsilon$

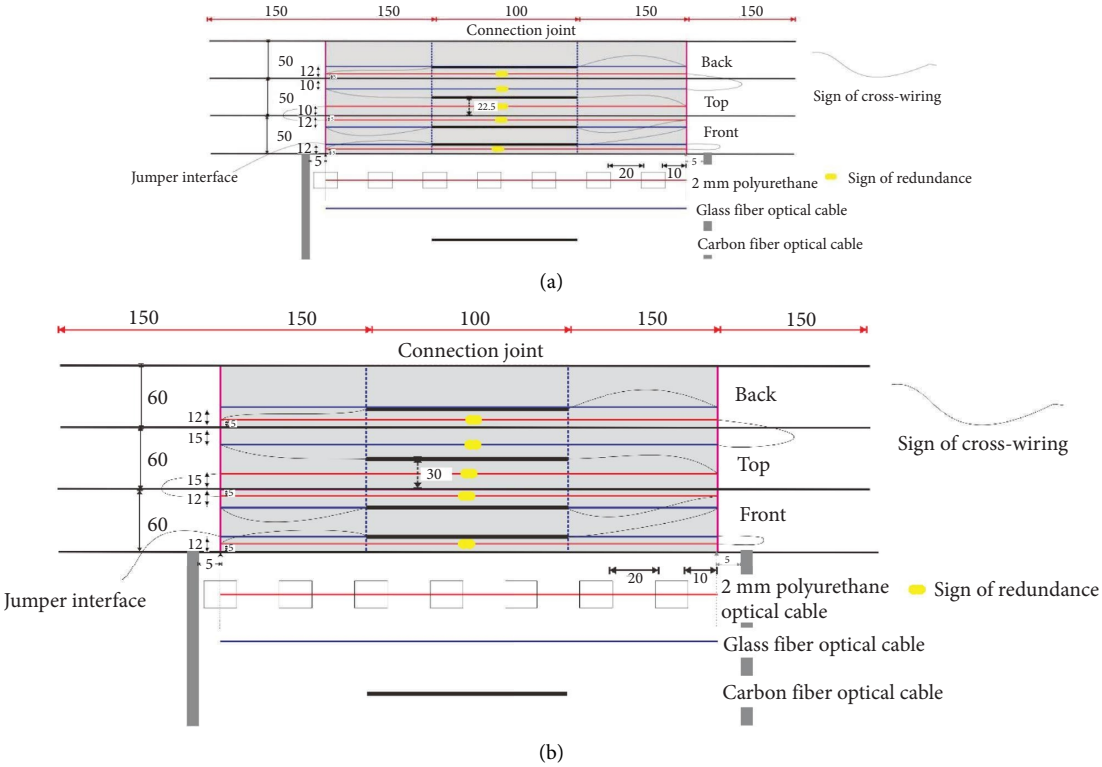

Figure 5: Actual layout of optical cable on the surface of CPCSP. (a) 500 mm. (b) 600 mm.

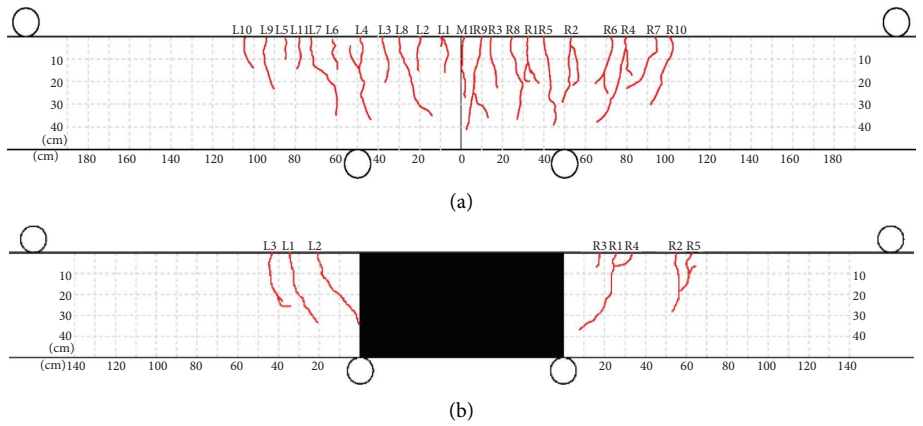

Figure 6: Actual distribution sketch of cracks in CPCSP and UPCSP. (a) 5A. (b) 5-1.

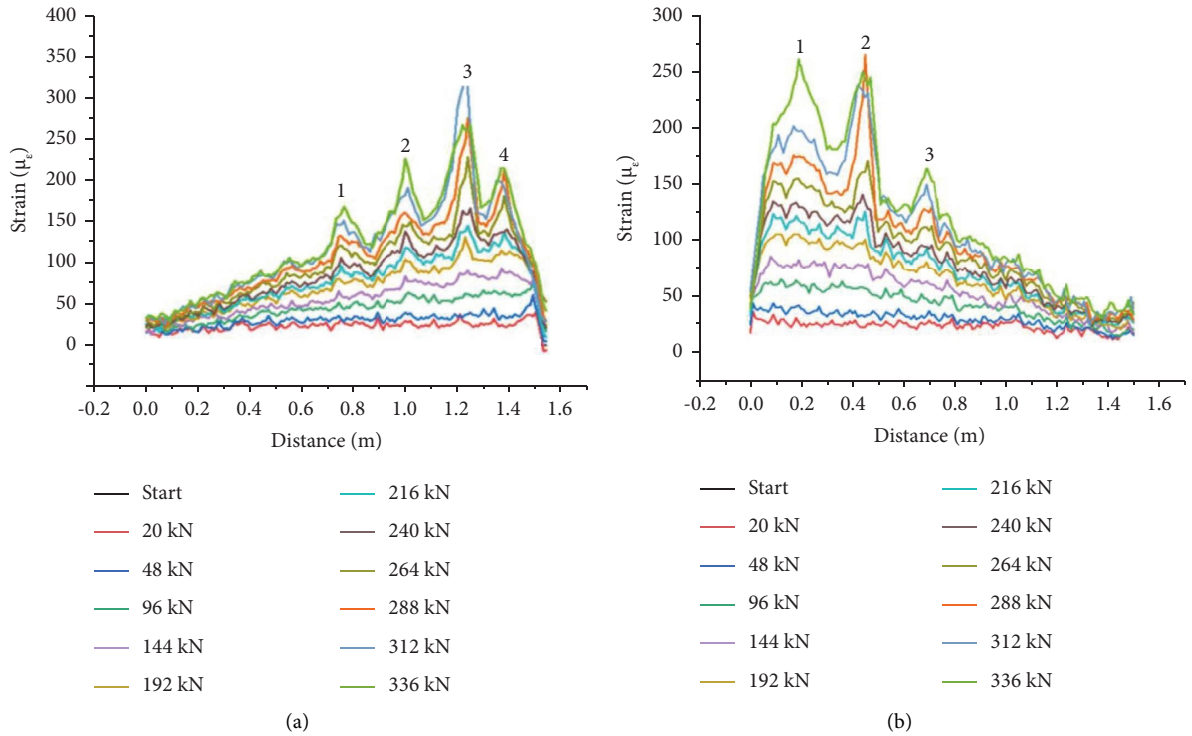

Figure 7: Test diagram of crack distribution law on left and right sides of 5-1. (a) Left side. (b) Right side.

piles with upper side under tension and lower side under compression. The crack density at the left side of 5A is 1.0/10 cm, and the crack density at the right side of 5A is 1.1/10 cm. The crack density at the left side of 5-1 is 0.7/10 cm, and the crack density at the right side of 5-1 is 0.8/10 cm. In comparison, the crack density of CPCSPs is significantly lower than that of UPCSPs, which is the main reason that the flexural deformation ability of UPCSPs is weakened.

Figure 7 shows the test crack distribution law of 5-1. There are 4 obvious strain peaks on the left side of 5-1 and 3 obvious strain peaks on the right side of 5-1. The experimental results show that the number and location of cracks are basically consistent with those of actual cracks. During the test, cracks first appeared at the middle of UPCSPs, while the middle of CPCSPs is the connection joint, which is co-affected by hoop steel plate and adhesive steel glue. The ductility and crack of CPCSPs are enhanced and reduced, respectively, by the coordination deformation of steel plate and concrete. The experimental results of other groups are similar to those of this test and will not be repeated.

4.2. Distribution Law of Stress and Strain. Since the stress state of each CPCSP is relatively consistent during the loading, 5-1 is also taken as an example to explore the stress and strain distribution law of CPCSPs. The experimental results are shown in Figures 8–10.

Figure 8 shows the strain diagram of glass fiber optical cable on the top, back, and front of 5-1. Before the load of 360 kN, the change of strain is small (within 200 μ_ε). The

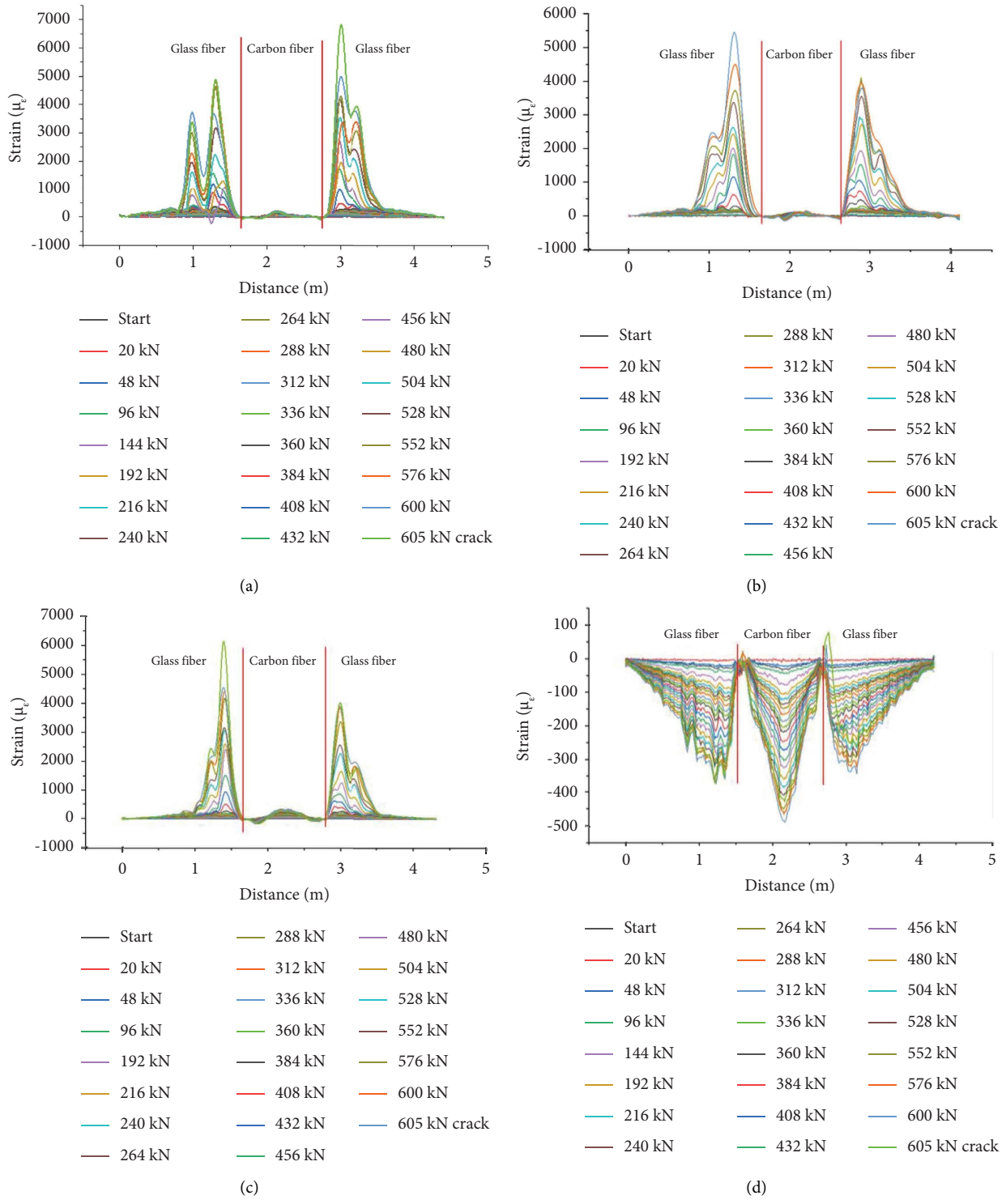

Figure 8: Strain diagram of glass fiber optical cable on the top, back, and front of 5-1. (a) Top. (b) Back. (c) Upper of front. (d) Lower of front.

stress is also small, and the crack is in the initial development stage. With the increase of load, the crack also starts to develop significantly after the load of 360 kN. The strain and stress increase significantly, and the stress concentration appears. In terms of whole 5-1, the stress at both ends is zero, and the stress increases gradually from both ends to connection joint. The stress on the top, upper of front, and back is positive, which is in tensile state. The stress on the lower of front is negative, which is in compressive state.

Figure 9 shows the strain diagram of polyurethane optical cable on the top, back, and front of 5-1. The test results are relatively consistent with the strain diagram of

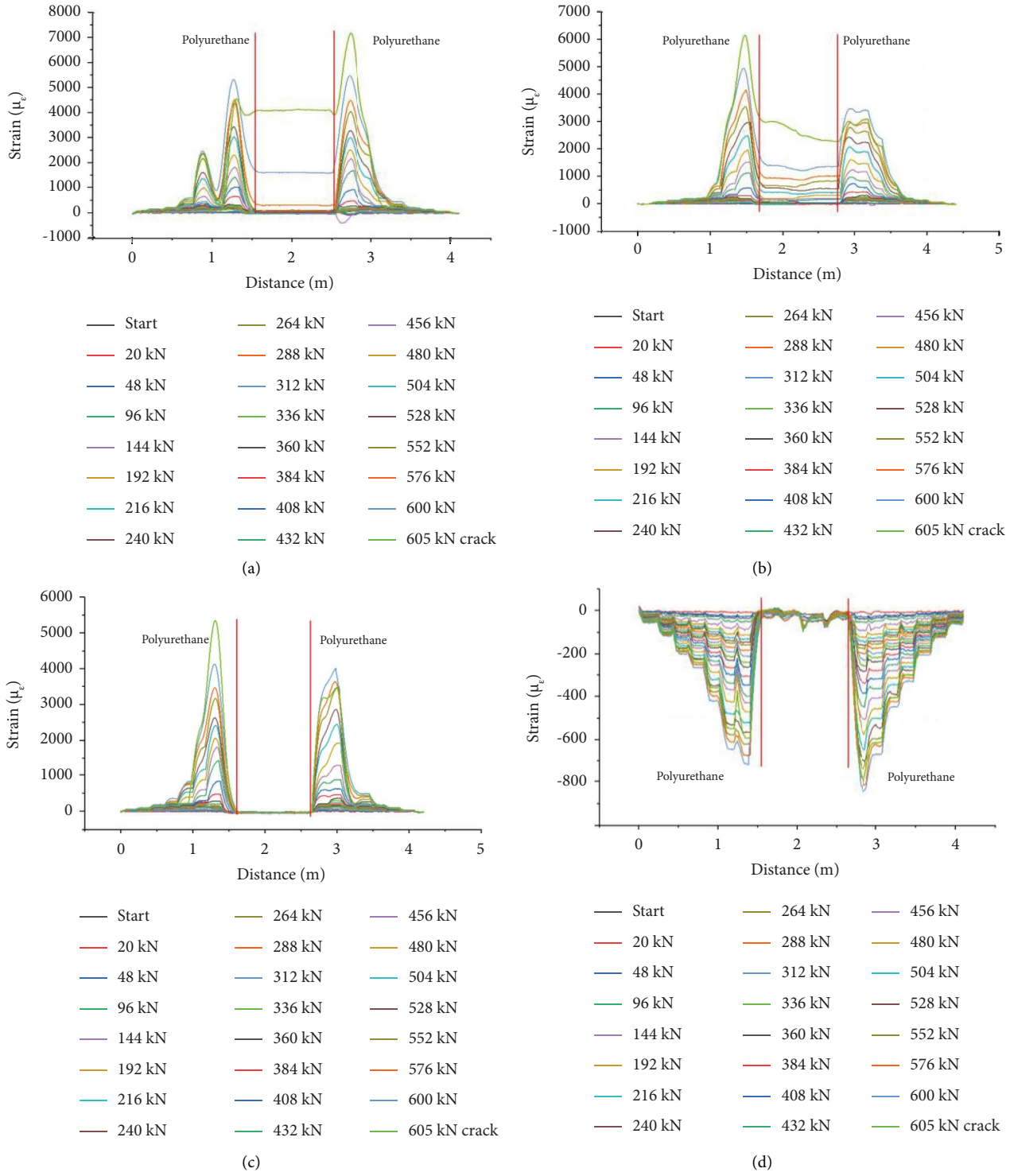

Figure 9: Strain diagram of polyurethane optical cable on the top, back, and front of 5-1. (a) Top. (b) Back. (c) Upper of front. (d) Lower of front.

glass fiber. Before the load of 360 kN, the change of strain is small. The stress is small, and the crack is in the initial development stage. With the increase of load, the crack starts to develop significantly after the load of 360 kN. The strain and stress also increase significantly. In terms of whole 5-1, the strain at both ends is zero, and the strain increases gradually from both ends to connection joint. The strain on the top, upper of front, and back is positive, which is in tensile state. The strain on the lower of front is negative, which is in compressive state.

Figure 10 shows the strain diagram of carbon fiber optical cable on the top (Figure 10 is the strain diagram of

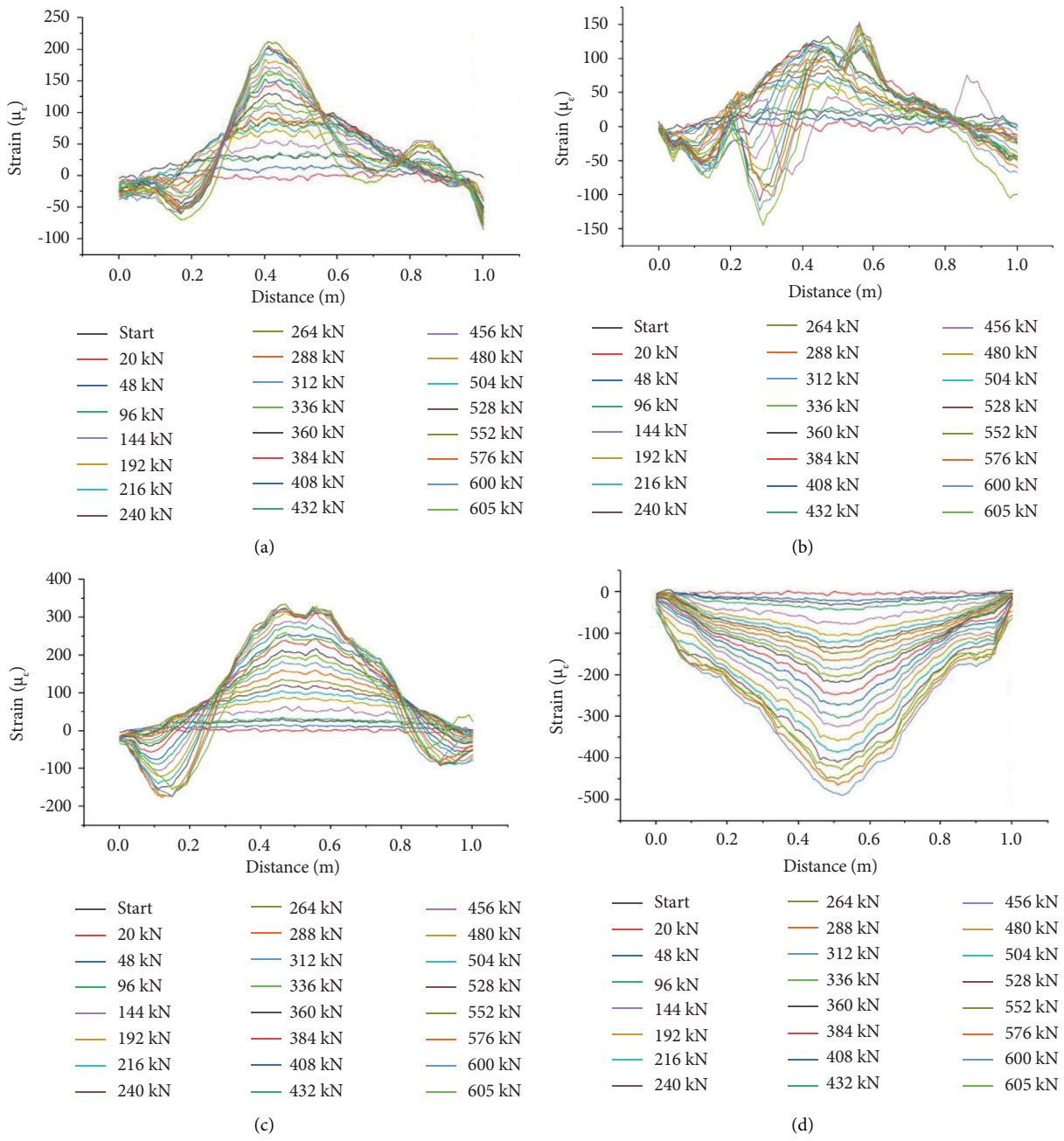

Figure 10: Strain diagram of carbon fiber optical cable on the top, back, and front of 5-1 (a) Top. (b) Back. (c) Upper of front. (d) Lower of front.

carbon fiber optical cable in the middle of Figure 8), back, and front of 5-1. The strain at the middle of connection joint is relatively large and concentrated, and the strain at both sides of connection joint is relatively small. In addition, the strain on the top, back, and front (except the lower of front) of the middle of connection joint is positive, which is in tension state. The strain at both sides of connection joint is negative, which is in compression state.

In summary, the pile has a tensile effect on the top, back, and front of hoop steel plate before the load of 144 kN, and the hoop steel plate is in tensile state. After the load of 144 kN and with the increase of load, the pile has a compressive effect on the back and upper of front of hoop steel plate, and the hoop steel plate is in compressive state. The pile has a downward tensile effect on the both sides for the top of hoop steel plate, and the hoop steel plate is in tensile state.

4.3. Comparison of Flexural Behavior between UPCSP and CPCSP. The anti-crack load, ultimate load, bending moment, and flexural deformation measured by tests are shown in Table 3. According to the test results of three CPCSPs with the side length of 500 mm (Nos. 5-1~5-3), the

Table 3: Anti-crack load, ultimate load, bending moment, and flexural deformation.

Number of pile	State of pile before test	Anti-crack load (kN)	Anti-crack bending moment (kN·m)	Maximum anti-crack flexural deformation (mm)	Ultimate load (kN)	Ultimate bending moment (kN·m)	Maximum ultimate flexural deformation (mm)	Design value of bending moment (kN·m)
5A	Complete without crack	332	257.9	16.36	577	454.7	40.95	260
6A		455	353.0	5.78	845	—	10.00	490
5-1		348	270.7	12.41	576	453.1	40.42	
5-2		396	309.1	12.08	576	453.1	30.90	260
5-3		444	347.5	21.56	600	472.3	49.46	
6-1		552	430.6	13.67	1072	846.6	40.42	
6-2		528	411.4	34.10	1056	833.8	39.17	490
6-3		552	430.6	11.99	975	769.0	47.94	

range of anti-crack load is 348~444 kN, and the average value is 396 kN. The range of anti-crack bending moment and maximum anti-crack flexural deformation is 270.7~347.5 kN·m and 12.08~21.56 mm, respectively, and the average value is 309.1 kN·m and 15.35 mm, respectively. The range of ultimate load is 576~600 kN, and the average value is 584 kN. The range of ultimate bending moment and maximum ultimate flexural deformation is 453.1~472.3 kN·m and 30.90~49.46 mm, respectively, and the average value is 459.5 kN·m and 40.26 mm, respectively. According to the test results of one UPCSP with the side length of 500 mm (No. 5A), the anti-crack load is 332 kN, and the anti-crack bending moment and maximum anti-crack flexural deformation are 257.9 kN·m and 16.36 mm, respectively. The ultimate load is 577 kN, and the ultimate bending moment and maximum ultimate flexural deformation are 454.7 kN·m and 40.95 mm, respectively. It can be seen that the anti-crack load and anti-crack bending moment of CPCSPs are greater than those of UPCSPs, and their value is increased by 19.28% and 19.85%, respectively. The ultimate load, ultimate bending moment, and maximum anti-crack or ultimate flexural deformation of CPCSPs and UPCSPs are basically equivalent. The strength and deformation characteristics of test are consistent with the results of mechanical theory analysis (the maximum tensile stress occurs in the middle of piles and at the top of cross section; because of the coordinated deformation of hoop steel plate and the pile concrete, the anti-bending strength and anti-crack ability of CPCSPs are enhanced, and its flexural deformation is weakened before the occurrence of crack). Therefore, the anti-crack strength of CPCSPs is greatly increased while the flexural deformation of CPCSPs is decreased. With the development of cracks, the outside areas of hoop steel plate show cracks. At this moment, the strength of CPCSPs is no longer controlled by the strength of middle areas, so it is shown that the ultimate strength of CPCSPs is basically equivalent to that of UPCSPs.

According to the test results of three CPCSPs with the side length of 600 mm (Nos. 6-1~6-3), the range of anti-crack load is 528~552 kN, and the average value is 544 kN. The range of anti-crack bending moment and maximum anti-crack flexural deformation is 411.4~430.6 kN·m and 11.99~13.67 mm (the maximum anti-crack flexural deformation of 6-2 is not accepted), respectively, and the average value is 424.2 kN·m and 12.83 mm, respectively. The range of ultimate load is 975~1072 kN, and the average value is 1034 kN. The range of ultimate bending moment and maximum ultimate flexural deformation is 769.0~846.6 kN·m and 40.42~47.94 mm, respectively, and the average value is 816.5 kN·m and 44.18 mm, respectively. According to the test results of one UPCSP with the side length of 600 mm (No. 6A), the anti-crack load is 455 kN, and the anti-crack bending moment is 353.0 kN·m. 6A shows crack under the load level of 520 kN. The test equipment produces deformation when the load reaches 845 kN, and the test is terminated. It is seen that the anti-crack load and ultimate load of CPCSPs are greater than those of UPCSPs, which again shows that the anti-bending strength of CPCSPs has been improved.

Table 4: Detailed data of flexural deformation (unit: mm).

Number of piles	No. 1	No. 2	No. 3	No. 4	No. 5
5A	23.88	34.52	40.95	36.99	24.52
6A	10	5.27	7.63	4.93	9.06
5-1	22.63	32.4	40.42	40.38	30.11
5-2	16.53	25.59	30.9	25.28	16.54
5-3	36.19	46.7	49.46	43.41	30.88
6-1	23.24	33.23	40.42	35.51	23.66
6-2	44.22	51.42	39.17	42.86	34.33
6-3	24.04	38.84	47.94	37.25	24.29

The flexural deformations of CPCSPs and UPCSPs are shown in Table 4. With the increase of load, the flexural deformation increases gradually. Except for 6-2 and 6A, which are affected by the deformation of simply supported beams, the flexural deformation at the center of other piles is greater than that of other positions. The maximum flexural deformation of 5-1~5-3 is between 30.90 and 49.46 mm, and the average value is 40.26 mm. The maximum flexural deformation of 5A is 40.95 mm. The maximum flexural deformation of 6-1 and 6-3 is 40.42 and 47.94 mm, respectively, and the average value is 44.19 mm. In summary, the anti-bending strength of CPCSPs is greater than that of UPCSPs.

5. Conclusions

The following conclusions are mainly obtained by experimental study on the flexural behavior of CPCSPs and UPCSPs:

(1) Most cracks of piles are similar to the inversive splay, which is consistent with the stress state of piles with upper side under tension and lower side under compression. The crack density of CPCSPs is significantly lower than that of UPCSPs

(2) The anti-crack bending moment of CPCSPs is about 19.85%~20.17% higher than that of UPCSPs before the occurrence of crack. The anti-crack strength of CPCSPs is greatly increased while the flexural deformation of CPCSPs is decreased. With the development of crack (failure stage), the outside areas of hoop steel plate exhibit cracks. At this moment, the strength of CPCSPs is no longer controlled by the strength of middle areas, so it is shown that the ultimate strength of CPCSPs is basically equivalent to that of UPCSPs.

(3) The ultimate bending moment of CPCSPs is not lower than that of UPCSPs and is about 66%~76% higher than its bending moment design value. Therefore, the selection of CPCSPs in the design of foundation pit support has good reliability.

Data Availability

The data used to support the findings of this study are included within the article.

Conflicts of Interest

The authors declare that they have no conflicts of interest.

Acknowledgments

This research was supported by the National Natural Science Foundation of China (grant nos. 51979225 and 51679199), the Key Research and Development Project of Shaanxi Province (2018SF-388), and the Special Research Projects of Shaanxi Provincial Department of Education (21JK0793).

References

[1] X. L. Huang, M. D. Liu, J. Y. Li, X. D. Zhou, and J. M. ten Cate, "Chemical composition of Galla chinensis extract and the effect of its main component(s) on the prevention of enamel demineralization in vitro," *International Journal of Oral Science*, vol. 4, no. 3, pp. 146–151, 2012.

[2] J. Xu, S. F. Yang, and H. Y. Wu, "Monito-ring and numerical analysis of pile-anchor supporting structure for deep and large foundation," *Journal of Xi'an University of Architecture and Technology*, vol. 51, no. 4, pp. 517–524, 2019.

[3] P. Lin, P. Liu, G. Ankit, and Y. J. Singh, "Deformation monitoring analysis and numerical simulation in a deep foundation pit," *Soil Mechanics and Foundation Engineering*, vol. 58, no. 1, pp. 56–62, 2021.

[4] T. Li, Y. W. Yang, and Y. Q. Zhou, "Analytical solution of horizontal displacement of retaining structures in deep foundation pit during dismantling inner support," *Chinese Journal of Rock Mechanics and Engineering*, vol. 41, no. 1, pp. 3021–3032, 2022.

[5] L. Z. Wang, B. He, Y. Hong, Z. Guo, and L. Li, "Field tests of the lateral monotonic and cyclic performance of jet-grouting-reinforced cast-in-place piles," *Journal of Geotechnical and Geoenvironmental Engineering*, vol. 141, no. 5, Article ID 06015001, 2015.

[6] L. Cai, S. D. Liang, and M. Gu, "Application of high reinforced prestressed concrete compounded pipe piles in deep foundation pit," *Geotechnical Investigation & Surveying*, vol. 46, no. 12, pp. 25–29, 2018.

[7] Z. P. Wang, "Discussion on connection of precast concrete square pile with high anti-pulling capacity," *Building Structure*, vol. 49, no. 2, pp. 846–849, 2019.

[8] D. J. Seo, D. M. Kang, H. G. Lee, and D. Y. Moon, "An experimental study on lateral load resistance of a wall structure composed of precast concrete and H-pile," *Journal of The Korea Institute for Structural Maintenance and Inspection*, vol. 24, no. 3, pp. 9–17, 2020.

[9] S. F. Zhao, G. L. Huang, and S. Q. Ma, "Application of precast concrete pipe piles in a deep excavation project," *Chinese Journal of Geotechnical Engineering*, vol. 36, no. 1, pp. 91–96, 2014.

[10] X. Y. Zhang, X. C. Chen, Y. Wang, D. Mingbo, and L. Jinhua, "Quasi-static test of the precast-concrete pile foundation for railway bridge construction," *Advances in Concrete Condtruction*, vol. 10, no. 1, pp. 49–59, 2020.

[11] W. X. Li, Y. R. Wan, and Q. B. Liu, "Design and experimental study on a new connection between PHC up lift pile segments of the Expo Theme Pavilion," *Journal of Building Structures*, vol. 31, no. 5, pp. 86–94, 2010.

[12] Z. M. Zhang, J. Yu, and G. X. Zhang, "Contrastive experimental analysis of bearing behaviors of PHC pile and precast square piles," *Rock and Soil Mechanics*, vol. 29, no. 11, pp. 3059–3065, 2008.

[13] Y. Guo, W. Cui, and F. B. Chen, "Analysis and experimental study of a PHC uplift pile with hold-hoop connection," *Chinese Journal of Geotechnical Engineering*, vol. 35, no. 2, pp. 1007–1010, 2013.

[14] J. L. Qi, P. H. Zhou, X. L. Yang, and Z. D. Zhou, "Application of mechanical-connection bamboo joint piles in the coastal soft soil foundation," *Building Structure*, vol. 44, no. 1, pp. 73–76, 2014.

[15] F. R. Liu, L. Jia, and C. Li, "The test study on welding joint flexural bearing capacity of prestressed concrete hollow square pile," *Journal of Wuhan University of Technology*, vol. 30, no. 5, pp. 105–108, 2008.

[16] Q. J. Fan, G. L. Huang, and H. L. Miao, "Computational analysis and experimental study on a new connection between segments of square uplift piles," *Chinese Journal of Geotechnical Engineering*, vol. 35, no. 2, pp. 1011–1015, 2013.

[17] X. W. Zhang, "Comprehensive detection ways and judgement of deflects of precast square concrete piles," *Building structure*, vol. 34, no. 4, pp. 48–50, 2004.

[18] M. C. M. Marcos, Y. J. Chen, and F. H. Kulhawy, "Evaluation of compression load test interpretation criteria for driven precast concrete pile capacity," *KSCE Journal of Civil Engineering*, vol. 17, no. 5, pp. 1008–1022, 2013.

[19] Y. F. Wang, G. Chen, and Q. B. Xu, "Study on tensile behavior of prestressed concrete square pile connection joint with

resilient clamping," *Journal of Disaster Prevention and Mitigation Engineering*, vol. 38, no. 6, pp. 1003–1011, 2018.

[20] J. W. Zhou, Y. F. Wang, and S. F. Gong, "Study on flexural behavior of prestressed concrete square pile connection joint with resilient clamping," *Building structure*, vol. 27, no. 13, pp. 121–127+133, 2020.

[21] Y. S. Xu, Z. F. Chen, J. Fan, Z. Li, K. Zhang, and X. Tu, "Study on the flexural performance of prestressed concrete solid square piles and resilient clamping connections," *KSCE Journal of Civil Engineering*, vol. 27, no. 1, pp. 285–298, 2022.

[22] Q. B. Xu, G. Chen, and J. F. He, "Flexural performance experiment of concrete of connection joint for composite reinforcement concrete prefabricated square piles," *Journal of Zhejiang University (Science Edition)*, vol. 51, no. 7, pp. 1300–1308, 2017.

[23] I. Ptuhina, R. Alzhanova, A. Akhatuly, and V. Maier, "Comparative analysis of pile joints," *Advanced Materials Research*, vol. 1082, pp. 270–276, 2014.

[24] D. Q. Song, X. L. Liu, J. Huang, Y. Zhang, J. Zhang, and B. N. Nkwenti, "Seismic cumulative failure effects on a reservoir bank slope with a complex geological structure considering plastic deformation characteristics using shaking table tests," *Engineering Geology*, vol. 286, Article ID 106085, 2021.

[25] D. Q. Song, X. L. Liu, J. Huang, and J. Zhang, "Energy-based analysis of seismic failure mechanism of a rock slope with discontinuities using Hilbert-Huang transform and marginal spectrum in the time-frequency domain," *Landslides*, vol. 18, no. 1, pp. 105–123, 2020.

[26] D. Q. Song, X. L. Liu, B. Li, J. Zhang, and J. J. V. Bastos, "Assessing the influence of a rapid water drawdown on the seismic response characteristics of a reservoir rock slope using time-frequency analysis," *Acta Geotechnica*, vol. 16, no. 4, pp. 1281–1302, 2021.

[27] D. Q. Song, Z. Chen, L. H. Dong, G. Tang, K. Zhang, and H. Wang, "Monitoring analysis of influence of extra-large complex deep foundation pit on adjacent environment: a case study of Zhengzhou City, China," *Geomatics, Natural Hazards and Risk*, vol. 11, no. 1, pp. 2036–2057, 2020.

[28] Y. Xue, J. Liu, P. G. Ranjith, F. Gao, H. Xie, and J. Wang, "Changes in microstructure and mechanical properties of low-permeability coal induced by pulsating nitrogen fatigue fracturing tests," *Rock Mechanics and Rock Engineering*, vol. 55, no. 12, pp. 7469–7488, 2022.

[29] Y. Xue, P. G. Ranjith, F. Gao, Z. Zhang, and S. Wang, "Experimental investigations on effects of gas pressure on mechanical behaviors and failure characteristic of coals," *Journal of Rock Mechanics and Geotechnical Engineering*, vol. 15, no. 2, pp. 412–428, 2023.

[30] Y. Xue, S. Liu, J. Chai et al., "Effect of water-cooling shock on fracture initiation and morphology of high-temperature granite: application of hydraulic fracturing to enhanced geothermal systems," *Applied Energy*, vol. 337, Article ID 120858, 2023.

Hindawi
Advances in Civil Engineering
Volume 2023, Article ID 7305238, 12 pages
https://doi.org/10.1155/2023/7305238

Research Article

The Effect of Different Fibers on Granite Residual Soil Reinforced with Alkaline Solution

Bingxiang Yuan,[1] **Jianhong Liang**,[1] **Jingkang Liang**,[1] **Weijie Chen**,[1] **Baifa Zhang**,[1] **Wei Chen**,[2] **and Tianying Chen**[1]

[1]*School of Civil and Transportation Engineering, Guangdong University of Technology, Guangzhou 510006, China*
[2]*School of Civil Engineering, Southeast University, Nanjing, China*

Correspondence should be addressed to Baifa Zhang; zhangbaifa@gdut.edu.cn

Received 7 September 2022; Revised 8 February 2023; Accepted 22 March 2023; Published 6 April 2023

Academic Editor: Danqing Song

This study explores the reinforcement effect of different fibers in an alkaline solution on the mechanical properties of granite residual soil using the single variable method. The macroscopic mechanical properties of the reinforced samples were studied using the unconfined lateral compressive strength test and the drop-weight load test, while the microscopic properties were characterized using techniques such as SME and XRD. The results indicated that the greatest reinforcing effect was attained when the ratio of SiO_2/Na_2O in the alkaline solution was 0.5 mol with the compressive strength of 4402.85 kPa. At the time, the reinforcing effect of glass fiber in an alkaline solution on granite residual soil was superior to that of basalt fiber. The inclusion of glass fibers and an alkaline solution of 0.5 mol SiO_2/Na_2O into the granite residual soil exhibited the best capacity for reinforcing, with the maximum impact load and compression reaching 120 kN and 12.1 mm, respectively. The findings of SME analysis revealed that GRS included a significant amount of kaolinite, which, when decomposed in an alkaline solution, generated a gel substance that bound the fibers and soil together and filled the pores between them, thereby enhancing the sample's compactness. XRD results demonstrated the formation of gel and a small amount of geopolymer in the soil under the alkaline solution of 0.5 mol SiO_2/Na_2O, which tighten the binding between soil particles and fibers and increase the overall strength.

1. Introduction

As China's economy is booming, the number of people living in urban areas increases, necessitating a rise in public transportation usage. Large public construction projects produce substantial amounts of construction waste. Up to two million tons of waste soil were generated in 2019 [1]. However, construction waste soil disposal has become a cause for concern. In general, only a small proportion of excavated waste soil can be utilized for low-level highways or infrastructure pit backfill; the bulk must be transferred to a landfill. This will inevitably result in a series of consequences. The release of soil particles during transportation endangers the local community's health by contaminating the road and the surrounding air environment. In addition, a large number of waste soil landfills consume a great deal of space, resulting in a tremendous waste of land resources. Therefore, the sustainable utilization of construction waste soil is a contemporary and environmentally-friendly topic [2]. Investigating a suitable approach to utilize the soil has major practical engineering significance because it can both alleviate the issue of random waste soil disposal and minimize energy usage [3].

The recycling of waste soils is generally popular among academics [4–6]. Several of these studies were instructive and prospective. The compressive strength of the reinforced kaolin clay samples significantly increased when industrial wastes such as steel slag and slag were employed as raw materials to strengthen the residual soil, together with activated magnesium oxide and calcium oxide [7]. Using scientific processes, cement blocks and waste granite cutting slag were regenerated with comparable strength to cement

blocks [8]. Construction waste has been converted into geogrids with certain tensile strength using a special technique [9]. The addition of kaolinite-containing waste soil to concrete increased its strength while decreasing the amount of cement required [10]. All of them indicate that the sustainable utilization of construction waste soil has attracted considerable attention.

Due to the unique geographical location and climate of South China, the majority of the construction waste soils in this region, including Guangdong and Fujian, are granite residual soils (GRS), which feature a very high bearing capacity under dry conditions but tend to soften and the bearing capacity decreases abruptly when exposed to water [11–13]. The region of South China is characterized by a hot and humid climate; hence, GRS is frequently regarded as a waste soil since its bearing capacity falls below the requirement upon contact with water due to its high porosity and hydrophilic kaolinite content [14]. Because of this, GRS is prone to soften in water, resulting in a loss of bearing capacity [15], making it difficult to preserve its original form [16–18]. In order to reuse GRS in a sustainable way, researches on mitigating the water disintegration property of GRS have been undertaken, including the use of polymer SH, which attaches a layer of hydrophobic groups to the surface of kaolinite to maintain its strength when exposed to water [19–25]. Some domestic studies have shown that transparent soil will also have similar characteristics to GRS under the action of alkali solution and cement [26–30]. At the same time, there is similar research abroad [31–34]. Others have used alkaline solutions to consume kaolinite in GRS in order to essentially remove its hydrophilicity and ensure its strength [35, 36]. Alternatively, numerous studies have resolved the issue by reinforcing GRS with fly ash or cement [37] to increase its compressive strength. Although methods such as adding cement or fly ash to GRS can boost its strength, they are rarely environmentally friendly enough, and the process generates significant carbon emissions [38, 39]. Therefore, it is essential to consider more sustainable reinforcing solutions.

Environmentally friendly and nonpolluting, alkaline solution is an inorganic solution that, at the right ratio, can be used to consume kaolinite in GRS and generate a geopolymer or gel substances. Since kaolinite has been consumed, this substance not only improves the soil to some degree but also solves the problem of GRS disintegrating rapidly in water [14, 40, 41]. Alkaline treatment of GRS has a number of advantages, but the treated GRS is exceptionally brittle, which could lead to a brittle effect comparable to that of cement reinforcement [42–44]. For this reason, the use of this material for large-scale applications is discouraged. [45–49]. Fiber has been studied as a potential solution for the brittleness of treated GRS. The addition of fibers from waste tire, sisal, cactus pulp, bamboo, and polypropylene has been demonstrated to decrease brittleness and increase the stress between soil particles and bearing capacity [50–55].

From the aforementioned literature, it is clear that although these researchers have made contributions to the field of reinforcing soils with fibers or other agents, there is a dearth of studies on reinforcing granite residual soils with fibers in alkaline solutions. In addition, the aforementioned researchers have only investigated the static load compressive strength of the treated granite residual soil, but little research has been conducted on the dynamic impact load performance of the reinforced soil and much less on its micromechanical characterization. Therefore, in this study, a comparison is made between glass fiber and basalt fiber in terms of GRS reinforcement in alkaline solution and the impact resistance of reinforced GRS under both static load and dynamic load, and the reinforcement mechanism of different fibers is examined from a microscopic perspective using SEM and XRD techniques as well.

2. Test Method

2.1. Materials

2.1.1. Granite Residual Soil. Granite residual soil has a distinctive structure and considerable strength in its dry state, but its strength drops rapidly after soaking in water or shaking (even if exposed to air for an extended period of time), causing engineering or geological disasters frequently. Consequently, it is considered "regional soil" or "unique soil." This experiment utilizes the granite residual soil excavated from the foundation pit of a Guangzhou subway station (Figure 1(a)). The soil is largely clayey and partially gravel clayey. It is primarily dark yellow in color. Its main soil mechanical properties are given in Table 1.

2.1.2. Sodium Hydroxide Analytical Reagent. Sodium hydroxide analytical reagent is a white (Figure 1(b)), uniform, granular solid that is water-soluble, has a density of 1.09 g/cm^3 and a molecular weight of 40, and forms a translucent aqueous solution upon dissolution in water.

2.1.3. Sodium Hydroxide Analytical Reagent. Sodium silicate analytical reagent is a white (Figure 1(c)), uniform, granular solid that is water-soluble, has a molecular weight of 284.22, contains around 64% of silicon dioxide and 22.5% of sodium oxide, and forms a translucent aqueous solution upon dissolution in water.

2.1.4. Basalt Fiber. Basalt fiber is an inorganic nonmetallic fiber material that is primarily manufactured from basalt ore that has been melted at a high temperature and then cast into a particular mold. It possesses outstanding characteristics such as high resilience strength, high modulus, resistance to high and low temperatures, and corrosion resistance. Its average length is 6 mm, and its diameter is 20 microns. The specific parameters of basalt fiber are shown in Table 2.

2.1.5. Glass Fiber. The glass fiber employed as the reinforcer in this experiment is an inorganic nonmetallic material with excellent performance, having an average length of 6 mm and a diameter of 10 microns, as shown in Figure 2. Nonpolluting and eco-friendly, it possesses excellent insulation, high heat resistance, superior corrosion resistance,

(a) (b) (c)

Figure 1: Material diagram: (a) granite residual soil, (b) sodium hydroxide, and (c) sodium metasilicate.

Table 1: Properties of granite residual soil samples.

Specific gravity (ds)	Water content ω (%)	Density (g/cm^3)	Liquid limit ω_1	Plastic limit (ωp)
2.67	13	16.5	48.3	27

Table 2: Fiber parameters.

Fiber type	Density (g/cm^3)	Linear density (dtex)	Elastic modulus (Mpa)	Tensile strength (Mpa)	Melting point (°C)	Elongation (%)
Basalt fiber	2.65	6.21	4500	330	958	30.0
Glass fiber	0.91	8.21	4286	346	169	36.4

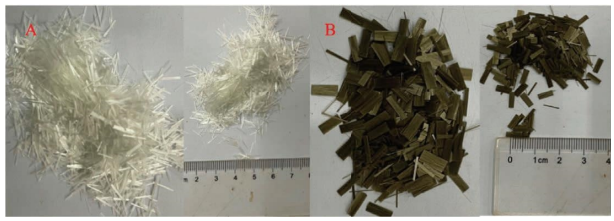

Figure 2: Material diagram: (a) glass fiber and (b) basalt fiber.

and high mechanical strength. The specific parameters of basalt fiber are given in Table 2.

2.2. Sample Preparation and Curing. In accordance with the Chinese Standard GB/T 50123-2019 (a standard for the geotechnical testing method), the samples were baked for 7 h at approximately 105°C and then crushed and sieved at 1.18 mm after cooling to room temperature. The 13% optimal water content used in this experiment was obtained in Yuan Bingxiang's previous research.

Different fibers and alkali solutions were added to the soil in varying amounts. The mixture was then well mixed, compacted into a cylinder with a diameter of 100 mm and a height of 50 mm using a geo-compaction equipment (Figure 3) in layers, and air-dried for 14 days in a well-ventilated indoor environment. The total weight of a sample is 1600 g.

2.3. Sample Numbering for the Unconfined Compressive Strength Test and the Drop-Weight Test. The optimal reinforcement ratio of the alkaline solution was determined by means of the unconfined compressive strength test as depicted in Table 3. For reinforcement, several molar ratios were used to prepare the alkaline solution. "0.5 mol" denotes an alkaline solution with a SiO_2/Na_2O ratio of 0.5 mol.

Table 4 illustrates the results of the drop-weight impact load test. The ideal content and length of glass fiber for reinforcement are 3% and 6 mm, whereas those of basalt fiber are 4% and 6 mm (chen et al). The optimal ratio of the alkaline solution determined by the static load test was 0.5 mol; hence, 0.5 mol alkaline solution was selected as the principal item for examination in the drop-weight test, alongside 0.7 mol and 0.4 mol alkaline solutions for comparison. In order to investigate the reinforcement effect of different fibers on granite residual soil in alkaline solution, glass fiber and basalt fiber were, respectively, incorporated into the soil based on the given ratios of alkaline solution. There are three examples for each condition. To label the samples, the drop-weight test was designated as "LC," the 0.7 mol alkaline solution ratio "0.7," and the addition of glass fiber and basalt fibers, "G" and "B", respectively. "GRS" refers to the pure soil sample. For instance, "LC-0.5-G" represents a sample containing glass fiber and an alkaline solution with a 0.5 mol ratio.

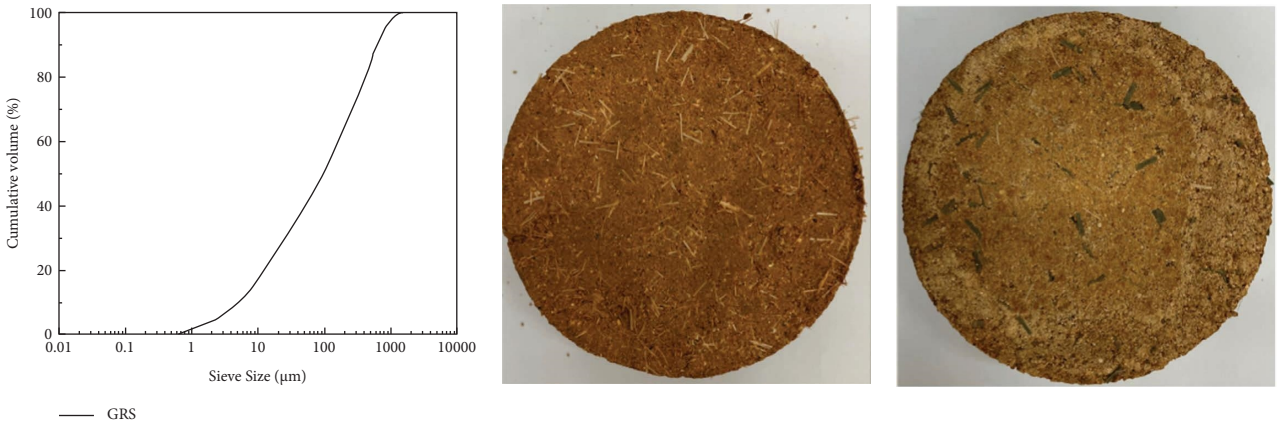

Figure 3: (a) GRS size, (b) glass fiber sample, and (c) basalt fiber sample.

Table 3: The unconfined compressive strength test plan.

	Group	Specimen number	Na_2SiO_3 (g)	NaOH (g)
Unconfined compressive strength tests	A	GRS	0	0
	B	2 mol	40	5.76
	C	1 mol	40	22.24
	D	0.7 mol	40	38.72
	E	0.5 mol	40	55.20
	F	0.4 mol	40	71.68

2.4. Method

2.4.1. Unconfined Compressive Strength Test. The uniaxial compressive strength of the sample was measured by a 4 W uniaxial compressive test instrument (see Figure 4). In accordance with GB/T 50123-2019 Standard for geotechnical testing methods, the sample was positioned in the exact center of the pressure plate of the press to rule out the possibility of eccentric loading at the loading rate of 0.5 MPa/s. The loading axial force at failure was recorded. The uniaxial compressive strength of each sample was calculated using the following formula:

$$R = \frac{P}{A}, \tag{1}$$

R is the ultimate compressive strength of the sample, P is the maximum load when the sample failed, and A is the cross-sectional area of the sample.

Based on the principle that the limit load should not exceed 15%, the average strength of three samples under the same ratio was calculated. To determine the optimal concentration of the alkaline solution, the unconfined compressive strength test was utilized to analyze the compressive strength of the samples at various ratios.

2.4.2. Drop-Weight Impact Test. The drop-weight test was conducted on an Instron Ceast 9350 floor-standingdrop-weight impact tester with a falling weight of 3.06 kg and a loading weight of 36.67 kg. The falling velocity was 4.5 m/s, and the corresponding instantaneous impact energy was 403.13 J. The pressure sensor on the surface of the falling weight recorded the impact load of samples, and the deformation was calculated by a computer (see Figure 5).

3. Results

3.1. Unconfined Compressive Strength Test. The GRS samples in Group A had a maximum compressive strength of 851.80 kPa. The maximum compressive strength of Group B, C, D, and E was 761.40 kPa, 1156.10 kPa, 4112.55 kPa, 4402.85 kPa, and 1750.70 kPa, respectively, when the alkali content was 2 mol, 1 mol, 0.7 mol, 0.5 mol, and 0.4 mol. Figure 6 depicts the maximum stress and error analysis of samples with varying SiO_2/Na_2O ratios in each group. Therefore, the effect of reinforcement on soil varies with the SiO_2/Na_2O ratio and is notable at the optimal ratio. Moreover, as seen in Figure 6, the addition of NaOH decreased the ratio of SiO_2/Na_2O by increasing the amount of Na_2O in the solution. A marked increase was witnessed when the ratio of SiO_2/Na_2O was reduced from 2 mol to 0.5 mol. The strength of samples comprising 0.7 mol and 0.5 mol SiO_2/Na_2O was almost 280% greater than that of samples comprising 2 mol and 1 mol SiO_2/Na_2O. However, the strength reduced to 1750.70 kPa when the ratio of SiO_2/Na_2O was increased to 0.4 mol, demonstrating that the ratio of SiO_2/Na_2O greatly enhances the strength and reinforcement effect only within a defined range and is not directly proportionate to the increase in strength. Based on the results of the unconfined compressive strength test, it was concluded that the ideal ratio of SiO_2/Na_2O for the

Table 4: The drop-weight test plan.

	Group	Specimen number	Na_2SiO_3 (g)	NaOH (g)	Glass fiber	Basalt fiber
Drop-weight test	H	LC-0.7-G	40	38.72	3	0
	I	LC-0.5-G	40	55.20	3	0
	J	LC-0.4-G	40	71.68	3	0
	K	LC-0.7-B	40	38.72	0	4
	L	LC-0.5-B	40	55.20	0	4
	M	LC-0.4-B	40	71.68	0	4
	N	GRS	0	0	0	0

alkaline solution's reinforcing effect on granite residual soil was 0.5 mol SiO_2/Na_2O.

3.2. Drop-Weight Test. Figures 7(a)–7(c) illustrate the ultimate bearing capacity of the specimens enhanced by different fibers under the differing ratios of alkali solution and impacted at an initial velocity of 4.5 m/s and an initial energy of 403.13 J, as well as the unreinforced GRS sample. As demonstrated in Figure 7(a), GRS has a bearing capacity of just 13.5 kN and deforms by 14 mm when subjected to an impact.

As shown in Figure 7(b), the addition of three molar ratios of alkaline solutions considerably improved the ultimate bearing capacity of glass fiber samples (LC-0.7-G, LC-0.5-G, and LC-0.4-G) in comparison to the GRS sample (40.6 kN, 120.0 kN, and 50.0 kN), with LC-0.5-G exhibiting the best reinforcement effect. This implies that the samples reinforced with an alkaline solution of 0.5 mol, SiO_2/Na_2O, and glass fiber were the strongest. In comparison to the deformation of the GRS sample (14.5 mm), the deformation of the samples containing glass fiber and alkali solution in three different ratios was reduced by 16.6% to 12.1 mm. The LC-0.5-G showed the least amount of distortion among them. It is possible to conclude that the addition of glass fiber and an alkaline solution containing 0.5 mol of SiO_2/Na_2O enhanced the reinforcing capacity of GRS in terms of both strength and deformation.

Figure 7(c) displays the impact resistance performance of GRS reinforced with basalt fiber in diverse alkaline solution ratios. The ultimate bearing capacities of the LC-0.7-B, LC-0.5-B, and LC-0.4-B increased by 211%, 507%, and 189%, respectively, compared to the GRS sample, to 42 kN, 82 kN, and 39 kN. LC-0.7-B exhibited the strongest reinforcing effect and the greatest ultimate bearing capacity. Despite the fact that LC-0.5-B has a greater bearing capacity, it appears that its deformation has not improved, as it has remained at around 14 mm. Similar conditions exist in the other two groups (LC-0.7-G and LC-0.4-G). Glass fiber has more advantages in enhancing the deformation of the samples than basalt fibers. In terms of bearing capacity, the optimal ratio of Si_2O/NaO_2 is 0.5 mol for the two kinds of fibers. This suggests that the optimal alkaline solution ratio for reinforcement is 0.5 mol Si_2O/NaO_2, which is consistent with the conclusion of the unconfined compressive strength test. The best reinforcement effect of the two fibers occurs in a 0.5 mol Si_2O/NaO_2 alkaline solution, but the reinforcement effect of glass fiber is superior, as evidenced by

Figure 4: uniaxial compression test instrument.

the fact that the ultimate bearing capacity and deformation of LC-0.5-G are 120 kN and 12.1 mm, or 46.3% and 13.6% higher than those of basalt fiber. In the optimal alkaline solution, it can be observed that glass fiber has a stronger reinforcing capacity than basalt fiber.

Figures 7(b) and 7(c) further demonstrate the relationship between impact force and deformation when a falling weight impacted the sample reinforced with various fibers and alkaline solutions. In each impact test, the compression deformation increased as the impact force increased. However, the decrease in impact force also resulted in a reduction in compression deformation. After an impact load was applied to the sample, pore compression and soil particle rearrangement would occur. These force-displacement curves can be divided into four distinct phases: the rearrangement phase, the increasing phase, the peak phase, and the weakening phase. Even though different types of fibers and an alkaline solution were employed to reinforce GRS, their impact forces and deformation curves are comparable as shown in Figures 7(b) and 7(c). In the deformation range of 0 to 2 mm, it is evident that the impact load of glass fiber samples (except for LC-0.5-G) rose sharply, reached the initial peak load, and then declined. Following its initial descent, the load ascended once more to an ultimate peak load of approximately 9 mm of deformation before the load dropped to 0 and remaining there ever since. The final deformation of the glass fiber sample was 12.1 mm. Within the 0–2 mm deformation range, the curves for basalt fiber samples went straight up, reached the

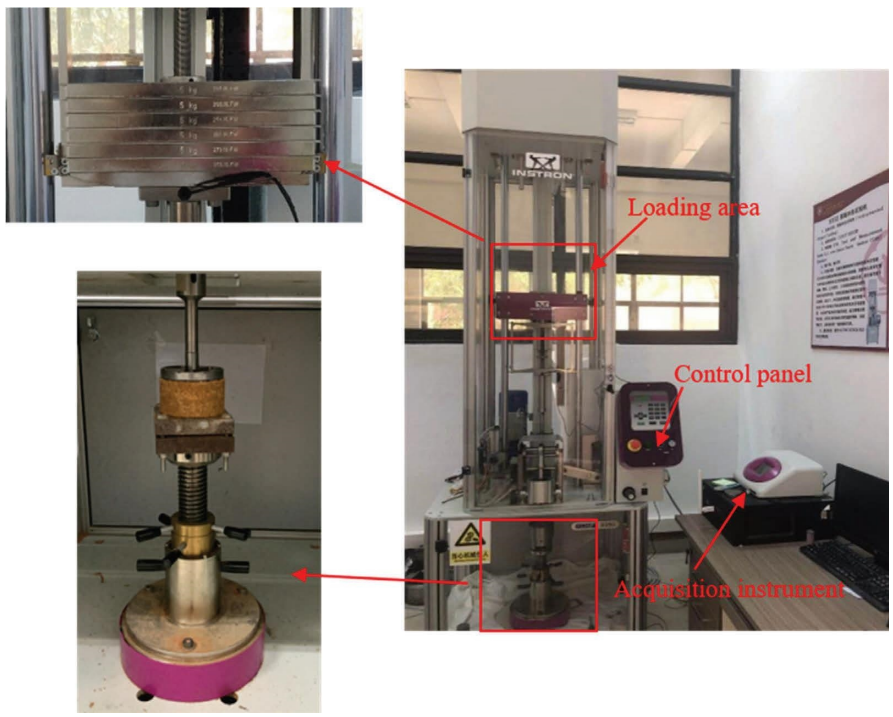

Figure 5: drop-weight tester.

first peak load, and then declined. After reaching the first lower point, the load climbed again, reached the ultimate peak load, and then dropped to 0 as the deformation increased to 14 mm.

As a result of the occurrence of instantaneous elastic deformation, the initial growth of the curves was approximately linear. At this point, the external force disturbed the soil granules, causing them to move and tumble, after which the granules rearranged and aggregated. As the pores narrowed and the effective stress between particles increased, the impact load increased linearly. After the elastic deformation reached its maximum, the impact force began to diminish because cracks in the samples exacerbated the compression deformation, resulting in a gradual decrease in the impact load. The impact load rebounded at approximately 2 mm of deformation and then increased to its maximum peak. This is because the soil was compacted, and its deformation modulus increased after it cracked to a certain extent. The mixture of glass fibers and soil absorbed the impact of the falling weight, allowing the sample to be further compressed without being destroyed.

However, the reinforcement effects of LC-0.5-G were different from LC-0.7-G and LC-0.4-G in the glass-fiber reinforced group, with LC-0.5-G being approximately 4 mm deformed at the rearrangement stage and LC-0.7-G and LC-0.4-G being approximately 1.5 mm deformed at that stage. This difference in reinforcement effects suggests that LC-0.5-G was more densely compacted, so there is less chance that the soil will move, roll, or tumble when resisting an external stress. As a result, the Si_2O/NaO_2 ratio of 0.5 mol produces the strongest reinforcement effect of glass fiber since this is

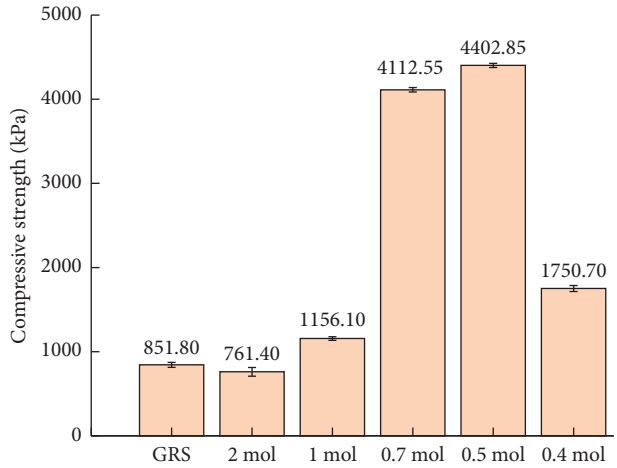

Figure 6: Compressive strength.

the ratio at which alkaline solution and glass fiber can work together most efficiently. It is determined that glass fiber and a 0.5 mol Si_2O/NaO_2 alkaline solution exhibit the maximum GRS reinforcing effect.

The optimal reinforcement effects of the two types of fibers added in the increase phase and the peak phase differ noticeably from one another. In samples of basalt fiber, the impact force gradually rose, and its deformation also dramatically increased to 14 mm with a maximum ultimate bearing capacity of just 82 kN. The final deformation of the glass fiber group, however, was only 12.1 mm when its impact force reached the maximum, over 13.6% lower than the basalt fiber. This is due to the fact that kaolinite in GRS

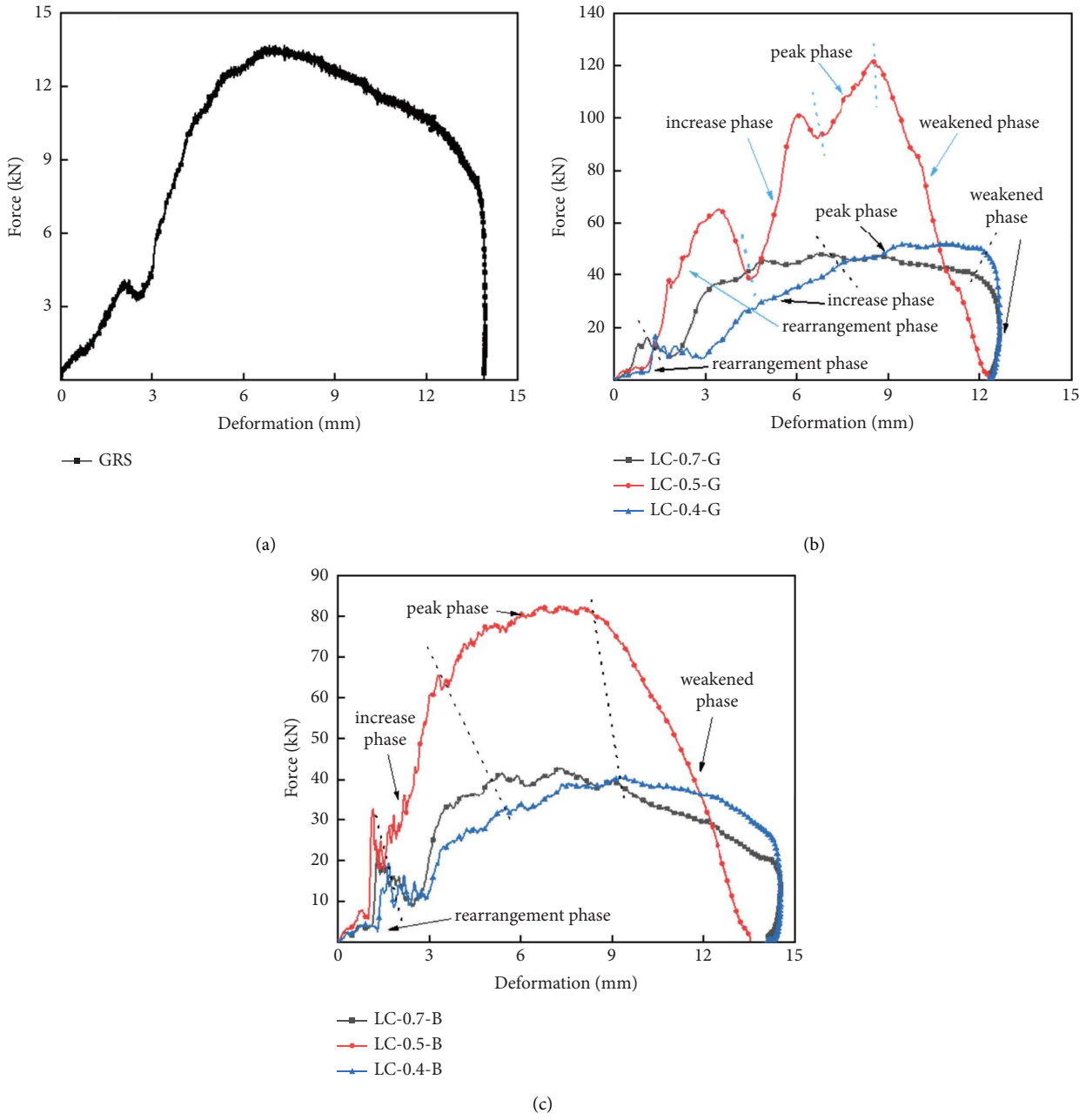

Figure 7: The diagram of impact force and compression deformation of the specimen.

was consumed and produced a gel substance under a 0.5 mol SiO_2/NaO_2 alkaline solution. Smaller glass fibers and the gel substance tightly and more firmly bind the soil together. Compared to glass fiber, which is assumed to have a better reinforcement capacity, basalt fiber's reinforcement effect is weaker under the optimal alkaline solution environment.

3.3. Scanning Electron Microscope. The SME images of GRS (Figure 8) reveal that the soil in the GRS sample is composed of granular particles with weak interaction. Under a microscope, the shape of the particles is hexagonal flaky or incomplete hexagonal flaky. This may be explained by the large amount of kaolinite in GRS. Kaolinite is in a hexagonal shape itself, and its incomplete hexagonal shape could be attributed to the compression and destruction of the soil during excavation that changes morphology. It was found that GRS contains a large amount of kaolinite, which is consistent with the results of XRD analysis.

The sample failed because it could not bear the impact load due to the relatively weak connection between soil particles in the original state of GRS. In contrast, the SEM images of the glass fiber group and the basalt fiber group (Figure 9) demonstrated that the soil mass remained relatively intact after being subjected to an external load and that a gel substance bound the soil particles and glass fibers into a cohesive whole that collectively bears the external impact load. The inclusion of fibers into the soil assisted in

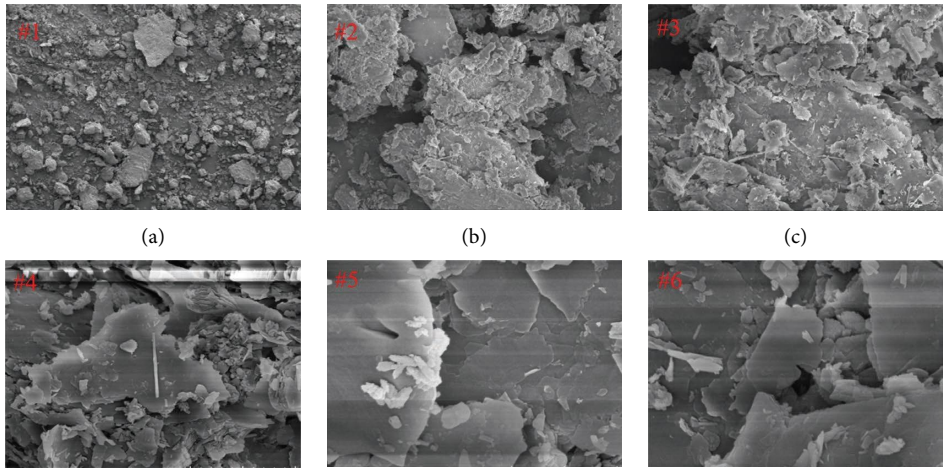

Figure 8: SEM images of material (GRS).

reinforcing the soil, thus enhancing the sample's structural integrity and, consequently, its ultimate bearing capacity.

In Figure 9, it is noticed that more glass fibers attached to the soil compared to the basalt fibers. The gel substance that formed after the addition of glass fiber to an alkaline solution may have bonded the soil particles and fibers closely and filled the pores, thereby increasing the compactness of the sample. In addition, the mixture of gel, soil particles, and fibers bears the load collectively, and the load can be transferred from soil to fiber and gel. Due to the high tensile strength of fibers and gel, the sample exhibits outstanding deformation under impact load, which explains why LC-0.5-G exhibits greater deformation than other samples. Due to the close combination of gel, fiber, and soil particles, a greater impact force is required to rearrange its particles when subjected to stress, which translates to a higher bearing capacity in mechanics. In comparison, basalt fiber samples contained less gel substance and fewer soil particles adhering to the surface of the fibers, resulting in a weaker connection between fiber and soil and a lower resistance to impact loads than glass fiber samples. The SME analysis provided additional understanding into the different reinforcing effects of glass fiber and basalt fibers on GRS in alkaline solution and revealed the reinforcement mechanism of the two fibers on GRS from a microscopic perspective.

3.4. XRF and XRD. XRF (Figure 10) results suggest that GRS (Figure 10(b)) contains a significant amount of silicon and aluminum, similar to the composition of MK (Figure 10(a)). In conjunction with the SEM and XRD analyses (Figures 11(a) and 11(b)), it is evident that GRS contains a significant amount of kaolinite, which was consumed and formed a gel with adhesion upon alkaline solution reinforcement.

Based on the results of the preceding analysis, the reinforcing effect of glass fiber in an alkaline solution is superior to that of basalt fiber; thus, only the group with the best reinforcement effect (LC-0.5-G) is chosen for XRD analysis. GRS is mostly composed of the minerals kaolinite, quartz, and a little amount of illite and low sodium potassium feldspar, according to the standard PDF of XRD, with kaolinite accounting for more than 50% of the total. Compared to the GRS sample, the kaolinite in sample LC-0.5-G exhibits multiple reflections, the strongest of which occurs at 12.3°. Although their reflection angle remained unchanged, their reflection intensity reduced dramatically, indicating a decrease in the crystallinity and content of kaolinite. A plausible explanation is that the alkaline solution consumes kaolinite particles, lowering the crystallinity of the kaolinite as a result. Microscopically, soil particles become more stable and solid, enhancing the sample's overall strength.

The quartz phase in LC-0.5-G was essentially similar to GRS and was integral, but the reflection intensity was greatly reduced, suggesting that the crystallinity and content of quartz have decreased. The most likely reason is that when kaolinite particles are mixed with alkali solution (0.5 mol SiO_2/Na_2O), the new substances formed had effect on the quartz reflection peak. Consequently, the intensity of the peak was diminished in XRD, but quartz is fundamentally stable, hence no significant change was seen.

At the reflection of 27.8°, a considerable increase in potassium feldspar content was observed, showing that the addition of alkaline solution promoted the formation of potassium feldspar in the sample, as evidenced by the sharp and noticeable potassium feldspar reflection peaks. Potassium feldspar belongs to the monoclinic crystal system, whose main components are alumina, silicon dioxide, and potassium oxide, and is distinguished by its high stability, high strength, and outstanding compressive performance. The majority of the substances in LC-0.5-G, quartz, and potassium feldspar are stable. The gel substance and geopolymer formed in LC-0.5-G had high viscosity and strength; they filled the pores of the particles and adhered them more firmly, thus significantly increasing the effective stress and enhancing the soil's strength.

From a microscopic perspective, the addition of a 0.5 mol, SiO_2/Na_2O alkaline solution and glass fiber

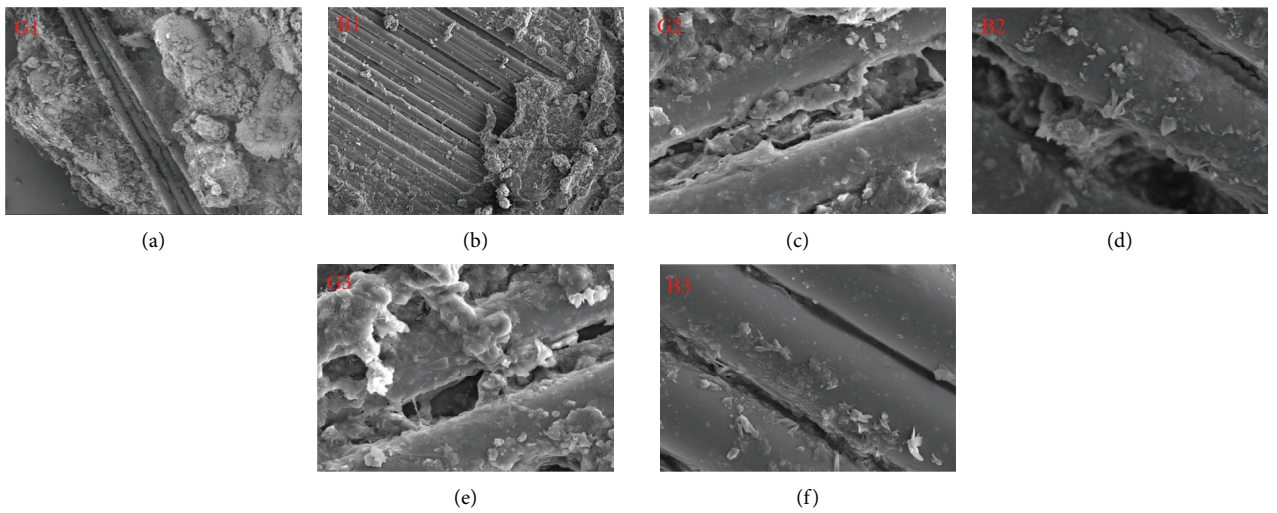

Figure 9: SEM of reinforcement soil of glass fiber (a), (c), and (e) and basalt fiber (b), (d), and (f).

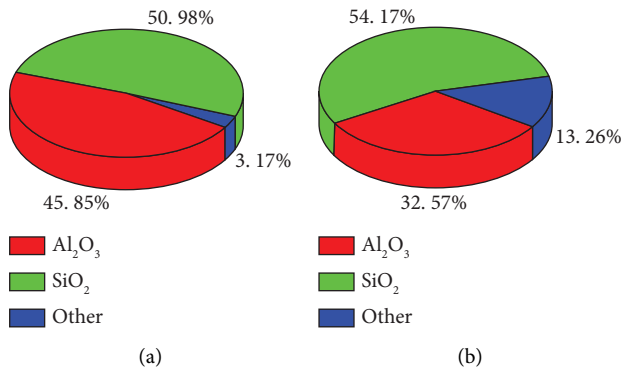

Figure 10: XRF patterns of MK (a) and GRS (b).

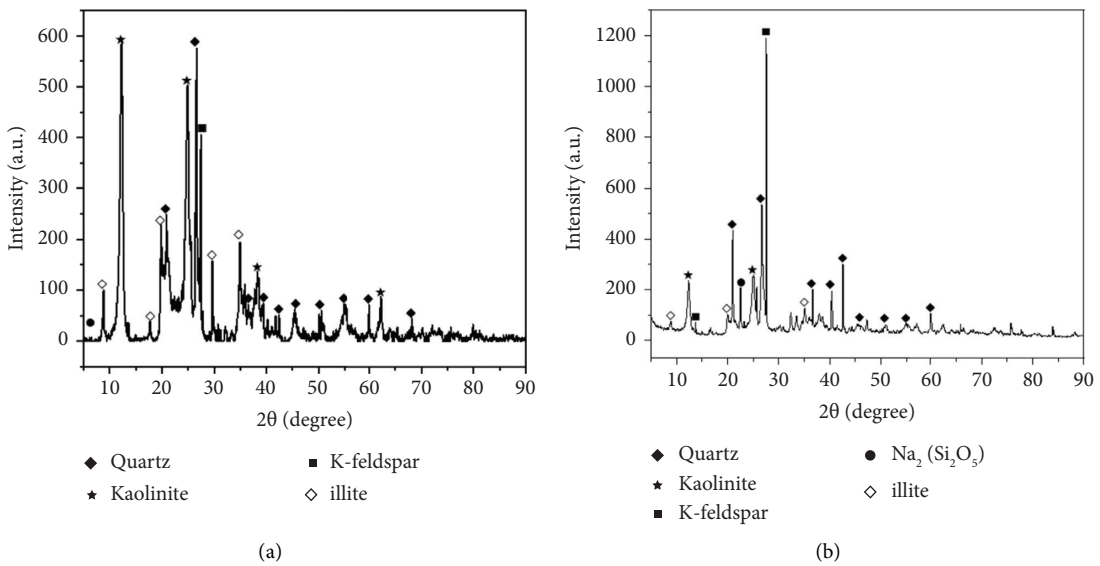

Figure 11: XRD patterns of GRS (a) and LC-0.5-G (b).2

produced more substances with greater strength and stability. Under the viscous envelopment of the geopolymer, the soil mixture formed a whole with enhanced compressive strength and stability.

The reasons for the distinct reinforcement effects of two different fibers on GRS in alkaline solution have been described from a macroperspective to microperspective. It was concluded that the reinforcing effect of glass fiber with GRS in an alkaline solution is superior to basalt fiber.

4. Conclusion

This article investigates the reinforcement effects of two different fibers on GRS in an alkaline solution, the influence of the SiO_2/Na_2O ratio in an alkaline solution on reinforcement performance, and the influence of glass fiber and basalt fiber on the mechanical properties of GRS in an alkaline solution and its microscopic mechanism using an unconfined compressive strength test and a drop-weight impact load test.

(1) The static load test showed that the samples' ultimate bearing capacity reached their highest value of 4402.85 kpa under a 0.5 mol SiO_2/Na_2O alkaline solution compared to samples of pure soil. Therefore, 0.5 mol of SiO_2/Na_2O is the ideal concentration for an alkaline solution.

(2) The drop-weight impact test demonstrates that the ultimate impact bearing capability of GRS is greatly enhanced after basalt fiber and glass fiber reinforcement in the optimal alkaline solution. Among them, the reinforcement effect of glass fiber is the most successful, as evidenced by the sample's deformation decreasing by 13.6% to 12.1 mm and its ultimate strength increasing by 789% to 120 kN.

(3) The significant increase in strength, as shown by SEM and XRD, is a result of the relatively high tensile strength of the glass fiber and the formation of a gel near the glass fiber in the alkaline solution, which binds the soil particles more closely and forms a whole that collectively bears the external load, thereby increasing the sample's strength. The smaller diameter of the glass fiber facilitates a better connection between the fiber and the soil particle. Basalt fiber, on the other hand, serves only as a connecting component during reinforcement because it does not produce an additional gel that binds the fibers together. Therefore, the reinforcement effect of basalt fiber with GRS in an alkaline solution is inferior to that of glass fiber.

Data Availability

The data supporting the findings of the current study are available from the corresponding author upon request.

Conflicts of Interest

The authors declare that there are no conflicts of interest.

Acknowledgments

The authors would gratefully like to acknowledge the support provided by the National Natural Science Foundation of China (51978177 and 41902288) and the Guangzhou Basic and Applied Basic Research Project (202201010391).

References

[1] S. Nanda and F. Berruti, "Municipal solid waste management and landfilling technologies: a review," *Environmental Chemistry Letters*, vol. 19, no. 2, pp. 1433–1456, 2020.

[2] L. C. Dang, H. Khabbaz, and B. J. Ni, "Improving engineering characteristics of expansive soils using industry waste as a sustainable application for reuse of bagasse ash," *Transportation Geotechnics*, vol. 31, Article ID 100637, 2021.

[3] R. Chen, S. S. C. Congress, G. Cai, W. Duan, and S. Liu, "Sustainable utilization of biomass waste-rice husk ash as a new solidified material of soil in geotechnical engineering: a review," *Construction and Building Materials*, vol. 292, Article ID 123219, 2021.

[4] Z. Nalbantoğlu, "Effectiveness of Class C fly ash as an expansive soil stabilizer," *Construction and Building Materials*, vol. 18, no. 6, pp. 377–381, 2004.

[5] P. Ghadir and N. Ranjbar, "Clayey soil stabilization using geopolymer and Portland cement," *Construction and Building Materials*, vol. 188, pp. 361–371, 2018.

[6] J. Xiao, J. Shen, M. Bai, Q. Gao, and Y. Wu, "Reuse of construction spoil in China: c," *Journal of Cleaner Production*, vol. 290, Article ID 125742, 2021.

[7] Q. Dong, G. Wang, X. Chen, J. Tan, and X. Gu, "Recycling of steel slag aggregate in portland cement concrete: an overview," *Journal of Cleaner Production*, vol. 282, Article ID 124447, 2021.

[8] E. S. Santos Nascimento, P. C. D. Souza, H. A. D. Oliveira, C. M. Melo Junior, V. G. D. Oliveira Almeida, and F. M. C. D. Melo, "Soil-cement brick with granite cutting residue reuse," *Journal of Cleaner Production*, vol. 321, Article ID 129002, 2021.

[9] C. S. Vieira, P. M. Pereira, and M. D. L. Lopes, "Recycled Construction and Demolition Wastes as filling material for geosynthetic reinforced structures. Interface properties," *Journal of Cleaner Production*, vol. 124, pp. 299–311, 2016.

[10] R. Muduli and B. B. Mukharjee, "Effect of incorporation of metakaolin and recycled coarse aggregate on properties of concrete," *Journal of Cleaner Production*, vol. 209, pp. 398–414, 2019.

[11] X. Liu, X. Zhang, L. Kong, G. Wang, and J. Lu, "Disintegration of granite residual soils with varying degrees of weathering," *Engineering Geology*, vol. 305, Article ID 106723, 2022.

[12] X. Liu, X. Zhang, L. Kong, G. Wang, and H. Liu, "Formation mechanism of collapsing gully in southern China and the relationship with granite residual soil: a geotechnical perspective," *Catena*, vol. 210, Article ID 105890, 2022.

[13] J. Xia, C. Cai, Y. Wei, and X. Wu, "Granite residual soil properties in collapsing gullies of south China: spatial variations and effects on collapsing gully erosion," *Catena*, vol. 174, pp. 469–477, 2019.

[14] B. Zhang, H. Guo, L. Deng, W. Fan, T. Yu, and Q. Wang, "Undehydrated kaolinite as materials for the preparation of geopolymer through phosphoric acid-activation," *Applied Clay Science*, vol. 199, Article ID 105887, 2020.

[15] Y. Wei, X. Wu, J. Xia et al., "The effect of water content on the shear strength characteristics of granitic soils in South China," *Soil and Tillage Research*, vol. 187, pp. 50–59, 2019.

[16] Y. Yao, J. Ni, and J. Li, "Stress-dependent water retention of granite residual soil and its implications for ground settlement," *Computers and Geotechnics*, vol. 129, Article ID 103835, 2021.

[17] B. Yuan, Z. Li, Y. Chen et al., "Mechanical and microstructural properties of recycling granite residual soil reinforced with glass fiber and liquid-modified polyvinyl alcohol polymer," *Chemosphere*, vol. 286, no. P1, Article ID 131652, 2022.

[18] B. Yuan, W. Chen, J. Zhao et al., "Addition of alkaline solutions and fibers for the reinforcement of kaolinite-containing granite residual soil," *Applied Clay Science*, vol. 228, Article ID 106644, 2022.

[19] B. Yuan, W. Chen, Z. Li et al., "Sustainability of the polymer SH reinforced recycled Granite Residual Soil: properties, physicochemical mechanism and applications," *Journal of Soils and Sediments*, vol. 23, no. 1, pp. 246–262, 2023.

[20] B. Yuan, M. Chen, W. Chen, Q. Luo, and H. Li, "Effect of pile-soil relative stiffness on deformation characteristics of the laterally loaded pile," *Advances in Materials Science and Engineering*, vol. 2022, Article ID 4913887, 13 pages, 2022.

[21] B. Yuan, M. Sun, Y. Wang, L. Zhai, Q. Luo, and X. Zhang, "Full 3D displacement measuring system for 3D displacement field of soil around a laterally loaded pile in transparent soil," *International Journal of Geomechanics*, vol. 19, no. 5, Article ID 04019028, 2019.

[22] B. Yuan, Z. Li, W. Chen et al., "Influence of groundwater depth on pile–soil mechanical properties and fractal characteristics under cyclic loading," *Fractal and Fractional*, vol. 6, no. 4, p. 198, 2022.

[23] Y. Wu, J. Cui, J. Huang, W. Zhang, N. Yoshimoto, and L. Wen, "Correlation of critical state strength properties with particle shape and surface fractal dimension of clinker ash," *International Journal of Geomechanics*, vol. 21, no. 6, Article ID 04021071, 2021.

[24] X. Que, Z. Zhu, Z. Niu, and W. Lu, "Estimating the strength and deformation of columnar jointed rock mass based on physical model test," *Bulletin of Engineering Geology and the Environment*, vol. 80, no. 2, pp. 1557–1570, 2021.

[25] L. Wang, Z. Yu, B. Liu, F. Zhao, S. Tang, and M. Jin, "Effects of fly ash dosage on shrinkage, crack resistance and fractal characteristics of face slab concrete," *Fractal Fract*, vol. 6, p. 335, 2022.

[26] L. Wang, S. Zhou, Y. Shi et al., "The influence of fly ash dosages on the permeability, pore structure and fractal features of face slab concrete," *Fractal Fract*, vol. 6, no. 9, p. 476, 2022.

[27] L. Wang, G. Li, X. Li et al., "Influence of reactivity and dosage of MgO expansive agent on shrinkage and crack resistance of face slab concrete," *Cement and Concrete Composites*, vol. 126, Article ID 104333, 2022.

[28] L. Wang, T. S. He, Y. X. Zhou et al., "The influence of fiber type and length on the cracking resistance, durability and pore structure of face slab concrete," *Construction and Building Materials*, vol. 282, Article ID 122706, 2021.

[29] B. B. Yang and Y. Liu, "Application of fractals to evaluate fractures of rock due to mining," *Fractal and Fractional*, vol. 6, no. 2, p. 96, 2022.

[30] B. B. Yang, J. Liu, X. Zhao, and S. Zheng, "Evaporation and cracked soda soil improved by fly ash from recycled materials," *Land Degradation & Development*, vol. 32, no. 9, pp. 2823–2832, 2021.

[31] B. B. Yang, S. Du, X. Zhao, D. Tang, and C. Yang, "Decision making of curriculum attainment degree for engineering geology based on fuzzy set theory," *Advances in Civil Engineering*, vol. 20216 pages, Article ID 1743778, 2021.

[32] F. Liu, G. Chen, L. Li, and Y. Guo, "Study of impact performance of rubber reinforced concrete," *Construction and Building Materials*, vol. 36, no. 11, pp. 604–616, 2012.

[33] Z. Lu, W. H. Zhou, and Z. Y. Yin, "Effect of viscosity on slurry infiltration in granular media," *International Journal of Geomechanics*, vol. 22, no. 9, Article ID 04022138, 2022.

[34] Z. Lu, W. H. Zhou, Z. Y. Yin, and J. Yang, "Numerical modeling of viscous slurry infiltration in sand," *Computers and Geotechnics*, vol. 146, Article ID 104745, 2022.

[35] H. Guo, B. Zhang, L. Deng, P. Yuan, M. Li, and Q. Wang, "Preparation of high-performance silico-aluminophosphate geopolymers using fly ash and metakaolin as raw materials," *Applied Clay Science*, vol. 204, Article ID 106019, 2021.

[36] B. X. Yuan, W. J. Chen, J. Zhao, F. Yang, Q. Luo, and T. Chen, "The effect of organic and inorganic modifiers on the physical properties of granite residual soil," *Advances in Materials Science and Engineering*, vol. 2022, Article ID 9542258, 13 pages, 2022.

[37] Y. S. Kim, T. Q. Tran, G. O. Kang, and T. M. Do, "Stabilization of a residual granitic soil using various new green binders," *Construction and Building Materials*, vol. 223, pp. 724–735, 2019.

[38] S. Hov, P. Paniagua, C. Sætre et al., "Lime-cement stabilisation of Trondheim clays and its impact on carbon dioxide emissions," *Soils and Foundations*, vol. 62, no. 3, Article ID 101162, 2022.

[39] S. Nie, J. Zhou, F. Yang et al., "Analysis of theoretical carbon dioxide emissions from cement production: m," *Journal of Cleaner Production*, vol. 334, Article ID 130270, 2022.

[40] B. Zhang, H. Guo, P. Yuan et al., "Geopolymerization of halloysite via alkali-activation: d," *Applied Clay Science*, vol. 185, Article ID 105375, 2020.

[41] B. Zhang, Y. Feng, J. Xie et al., "Effects of fibres on ultra-lightweight high strength concrete: dynamic behaviour and microstructures," *Cement and Concrete Composites*, vol. 128, Article ID 104417, 2022.

[42] M. Ohno and V. C. Li, "A feasibility study of strain hardening fiber reinforced fly ash-based geopolymer composites," *Construction and Building Materials*, vol. 57, pp. 163–168, 2014.

[43] Z. Chen, H. Zhou, F. Ye, B. Liu, and W. Fu, "The characteristics, induced factors, and formation mechanism of the 2018 Baige landslide in Jinsha River, Southwest China," *Catena*, vol. 203, Article ID 105337, 2021.

[44] Z. Chen, H. Zhou, F. Ye, B. Liu, W. Fu, and M. Moscatelli, "Landslide susceptibility mapping along the anninghe fault zone in China using SVM and ACO-PSO-SVM models," *Lithosphere*, vol. 2022, no. 1, Article ID 5216125, 2022.

[45] A. Saludung, T. Azeyanagi, Y. Ogawa, and K. Kawai, "Alkali leaching and mechanical performance of epoxy resin-reinforced geopolymer composite," *Materials Letters*, vol. 304, Article ID 130663, 2021.

[46] S. Samal, "Interface failure and delamination resistance of fiber-reinforced geopolymer composite by simulation and experimental method," *Cement and Concrete Composites*, vol. 128, Article ID 104420, 2022.

[47] S. Narani, M. Abbaspour, S. M. Mir Mohammad Hosseini, E. Aflaki, and F. Moghadas Nejad, "Sustainable reuse of Waste Tire Textile Fibers (WTTFs) as reinforcement materials for expansive soils: with a special focus on landfill liners/covers,"

Journal of Cleaner Production, vol. 247, Article ID 119151, 2020.

[48] R. Mattone, "Sisal fibre reinforced soil with cement or cactus pulp in bahareque technique," *Cement and Concrete Composites*, vol. 27, no. 5, pp. 611–616, 2005.

[49] M. F. Ma'Ruf, "Shear strength of Apus bamboo root reinforced soil," *Ecological Engineering*, vol. 41, pp. 84–86, 2012.

[50] M. Mirzababaei, A. Arulrajah, A. Haque, S. Nimbalkar, and A. Mohajerani, "Effect of fiber reinforcement on shear strength and void ratio of soft clay," *Geosynthetics International*, vol. 25, no. 4, pp. 471–480, 2018.

[51] K. Meng, C. Cui, Z. Liang, H. Li, and H. Pei, "A new approach for longitudinal vibration of a large-diameter floating pipe pile in visco-elastic soil considering the three-dimensional wave effects," *Computers and Geotechnics*, vol. 128, Article ID 103840, 2020.

[52] C. Cui, K. Meng, Y. J. Wu, D. Chapman, and Z. M. Liang, "Dynamic response of pipe pile embedded in layered visco-elastic media with radial inhomogeneity under vertical excitation," *Geomechanics and Engineering*, vol. 16, no. 6, pp. 609–618, 2018.

[53] N. Jain, A. Verma, and V. K. Singh, "Dynamic mechanical analysis and creep-recovery behaviour of polyvinyl alcohol based cross-linked biocomposite reinforced with basalt fiber," *Materials Research Express*, vol. 6, no. 10, Article ID 105373, 2019.

[54] M. Karthick, M. Meikandan, S. Kaliappan et al., "Experimental investigation on mechanical properties of glass fiber hybridized natural fiber reinforced penta-layered hybrid polymer composite," *International Journal of Chemical Engineering*, vol. 2022, Article ID 1864446, 9 pages, 2022.

[55] A. Verma, A. Parashar, N. Jain, V. K. Singh, S. M. Rangappa, and S. Siengchin, "Surface modification techniques for the preparation of different novel biofibers for composites," *Biofibers and Biopolymers for Biocomposites: Synthesis, Characterization and Properties*, pp. 1–34, Springer International Publishing, Cham, Switzerland, 2020.

Hindawi
Advances in Civil Engineering
Volume 2023, Article ID 7738042, 15 pages
https://doi.org/10.1155/2023/7738042

Research Article

Analysis of Influence of Ultra-High Pressure Water Jet Cutting Pressure Sequence on Pressure Relief and Reflection Improvement of Coal Seam

Shoulong Ma [1,2]

[1]*School of Civil Engineering and Architecture, Anhui University of Science and Technology, Huainan, Anhui 232001, China*
[2]*China Coal Xinji Energy Co., Ltd., Huainan, Anhui 232001, China*

Correspondence should be addressed to Shoulong Ma; 2020100046@aust.edu.cn

Received 15 October 2022; Revised 6 November 2022; Accepted 23 February 2023; Published 1 April 2023

Academic Editor: Zhuo Chen

In order to explore the pressure relief effect of the two combined pressure relief and antireflection technologies of ultra-high pressure water jet cutting before pressure and pressure before cutting, theoretical analysis, numerical simulation, and field test were used to study the main control factors of the combined high-pressure water jet slit cutting and fracturing antireflection technology. This paper introduces the combined technology of ultra-high pressure hydraulic fracturing, and analyses the mechanism of pressure relief and transparency enhancement of the combination of cutting before pressure and pressure relief after cutting. The results show that the starting pressure of the coal seam with ultra-high pressure water jet cutting and pressure relief is 13 MPa, the influence radius of hydraulic fracturing is 45–55 m, the starting pressure of the coal seam with pressure cutting and pressure relief is 16 MPa, and the influence radius of hydraulic fracturing is 35–45 m. Compared with pressure cutting combined pressure relief and permeability enhancement technology, cutting pressure relief and permeability enhancement technology can improve the permeability of coal seams more evenly and effectively, and reduce the stress of coal seams near the hole. The ultra-high pressure cutting and pressure combined technology can make the pressure relief of coal body uniform and sufficient, and the overall permeability coefficient of the coal body is greatly improved. The drilling purity is 2.3 times of the extraction purity of the ordinary single hole drilling, and the extraction influence range is increased, and the extraction effect is significantly improved. At the same time, the stress of coal body is reduced after slitting, and the starting pressure of hydraulic fracturing is reduced. The research results provide a scientific basis for the coal seam pressure relief and permeability enhancement under similar conditions in the mining area and have a broad application prospect.

1. Introduction

At present, there are more than 2000 coal and gas outburst, rock burst, and high gas mines in China, accounting for 30% of the total number of mines. After entering deep mining, the problems of high gas and high ground stress are prominent, the permeability of coal seam is reduced, and the difficulty of disaster management is increased [1–3]. Under the condition of deep mining, the coal seam is upgraded to the protruding coal seam. For the protruding coal seam without protective layer mining or first mining, the anti-protruding measures in the prepumping area of dense conventional borehole are still the main measures. In order to achieve efficient control of gas disasters in deep mines, the conventional pressure relief and reflection improvement technologies in coal mines in China at the present stage mainly include hydraulic punching, hydraulic cutting, hydraulic fracturing, and deep-hole presplitting blasting [4–6].

Although the deep-hole presplit blasting technology can significantly improve the pressure relief and antireflection effect of coal seam, it is relatively less applied in the pressure relief and antireflection improvement of coal seam, because the long borehole coal seam is prone to collapse, resulting in charging difficulties, and it is difficult to eliminate the risk of misfiring and explosion refusal in blasting operation. In recent years, the reflection improvement technology of

hydraulic coal seam in China has entered a stage of rapid development. The individual technology is constantly improved, and the overall development is in the direction of integration and diversification. The hydraulic measures such as low-pressure hydraulic punching, hydraulic cavitation, hydraulic fracturing, and hydraulic slotting have become the hot spots of research in scientific research institutions, which provide support for the control of coal mine gas disasters and have achieved results under certain conditions [7–10]. The hydraulic technology is often used in the field, and the hydraulic punching pressure is generally 5–20 MPa, which has a certain effect on the pressure relief and reflection improvement of soft coal seam, while the hydraulic punching efficiency of medium and hard coal seam is low. However, it is difficult to control the shape of punching holes in soft coal seam, and the amount of slag is not uniform, so there may be hole collapse, hole injection, or roadway gas overlimit during operation. The hydraulic fracturing has a large influence range and good antireflection effect, and is mostly used in medium and hard coal seams. However, it is difficult to control the fracture propagation direction in the coal body [11–13]. Hydraulic cutting seam technology is based on high-pressure water cutting technology of coal seam, improve coal seam gas flow state, reduce the stress, can effectively prevent coal, and gas outburst and the impact of ground pressure disasters happen, suitable for high ground stress, gas and low permeability coal seam (seam hardness $f > 0.4$) bedding face drilling, wear layer drilling, and shimen uncovering coal unloading antireflection and so on [14–16].

The ultra-high pressure water jet cuts the coal body, and the coal body around the slot produces deformation space so that the coal body around the slot can be fully depressurized. At the same time, because a part of the coal body around the drill hole is transported out of the drill hole by the water jet, a large number of cracks are generated in the expansion and deformation of the coal rock, changing the permeability conditions of the coal rock. Ge et al. established a fluid-solid coupling gas drainage model of slotted borehole. Through numerical simulation analysis, it is believed that the influence radius of the borehole drainage after hydraulic slotting has a power function relationship with slot disc, permeability, drainage time, gas pressure, and other factors. Through model research, it is determined that the influence significance of each factor from large to small is permeability, drainage time, gas pressure, and slotting depth [17]. Li et al. used a dynamic damage model to study the cutting process of soft coal rock by water jet. During the cutting process, with the gradual release of stress around the slot, the crack continued to expand in some directions. The tension and shear fractures in coal and rock continue to develop during the damage accumulation process, in which short pulses with high peak stress can form relatively short fractures, and long pulses with low peak stress can form relatively long fractures. Under the continuous action, the cracks around the slot cut by the jet gradually develop and then connect to each other to form a breakthrough failure [18]. Tang et al. conducted numerical simulation on the influence of different hydraulic slotting arrangements on the coal seam pressure relief and outburst prevention, and analyzed the influence of parallel, diamond, and staggered pressure relief. The results show that the coal rock pressure relief effect above the fracture groove is most obvious. The results showed that the pressure relief effect of coal and rock above the slot was the most obvious [19]. Through indirect measurement of gas flow through similar material test, it is confirmed that the pressure relief of coal seam has a significant impact on permeability, and the permeability coefficient of coal and rock increases synchronously with the degree of pressure relief. By studying the displacement and stress changes of coal body under different slit widths after high-pressure water jet slotting, the influence of slit depth on coal rock disturbance is analyzed. Numerical simulation shows that the pressure relief range of 1.0 m, 1.5 m, and 2.0 m slotting on coal body reaches 2.6 m, 3.8 m, and 5.0 m, and the influence range of slit on coal body increases with the increase of slit width. The larger the slit depth is, the more conducive to coal seam pressure relief.

The antireflection technology of hydraulic fracturing was first used in the exploitation of oil and gas fields, as a main measure of oil and gas well stimulation. In the 1960s, the hydraulic fracturing technology began to be used in coal mines to increase in coal seam permeability, mainly by drilling deep into the coal body through injection of high-pressure water, and fracturing the coal body with water as the energy transmission medium. After high-pressure water fracturing, the stress of surrounding coal body was reduced, and the stress concentration was transferred to the depth of the coal body, thus improving the permeability of coal body around the borehole, providing a good condition for drilling gas extraction [12, 20–22]. The research on the hydraulic fracturing technology in coal mine mainly focuses on the theoretical research on the initiation and extension laws of the hydraulic fractures, or the establishment of hydraulic fracturing mathematical model for numerical calculation research, or the physical experiment research of hydraulic fracturing in the laboratory. Hubbert and Willis described the stress distribution law of hydraulic fracturing wall and surrounding coal and rock mass based on classical elastic mechanics, and thus obtained the theoretical calculation model of tensile failure fracture pressure of coal and rock mass: $P_b = 3\sigma_{\min} - \sigma_{\max} + f_t$ ($\sigma_{\min}$, $\sigma_{\max}$, and f_t are the minimum horizontal stress, the maximum horizontal stress, and the tensile strength of coal rock, respectively); the comprehensive effects of the tangential principal stress σ_θ, straight principal stress σ_v, and radial principal stress σ_r on the wall of the borehole are not fully considered in this theory [23]. Ma et al. conducted an experimental study on the influence of water pressure with different water flow rates on the fracture initiation characteristics of coal. The results show that the increase in water flow rate makes the fracture morphology more complex, and the research results have important theoretical significance for revealing the fracture initiation behavior of boreholes [24]. According to the first strength criterion, Lv deduced the critical value calculation formula of pressure crack initiation pressure and successfully tried it in Pingmei Ten Mine [25]. Bouteca developed a full 3D morphological mathematical model of hydraulic fracturing

by combining the 3D spatial fluid flow field model with the elliptical fracture deformation model of Shah and Kobagashi [26]. Based on the fluid-solid interaction theory, Lian et al. analyzed the problem of hydraulic fracture propagation, took the critical stress as the criterion of the fracture initiation and extension, deduced the pressure drop equation expression in the fracture wall, and established the calculation model. ABAQUS software was used to simulate the influence of surrounding rock stress, rock mechanical properties, fracturing fluid seepage characteristics, and other external factors on hydraulic fracture propagation [27]. Bjerrum et al. carried out hydraulic fracturing tests by injecting high-pressure water into a small circular tube at the bottom of the fracturing sample in a triaxial pressure test device, and concluded that the propagation direction of hydraulic fractures was generated along the minimum principal stress surface [28]. Chen et al. used the true triaxial test device to conduct AE monitoring on the fracture of raw coal samples under fracturing. The research results can reveal the source characteristics of the whole fracture process of raw coal samples in the true triaxial hydraulic fracturing process, and evaluate the safety of the fracture process [29]. Deng et al. studied the control parameters of hydraulic crack propagation behavior by the method of hydraulic fracturing under the control of ground stress field, and conducted a systematic experimental study on the relationship between the formation and expansion of hydraulic crack and the change of coal permeability and the action of hydraulic pressure. The research results have practical significance for improving the design effect of top coal precracking [30]. Liu et al. studied the internal microstructure evolution mechanism of different coals under liquid nitrogen cooling. The experimental results show that the total pore volume and pore surface area of coal are increased after cold leaching, the heterogeneity of pore structure is enhanced, the fractal dimension is increased, and the development of porous structure of coal is promoted by cold leaching [31]. Zhou et al. took Longhu coal mine in Qitaihe mining area as the research object to study the stability of roadway floor heave. The new support scheme is adopted to reduce the floor heave of roadway by 81%. The research results can provide guidance for the optimization of roadway support [32]. Surrounding rock control and support stability of super high mining face was studied by Wang Sheng. The results of this study can provide guidance for the selection of scaffolds and the adoption of measures to improve the stability of scaffolds when they are used in ultra-high height conditions [33]. Taking Linyi mining area as the research object, Li Xuelong studied the distribution law of ground stress in deep mines. It is found that the relationship between principal stresses is $\sigma(H) > \sigma(v) > \sigma(h)$, which belongs to the strike-slip stress system. Under this stress condition, the soil lateral pressure coefficients are all greater than 1, and the magnitude of the three principal stresses increases with the increase in depth. The research results have certain reference significance for mine disaster prevention and safety production [34]. Liu Haiyan studied the failure mechanism and control technology of cave-side stoping roadway in close distance coal seam. It is proposed that *U*-shaped steel telescopic support erection and backwall filling are used to control the surrounding rock of goaf mining in the process of roadway excavation, and the on-site monitoring results also meet the engineering requirements. The research results can provide guidance for roadway design of goaf under similar mining geological conditions [35–51].

The application of ultra-high pressure hydraulic slotting technology can realize the precise seam cutting, rapid pressure relief, and efficient permeability increase, and drilling engineering quantity is reduced on the basis of the extraction standard time to shorten 30% of the effect. With the application of hydraulic fracturing technology, the impact area of hydraulic fracturing is more than 50 m, with a large impact area and obvious antireflection effect in the region. After the application of ultra-high pressure hydraulic slit technology and hydraulic fracturing technology, the antireflection effect of coal seam is remarkable. Therefore, in the hydraulic cutting seam technology and hydraulic fracturing technology in the application process, there exist the following problems: the super high-pressure hydraulic cutting seam to improve the unloading antireflection effect at the same time, greatly reduce drilling of quantities, as local antireflection measures that it is obvious, but for large area still needs to undertake a large number of slotted drilling construction slot unloading antireflection. Although the antireflection effect of hydraulic fracturing technology has a large influence range, it is difficult to control the fracture propagation direction in the coal body, and the pressure relief and antireflection improvement are not uniform, and there is stress concentration phenomenon.

To sum up, to better carry out uniform permeability improvement in low permeability coal seam, accurately control the pressure relief and permeability improvement area, greatly reduce the drilling engineering quantity, and solve the technical problems of gas extraction and control in low permeability coal seam. The combined technology of ultra-high pressure hydraulic slit cutting and hydraulic fracturing is explored, and the mechanism of pressure relief and reflection improvement by cutting and pressure relief and cutting is analyzed. The hydraulic cutting pressure scientific model is established, and the influence range of high pressure hydraulic cutting pressure is solved through theoretical analysis. The PFC software based on the theory of discontinuous media mechanics was used to simulate the initiation and expansion characteristics of seam cutting and fracturing fractures in coal seam, and the distribution rules of fractures and stresses in coal seam were compared and analyzed by hydraulic cutting before pressure and pressure relief after cutting. Combined with the field research on ultra-high pressure hydraulic cutting before pressure and pressure before cutting and combined pressure before cutting and permeability improvement, the influence law of ultra-high pressure water jet cutting pressure sequence on pressure relief and permeability improvement of coal seam is further revealed. The research results are of great significance to enrich the comprehensive gas control technology of low permeability coal seam.

2. Ultra-High Pressure Hydraulics First Cut and Then Pressure Combined with the Principle of Permeation

The concept of hydraulics first cut and then pressurized joint mode is to use ultra-high pressure hydraulic cuts to cut the coal seam in the coal seam first, and then use hydraulic fracturing to fracturing the coal seam after the gap is generated. The groove generated by the hydraulic cutting in the early stage can guide the hydraulic fracturing so that the extension direction of the fracture in the plastic zone is basically the same as the direction of cracking. The crack expansion is more uniform.

By forming a slot by hydraulic cutting in the coal body in advance, the effective influence range of the single hole can be expanded to a certain extent. The original stress balance of the coal body can be destroyed. The coal body around the cut hole is transported to the space of the slot space, and the pressure relief, deformation, and expansion of the coal seam can occur, further generating more cracks and expanding the plastic area of the coal body near the cut hole. Combined with the empirical formula of plastic theory, it can be seen that the radius of the plastic zone is about 3 to 5 times the radius of the cut groove, and the radius of the high-pressure water groove is determined to be about 2.5 m through field tests. It is inferred that the radial plastic zone range outside the hydraulic groove is about 7.5 to 12.5 m. After the hydraulic cut is formed into a crevice, a weak surface is generated in the drilling hole, and after the fracturing water enters the crack, it promotes the cracking, expansion, and extension of the weak side crack, resulting in the full and uniform development of the coal body fracture near the borehole. Through the rational arrangement of the cut-pressure joint hole, a three-dimensional fracture network of interpenetration is formed between the drilled holes, which effectively solve the problems of disorderly expansion of the fracture in the coal body during the ordinary hydraulic fracturing, local stress concentration, and pressure relief blind zone after fracturing.

This joint mode not only solves the problems that the direction of hydraulic fracturing crack is not easy to control, but also the crack propagation in the fracturing area is uneven. It is easy to form a high stress concentration area, and there is a "blind zone" of fracturing, but also increases the scope of impact of fracturing, which saves a lot of drilling engineering compared with ordinary drilling holes and improves the efficiency of pressure relief and antiextrusion. At the same time, the problems of uneven pressure relief and stress concentration in individual areas are supplemented by fixed-point hydraulic cutting to achieve uniform and efficient antipenetration purposes. A schematic diagram of the first cut and then press joint is shown in Figure 1.

3. Ultra-High Pressure Hydraulics First Press and Then Cut and Increase the Principle of Penetration

Hydraulics first press and then cut joint mode, that is, hydraulic fracturing is used to supplement the fracture within the influence range of hydraulic fracturing. The gap fracture is formed in the blank zone of the hydraulic fracturing affected area, and the fracture formed by hydraulic fracturing is conducted, and more fractures are formed. Through hydraulic fracturing operations to rapidly improve the permeability of the coal seam in the area and the gas extraction effect, after the completion of the hydraulic fracturing construction, the fracturing crack is uncontrollable. Although the cracks in the coal seam are generated in a large range, the permeability of the coal seam increases, and the coal body plays a decompression and permeability effect within the scope of the crack. However, the inhomogeneity of the physical and mechanical properties of the coal leads to the uncontrollable weak surface in the coal seam, resulting in uncontrollable hydraulic fracturing cracks. There is a blank zone affected by hydraulic fracturing within the scope of influence of the hydraulic fracturing, and the area with poor pressure relief effect is used as a "blind spot" of hydraulic fracturing, and there is a stress concentration in the uncontrolled area of the crack. The use of hydraulic cutting joints to accurately increase penetration and strengthen extraction, under the action of ground stress, and the fracturing cracks are connected with the fractured area of the joints, forming an overall pressure relief area, reducing the stress concentration, and effectively improving the gas permeability of the coal seam. This mode effectively combines the advantages of fracturing and fracture, solves the problem of stress concentration and uneven fracturing in the fracturing area, and realizes the accuracy of antiprotrusion. The precise antiprotrusion mode of pressing first and cutting is shown in Figure 2.

4. Ultra-High Pressure Hydraulics First Press and Then Cut and Increase the Principle of Penetration

Under the action of ultra-high pressure hydraulic force, when the coal body around the borehole exceeds its own strength, the hole wall is the plastic softening zone and the elastic zone are from inside to outside. The drilling mechanical model is shown in Figure 3. The model assumes the following:

① The borehole is subject to the stress P_0 of the original rock, and the side pressure coefficient $\lambda = 1$ is treated according to the axial symmetry problem, which is simplified to planar strain

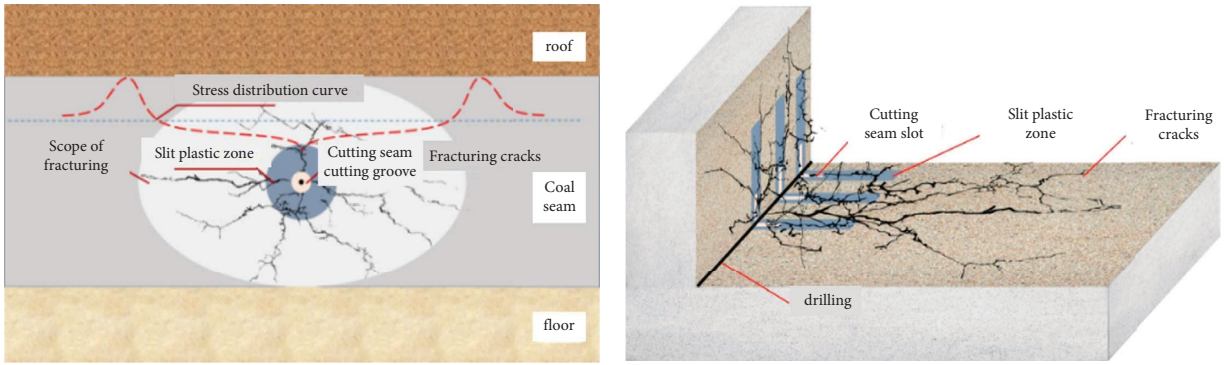

Figure 1: Schematic diagram of high efficiency anti-penetration mode of cutting before pressing. (a) Schematic diagram of fracture propagation profile after cutting. (b) Schematic diagram of the distribution plane of the slit after cutting.

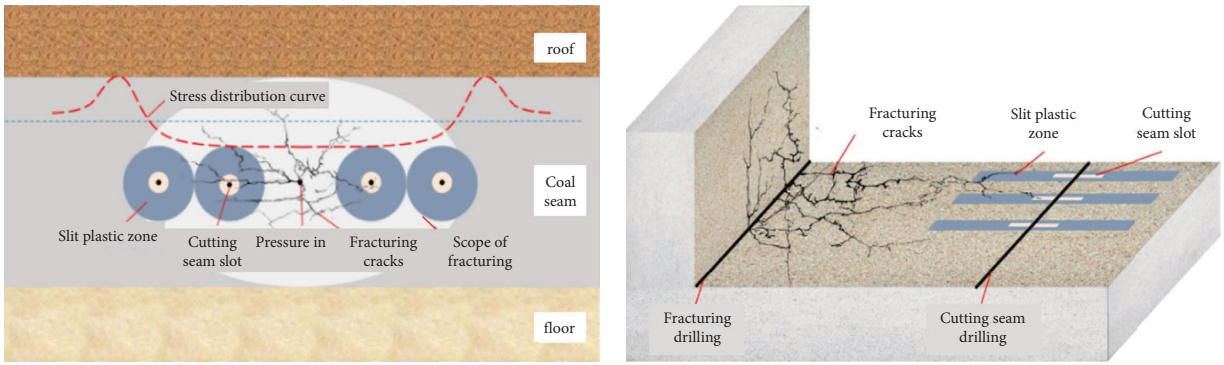

Figure 2: Schematic diagram of high efficiency anti-spike mode of pressing before cutting. (a) Schematic diagram of fracture propagation profile after compression. (b) Schematic diagram of the distribution plane of the crack before pressing and cutting.

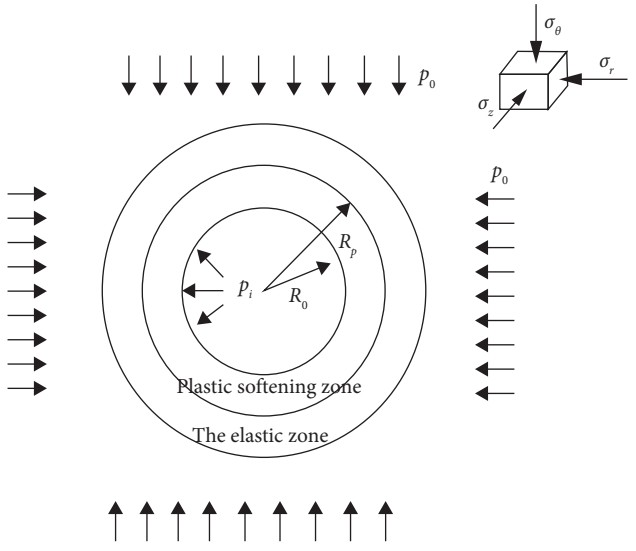

Figure 3: Borehole mechanical model.

② The coal around the borehole is homogeneous and isotropic, and the influence of borehole pressure relief on the borehole is not considered

③ R_0 is the drilling radius; σ_p is the peak intensity; σ_c is the residual strength; the hydraulic fracturing pressure p_i acts evenly on the wall of the drilled hole

Assuming that the compressive stress is positive and the tensile stress is negative, the deep borehole is subjected to ground stress, at this time:$\sigma_1 = \sigma_\theta$, $\sigma_3 = \sigma_r$, and $\sigma_2 = \sigma_z = \mu(\sigma_\theta + \sigma_r)$. The strength characteristics of the elastoplastic state of the borehole wall are described by the unified strength theory, and the expression is as follows:

$$\sigma_\theta = A_j \sigma_r + B_j, \tag{1}$$

$$\left.\begin{aligned} A_j &= \frac{(1+b\mu)\left(1+\sin\phi_j\right)}{\left(1-\sin\phi_j\right)(1+b)-b\mu\left(1+\sin\phi_j\right)} \\ B_j &= \frac{2(1+b)c_j\cos\phi_j}{\left(1-\sin\phi_j\right)(1+b)-b\mu\left(1+\sin\phi_j\right)} \end{aligned}\right\}, \tag{2}$$

where σ_θ, σ_r are the tangential stress and radial stress of the borehole wall, respectively. Since A_j, B_j are characterizing the parameters of the coal body, representing the relationship between the maximum principal stress and the minimum principal stress. The μ is for Poisson's ratio; j is the symbolic parameter; $j = e$ represents the initial internal friction angle φ_e and cohesion force c_e of the coal body; $j = p$ represents the friction angle φ_p and cohesion c_p of the plastic softening region; b is the median principal stress coefficient, $0 \le b \le 1$.

In the stress-strain curve, failure occurs when the strength of the coal body exceeds its ultimate strength, and this paper assumes that the residual friction angle φ_c and the residual cohesion c_c are unchanged. Plastic softening occurs when the strength of the coal body exceeds its peak strength, and the values of the friction angle φ_p and cohesion c_p in the plastic region gradually decrease with the increase in plastic strain, assuming that φ_p and c_p are linearly softened with the initial internal friction angle φ_e and cohesion force c_e. The softening coefficients k_φ and k_c are introduced, which are as follows:

$$\phi_p = \begin{cases} \phi_e, & \left(r \ge R_p\right), \\ k_\phi \phi_e, & \left(r \le R_p \text{and} \dfrac{\phi_s}{\phi_e} \le k \le 1\right), \end{cases}$$

$$c_p = \begin{cases} c_e, & \left(r \le R_p\right), \\ k_c c_e, & \left(r \le R_p \text{and} \dfrac{c_s}{c_e} \le k_c \le 1\right), \end{cases} \tag{3}$$

where k_φ, k_c are the internal friction angle and the cohesive softening coefficient. φ_e, φ_p, and φ_s are the initial internal friction angle, the friction angle of the plastic softening zone, and the residual internal friction angle of the coal body, respectively. c_e, c_p,c_s are the initial cohesion of the coal body, the cohesion, and residual cohesion in the plastic softening area, MPa. R_p is the radius of the plastic zone, m.

The drilled coal body is in the linear elastic state, p_y is set as the radial stress at the junction of the elastic zone of the coal body and the plastic softening zone, and the elastic zone of the coal body is regarded as a thick-walled cylinder under the joint action of p_y and ground stress p_0. It can be seen that the elastic zone stress is as follows:

$$\begin{cases} \sigma_{re} = p_y \dfrac{R_p^{\,2}}{r^2} + p_0\left(1 - \dfrac{R_p^{\,2}}{r^2}\right), \\ \sigma_{\theta e} = -p_y \dfrac{R_p^{\,2}}{r^2} + p_0\left(1 + \dfrac{R_p^{\,2}}{r^2}\right), \end{cases} \tag{4}$$

where σ_{re} is radial stress in the elastic zone, MPa. $\sigma_{\theta e}$ is the tangential stress of the elastic region, MPa. r is the distance from any point in the coal body to the center of the circle, m. p_0 is the ground stress, MPa. p_y is the stress at the elastoplastic junction, MPa.

At the elastoplastic junction $r = R_p$, formula (5) satisfies formula (1) and the radial stress is continuous, and the finishing can be obtained as follows:

$$p_y = \frac{2p_0 - B_e}{1 + A_e}. \tag{5}$$

Any of the study unit points in the coal body satisfy the equilibrium differential equation:

$$\frac{\mathrm{d}\sigma_r}{\mathrm{d}r} + \frac{\sigma_r - \sigma_\theta}{r} = 0. \tag{6}$$

Substituting equation (1) into equation (6) and integrating, take $\sigma_r | r = R_0 = p_i$ as the boundary condition, the radial and tangential stresses of the plastic region can be obtained as follows:

$$\begin{cases} \sigma_{rp} = S_1 + \left(p_i - S_1\right)\left(\dfrac{R_0}{r}\right)^{1-A_p}, \\ \sigma_{\theta p} = S_1 + A_p\left(p_i - S_1\right)\left(\dfrac{R_0}{r}\right)^{1-A_p}. \\ S_1 = \dfrac{B_p}{1 - A_p}. \end{cases} \tag{7}$$

The radial stress σ_r is continuous at the elastoplastic junction, which is $\sigma_{rp} | r = R_\mathrm{p} = \sigma_{re} | r = R_\mathrm{p}$.The radius of the plasticity zone of the first type (7) and the first type of (4) of the first type of plasticity zone is as follows:

$$R_p = R_0 \cdot \left[\frac{p_y - S_1}{p_i - S_1}\right]^{1/1-A_p}. \tag{8}$$

5. Numerical Simulation Analysis of Ultra-High Pressure Hydraulics Combined with Permeation PFC

Under the action of ultra-high pressure hydraulic force, when the coal body around the borehole exceeds its own strength, the hole wall is the plastic softening zone and the elastic zone from the inside to the outside. The drilling mechanical model is shown in Figure 3. The model assumes the following:

The particle flow discrete element method (PFC) is based on the mechanics of discontinuous media to study the germination, expansion, and penetration of fractures, which can truly express the geometric characteristics of jointed rock masses, facilitate the handling of nonlinear deformation and destruction, and reflect the different physical relationships between multiphase media through a variety of connection methods between cells, which can effectively study noncontinuous phenomena such as cracking and separation. There are countless mesoscopic cracks in coal rocks, especially soft coal bodies, showing obvious inelastic deformation characteristics, and these mesoscopic cracks develop into macroscopic cracks or until they break down under increased loads. In the particle flow discrete element, when the contact point node is destroyed, the corresponding particles will produce cracks, and new cracks will be generated at the initial crack tip as a sign of hydraulic fracturing. The nonlinear deformation failure process of the fracture can be analyzed by direct and indirect methods. The indirect method uses the constitutive relationship to analyze the failure process, generally assumes the fractured coal body as an ideal uniform material, reflects the weakening of the overall strength of the fractured coal body through a certain constitutive relationship, and expresses the microstructure failure process in the coal body in this way. The direct method is a mesoscopic simulation method, which assumes that the fracture coal material is a collection of various microstructures, or some particle combinations connected at the contact point. The failure process of the fractured coal body can be directly simulated by the microstructure and particle rupture, and the fractured coal body can be studied mescologically without simulation through complex constitutive models.

The PFC numerical calculation software is a kind of software based on particle flow theory, which links the microstructure of materials with macroscopic mechanical reactions, and directly simulates material failure from a mesoscopic perspective, which is suitable for materials that are difficult to accurately describe their properties through constitutive relationships based on uniform media, such as fractured rock masses. The bonding parameters of the particles determine the location and number of initial microcracks, so microcracks can only be formed in the connection contact model. The position and size of the two particles determine the location and geometry of the cracks, which can be simplified to a cylindrical surface represented by the center point position, normal direction, thickness, and radius parameters.

5.1. First Cut and Then Press Combined with Unloading Coal Seam Fracture and Stress Distribution. The model adopts a two-dimensional plane model. The direction length is 200 m, the height is 200 m, the drilling diameter is 113 mm, the cutting pressure is 100 MPa, the test site elevation is about 550 m, the vertical stress reaches 17.7 MPa, the pressure measurement coefficient is 1, and the horizontal stress is 17.7 MPa. The model schematic diagram is shown in Figure 4.

First, hydraulic cutting is used to form a slot, and a pressure of 25 MPa is applied to the periphery of the groove for fracturing, and the distribution of fracture, main stress, and permeability of the coal seam after fracturing is analyzed. The fissure distribution of coal seam in the process of drilling construction, hydraulic cutting, and hydraulic fracturing is shown in Figures 5–7, respectively, and the maximum main stress distribution curve on the midline of the test borehole level is monitored in the simulation.

Figure 5 shows the distribution of coal cracks after drilling construction. It can be seen from the figure that the fissures in the coal body around the drilling hole are not obvious after the construction of the borehole, and basically maintain the original state. The stress of the coal body around the borehole is evenly distributed and is basically in a state of stress equilibrium. Only the drilling is excavated, creating plastic deformation zones and elastic zones around the borehole, resulting in reduced seam stress. Figure 6 shows the distribution of coal cracks after drilling and cutting. It can be seen that after drilling and cutting, a circular gap is formed around the drilling hole, and the coal body around the gap groove is damaged or plastically deformed, forming a crack. The stress of the coal body around the trough is concentrated and transferred to the deep part of the coal body, and a stress-reduced pressure relief zone is formed around the slot area. Figure 7 shows the distribution of fractures in coal with a fracturing pressure of 25 MPa, as the water injection pressure increases, when the fissure expands to a certain extent. The expansion rate begins to slow down, and the secondary fissures are gradually interconnected to form a highly complex fracture network, but with the continuous development of the fissures in the coal seam, the degree of stress concentration is becoming more and more serious.

In the affected area of fracturing, the fractures are mainly elliptical in distribution. In terms of the degree of damage of the coal body, the coal body in the area near the fracturing hole is better than the coal body far from the fracturing hole area. From the change of water injection pressure during the fracturing process, it can be seen that the cracking pressure is about 13 MPa, and the radius of influence of hydraulic fracturing can reach 45–55 m.

After hydraulic fracturing of the coal seam, the original stress balance state of the coal seam is destroyed, resulting in a decrease in the stress value of the coal seam in the area near the fracturing hole, forming a pressure relief zone. However, the stress value of the coal seam around the pressure discharge zone increases, forming a stress concentration area. Therefore, according to the stress distribution of the coal seam after fracturing, the coal seam around the fracturing

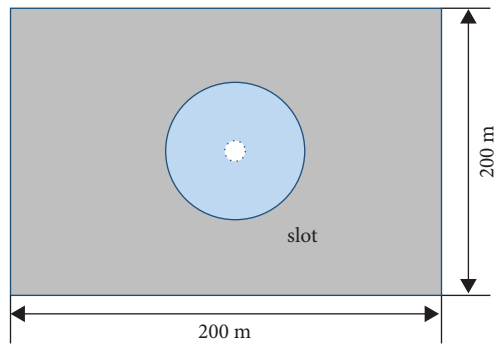

Figure 4: Joint numerical model of coal seam cutting pressure.

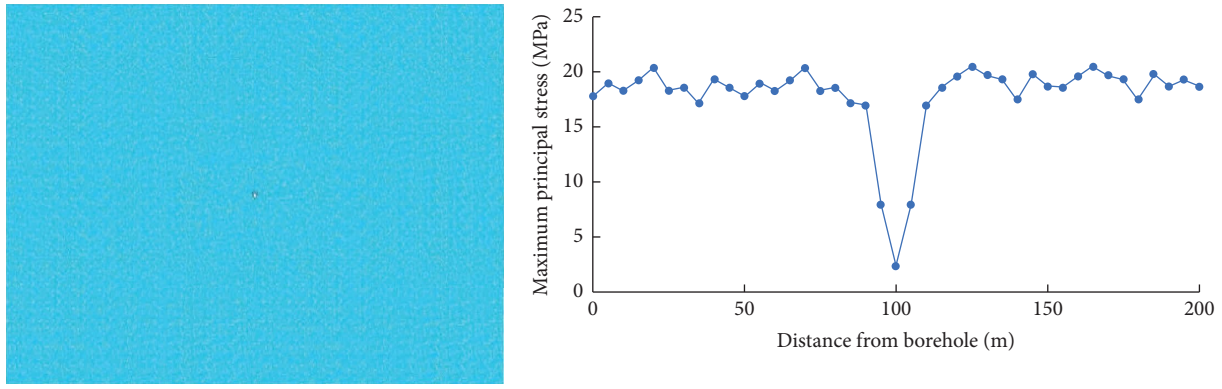

Figure 5: Fracture and stress distribution of coal seam after drilling. (a) Distribution of fractures. (b) Stress distribution condition.

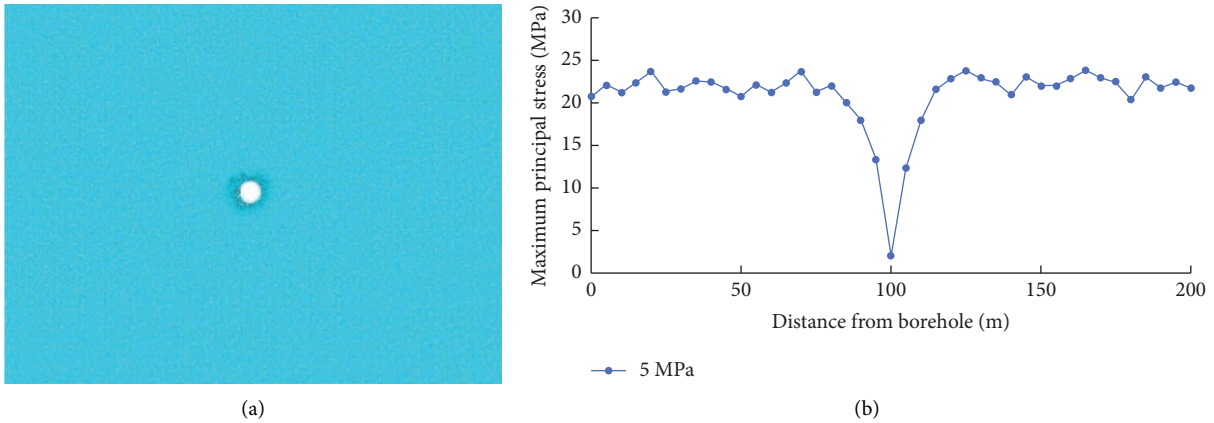

Figure 6: Fracture and stress distribution of borehole after slit. (a) Distribution of fractures. (b) Stress distribution condition.

hole can be divided into stress reduction zone (pressure relief area), stress concentration area, stress transition area, and original stress area from near and far.

5.2. First Press and Then Cut Combined with Unloading Coal Seam Fracture and Stress Distribution. The model adopts a two-dimensional plane model, the direction length is 200 m, the height is 200 m, and the drilling diameter is 113 mm, which is consistent with the model of Figure 4, as shown in Figure 8. The central fracturing hole is located in the center of the coal seam and is set to 113 mm in diameter. The test site elevation is about 550 m, the vertical stress reaches 17.7 MPa, the side pressure coefficient is 1, and the horizontal stress is 17.7 MPa. 25 MPa pressure is applied to the periphery of the borehole for fracturing, and after the completion of the fracturing, hydraulic fracture drilling is

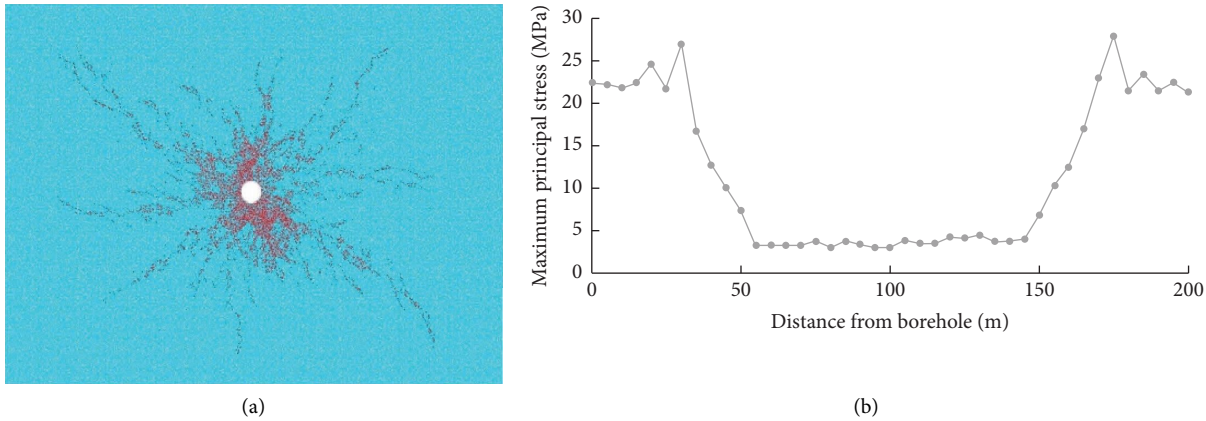

(a) (b)

Figure 7: Fracture and stress distribution when fracturing pressure is 25 MPa. (a) Distribution of fractures. (b) Stress distribution condition.

carried out in the blank area of the fracture according to the fracture and stress distribution. The distribution of fracture, main stress, and permeability of the coal seam after fracturing and cutting is analyzed.

Figures 9–11 are the fissure distribution of the coal seam and the maximum main stress distribution curve on the midline of the drilling level of the ordinary borehole hydraulic fracturing process, respectively.

Figure 9 shows the distribution of coal cracks after drilling construction. It can be seen from the figure that after the construction of the borehole, the fracture of the coal body around the borehole is not obvious and basically maintains the original state. The stress of the coal body around the borehole is evenly distributed and is basically in a state of stress equilibrium. Only due to the excavation of the drilled hole, the plastic deformation zone and the elastic zone are generated around the drilled hole, resulting in a reduction in the stress of the coal seam.

Figure 10 shows the fracture distribution of coal with a fracturing pressure of 25 MPa. As can be seen from the figure, when the fissure expands to a certain extent, the number of new fissures decreases, and there is a stress-concentrated area. In the affected area of fracturing, the distribution of fracture fractures is mainly in the direction of main stress, and the other regions have less fracture development and there are blank areas. The fracture development is uneven. After the use of hydraulic cuts, the number of cracks increases, and the stress concentration area caused by hydraulic fracturing is significantly relieved. From the change of water injection pressure during the fracturing process, it can be seen that the cracking pressure is about 16 MPa, and the influence radius of hydraulic fracturing can reach 35~45 m.

Figure 11 shows the fracture distribution and stress distribution after hydraulic fracture in the nonformation area of the coal seam after the fracturing pressure is 25 MPa. As can be seen from the figure, after the hydraulic fracture is carried out in the later stage, the fracture blank zone within the influence range of the original hydraulic fracturing generates a crack. The fracture that has been generated can be further increased. The stress concentration area is redistributed to play a role in depressurization.

Compared with the same model, there is a big difference between the cutting sequence of ultra-high pressure water jet and the fracture and horizontal direction of the discharge coal seam:

(1) The cracking pressure of the coal seam with the combined pressure of cutting first and then pressing is 13 MPa, and the radius of influence of hydraulic fracturing can reach 45–55 m. The cracking pressure of the coal seam of first pressure and then cutting and unloading coal seam is 16 MPa, and the radius of influence of hydraulic fracturing can reach 35–45 m.

(2) The first cut and then the combined pressure discharge coal seam destroys the original stress balance state of the coal seam, causing the stress value of the coal seam in the area near the fracturing hole to decrease, forming a pressure relief area. The stress distribution is more uniform, at a low value, forming a better pressure relief area, and the stress value of the coal seam around the pressure relief area is increased, forming a stress concentration area. In the area affected by fracturing, the distribution of fracture fractures is mainly along the direction of main stress. The fracture development in other areas is less, and there are blank areas. The development of fractures is uneven, after the use of hydraulic fractures, the number of fractures increases, and the stress concentration area caused by hydraulic fracturing is obvious. But there are pressure fluctuations and instability in the pressure relief area.

In summary, after the cutting pressure combination, the pressure relief of the coal body can be uniform and sufficient. The overall gas permeability coefficient of the coal body can be greatly improved. The scope of influence of extraction can be increased, and the extraction effect can be significantly improved. At the same time, the stress after the coal body is cut and the cracking pressure during hydraulic fracturing is reduced.

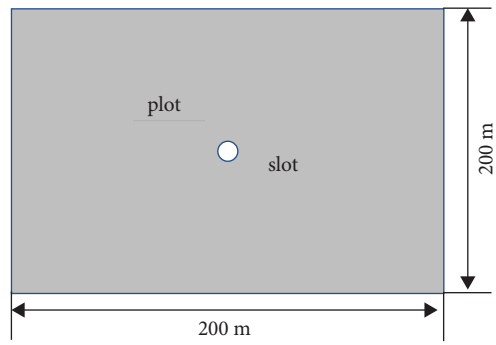

Figure 8: Numerical model for hydraulic fracturing of coal seam.

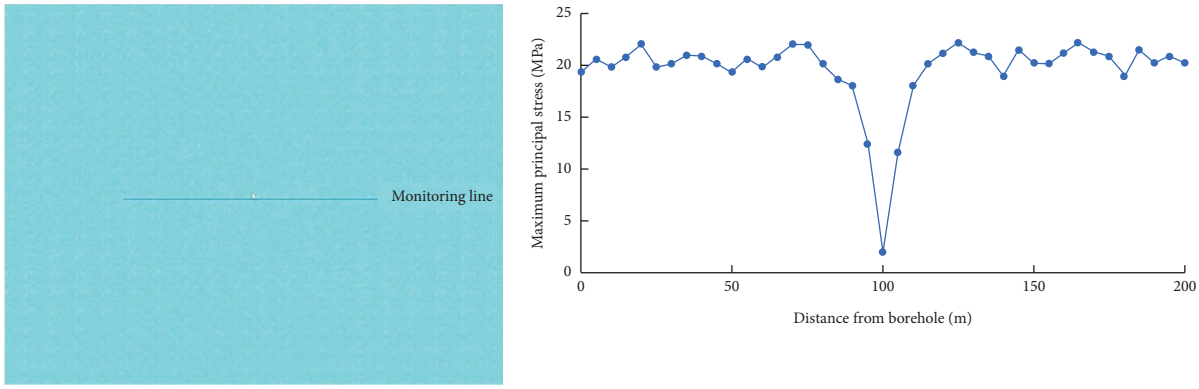

(a) (b)

Figure 9: Fracture and stress distribution of coal seam after drilling. (a) Distribution of fractures. (b) Stress distribution condition.

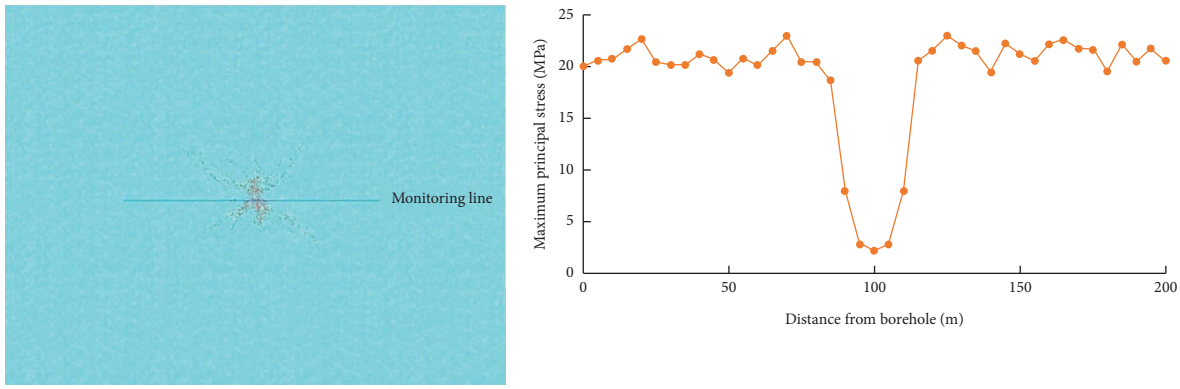

(a) (b)

Figure 10: Fracture and stress distribution of 25 MPa pressure fractured coal seam. (a) Distribution of fractures. (b) Stress distribution condition.

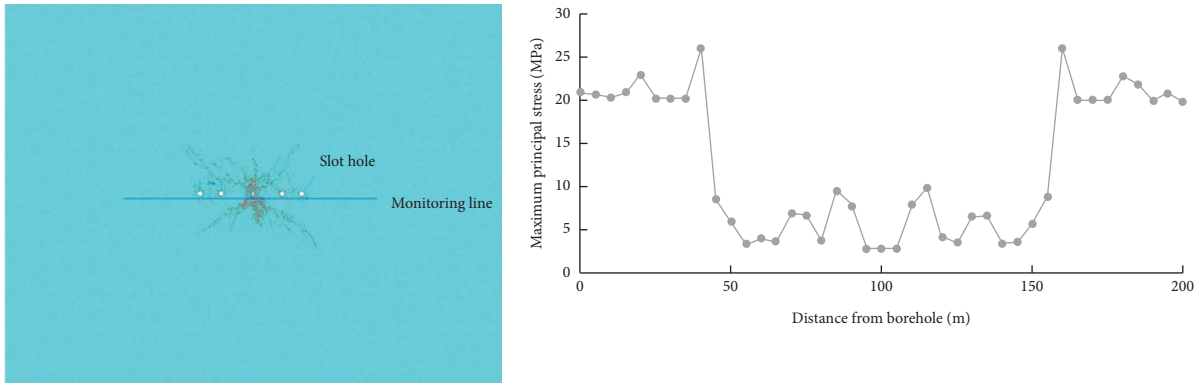

(a) (b)

Figure 11: Fracture and stress distribution of seam after hydraulic fracturing. (a) Distribution of fractures. (b) Stress distribution condition.

6. Engineering Application of Ultra-High Pressure Hydraulic Cutting Combined Process Technology

6.1. Application of Combined Pressure Relief and Antireflection after Cutting through Layer Drilling

6.1.1. Project Summary. 220106 working surface is located in the 2201 mining area, the maximum gas content of 1 coal seam is 6.8 m^3/t, and the gas pressure is 1.22 MPa. The first coal seam group includes 1 coal and 1 upper coal. The average upper coal is 3.9 m, the average upper coal is 2.8 m, and the average gangue lost between 1 coal and 1 upper coal is 1.0 m. The inclination angle of the coal seam is 2°–12°, and the average is 6°. The working surface is directly topped with sandy mudstone with an average thickness of 6.7 m, and the old top is quartz sandstone with an average thickness of 17.8 m. The application site elevation is about 523.0−−559.6 m, a total of 7 cut pressure combined drilling holes are constructed, and the floor plan is shown in Figure 12.

6.1.2. Application of Cutting Pressure Combined with Anti-reflection Technology

(1) Cut-Pressure Combined Drilling Implementation. The length of the seven cutting pressure combined drilling coal hole sections is 11–16 m. The maximum pressure during the cutting period is 90–100 MPa. The cutting gap is 3 m, and the single knife cutting time is 5–10 min. During the cutting operation, the drilling and rebating water and slag return is smooth. The coal output of a single knife is 0.34–0.56 t. The average single knife output is about 0.43 t, and the equivalent radius of the average cut is 2.54 m.

After the completion of drilling and cutting, the hole is sealed immediately. The hydraulic fracturing is carried out after 48 h. The maximum pressure of fracturing is 22–27 MPa. The number of fractures per drilling hole is 3 times. The fracturing time is 19–28 h, and the total amount of water injection per borehole is 109.6–132.4 m^3.

(2) Drilling Quantity Analysis. The spacing between the layout of the extraction drilling holes in the application area is 13 m × 13 m, and a total of 183 extraction drilling holes are constructed, with a drilling volume of about 11800 m. Compared with the conventional drilling arrangement of the mine (the layout spacing is 10 m × 10 m, and 297 extraction drilling holes need to be constructed, about 19200 m), the drilling volume can be saved by about 38%.

(3) Pumping Volume Analysis, Pumping Pure Volume. The concentration and extraction scalculus of the drilling hole in the application area are shown in Figures 13 and 14.

It can be seen from the figure that the extraction concentration in the combined cutting pressure area is 10% to 40%. The concentration fluctuation is relatively stable. The attenuation is small. The extraction purity is 5.12–10.13 m^3/min, and the average single-hole extraction purity is 0.0245 m^3/min, which is 2.3 times that of the ordinary drilling single-hole extraction purity of 0.0108 m^3/min.

(4) Extraction Standard Time. According to the drilling and extraction situation in the application area, when the extraction drilling hole extraction is 47 days, the extraction rate reaches 30%. A total of 14 residual gas content were tested, and the test result was 3.98–4.75 m^3/t. The extraction standard was achieved. The extraction time is 41% lower than the 80 days of ordinary drilling and extraction.

6.2. Application of Combined Pressure Relief and Anti-Reflection Improvement through Layer Drilling

6.2.1. Project Summary. The application site of the drilling is 220106, the working surface is located in the outer section of the 2201 mining area (the strike length is about 170 m, and the strike width is about 190 m), a total of 3 fracturing

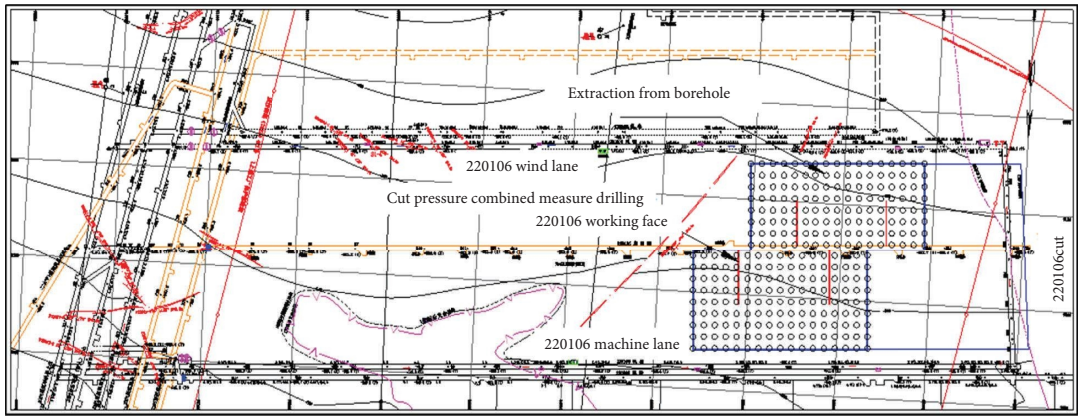

Figure 12: Cut pressure combined measures plan.

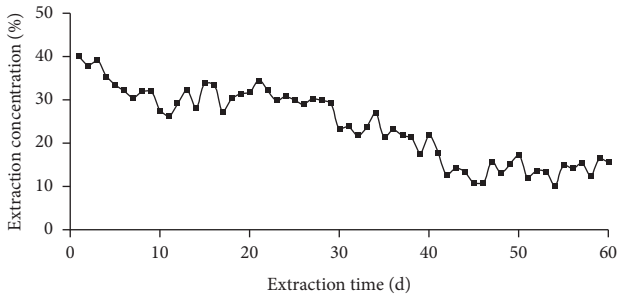

Figure 13: Change curve of extraction concentration.

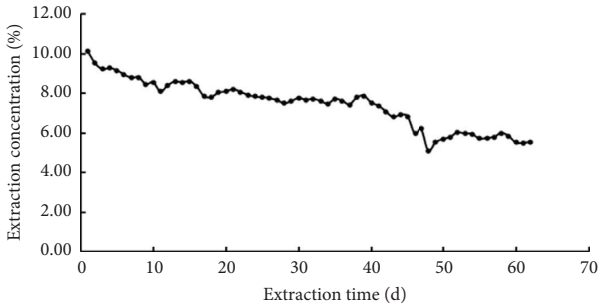

Figure 14: The net volume change curve of extraction.

drilling holes are constructed, and the spacing is cut according to the 26 m × 26 m spacing, and the floor plan is shown in Figure 15.

6.2.2. Application of Compression Cutting Combined with Antireflection Technology

(1) Cut-Pressure Combined Drilling Implementation. The maximum pressure of fracturing is 22–27 MPa, and the number of fracturing times for each borehole is 3 times. The fracturing time is 21–32 h, and the total water injection of each borehole is 117.8–145.2 m^3.

After the completion of fracturing, the drilling hole is drilled according to the construction of 13 m × 13 m spacing in the control area, and the hydraulic cutting measures are constructed according to the 20 m × 20 m spacing. The maximum pressure during the cutting period is 90–100 MPa. The cutout spacing is 3 m, and the single knife cutting time is 5–10 min. A total of 91 cut holes were implemented, and the drilling reflow water and slag return was smooth during the seam operation. The coal output of a single knife was 0.31–0.62 t. The average single knife coal output was about 0.41 *t*, and the equivalent radius of the average cut was 2.52 m.

(2) Drilling Quantity Analysis. The spacing between the layout of the extraction drilling holes in the application area is 13 m × 13 m, and a total of 183 extraction drilling holes are constructed, with a drilling volume of about 11800 m. Compared with the conventional drilling arrangement of the mine (the layout spacing is 10 m × 10 m, and 297 extraction drilling holes need to be constructed, about 19200 m), the drilling volume can be saved by about 38%.

(3) Pumping Volume Analysis, Pumping Pure Volume. The concentration and extraction scalarity of drilling in the application area are shown in Figures 16 and 17. It can be seen from the figure that the extraction concentration in the combined cutting pressure area is 30% to 40%. The concentration fluctuation is relatively stable. The attenuation is small. The extraction purity is 3.6–6.8 m^3/min, and the average single-hole extraction purity is 0.026 m^3/min, which is 2.4 times that of the ordinary drilling single-hole extraction purity of 0.0108 m^3/min.

(4) Extraction Standard Time. According to the drilling and extraction situation in the application area, when the extraction drilling hole extraction is 43 d, the extraction rate reaches 30%. A total of 5 residual gas content were tested, and the test result was 3.76–4.52 m^3/t, and the extraction standard was achieved. The extraction time is 35% less than the ordinary drilling and extraction time of 66 d.

6.3. Economic Benefits

6.3.1. Direct Economic Benefit Analysis. After the 220106 working surface adopts the measures of cutting pressure

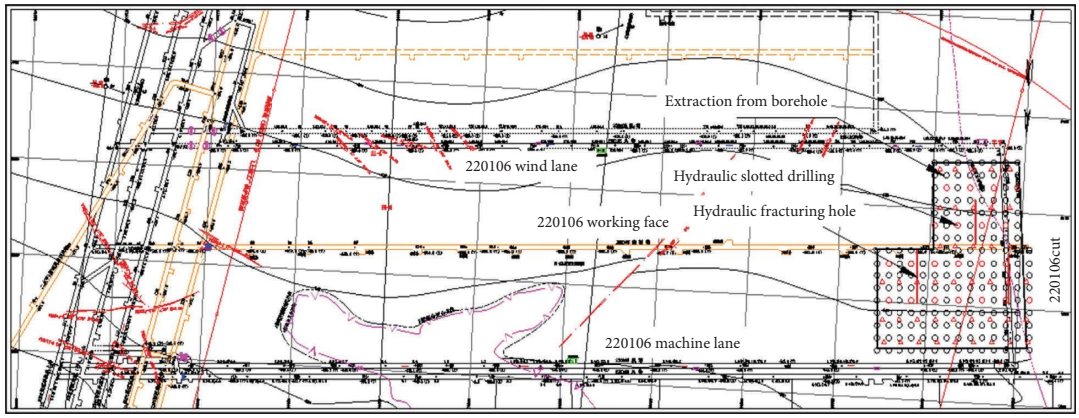

Figure 15: Pressure before cutting combined measures floor plan.

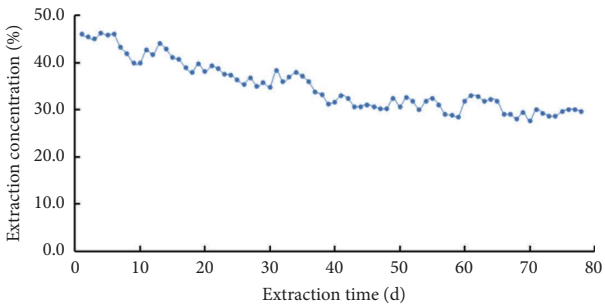

Figure 16: Change curve of extraction concentration.

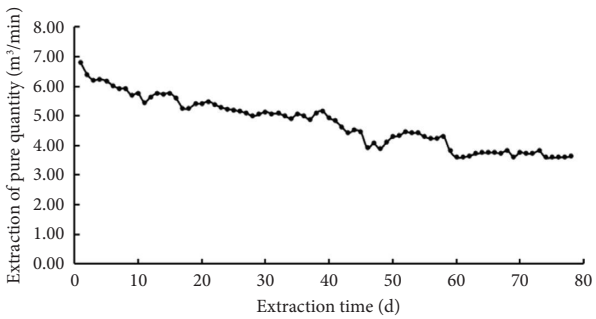

Figure 17: The net volume change curve of extraction.

combined pressure relief and removal. The amount of drilling engineering by 34000 m and the amount of drilling by 10000 m is reduced by 10000 m. It can reduce the maintenance of 33 d of drilling holes in the 220106 working surface (length 860 m) and 36 d of maintenance of the bottom plate lane (900 m long) extraction drilling, calculated at 30 yuan/m·d.

Save engineering costs: (34000 + 10000) m × 300 yuan/m = 13.2 million yuan

Saving maintenance investment: 860 m × 2 × 30 yuan/m·d × 33 d + 900 m × 30 yuan/m·d × 36 d = 2.6748 million yuan

In summary, a total of 15.8748 million yuan of direct economic benefits have been generated.

6.3.2. Indirect Economic Benefit Analysis. 220106 working surface drilling and extraction time are shortened by 33 and 25 d. The working surface is returned to the production in advance, and the early recovery of the working surface produces indirect economic benefits:

$$25 \times 6000\ \text{t/d} \times 600\ \text{yuan/t} = 90\ \text{million yuan}$$

Xinji No.2 mine generated a total of 90 million yuan in indirect economic benefits.

7. Conclusions

(1) The coal seam initiation pressure of ultra-high pressure water jet cutting pressure combined with pressure relief is 13 MPa, and the influence radius of hydraulic fracturing is 45–55 m. The initiation pressure of coal seam is 16 MPa, and the influence radius of hydraulic fracturing is 35–45 m. The combined technology of cutting pressure can make the pressure relief of coal body uniform and sufficient, the overall permeability coefficient of coal body is greatly improved, the influence area of extraction is enlarged, and the extraction effect is significantly improved. At the same time, the stress after the coal seam cutting is reduced, and the fracturing pressure during hydraulic fracturing is reduced.

(2) After hydraulic slit, the initiation pressure of coal seam decreases, and the influence radius of hydraulic fracturing increases, with an influence range of 46–56 m. The permeability within the influence area increases by 25 to 30 times. The permeability coefficient of coal seam is 0.775 m^2/MPa^2·d after the process of cutting pressure combined with pressure relief and permeability improvement, which is 23 times of the original coal body. The gas permeability of coal seam is increased significantly by hydraulic cutting first and then fracturing.

(3) The extraction concentration in the combined area of drilling and cutting pressure is 10%–40%, and the concentration fluctuation is relatively stable and the attenuation is small. The extraction purity is

5.12–10.13 m^3/min, and the average single hole extraction purity is 0.0245 m^3/min, which is 2.3 times of the single hole extraction purity of ordinary drilling. The time to reach the standard of extraction is 32.8 d shorter than that of ordinary drilling. The extraction concentration in the combined area of borehole and pressure cutting is 30%–40%, the concentration fluctuation is relatively stable and the attenuation is small. The extraction pure volume is 3.6–6.8 m^3/min, and the average single hole extraction pure volume is 0.026 m^3/min, which is 2.4 times of the single hole extraction pure volume is 0.0108 m^3/min of ordinary drilling. The time to reach the standard of extraction is 25 d shorter than that of ordinary drilling.

(4) The pressure cutting combined with pressure relief and antireflection technology has been successfully applied in Xinji coal mine, and has created good economic benefits. This technology has a wide application prospect.

Data Availability

The data presented in this study are available upon request from the corresponding author.

Conflicts of Interest

The authors declare that they have no conflicts of interest.

Acknowledgments

This work was supported by the Open Project of Building Structure and Underground Engineering Key Laboratory of Anhui Province (grant no. KLBSUE-2022-03).

References

[1] D. Y. Hao, Q. S. Bai, W. L. Li, and Z. Q. Yang, "Mining technology of "mining, dressing and filling + pumping" with less gangue in deep high gas mine protection layer," *Journal of Mining & Safety Engineering*, vol. 37, no. 1, pp. 93–100, 2020.

[2] W. P. Xiang, P. H. Zhang, Z. C. Li et al., "Discussion on abnormal geological characteristics and development technology of deep coalbed methane," *Coal Engineering*, vol. 54, no. 6, pp. 158–164, 2022.

[3] Y. P. Cheng, H. Y. Liu, P. K. Guo, R. K. Pan, and L. Wang, "Permeability evolution and unloading antireflection theoretical model of deep gas-bearing coal body," *Journal of China Coal Society*, vol. 39, no. 8, pp. 1650–1658, 2014.

[4] Y. Ding, Y. Wei, Z. C. Wang, L. Qin, P. X. Zhao, and H. F. Lin, "Numerical simulation and application of hydraulic slit relief and reflection improvement in coal seam drilling through layers," *Mining Research and Development*, vol. 42, no. 8, pp. 182–188, 2022.

[5] F. F. Liu, Y. Y. Huang, Q. Xu et al., "Effect of high pressure water jet slotting on pressure relief and reflection improvement of coal seam," *Safety In Coal Mines*, vol. 45, no. 9, pp. 165–168, 2014.

[6] Y. Liu, A. He, M. J. Wei, and H. Z. Wen, "Inducement and new method of water jet pressure relief and permeability improvement for hole plugging," *Journal of China Coal Society*, vol. 41, no. 8, pp. 1963–1967, 2016.

[7] H. Li, M. B. Shi, and Y. Li, "Research on anti-outburst technology of strong outburst and soft close distance coal seam Group in Shimen," *Journal of Safety Science and Technology*, vol. 10, no. 1, pp. 98–102, 2014.

[8] Z. X. Xu, "Combined anti-reflection technology of ultra-high pressure hydraulic slit and hydraulic fracturing in low permeability coal seam," *Coal Science and Technology*, vol. 48, no. 7, pp. 311–317, 2020.

[9] K. S. Zhao, J. Y. Li, T. H. Chai et al., "Optimization of pre-slit inclination Angle and anti-punching practice in directional hydraulic fracturing of thick and hard sandstone roof in Shaan-Mongolia area," *Journal of China Coal Society*, vol. 45, no. S1, pp. 150–160, 2020.

[10] L. W. Cao, J. Nian, and B. X. Lv, "Study on comprehensive anti-reflection technology of hydraulic slit (fracturing)," *Coal Technology*, vol. 36, no. 7, pp. 199–201, 2017.

[11] K. Zhong, Z. W. Chen, S. W. Zhao, K. C. Qin, X. H. Cao, and D. H. Xie, "Monitoring and evaluation of anti-flood effect of hydraulic fracturing of hard roof in coal mine," *Journal of Central South University*, vol. 53, no. 7, pp. 2582–2593, 2022.

[12] H. X. Shi, P. L. Zhao, T. J. Li, J. R. Wang, and F. C. Wu, "Anti-reflection technology of hydraulic fracturing for low permeability and high gas coal seam in complex structural belt," *Mining Safety & Environmental Protection*, vol. 49, no. 3, pp. 101–106, 2022.

[13] G. Q. Li, Z. Y. Deng, T. Q. Hu et al., "Mesoscopic law of hydraulic fracturing stress and fracture evolution in coal seam," *Coal Geology & Exploration*, vol. 50, no. 6, pp. 30–40, 2022.

[14] J. Y. Zhang, F. Z. Huang, and F. Ji, "Coal, rock and gas dynamic disaster prevention and control technology based on hydraulic slit pressure relief," *Coal Science and Technology*, vol. 49, no. 1, pp. 133–141, 2021.

[15] Z. S. Li and J. Z. Lu, "Application of ultra-high pressure hydraulic slotting technology in bedding drilling to strengthen gas extraction," *Coal Technology*, vol. 39, no. 2, pp. 121–124, 2020.

[16] X. B. Feng, M. C. Huang, and J. L. Zhang, "Application of high pressure hydraulic slit technology in coal seam gas drainage through floor," *Coal Engineering*, vol. 6, pp. 35–37, 2010.

[17] L. Z. Ge, D. X. Mei, J. Y. Jia, Y. Y. Lu, and W. B. Xia, "Study on the influence radius of high pressure water jet slotting drilling," *Journal of Mining & Safety Engineering*, vol. 31, no. 4, pp. 657–664, 2014.

[18] H. X. Li, Y. Y. Lu, Y. Zhao, Y. Kang, and P. D. Zhou, "Study on improving permeability of soft coal seam by high pressure pulse water jet," *Journal of China Coal Society*, vol. 33, no. 12, pp. 1386–1390, 2008.

[19] P. J. Tang, L. S. Yang, and P. L. Li, "Numerical simulation of the effect of different hydraulic slit arrangement on pressure relief and outburst prevention," *Chinese Journal of Geological Hazard and Control*, vol. 23, no. 1, pp. 61–66, 2012.

[20] Z. J. Jia, Q. J. Ge, H. W. Zhen, and D. Zhao, "Study on anti-reflection technology and application of hydraulic fracturing," *China Safety Science Journal*, vol. 30, no. 10, pp. 63–68, 2020.

[21] D. D. Chen, Q. S. Sun, J. Zhang, Z. J. Zhao, G. K. Zheng, and Y. B. Jia, "Anti-reflection technology system and engineering practice of directional long borehole hydraulic fracturing coal seam," *Coal Science and Technology*, vol. 48, no. 10, pp. 84–89, 2020.

[22] B. Q. Mou, "Enhanced anti-reflection technology of hydraulic fracturing of long borehole through borehole," *Journal of Safety Science and Technology*, vol. 13, no. 8, pp. 164–169, 2017.
[23] M. K. Hubbert and D. G. Willis, "Mechanics of hydraulic fracturing," *Transactions of the AIME*, vol. 210, no. 1, pp. 153–168, 1957.
[24] K. Y. Ma, G. Z. Liu, and J. Zhou, "Experimental study on the correlation between fracture wall failure behavior and water injection flow rate," *Journal of Safety Science and Technology*, vol. 12, no. 6, pp. 82–87, 2016.
[25] C. Y. Lv, "Application of hydraulic fracturing technology in mine with high gas and low permeability," *Journal of Chongqing University*, vol. 33, no. 7, pp. 102–107, 2010.
[26] M. J. Bouteca, "Hydraulic fracturing model based on a three-dimensional closed form: tests and analysis of fracture geometry and containment," *SPE Production Engineering*, vol. 3, no. 4, pp. 445–454, 1988.
[27] L. Z. Lian, J. Zhang, A. H. Wu, X. X. Wang, and B. Xue, "Fluid-structure coupling numerical simulation of hydraulic fracturing expansion," *Rock and Soil Mechanics*, vol. 11, no. 3, pp. 3021–3026, 2008.
[28] L. Bjerrum, J. K. T. L. Nash, R. M. Kennard, and R. E. Gibson, "Hydraulic fracturing in field permeability testing," *Géotechnique*, vol. 22, no. 2, pp. 319–332, 1972.
[29] D. Chen, N. Li, and W. C. Sun, "Rupture properties and safety assessment of raw coal specimen rupture process under true triaxial hydraulic fracturing based on the source parameters and magnitude," *Process Safety and Environmental Protection*, vol. 158, pp. 661–673, 2022.
[30] Z. G. Deng, B. S. Wang, and X. B. Huang, "Study on hydraulic fracture propagation behavior of coal rock," *Chinese Journal of Rock Mechanics and Engineering*, vol. 20, no. 3, pp. 3489–3493, 2004.
[31] S. M. Liu, X. L. Li, D. K. Wang, and D. M. Zhang, "Investigations on the mechanism of the microstructural evolution of different coal ranks under liquid nitrogen cold soaking," *Energy Sources*, pp. 1–17, 2020.
[32] X. M. Zhou, S. Wang, X. L. Li et al., "Research on theory and technology of floor heave control in semicoal rock roadway: taking longhu coal mine in Qitaihe mining area as an Example," *Lithosphere*, vol. 2022, no. 11, Article ID 3810988, 2022.
[33] S. Wang, X. L. Li, and Q. Z. Qin, "Study on surrounding rock control and support stability of Ultra-large height mining face," *Energies*, vol. 15, no. 18, 2022.
[34] X. L. Li, S. J. Chen, S. Wang, M. Zhao, and H. Liu, "Study on in situ stress distribution law of the deep mine taking Linyi Mining area as an example," *Advances in Materials Science and Engineering*, vol. 2021, no. 4, Article ID 5594181, 11 pages, 2021.
[35] H. Y. Liu, B. Y. Zhang, X. L. Li et al., "Research on roof damage mechanism and control technology of gob-side entry retaining under close distance gob," *Engineering Failure Analysis*, vol. 138, no. 5, Article ID 106331, 2022.
[36] S. Tang, J. Li, S. Ding, and L. Zhang, "The influence of water-stress loading sequences on the creep behavior of granite," *Bulletin of Engineering Geology and the Environment*, vol. 81, no. 11, 2022.
[37] X. Liang, S. Tang, C. Tang, L. Hu, and F. Chen, "Influence of water on the mechanical properties and failure behaviors of sandstone under triaxial compression," *Rock Mechanics and Rock Engineering*, vol. 56, 2023.
[38] Q. Yin, J. Wu, Z. Jiang et al., "Investigating the effect of water quenching cycles on mechanical behaviors for granites after conventional triaxial compression," *Geomechanics and Geophysics for Geo-Energy and Geo-Resources*, vol. 8, no. 2, 2022.
[39] Y. Wang, C. Zhu, M. He, X. Wang, and H. Le, "Macro-meso dynamic fracture behaviors of Xinjiang marble exposed to freeze thaw and frequent impact disturbance loads: a lab-scale testing," *Geomechanics and Geophysics for Geo-Energy and Geo-Resources*, vol. 8, no. 5, 2022.
[40] Q. Wang, B. Jiang, S. Xu et al., "Roof-cutting and energy-absorbing method for dynamic disaster control in deep coal mine," *International Journal of Rock Mechanics and Mining Sciences*, vol. 158, Article ID 105186, 2022.
[41] Q. Wang, S. Xu, Z. Xin, M. He, H. Wei, and B. Jiang, "Mechanical properties and field application of constant resistance energy-absorbing anchor cable," *Tunnelling and Underground Space Technology*, vol. 125, Article ID 104526, 2022.
[42] F. Xiong, H. Sun, Z. Ye, and Q. Zhang, "Heat extraction analysis for nonlinear heat flow in fractured geothermal reservoirs," *Computers and Geotechnics*, vol. 144, Article ID 104641, 2022.
[43] F. Xiong, H. Sun, Q. Zhang, Y. Wang, and Q. Jiang, "Preferential flow in three-dimensional stochastic fracture networks: the effect of topological structure," *Engineering Geology*, vol. 309, Article ID 106856, 2022.
[44] F. Miao, Y. Wu, Á. Török, L. Li, and Y. Xue, "Centrifugal model test on a riverine landslide in the Three Gorges Reservoir induced by rainfall and water level fluctuation," *Geoscience Frontiers*, vol. 13, no. 3, Article ID 101378, 2022.
[45] F. Miao, Y. Wu, Y. Xie, and Y. Li, "Prediction of landslide displacement with step-like behavior based on multialgorithm optimization and a support vector regression model," *Landslides*, vol. 15, no. 3, pp. 475–488, 2018.
[46] D. Song, Z. Chen, Y. Ke, and W. Nie, "Seismic response analysis of a bedding rock slope based on the time-frequency joint analysis method: a case study from the middle reach of the Jinsha River, China," *Engineering Geology*, vol. 274, Article ID 105731, 2020.
[47] Z. Chen, D. Song, C. Hu, and Y. Ke, "The September 16, 2017, Linjiabang landslide in Wanyuan County, China: preliminary investigation and emergency mitigation," *Landslides*, vol. 17, no. 1, pp. 191–204, 2020.
[48] F. Xiong, C. Zhu, G. Feng, J. Zheng, and H. Sun, "A three-dimensional coupled thermo-hydro model for geothermal development in discrete fracture networks of hot dry rock reservoirs," *Gondwana Research*, 2022.
[49] X. Cheng, Q. Zhang, Z. Zhang, Y. Zou, and G. Junjie, "Stress relief and stimulation of coal reservoir by hydraulic slotting," *Advances in Civil Engineering*, vol. 2021, Article ID 6664696, 13 pages, 2021.
[50] J. Zou, X. Hu, Y. Y. Jiao et al., "Dynamic mechanical behaviors of rock's joints quantified by repeated impact loading experiments with digital imagery," *Rock Mechanics and Rock Engineering*, vol. 55, no. 11, pp. 7035–7048, 2022.
[51] Z. C. Tang, Z. L. Wu, and J. Zou, "Appraisal of the number of asperity peaks, their radii and heights for three-dimensional rock fracture," *International Journal of Rock Mechanics and Mining Sciences*, vol. 153, Article ID 105080, 2022.

Hindawi
Advances in Civil Engineering
Volume 2023, Article ID 6962648, 14 pages
https://doi.org/10.1155/2023/6962648

Research Article

Effect of Eccentricity on Breakout Propagation around Noncircular Boreholes

Mohammad Bahrehdar and Ali Lakirouhani

Department of Civil Engineering, Faculty of Engineering, University of Zanjan, Zanjan, Iran

Correspondence should be addressed to Ali Lakirouhani; rou001@znu.ac.ir

Received 15 September 2022; Revised 12 October 2022; Accepted 13 October 2022; Published 28 February 2023

Academic Editor: Zhuo Chen

Investigating the shear failure caused by the concentration of compressive stress around noncircular boreholes is important both in the field and in the laboratory. This article deals with the numerical analysis of elliptical boreholes under a nonisotropic in situ stress field using the Mogi–Coulomb nonlinear failure criterion. The purpose of the presented numerical model is to simulate the progressive shear failure (breakout) around the borehole and investigate the impact of the eccentricity of the borehole on the stability and depth and width of the failure area. According to the obtained results, the breakout is V-shaped and is formed along the minimum principal stress. As the eccentricity of the borehole increases, the final dimension of the breakout becomes smaller; in other words, the increase in ellipticity strengthens the borehole against shear failure. However, as the eccentricity increases, the stress concentration at the breakout tip increases. Another finding of the study conducted in this article is the significant relationship between the width and the depth of the breakout failure, which makes the idea of estimating both horizontal in situ stresses using breakout dimensions seriously doubtful. Also, the interesting result obtained is that the stress concentration factor at the breakout tip for boreholes with different eccentricities is the same at the end of the breakout.

1. Introduction

Often 10–20% of the total drilling cost is related to borehole instability, this causes a loss of about 500 to 1000 million dollars in the oil industry worldwide. Therefore, maintaining well stability is one of the main concerns of drilling engineers in the oil and gas industry [1–4]. One of the instabilities of the borehole is related to the shear instability of the rock in the borehole wall, which is known as the borehole breakout.

When the shear stress of the material reaches its shear strength in the borehole wall, the rock is crushed and falls into the borehole. The main driver of this type of failure is the concentration of compressive stress that occurs due to the drilling of the borehole. This phenomenon was first observed and reported by Cox [5] in Alberta wells and later confirmed by Babcock [6]. As the degree of in situ stress anisotropy increases, the intensity of stress concentration increases, and as a result, the failure zone becomes wider and deeper [7–14].

Breakout is formed symmetrically on both sides of the borehole along the minor principal in situ stress where the compressive stress is most concentrated. For this reason, in the last two decades, breakout has been used as an indicator to determine the direction and magnitude of in situ stresses [15–17]. Also, several laboratory studies conducted on predrilled rock samples show that the size of the borehole (hole radii) has a significant effect on the breakout initiation stress [9, 18–21].

In addition to physical models and laboratory studies on borehole breakouts, various theoretical and numerical models have also been conducted to investigate breakouts. Although the first theoretical models presented for the breakout had simple assumptions, the episodic progression of the breakout was not investigated in them [7, 22], but in the following, more complete numerical models based on the finite element method and the discrete element method were presented, which are able to predict the breakout in a proper way [23–32].

Setiawan and Zimmerman [33] presented a semi-analytical method to investigate breakout progression and stabilization using the conformal mapping procedure, and the analysis carried out by them led to a correlation between the breakout geometry, the properties of the rock materials, and the in situ stresses.

Zhang et al. [34] investigated borehole breakout using a finite element model based on the Mogi–Coulomb failure criterion, and the results of their analysis showed that the inverse analysis using the finite element model and neural network can effectively determine the in situ stresses.

Li et al. [35] presented a hydromechanical finite element model for sand production and erosion and observed that sand production is mainly controlled by the plastic strain magnitude and flow velocity in the vicinity of the borehole.

Ma et al. [36] presented a finite element numerical simulation method based on elastic damage mechanics for progressive sand production in inhomogeneous formations, and the results obtained by them showed that the sand production area is controlled by the rock formation heterogeneity and the expansive failure process.

In addition to various studies conducted on circular boreholes, several studies have also been conducted on noncircular and elliptical boreholes. By investigating the tangential stresses around the elliptical boreholes, Aadnoy and Angell-Olsen [37] observed that the fracture initiation pressure in the elliptical borehole is different from the circular borehole, but as long as the ratio of in situ stresses is not greater than ellipticity, the position of fracture in the elliptical and circular borehole is the same, and in their study, ellipticity is the ratio of the small diameter of the ellipse to its larger diameter.

Aadnoy and Kaarstad [38] presented an elliptic geometry model to investigate sand production, and they observed that the anisotropy of the in situ stresses is a critical factor for the elliptic shape of the borehole.

Using the ellipsoidal solution of stresses acting on the borehole wall and the Mohr–Coulomb failure criterion, Aadnoy et al. [39] found that the ellipsoidal geometry presents the collapsed borehole shape better than the circular Kirsch's analytical solution.

Using an inverse analysis, Han et al. [40] estimated the horizontal in situ stresses around the elliptical borehole using data from the leak-off test, and their studies showed that even a 2% difference in the axis of the elliptical borehole causes a 5% to 10% difference in the estimation of horizontal in situ stresses. Papamichos et al. [41] investigated hollow cylinders with different geometries experimentally and numerically, and their studies showed that holes with elliptical breakouts are more stable; in other words, the stability of the hole increases as the breakout depth increases.

What has not been addressed so far is the investigation of the impact of the eccentricity of the borehole on the stability of the borehole as well as its strength to shear failure. The purpose of this article is to present a model based on the finite element numerical method to investigate the episodic progression of breakouts around noncircular boreholes and specifically boreholes with an elliptical cross section. The presented model is two-dimensional and assumes plane strain conditions, and by it, the effect of anisotropic in situ stresses and borehole eccentricity on the final dimensions of the breakout is investigated.

2. Problem Definition

There are various reasons that boreholes with noncircular cross sections may also be formed. Possible causes include the mechanical action of the drill string on the well after drilling or the horizontal cross section of the deviated boreholes becomes an ellipse.

An elliptical cavity with major axis a and minor axis b is considered in a linear elastic medium under plane strain conditions (Figure 1). σ_H is the maximum horizontal principal stress, σ_h is the minimum horizontal principal stress, and σ_v is the vertical stress along the axis of the borehole so that $\sigma_h < \sigma_v < \sigma_H$. It is often assumed that the major axis of the ellipse is along the minor principal stress (σ_h) and its minor axis is along the major principal stress (σ_H). This assumption is suitable for examining holes that have previously had shear failure and are again subjected to a new stress condition.

In these conditions, local stresses including tangential stress $(\sigma_{\theta\theta})$, radial stress (σ_{rr}), vertical stress (σ_{zz}), and shear stress $(\tau_{r\theta})$ are obtained for the points around the borehole, and it is observed that the highest concentration of compressive stress occurs in the wall of the borehole at point A because this point has the minimum radius of curvature. However, in the vicinity of point A, the concentration of compressive stress may also occur in other points and they may suffer shear failure (breakout) as a result. To find all the failure points, it is necessary to first calculate the principal stresses based on the local stresses, and then by choosing an appropriate shear failure criterion, the points that have failed can be found.

The failed points are removed from the borehole wall, and a new cross section is obtained. The stresses are redistributed around the borehole, which causes other points to reach shear failure. Again, the points that have suffered shear failure are removed and the new stresses in the environment are calculated. In this way, step by step, the breakout proceeds so that no point will fail again.

As shown in Figure 1, in breakout, the rock is separated from the borehole wall in spalls; although from a micromechanical point of view, the failure mechanism may be a combination of shear failure and tension failure.

In all breakout stages, to calculate the stresses of the environment, the environment must first be divided into fine elements, and then, using the appropriate numerical method, the stresses in the center of each element should be calculated. However, only in the wall of the borehole before the initiation of the breakout can the stresses be obtained using the analytical method that is given in the next section.

After completing the numerical analysis, the V-shaped (dog-eared) breakout is observed on both sides of the borehole symmetrically along the minimum principal stress.

The maximum breakout width (θ_d) is the same width that is obtained in the first step of failure, and the final depth of the breakout (r_d) is obtained after the last step at the end of the analysis. It can be seen in Figure 1 that (r_d) is measured from the center of the borehole.

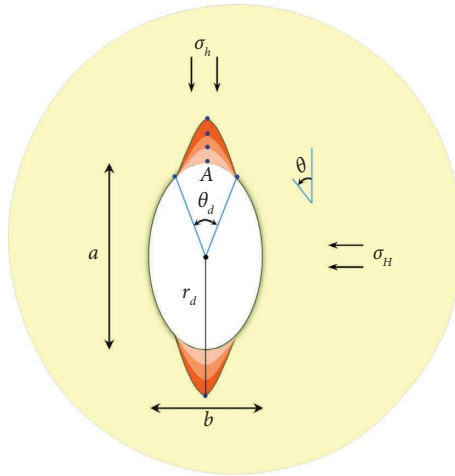

Figure 1: Elliptical borehole and shear failure around it.

2.1. Analytical Stress Distribution around the Elliptical Borehole. In this section, the stress distribution around the elliptical holes is presented [42]:

$$\begin{aligned}
\sigma_{rr} &= \frac{\sigma_H}{J^2}(e_o - e)\left\{(1+K)\left(e^2-1\right)\frac{C}{2e_o} + (1-K)\left[\left[\frac{J}{2}(e-e_o) + C\,e\right]\cos 2(\theta+\omega) - C\cos 2\omega\right]\right\},\\
\sigma_{\theta\theta} &= \frac{\sigma_H}{J}\left\{(1+K)\left(e^2-1\right) + 2(1-K)e_o\left[e\cos 2(\theta+\omega) - \cos 2\omega\right]\right\} - \sigma_{rr},\\
\tau_{r\theta} &= \frac{\sigma_H}{J^2}(e_o - e)\left\{(1+K)\frac{C\,e}{e_o}\sin 2\theta + (1-K)\left[e\left(e_o+e\right)\sin 2\omega + e\sin 2(\theta-\omega) - \left[\frac{J}{2}(e_o+e) + e^2 e_o\right]\sin 2(\theta+\omega)\right]\right\},\\
\sigma_{zz} &= \sigma_h - \upsilon\left(\sigma_H + \sigma_v\right) + \upsilon\left(\sigma_{rr} + \sigma_{\theta\theta}\right),
\end{aligned} \tag{1}$$

where

$$\begin{aligned}
e_o &= \frac{a+b}{a-b},\\
e &= u + \frac{e_o}{|e_o|}\left(u^2-1\right)^{1/2},\\
u &= b_o + \frac{e_o}{|e_o|}\left(b_o^2 - d\right)^{1/2},\\
b_o &= 4\frac{x_1^2 + y_1^2}{a^2 - b^2},\\
d &= 8\frac{x_1^2 - y_1^2}{a^2 - b^2} - 1,\\
\theta &= \tan^{-1}\left(\frac{y_1}{x_1}\times\frac{e+1}{e-1}\right),\\
C &= 1 - e\,e_o,\\
J &= 1 + e^2 - 2\,e\cos(2\theta),\\
K &= \frac{\sigma_h}{\sigma_H}.
\end{aligned} \tag{2}$$

θ and ω are also shown in Figure 2.

2.2. Numerical Model for the Episodic Breakout. A two-dimensional plane strain model is used to analyse the progressive breakout phenomenon. The presented model is solved numerically using the finite element numerical method.

The finite element method, sometimes called finite element analysis, is a computational technique used to obtain approximate solutions of boundary value problems. Boundary value problems are also sometimes referred to as field problems. The field is the domain of interest and often represents a physical structure. The field variables are the dependent variables of interest that are governed by the differential equation. Boundary conditions are the specified values of field variables at field boundaries. The finite element method is a numerical technique for solving a system of equations governing the domain of a continuous physical system, which is discretized into simple geometric forms called finite elements. Modeling a body is conducted by dividing it into an equivalent system of finite elements that are connected at a finite number of points on each element called nodes. There are fundamental unknowns in engineering problems, and if they are found, the behavior of the entire system is predictable. The basic unknowns or field

variables encountered in engineering problems are displacements. In a continuum body, these unknowns are infinite. The finite element method reduces such unknowns to a finite number by dividing the solution area into small parts called elements and by expressing the unknown field variables in terms of hypothetical approximate functions (interpolation functions/shape functions) in each element. Approximate functions are defined in terms of field variables of specified points called nodal points. Thus, in the finite element method, the unknowns are the field variables of the nodes. Once these are found, the field variables at each node can be found using the interpolation functions. After selecting elements, the next step in the finite element method is to collect element properties for each element; in other words, the stiffness characteristics of each element must be found. Mathematically, this relationship is as follows [43]:

$$[k^e] = h^e \iint [B^e]^T [D^e] [B^e] \mathrm{d}x\, \mathrm{d}y, \tag{3}$$

where $[k^e]$ is the element stiffness matrix, $[B^e]$ is the gradient matrix, and h^e is the element thickness. $[D^e]$ implies the elastic stiffness matrix which in plane strain conditions is given by

$$[D^e] = \frac{E(1-v)}{(1+v)(1-2v)} \begin{bmatrix} 1 & \frac{v}{1-v} & 0 \\ \frac{v}{1-v} & 1 & 0 \\ 0 & 0 & \frac{1-2v}{2(1-v)} \end{bmatrix}, \tag{4}$$

where E and v are the modulus of elasticity and Poisson's ratio, respectively.

Derivation of the element stiffness matrix is based on equilibrium conditions. The same procedure can be applied by writing the equilibrium equation for each node for all connected elements in the model. This process is described as "assembly" because the system equations are obtained by taking the individual stiffness components and putting them together; therefore, the main relation is written as follows:

$$[K]\{U\} = \{F\}, \tag{5}$$

where $[K]$ is the global stiffness matrix, $\{U\}$ is the nodal displacement vector, and $\{F\}$ is the nodal force vector.

The criterion of shear failure used in this article is the nonlinear Mogi–Coulomb criterion, in which the effect of the intermediate principal stress is also present in the failure function [44]:

$$\tau_{oct} = a' + b' \sigma_{m,2}. \tag{6}$$

In this equation,

$$\begin{aligned} \sigma_{m,2} &= \frac{\sigma_1 + \sigma_3}{2}, \\ \tau_{oct} &= \frac{1}{3}\sqrt{(\sigma_1 - \sigma_2)^2 + (\sigma_2 - \sigma_3)^2 + (\sigma_3 - \sigma_1)^2}, \end{aligned} \tag{7}$$

where σ_1, σ_2, and σ_3 are the maximum, intermediate, and minimum principal stresses, respectively, and

$$\begin{aligned} a' &= \frac{2\sqrt{2}}{3} \frac{\sigma_c}{q+1}, \\ b' &= \frac{2\sqrt{2}}{3} \frac{q-1}{q+1}, \\ q &= \frac{1+\sin\phi}{1-\sin\phi}, \\ \sigma_c &= \frac{2c\cos\phi}{1-\sin\phi}, \end{aligned} \tag{8}$$

where σ_c is the uniaxial compressive strength of the rock material. The failure function for the Mogi–Coulomb failure criterion is defined as follows [45]:

$$F_{MG} = \tau_{oct} - a' - b' \sigma_{m,2} = 0. \tag{9}$$

Figure 3 shows the Mogi–Coulomb failure criterion in the principal stress space.

2.3. Algorithm, Problem Domain, Boundary Conditions, and Meshing. To simulate the episodic breakout around the elliptical borehole, a computer program was coded based on the governing equations and failure criteria presented in the previous section.

Coding is conducted in MATLAB software. To increase the accuracy of the simulation, every element that fails is removed from the borehole wall by 0.1 of its length. In this way, the number of numerical analysis iterations increases until the breakout reaches stability but the breakout geometry is obtained with proper accuracy. The problem domain, boundary conditions, and meshing shown in Figure 4 are considered, in which only a quarter of the model is analyzed due to symmetry.

The dimensions of the model are 40 cm × 40 cm, and a fine mesh has been used around the borehole. The number of 4-node quadrilateral elements for the model is equal to 2560. According to Figure 4, the bottom mesh boundary is restricted for vertical displacement while it is left free for horizontal displacement. Also, the right vertical boundary is free to move vertically while its horizontal movement is restricted. The maximum horizontal principal stress is applied to the right vertical boundary, and the minimum horizontal principal stress is applied to the upper horizontal boundary. For the numerical solution of the problem shown in Figure 4 and the specifications given previously, the following simple algorithm is presented:

(1) First, based on the finite element method formulation, local stresses are calculated for each element

(2) Then, the principal stresses are calculated according to the local stresses

(3) Using the principal stresses, the failure function is calculated for each element according to the selected failure criteria

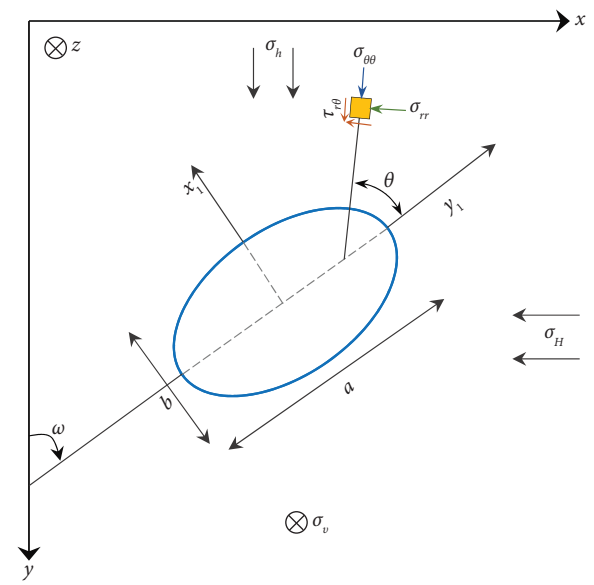

Figure 2: Elliptical borehole, global and local axes, and in situ stresses.

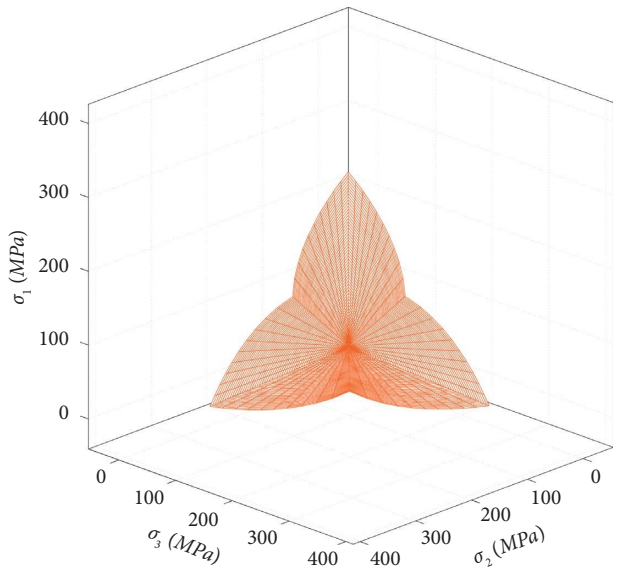

Figure 3: Mogi–Coulomb failure criterion in the principal stress space.

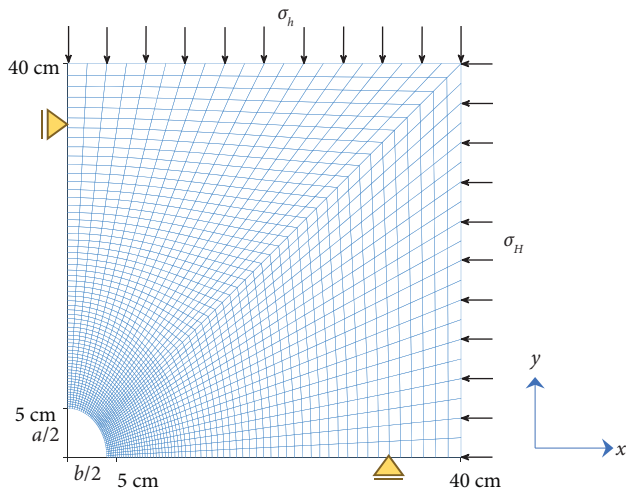

Figure 4: Problem domain, meshing, and boundary conditions.

(4) If the failure function for a certain element is greater than one ($F_{MG} \rangle 1$), that element is removed from the model geometry and the rest of the elements remain

(5) For the new geometry, steps 1 to 4 are repeated until the failure function for all elements becomes smaller than one and the breakout reaches stability

3. Validation

3.1. Stress around the Borehole and Comparison of the Numerical Method with Analytical Solution. To validate the presented numerical method, the stresses around the borehole have been obtained using the numerical method as well as the analytical relations presented in the section "Analytical stress distribution around elliptical borehole." The comparison of the stresses is shown in Figures 5–8. Stresses are presented for three different eccentricities, and the eccentricity of an ellipse is equal to

$$m = \sqrt{1 - \left(\frac{b^2}{a^2}\right)}, \quad (a > b), \tag{10}$$

where according to Figure 1, a and b are the major and minor axes of the ellipse, respectively.

m is between zero and one $(0 \leq m < 1)$, such that the circular borehole has zero eccentricity. In this article, to create boreholes with different eccentricities, the major axis of the ellipse is assumed to be fixed $(a = 5\,cm)$ and its minor axis is changed (Figure 1).

Figure 5 shows the tangential stress in the borehole wall for different values of eccentricity, and as can be seen in the figure, there is a good agreement between the stresses obtained from the numerical model and the stresses obtained from the analytical relations.

It should be noted that in Figures 5–8, the values of the field stresses are as follows:

$$\begin{cases} \sigma_h = 20\ MPa, \\ \sigma_v = 25\ MPa, \\ \sigma_H = 50\ MPa. \end{cases} \tag{11}$$

Figure 5 also shows that the maximum tangential stress or the highest compressive stress concentration occurs for $\theta = 0^0$ and $\theta = 180^0$, that is, along the minor principal stress; therefore, these two points will be the starting points of the breakout. It can also be seen that with the increase of eccentricity, the concentration of compressive stress also increases. The lowest tangential stress also occurs at $\theta = 90^0$ and $\theta = 270^0$, and with the increase of eccentricity, the tangential stress decreases at these points. In Figure 6, similar results have been obtained for vertical stress. Figures 6 and 7 also show the stresses for $\theta = 0^0$, and along the minor principal stress for 0 and 0.6 eccentricity, respectively, there is a good agreement between the numerical model and the analytical relationships, and by moving away from the center of the hole, the stresses converge to the field stresses.

3.2. Failure Shape and Comparison of the Numerical Method with Other Models. Ma et al. [36] presented a numerical simulation method for sand production in inhomogeneous formations, in which the effects of heterogeneity, progressive fracture process, and borehole pressure were investigated. Zhang et al. [34] also used the machine learning method to invert the relationship between in situ stresses and borehole breakout shape. Figure 9 shows the comparison between the depth and the width of the breakout failure zone obtained from the numerical model presented in this article with the model provided by Zhang et al. [34] and Ma et al. [36] for circular borehole $(m = 0)$. The analysis of this section has been performed for the mechanical and geometrical specifications presented in Table 1. According to Figure 9, the failure width is formed in the first iteration and does not increase in subsequent iterations. The half width of failure $(\theta_d/2)$ obtained from the numerical model presented in this article is 31°, and the half widths of failure obtained from Zhang et al.'s model and Ma et al.'s model are 32.5° and 32°, respectively, which can be seen that there is a relatively good agreement between the models.

However, in all three models, the depth of failure (r_d) increases with increasing iterations until a stable state is established. The evolution of r_d is linear in the model presented in this article, but it is nonlinear in other models. This is because in the numerical model in this article, to increase the accuracy of the results with the failure of each element as much as one tenth of the element length, the borehole wall is removed, but in other models, the failed element is completely removed from the model. r_d obtained from the numerical method presented in this article is 26.80 mm and r_d obtained from Zhang et al.'s model and Ma et al.'s model is 22.4 mm and 20.75 mm, respectively. The difference between the values obtained from different models can be due to the different failure criteria used in each of the models. The failure criterion used in this article is the Mogi–Coulomb criterion, while the failure criteria used in Zhang et al.'s model and Ma et al.'s model are the Mohr–Coulomb criterion and the Drucker–Prager criterion, respectively.

4. Results and Discussion

In this section, the results of the numerical analysis performed using the program written in MATLAB software are given. The properties selected in the analysis for the rock materials are those provided for Tablerock sandstone. The Tablerock sandstone belongs to the Cloverdale Nursery area in the United States and belongs to a group of sandstone layers in the Upper Miocene, the Lower Idaho Group; this sandstone consists of 55% quartz and 37% feldspar. Due to the high percentage of feldspar, this sandstone is classified as arkosic. For this type of rock material, the internal friction angle and cohesion are, respectively, equal to $\phi = 39.7^0$ and $c = 10.38\ MPa$ [13].

For the borehole with different eccentricities, breakout progression steps were obtained using the presented model and some of these stages are shown in Figure 10. The cross section shown in the last column is the final breakout shape after reaching stability. The values of in situ stresses in this analysis are equal to $\sigma_h = 20\,MPa, \sigma_v = 25\,Mpa, \sigma_H = 50\,Mpa$.

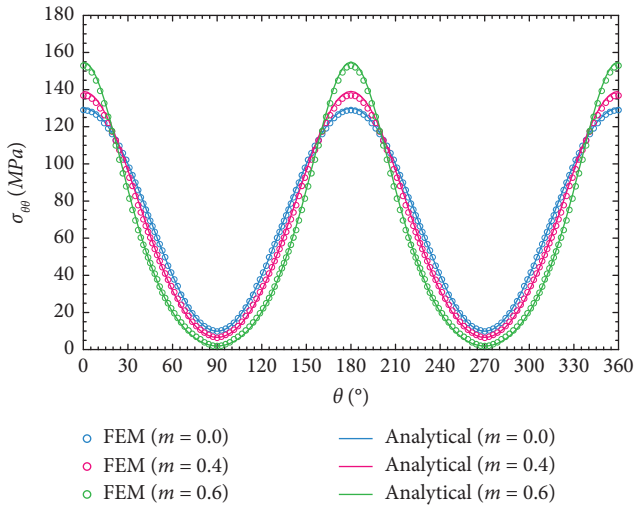

Figure 5: Tangential stress in the borehole wall for different values of m.

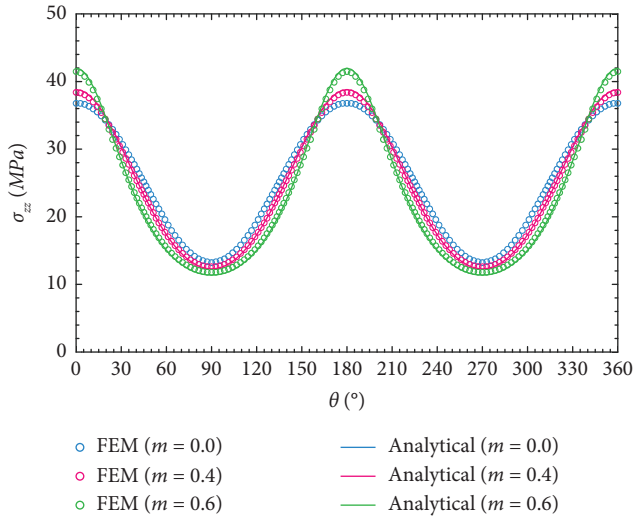

Figure 6: Vertical stress in the borehole wall for different values of m.

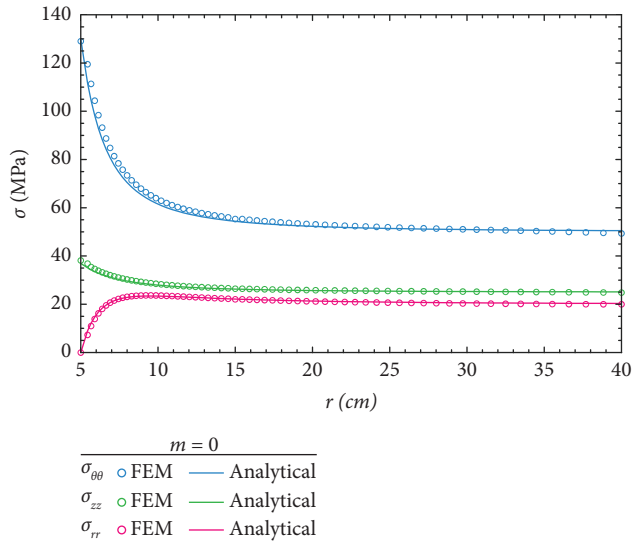

Figure 7: The stresses along the minimum in situ stress ($\theta = 0^0$).

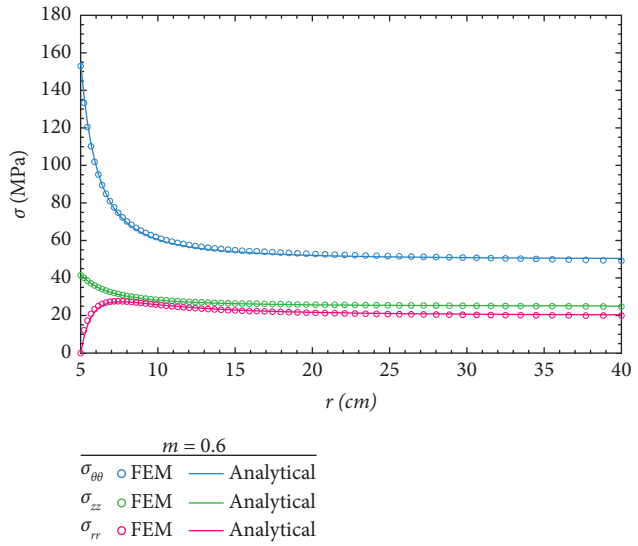

Figure 8: The stresses along the minimum in situ stress ($\theta = 0^0$).

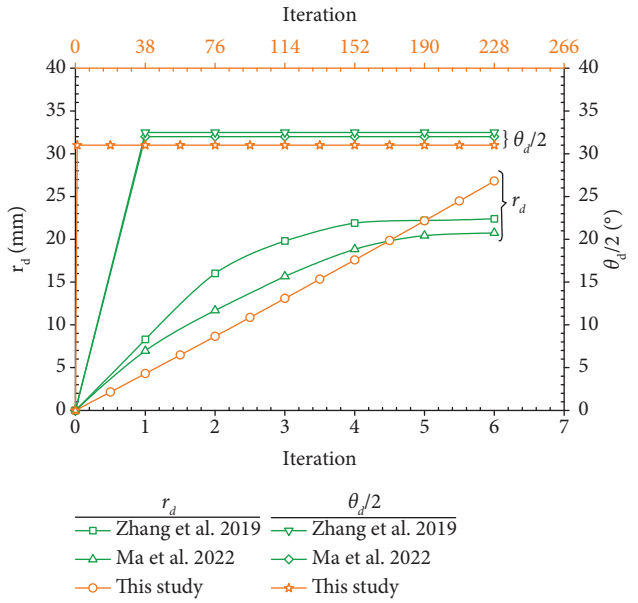

Figure 9: Depth and width of failure in different iterations and comparison of the numerical method in this study with other models.

Table 1: Geometric and mechanical parameters [34, 36].

Parameters	Value	Unit
Young's modulus	14.4	*GPa*
Poisson's ratio	0.2	—
Cohesion	20	*MPa*
Internal friction angle	40	(°)
Borehole pressure	20	*MPa*
Maximum horizontal in situ stress	100	*MPa*
Minimum horizontal in situ stress	60	*MPa*
Borehole radius	0.15	*m*

In the figure, it can be seen that for the borehole with zero eccentricity, the breakout reaches stability after 383 iterations, and as the eccentricity increases, the number of breakout progress iterations decreases. For example, for the borehole with an eccentricity of 0.8, the number of iterations is reduced to 223. It can be seen that the final shape of the breakout is V-shaped, and its formation and propagation occurred along the minor principal stress, and also, with the

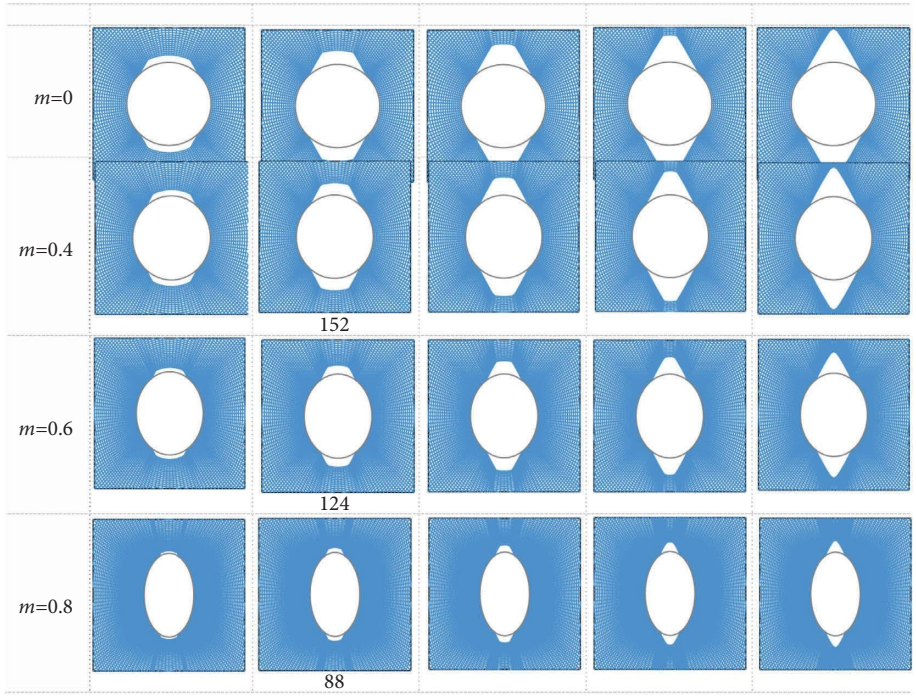

Figure 10: Episodic breakout progression for holes with different eccentricities; the last column shows the final shape of the breakout.

increase in the eccentricity of the borehole, the final dimensions of the breakout became smaller.

Figure 11 shows the increase in the depth (r_d) and width (θ_d) of the breakout failure area as the breakout progressed to stability. As can be seen in the figure, the failure width is formed in the first iteration and does not increase in subsequent iterations, but the depth of failure increases linearly until the breakout reaches stability.

Figure 12 shows the final normalized breakout depth $(r_d/(a/2))$ versus eccentricity, and Figure 13 shows the breakout failure width (θ_d) versus eccentricity. In Figure 12, the breakout depth is normalized to the semimajor axis of the ellipse. It can be seen in the two figures that the dimensions of the breakout become smaller as the eccentricity increases. The general result is that although the stress concentration at the two vertices of the ellipse along the minimum principal stress increases with the increase of borehole eccentricity, the final dimension of the breakout becomes smaller. In other words, increasing the ovality strengthens the borehole against shear failure.

Another influencing parameter on the dimensions of the breakout is the ratio of in situ stresses. Numerous numerical analyses were performed with different in situ stress ratios and eccentricities, and their results are shown in Figures 14–16. In Figures 14 and 15, it can be seen that with the increase in the ratio of in situ stresses, the normalized breakout depth and the breakout width increase, respectively. Also, for a certain in situ stress ratio, the depth and width of failure decrease with the increase of eccentricity. Figures 14 and 15 can also be used to determine the final dimensions of the breakout after increasing the ratio of in situ stresses to another given ratio. This application is of particular importance in breakout laboratory studies.

Figure 16 is obtained from the combination of Figures 14 and 15. Figure 16 shows a significant relationship between the final breakout failure depth and the breakout failure width for a given eccentricity. The meaningful relationship between the depth and the width of breakout failure in geomechanics is important because if the horizontal in situ stresses are to be determined based on the dimensions of the breakout, only one of them can be determined. In other words, the minimum principal stress can be obtained from the hydraulic fracturing test [46, 47], and the maximum horizontal principal stress can be determined based on the dimensions of the breakout.

The stress concentration factor (SCF) is the ratio of the tangential stress at the breakout tip to the maximum in situ stress, which is as follows:

$$SCF = \frac{\sigma_{\theta\theta,(A)}}{\sigma_H}, \tag{12}$$

where $\sigma_{\theta\theta,(A)}$ is the tangential stress at point A at the breakout tip (Figure 1). Point A also moves as the breakout progresses.

Figure 17 shows the evolution of the stress concentration factor (SCF) versus the breakout depth for three different eccentricities. The highest concentration of compressive stress occurs in the borehole wall and at the tip of the breakout, which is the cause of shear failure progression.

The remarkable point that can be concluded from Figure 17 is that, before the breakout failure and at the beginning of the analysis, the greater the eccentricity, the greater the stress concentration factor, but with the progress of breakout failure and at the end of the analysis, it can be seen that the stress concentration factor for boreholes with different eccentricities has become the

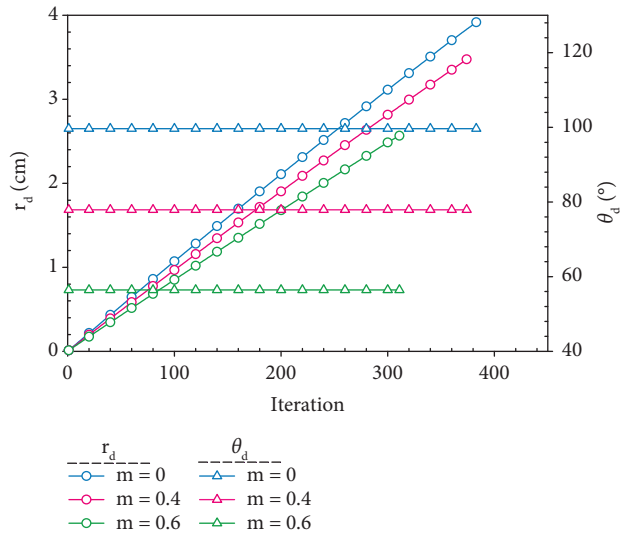

Figure 11: The evolution of the breakout depth and width, from breakout initiation to stability.

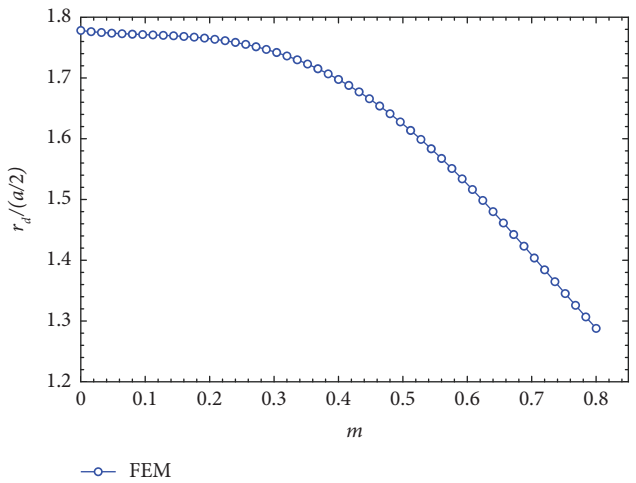

Figure 12: Breakout failure normalized depth versus eccentricity.

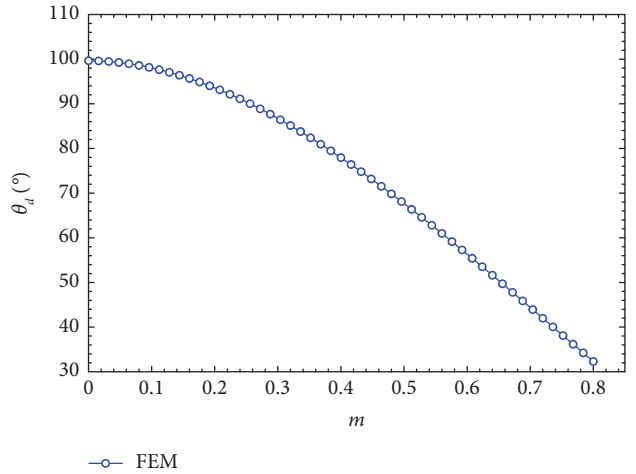

Figure 13: Breakout failure width versus eccentricity.

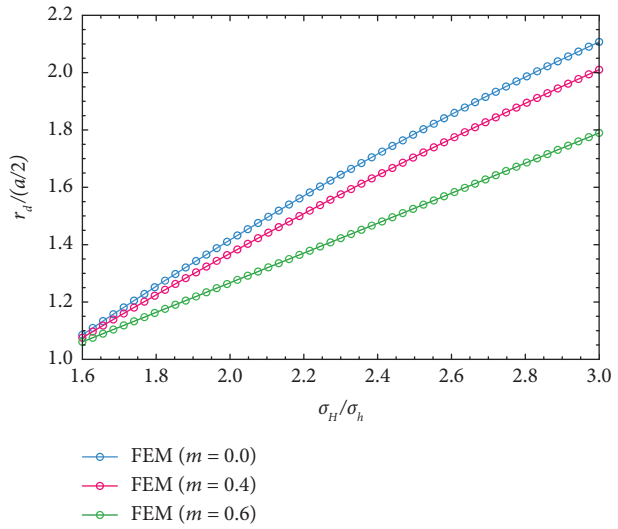

Figure 14: Final normalized breakout depth versus in situ stress ratio for different eccentricities.

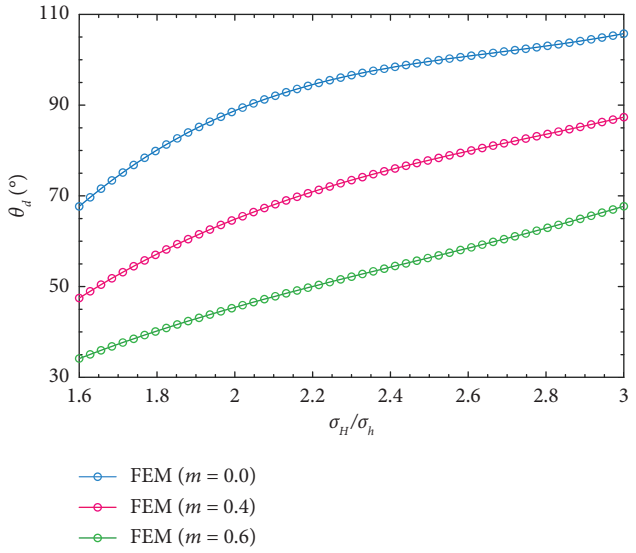

Figure 15: Final breakout width versus in situ stress ratio for different eccentricities.

same with a relatively small difference. This is due to the fact that in the studied problem, the tangential stress in the borehole wall is the only principal stress in the Mogi–Coulomb failure criterion, and the breakout failure progresses to the point where the tangential stress can no longer satisfy the failure criterion. Therefore, the stress concentration factor at the breakout tip, which is dependent on the tangential stress, at the end of the breakout, is the same for the boreholes with any eccentricity, even though the breakout depth is different.

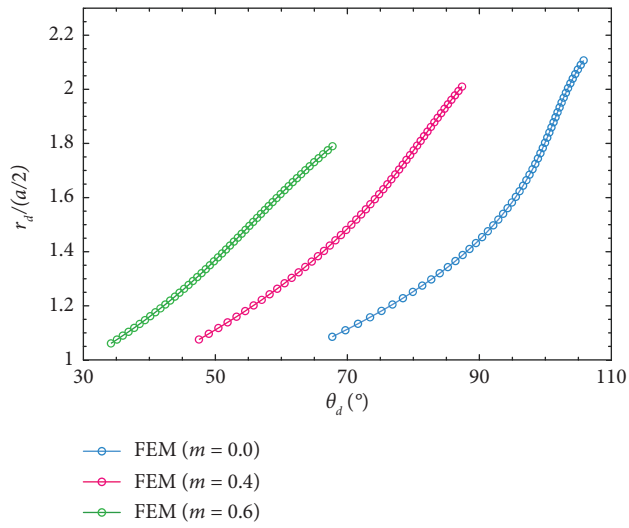

Figure 16: Final normalized breakout depth versus breakout width.

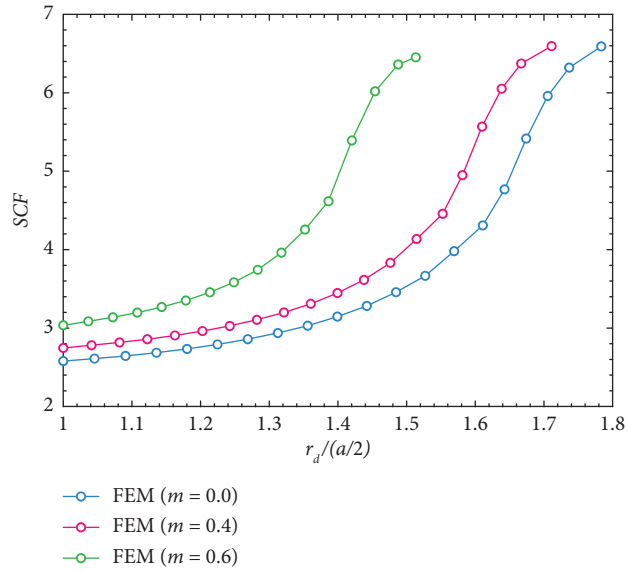

Figure 17: Evolution of the stress concentration factor at the breakout tip with the progression of the breakout.

5. Conclusion

The work performed in this article was the numerical analysis of the progressive failure around noncircular boreholes. This problem, which has an unconventional shape, was investigated in the field of nonisotropic stresses and using a nonlinear failure criterion. For these reasons, solving the problem had to be performed numerically. In addition to the abovementioned, the progress of failure occurs episodically, which means that at each step, the geometry of the problem changes and meshing must be conducted again. To solve this problem, a simple algorithm based on the finite element method is presented. Using the algorithm, a computer program is coded in MATLAB software.

To investigate the effect of the borehole eccentricity parameter on the breakout, boreholes with different eccentricities are analyzed, and it was observed that with the increase of eccentricity, the depth and width of the V-shaped breakout failure area decrease, but the stress concentration factor at the breakout tip becomes the same for all models. Also, the rate of decrease in the breakout depth and width with increasing eccentricity is low until $m = 0.3$ and then increases. In other words, eccentricity strengthens the borehole against shear failure.

With the increase of the ratio of in situ stresses, the depth and width of the breakout increase and the rate of increase of the failure depth is higher for the borehole with smaller eccentricity. Also, according to the obtained results, it was observed that the depth and width of the breakout have a significant relationship with each other. Therefore, by using breakout dimensions, only one of the in situ stresses can be obtained; for example, the maximum horizontal stress (σ_H) can be obtained using breakout dimensions, and the minimum horizontal stress (σ_h) can be obtained using the hydraulic fracturing test.

Data Availability

The data that support the findings of this study are available from the corresponding author upon reasonable request.

Conflicts of Interest

The authors declare that they have no conflicts of interest.

References

[1] F. J. Santarelli, M. E. Chenevert, and S. O. Osisanya, "On the stability of shales and its consequences in terms of swelling and wellbore stability," in *Proceedings of the IADC/SPE Drilling Conference*, New Orleans, LA, USA, Feburary 1992.

[2] G. Chen, M. E. Chenevert, M. M. Sharma, and M. Yu, "A study of wellbore stability in shales including poroelastic, chemical, and thermal effects," *Journal of Petroleum Science and Engineering*, vol. 38, no. 3-4, pp. 167–176, 2003.

[3] J. Lang, S. Li, and J. Zhang, "Wellbore stability modeling and real-time surveillance for deepwater drilling to weak bedding planes and depleted reservoirs," in *Proceedings of the SPE/IADC Drilling Conference and Exhibition*, Amsterdam, The Netherlands, March 2011.

[4] S. Chen, *Analytical and Numerical Analyses of Wellbore Drilled in Elastoplastic Porous Formations*, University of Oklahoma, Norman, OK, USA, 2012.

[5] J. W. Cox, "The high resolution dipmeter reveals dip-related borehole and formation characteristics," *Journal of Canadian Petroleum Technology*, vol. 11, no. 01, 1972.

[6] E. A. Babcock, "Measurement of subsurface fractures from dipmeter logs," *AAPG Bulletin*, vol. 62, no. 7, pp. 1111–1126, 1978.

[7] M. D. Zoback, D. Moos, L. Mastin, and R. N. Anderson, "Wellbore breakouts and in situ stress," *Journal of Geophysical Research: Solid Earth*, vol. 90, no. B7, pp. 5523–5530, 1985.

[8] B. C. Haimson and C. G. Herrick, "Borehole breakouts-a new tool for estimating *in situ* stress?" in *Proceedings of the International. Symposium On Rock Stress and Rock Stress Measurements*, pp. 271–280, Stockholm, Sweden, August 1986.

[9] B. C. Haimson and C. G. Herrick, "Borehole breakouts and in situ stress," in *Proceedings of Drilling Symposium 1989, 12th Annual Energy-Sources Technical Conference and Exhibit*, J. C. Rowley, Ed., pp. 17–22, Houston, TX, USA, July 1989.

[10] B. Haimson, M. Lee, and C. Herrick, "Recent advances in in-situ stress measurements by hydraulic fracturing and borehole breakouts," in *Proceedings of the 7th ISRM Congress*, Aachen, Germany, September 1991.

[11] C. G. Herrick and B. C. Haimson, "Modeling of episodic failure leading to borehole breakouts in alabama limestone," in *1st North American Rock Mechanics Symposium*, Austin, TX, USA, June 1994.

[12] B. Haimson and H. Lee, "Borehole breakouts and compaction bands in two high-porosity sandstones," *International Journal of Rock Mechanics and Mining Sciences*, vol. 41, no. 2, pp. 287–301, 2004.

[13] H. Lee, T. Moon, and B. C. Haimson, "Borehole breakouts induced in arkosic sandstones and a discrete element analysis," *Rock Mechanics and Rock Engineering*, vol. 49, no. 4, pp. 1369–1388, 2016.

[14] D. P. Sahara, M. Schoenball, E. Gerolymatou, and T. Kohl, "Analysis of borehole breakout development using continuum damage mechanics," *International Journal of Rock Mechanics and Mining Sciences*, vol. 97, pp. 134–143, 2017.

[15] M. D. Zoback, C. A. Barton, M. Brudy et al., "Determination of stress orientation and magnitude in deep wells," *International Journal of Rock Mechanics and Mining Sciences*, vol. 40, no. 7-8, pp. 1049–1076, 2003.

[16] W. Lin, M.-L. Doan, J. C. Moore et al., "Present-day principal horizontal stress orientations in the Kumano forearc basin of the southwest Japan subduction zone determined from IODP NanTroSEIZE drilling Site C0009," *Geophysical Research Letters*, vol. 37, no. 13, 2010.

[17] A. Malinverno, S. Saito, and P. Vannucchi, "Horizontal principal stress orientation in the Costa Rica Seismogenesis Project (CRISP) transect from borehole breakouts," *Geochemistry, Geophysics, Geosystems*, vol. 17, no. 1, pp. 65–77, 2016.

[18] B. J. Carter, E. Z. Lajtai, and A. Petukhov, "Primary and remote fracture around underground cavities," *International Journal for Numerical and Analytical Methods in Geomechanics*, vol. 15, no. 1, pp. 21–40, 1991.

[19] P. J. Van den Hoek, D. J. Smit, A. P. Kooijman, P. de Bree, C. J. Kenter, and M. Khodaverdian, "Size dependency of hollow-cylinder stability," in *Proceedings of the Rock Mechanics in Petroleum Engineering*, Delft, Netherlands, August 1994.

[20] G. Dresen, S. Stanchits, and E. Rybacki, "Borehole breakout evolution through acoustic emission location analysis," *International Journal of Rock Mechanics and Mining Sciences*, vol. 47, no. 3, pp. 426–435, 2010.

[21] T. Meier, E. Rybacki, A. Reinicke, and G. Dresen, "Influence of borehole diameter on the formation of borehole breakouts in black shale," *International Journal of Rock Mechanics and Mining Sciences*, vol. 62, pp. 74–85, 2013.

[22] J. S. Bell and D. I. Gough, "Northeast-southwest compressive stress in Alberta evidence from oil wells," *Earth and Planetary Science Letters*, vol. 45, no. 2, pp. 475–482, 1979.

[23] L. G. Mastin, "Development of borehole breakouts in sandstone," MSc Thesis, Stanford University, Stanford, CA, USA, 1984.

[24] Z. Zheng, J. Kemeny, and N. G. W. Cook, "Analysis of borehole breakouts," *Journal of Geophysical Research*, vol. 94, no. B6, pp. 7171–7182, 1989.

[25] W. Cheng, G. Jiang, Z. Zhou, Z. Wei, and X. Li, "Numerical simulation for the dynamic breakout of a borehole using boundary element method," *Geotechnical and Geological Engineering*, vol. 37, no. 4, pp. 2873–2881, 2019.

[26] X. Li, C. S. El Mohtar, and K. Gray, "3D poro-elasto-plastic modeling of breakouts in deviated wells," *Journal of Petroleum Science and Engineering*, vol. 174, pp. 913–920, 2019a.

[27] X. Li, C. S. El Mohtar, and K. Gray, "Modeling progressive breakouts in deviated wellbores," *Journal of Petroleum Science and Engineering*, vol. 175, pp. 905–918, 2019b.

[28] E. Gerolymatou and A. Petalas, "Situ stress assessment based on width and depth of brittle borehole breakouts," in *Recent Developments Of Soil Mechanics And Geotechnics In Theory And Practice*, pp. 297–319, Springer, Berline, Germany, 2020.

[29] H. Lin, W. H. Kang, J. Oh, I. Canbulat, and B. Hebblewhite, "Numerical simulation on borehole breakout and borehole size effect using discrete element method," *International Journal of Mining Science and Technology*, vol. 30, no. 5, pp. 623–633, 2020.

[30] A. Lakirouhani, M. Bahrehdar, J. Medzvieckas, and R. Kliukas, "Comparison of predicted failure area around the boreholes in the strike-slip faulting stress regime with Hoek-

Brown and Fairhurst generalized criteria," *Journal of Civil Engineering and Management*, vol. 27, no. 5, pp. 346–354, 2021.

[31] M. Bahrehdar and A. Lakirouhani, "Evaluation of the depth and width of progressive failure of breakout based on different failure criteria, using a finite element numerical model," *Arabian Journal for Science and Engineering*, vol. 47, no. 9, pp. 11825–11839, 2022.

[32] S. Jolfaei and A. Lakirouhani, "Sensitivity analysis of effective parameters in borehole failure, using neural network," *Advances in Civil Engineering*, vol. 2022, Article ID 4958004, 16 pages, 2022.

[33] N. B. Setiawan and R. W. Zimmerman, "Semi-analytical method for modeling wellbore breakout development," *Rock Mechanics and Rock Engineering*, vol. 55, no. 5, pp. 2987–3000, 2022.

[34] H. Zhang, S. Yin, and B. S. Aadnoy, "Poroelastic modeling of borehole breakouts for in-situ stress determination by finite element method," *Journal of Petroleum Science and Engineering*, vol. 162, pp. 674–684, 2018.

[35] X. Li, Y. Feng, and K. E. Gray, "A hydro-mechanical sand erosion model for sand production simulation," *Journal of Petroleum Science and Engineering*, vol. 166, pp. 208–224, 2018.

[36] T. Ma, Y. Qiu, Y. Zhang, and Y. Liu, "Numerical simulation of progressive sand production of open-hole completion borehole in heterogeneous igneous formation," *International Journal of Rock Mechanics and Mining Sciences*, vol. 150, Article ID 105030, 2022.

[37] B. S. Aadnoy and F. Angell-Olsen, "Some effects of ellipticity on the fracturing and collapse behavior of a borehole," *International Journal of Rock Mechanics and Mining Sciences and Geomechanics Abstracts*, vol. 32, no. 6, pp. 621–627, 1995.

[38] B. S. S. Aadnoy and E. Kaarstad, "Elliptical geometry model for sand production during depletion," in *Proceedings of the IADC/SPE Asia Pacific Drilling Technology Conference and Exhibition*, Ho Chi Minh City, Vietnam, November 2010.

[39] B. S. Aadnoy, E. Kaarstad, and J. D. C. Goncalves, "Obtaining both horizontal stresses from wellbore collapse," in *Proceedings of the SPE/IADC Drilling Conference*, Amsterdam, The Netherlands, March 2013.

[40] H. X. Han, S. Yin, and B. S. Aadnoy, "Impact of elliptical boreholes on in situ stress estimation from leak-off test data," *Petroleum Science*, vol. 15, no. 4, pp. 794–800, 2018.

[41] E. Papamichos, P. Liolios, and P. J. van den Hoek, "Breakout stability experiments and analysis," in *Proceedings of the Gulf Rocks 2004, the 6th North America Rock Mechanics Symposium (NARMS)*, Houston, TX, USA, June 2004.

[42] B. H. G. Brady and E. T. Brown, *Rock Mechanics for Underground Mining*, Springer, Berline, Germany, Third edition, 2006.

[43] S. S. Rao, *The Finite Element Method in Engineering*, Butterworth-Heinemann, Oxford, UK, Sixth edition, 2018.

[44] A. M. Al-Ajmi and R. W. Zimmerman, "Relation between the Mogi and the coulomb failure criteria," *International Journal of Rock Mechanics and Mining Sciences*, vol. 42, no. 3, pp. 431–439, 2005.

[45] A. Lakirouhani and H. Hasanzadehshooiili, "Review of rock strength criteria," in *Proceedings Of the 22nd World Mining Congress and Expo*, pp. 473–482, Istanbul, Turkey, September 2011.

[46] A. P. Bunger, A. Lakirouhani, and E. Detournay, "Modelling the effect of injection system compressibility and viscous fluid flow on hydraulic fracture breakdown pressure," in *Proceedings of the ISRM International Symposium on In-Situ Rock Stress*, Beijing, China, August 2010.

[47] A. Lakirouhani, E. Detournay, and A. P. Bunger, "A reassessment of in situ stress determination by hydraulic fracturing," *Geophysical Journal International*, vol. 205, no. 3, pp. 1859–1873, 2016.

Hindawi
Advances in Civil Engineering
Volume 2023, Article ID 1259527, 7 pages
https://doi.org/10.1155/2023/1259527

Research Article

Study on the Seepage Mechanism of Rainwater on Granite Residual Soil Cut Slopes

Yunhong Guo,[1] Songtao Li,[1] Junzhen Zhang,[2] Baolin Wang,[3] and Yanlong Gao[3]

[1]*Railway Engineering College, Zhengzhou Railway Vocational & Technical College, Zhengzhou 450001, China*
[2]*China Railway Zhengzhou Group Co., Ltd., Zhengzhou 450052, China*
[3]*School of Water Conservancy Engineering, Zhengzhou University, Zhengzhou 450001, China*

Correspondence should be addressed to Songtao Li; list16@126.com and Baolin Wang; wangbaolin7@126.com

Received 28 September 2022; Revised 1 November 2022; Accepted 25 January 2023; Published 15 February 2023

Academic Editor: Zhuo Chen

In order to study the seepage process of rainwater on granite residual soil cut slopes, a numerical model for seepage analysis of granite residual soil cut slopes was established. Then, by applying the rainfall boundary condition, the seepage path of rainwater on the slope was analyzed under the condition of rainfall infiltration. Finally, during rainwater seepage, the volumetric water content and pore-water pressure change characteristics inside the slope were analyzed, and the seepage mechanism of rainwater in the granite residual soil slope was revealed. The results show that, under the condition of rainfall infiltration, the surface area of the slope gradually forms a saturated area in a temporary stable state. As the saturated area in the temporary stable state gradually extends to the inside of the slope, the area gradually increases and a groundwater level recharge area is gradually formed at the foot of the slope. Rainwater infiltration changes the original stable state of the slope, causing the granite residual soil slope to change from the two original distribution states of the unsaturated area and saturated area to the three distribution states of the temporarily stable saturated area, unsaturated area, and saturated area from top to bottom. The volumetric moisture content of slope-monitoring points increased gradually with an increase in the duration, and the overall distribution showed an "S" shape. The infiltration of rainwater causes the pore-water pressure of the granite residual soil to increase gradually, and matric suction gradually disappears. In particular, the disappearance of the matric suction at the foot of the slope will lead to the gradual weakening of the shear strength of the slope soil, thus affecting the slope stability.

1. Introduction

Granite residual soil is a special rock and soil mass formed by long-term weathering of granite. In the world, granite residual soil is widely distributed. With the rapid development of the transportation industry, in railway and highway construction projects, in order to ensure the stability of the route, some granite residual soil is often excavated, thus forming a large number of cut-slope projects [1–3]. Granite residual soil has good compressive strength, but its cohesion is poor. Whenever the rainy season comes, the infiltration of a large amount of rainwater further weakens the cohesion of the granite residual soil, resulting in landslide disasters on the slope, which seriously affect traffic safety.

Taking the granite-disabled soil slope as the research object, domestic and foreign scholars have carried out a lot of research. In terms of engineering characteristics of granite residual soil, Tang et al. used a self-developed tensile strength tester to analyze the variation law of the tensile strength of granite residual soil with different moisture content during humidification and drying and clarified the compressive strength of granite residual soil during humidification and drying [4]. Alias et al. analyzed the variation law of shear strength of granite residual soil through a triaxial test and revealed the formation characteristics of shear strength of granite residual soil [5]. Ferreira et al. analyzed the effect of cyclic loading on the interfacial cohesion between granite residual soil and geogrids and studied the main control of

the loading frequency, amplitude, and other influencing factors affecting the interfacial strength [6].

In the aspect of granite residual soil slope stability, Yang et al. studied the development and formation process of fissures in granite residual soil slopes under the condition of a dry-wet cycle and believed that the development degree of fissures in granite residual soil slopes had a positive correlation with the number of dry-wet cycles. The slope instability time has been advanced [7]. Guo et al. believed that rainfall is the key factor leading to the catastrophic occurrence of granite residual soil slopes. Therefore, the improved Mein–Larson model was used to analyze the variation law of the wetting front on the slope under the condition of rainfall infiltration [8]. By burying the moisture sensor, Fei and Qian measured the variation characteristics of matric suction and moisture content of the granite residual soil slope during rainfall. The results show that rainfall infiltration changes the distribution of matric suction on the granite residual soil slope, thus causing the slope stability to change, but this effect decreases gradually with an increase in depth [9]. Wang et al. analyzed the variation law of the wetting front on the granite residual soil slope under the condition of rainfall infiltration and proposed a slope stability analysis method considering the time-varying effect. The results show that the probability of slope failure is controlled by the position of the slip surface [10]. Wei et al. used a combination of numerical and laboratory model tests to analyze the influence of different slopes and heights of cut slopes on the slope stability under rainfall conditions, taking artificially cut slopes of granite residual soil as the research object [11]. It can be seen from the abovementioned research study that rainfall is the key factor that induces the instability of granite residual soil cut slopes. However, the existing research results are still not deep enough to study the seepage mechanism of rainwater in granite residual soil.

In view of this, this paper takes the granite residual soil cut slope as the research object, focuses on the rainfall factor, and uses numerical software to establish the seepage model of rainwater on the granite residual soil slope. The seepage evolution characteristics of the granite residual soil slope during rainwater infiltration were deeply analyzed, the seepage path of rainwater on the slope was clarified, and the seepage mechanism of rainwater on the granite residual soil slope was revealed. This study provides theoretical reference for the stability control measures of granite residual soil slopes.

2. Seepage Model of Granite Residual Soil Cut Slopes

2.1. Construction of Percolation Differential Units. Granite residual soil has certain porosity. When rainwater infiltrates into the interior of the granite residual soil slope, the flow of rainwater in the void will break the original saturated-unsaturated stable state in the slope, thereby affecting the slope stability. The migration rate of rainwater in the granite residual soil slope can be described by Darcy's law [12–14].

$$v_w = -k_w \frac{\partial h_w}{\partial y}, \tag{1}$$

where V_w is the Darcy velocity of rainwater seepage, k_w is the saturated permeability coefficient, and $\partial h_w/\partial y$ is the hydraulic gradient in a Y direction. The seepage process of rainwater in the granite residual soil slope is a complex flow process. Under normal conditions, the water flow continuity equation can be used to solve the problem by setting boundary conditions. Any tiny space unit $dxdydz$ in the granite residual soil slope is selected to establish a differential unit of rainwater seepage on the slope, as shown in Figure 1. It can be seen from Figure 1 that, in any period of time dt, the difference between the inflow and outflow of rainwater due to the action of gravity and matric suction can be expressed as the seepage flow in this period of time.

2.2. Theoretical Derivation of the Water Flow Continuity Equation. Since the granite residual soil slope is an integral structure, the seepage of rainwater on the slope is continuous. Then, according to the principle of energy conservation, the water flow continuity equation of rainwater on the granite residual soil slope can be expressed as follows [15–17]:

$$p_w\left[v_x dydz + v_y dxdz + v_z dxdy\right] - p_w\left[\left(v_x + \frac{\partial v_x}{\partial x}dx\right)dydz + \left(v_y + \frac{\partial v_y}{\partial y}dy\right)dxdz + \left(v_z + \frac{\partial v_z}{\partial z}dz\right)dxdy\right] = \frac{\partial\left(np_w dxdydz\right)}{\partial t}dt, \tag{2}$$

where n is the porosity and p_w is the density of water.

Through mathematical transformation, formula (2) can be simplified to

$$p_w\frac{\partial v_x}{\partial x} + \frac{\partial v_y}{\partial y} + \frac{\partial v_z}{\partial z}dxdydz = \frac{\partial\left(np_w dxdydz\right)}{\partial t}dt. \tag{3}$$

The change in water quality infiltrated into the granite residual soil is related to the compressive modulus of the granite residual soil, and the right end of formula (3) can be expressed as

$$\frac{\partial\left(np_w dxdydz\right)}{\partial t}dt = p_w\left(\frac{1}{\Gamma} + n\frac{1}{\Gamma_w}\right)\frac{\partial u}{\partial t}dxdydzdt, \tag{4}$$

where Γ is the bulk compressive modulus of the soil, Γw is the bulk compressive modulus of water, and u is the negative pore-water pressure.

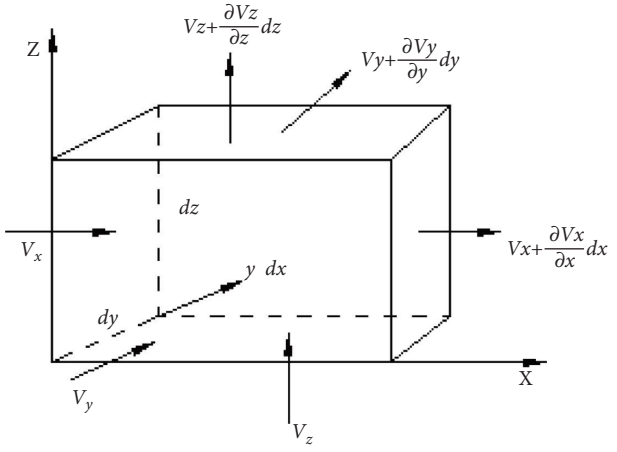

Figure 1: Percolation differential units.

The water head at the seepage differential unit of granite residual soil can be expressed as $(h - z)$so $u = \rho_w g(h - z)$. Then, there is

$$\frac{\partial u}{\partial t} = \rho_w g \frac{\partial h}{\partial t}. \quad (5)$$

In order to further simplify the seepage analysis model, this paper does not consider the anisotropy of the granite residual soil when analyzing the seepage characteristics of rainwater on the granite residual soil slope.

$$\frac{\partial v_x}{\partial x} + \frac{\partial v_y}{\partial y} + \frac{\partial v_z}{\partial z} dx\, dy\, dz = 0. \quad (6)$$

According to the water flow continuity condition, by substituting Darcy's law into formula (6), the partial differential equation of water flow continuity of rainwater on the granite residual soil slope can be obtained as follows:

$$\frac{\partial}{\partial x}\left[k_x(\theta)\frac{\partial h_w}{\partial x}\right] + \frac{\partial}{\partial y}\left[k_y(\theta)\frac{\partial h_w}{\partial y}\right] + \frac{\partial}{\partial z}\left[k_z(\theta)\frac{\partial h_w}{\partial z}\right] = 0. \quad (7)$$

2.3. Establishment of the Seepage Model. This paper takes the granite residual soil cut slope on one side of a railway as the research object and studies the seepage mechanism of rainwater on the slope. The overall excavation height of the slope was 16 m, and the excavation was divided into two levels. The height of the first-level slope was 10 m with a slope ratio of 1 : 1.75, and the height of the second-level slope was 6 m with a slope ratio of 1 : 1.5. A 2 m wide platform is set at the intersection of the two-level slopes, and the specific dimensions are shown in Figure 2. In order to simulate the groundwater level, the groundwater level elevation on the left side of the model was set to 6 m and the groundwater level on the right side was set to 3 m. In order to ensure the calculation time and accuracy, the four-node grid was used to divide the whole model into 7076 units, totaling 7286 nodes.

Reasonable boundary condition settings can accurately simulate the seepage characteristics of rainwater on the granite residual soil slope. Therefore, in the seepage numerical model, the top and the slope surface of the granite residual soil slope were set as the boundary conditions of rainfall infiltration and the road structure on the right side of the model was set as the impermeable boundary condition. Other boundaries in the numerical model of seepage were also set as impervious boundary conditions. In this paper, in order to monitor the seepage characteristics of rainwater on the granite residual soil slope, six monitoring points were set up at the top, middle, and bottom of the two-level slope at a depth of 1 m. At the same time, in order to monitor the variation law of the matric suction on the slope with the elevation, a monitoring section was set up at the top of the second-level slope.

3. Seepage Numerical Model Calculation Scheme

3.1. Physical Parameters of Granite Residual Soil. The granite residual soil slope soil samples were selected from the site, the saturated volumetric moisture content of the granite residual soil layer on the slope was measured by relevant laboratory tests to be 0.26, and the residual volumetric moisture content was 0.11. The saturated permeability coefficient was 1.91×10^{-7} cm/s. The parameters were obtained by referring to the field survey data. The specific physical parameters of granite residual soil are shown in Table 1.

The seepage of rainwater in the rock and soil body is mainly carried out through the pores between soil particles, and the size of the pores also affects the volumetric water content and matric suction of the rock and soil body. Numerous studies have shown that there is a negative relationship between the volumetric water content in rock and soil and matric suction; that is, with a gradual increase in rock-soil matric suction, the volumetric water content of soil gradually decreases. When studying the seepage mechanism of rainwater on the granite residual soil slope, the classical van Genuchten model was used to fit the curve of the volumetric water content of the granite residual soil with matric suction and the permeability coefficient with matric suction [18–20]. The fitting results are shown in Figures 3 and 4.

3.2. Slope Rainfall Program. In this paper, in order to study the seepage mechanism of rainwater on the granite residual soil slope, the rainfall grade was selected as heavy rain, the rainfall intensity was 8.7×10^{-4} mm/s, the total duration was set as 45 h, and the cumulative rainfall was 150 mm. In the seepage numerical model shown in Figure 2, slope rainfall infiltration in Table 2 was realized by applying the infiltration boundary condition.

4. Seepage Simulation Calculation Results

4.1. Slope Volumetric Water Content Distribution Law. In order to analyze the distribution law of rainwater on the slope, the cloud map of the volumetric water content of the granite residual soil slope under different rainfall times was drawn, as shown in Figure 5. As can be seen in Figure 5,

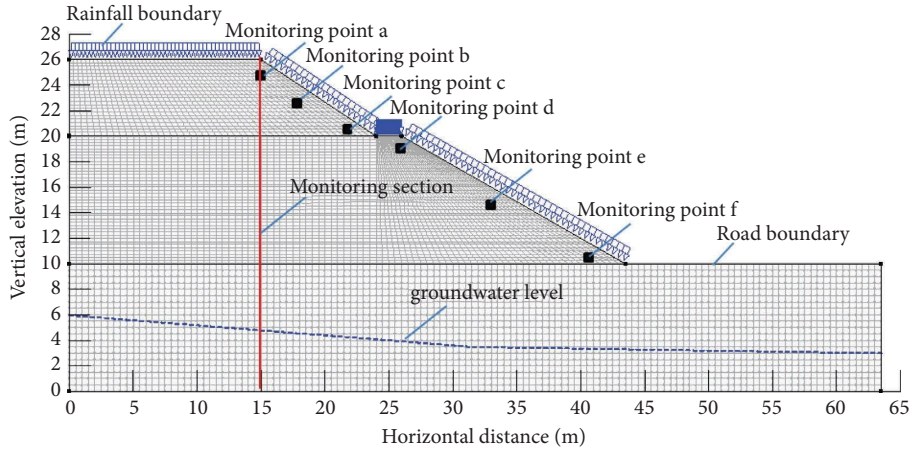

Figure 2: Seepage numerical model.

Table 1: Physical parameters of granite residual soil.

Lithology	Severe (γ/(kN•m^{-3}))	Saturated volume moisture content (%)	Residual volume moisture content (%)	Poisson's ratio (μ)	Permeability coefficient (K/(cm•s^{-1}))
Granite residual soil	23	26	18	0.32	1.91×10^{-7}

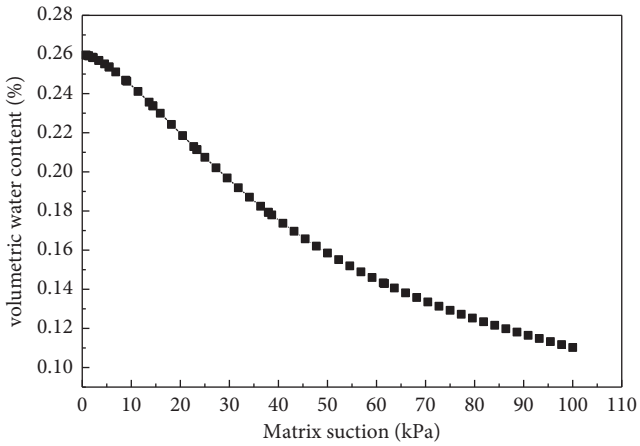

Figure 3: Variation curve of the volumetric water content with matric suction.

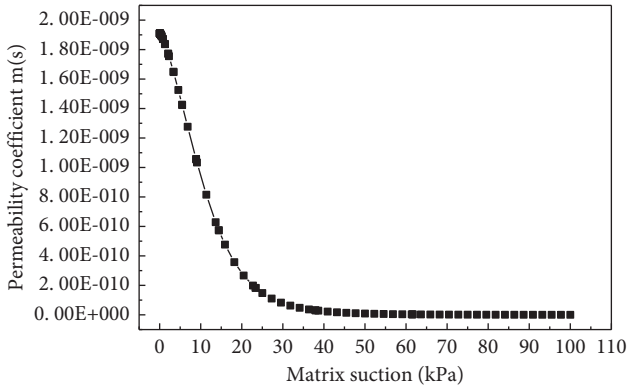

Figure 4: Variation curve of the permeability coefficient with matric suction.

when there is no rainfall, below the overall groundwater level of the slope is the saturated area and above the groundwater level is the unsaturated area. When rainfall reaches 6 hours, the rainwater has infiltrated from the surface of the slope to the interior of the slope. With a gradual increase in the infiltration amount, the volumetric water content of the soil in the surface area of the slope gradually increases to a saturated state, resulting in the surface soil of the slope. A transient steady-state saturation region occurs. With a gradual increase in duration, a large amount of rainwater seeps downwards inside the slope and the area of the temporary steady-state saturation area of the slope gradually increases. When rainfall reaches 24 h, a large amount of rainwater infiltrating into the inside of the slope gathers at the foot of the first-level slope and seeps down to replenish the groundwater level. When rainfall reaches 48 h, the volumetric water content at the toe of the slope reaches a saturated state, which increases the overall bulk density of the slope and weakens the shear strength of the soil at the toe of the slope.

4.2. Distribution Law of the Wet Front on Slopes. Figure 6 shows the evolution law of the wetting front on the granite residual soil slope with rainfall under the condition of rainfall infiltration. As can be seen in Figure 6, in the early stage of rainfall, with the infiltration of rainwater into the granite residual soil slope, the soil particles on the surface of the slope are gradually filled with rainwater and gradually form a critical surface with the dry soil inside the slope, that

Table 2: Rain program.

Rain level	Rainfall intensity (mm/s)	Rain duration (h)	Rain stopped (h)	Total accumulated rainfall (mm)
Rainstorm	8.7×10^{-4}	48	24	150

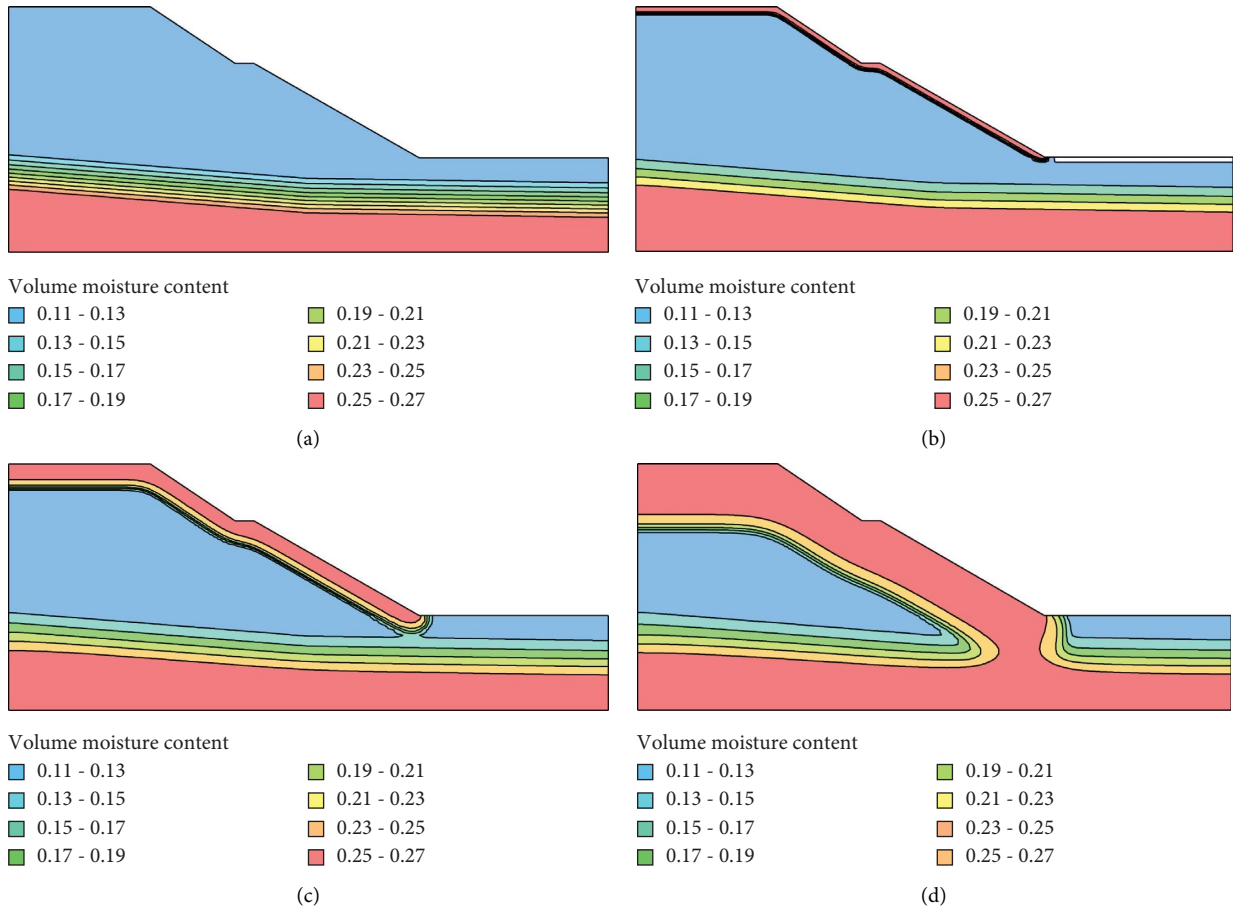

Figure 5: Slope volumetric water content distribution law. (a) Slope initial state. (b) Rain lasted 6 hours. (c) Rain lasted 24 hours. (d) Rain lasted 48 hours.

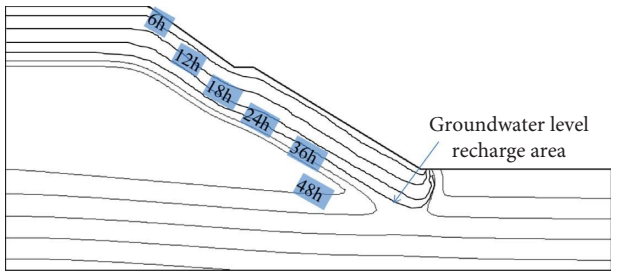

Figure 6: Distribution law of the wet front on slopes.

is, the wetting front. The overall tendency of the wetting front is distributed along the slope. With a gradual increase in duration, the wetting front gradually extends to the interior of the slope. When the amount of rainfall infiltration reaches a certain level, the wetting front curve will gradually form a concave distribution at the foot of the slope and a groundwater level recharge area will gradually be formed at the foot of the slope.

4.3. Variation Law of Volumetric Water Content at Monitoring Points. In order to analyze the variation law of the volumetric water content of the nodes on the slope under the condition of rainwater seepage from a microscopic perspective, the water content of six characteristic monitoring points was selected to analyze the seepage characteristics of rainwater on the granite residual soil slope during rainfall. Figure 7 shows the variation law of the volumetric water content of the six monitoring points of the slope under the condition of rainfall infiltration. As can be seen in Figure 7, the volumetric water content of the 6 monitoring points gradually increased to the saturated state with an increase in duration, and the overall distribution showed an "S" shape. The increase rate of the volumetric water content at the top of the two-level slope is largest, and the increase rate of the

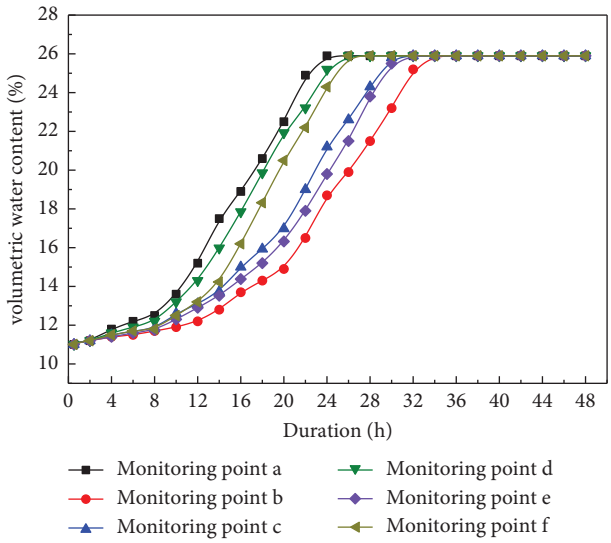

Figure 7: Variation law of the volumetric moisture content at monitoring points with duration.

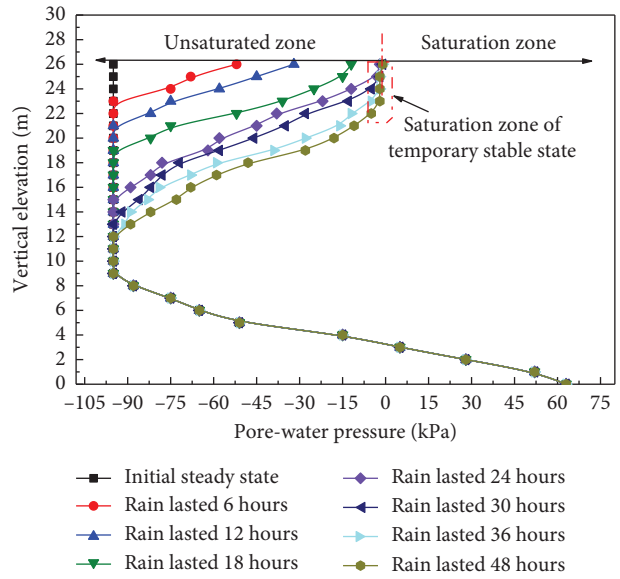

Figure 8: Variation law of the slope pore-water pressure with duration.

volumetric water content at the foot of the slope is smallest. The increasing rates of water content at the corresponding monitoring points on the two-level slopes are different. The increasing rates of the 6 monitored volumetric water contents are as follows: monitoring point a > monitoring point d > monitoring point f > monitoring point c > monitoring point e > monitoring point b. This is because with the continuous infiltration of rainwater on the slope surface, the pores of the granite residual soil at the monitoring points are gradually filled with rainwater and the volumetric water content gradually increases. Since the top of the second-level slope also produces rainfall infiltration, the volumetric water content of monitoring point a located at the top of the second-level slope has the highest rate of increase. Since a large amount of rainwater infiltrates at the platform, rainfall there will be greater than that of other places. Therefore, the increase rate of the volumetric water content of monitoring point d at the top of the first-level slope and below the platform is second only to that of monitoring point a. Since the rainwater on the slope is affected by the combined action of gravity and matric suction, the seepage direction will follow the slope. Therefore, the volumetric water content of monitoring point b located in the middle of the first-level slope is smallest.

4.4. Variation Law of Pore-Water Pressure. During rainfall, the pore-water pressure of a monitoring section was selected to analyze the seepage characteristics of rainwater on the granite residual soil slope. Figure 8 shows the variation law of the pore-water pressure of the monitoring section of the granite residual soil slope with the duration under the condition of rainfall infiltration. As can be seen in Figure 8, in the initial state, the pore-water pressure of the soil below the groundwater level is basically positive and the pore-water pressure of the soil above the groundwater level is basically negative. As the elevation increases, the soil pore-water pressure gradually decreases, indicating that soil matric suction gradually increases. In the early stage of rainfall, rainwater gradually infiltrated through the slope surface and the pores between soil particles at the top of the slope were gradually filled with rainwater, resulting in a gradual decrease in soil matric suction and a gradual increase in the pore-water pressure. With a gradual increase in duration, a large amount of rainwater infiltrates into the interior of the slope, resulting in a temporary stable saturation zone of the surface soil of the slope. With the continuous infiltration of rainwater, the temporarily stable saturated zone gradually extends to the interior of the slope and the area gradually increases. As a result, under the condition of rainfall infiltration, the original unsaturated area-saturated area distribution state of the slope from top to bottom evolves into a temporary stable state of the saturated area-unsaturated area-saturated area distribution state.

5. Conclusions

(1) Under the condition of rainfall infiltration, rainwater first infiltrated into the surface area of the slope and gradually formed a temporary stable saturation area in the surface area of the slope. With the continuous infiltration of rainwater, the temporarily stable saturated area gradually extends to the inside of the slope, the area gradually increases, and the groundwater level recharge area is gradually formed at the foot of the slope.

(2) Under the condition of rainwater seepage, the granite residual soil slope changes from the two original distribution states of the unsaturated area and saturated area to the temporary stable state of the saturated area and three distribution states of the unsaturated area and saturated area from top to bottom.

(3) During rainfall, the volumetric water content of the second-level slope of granite residual soil increased fastest at the top and slowest in the middle. The volumetric water content of the slope-monitoring points all increased gradually with an increase in duration, and the overall distribution showed an "S" shape.

(4) The infiltration of rainwater causes the pores of granite residual soil particles to be filled, the soil pore-water pressure gradually increases, and matric suction gradually disappears. In particular, the disappearance of the matric suction at the toe of the slope will lead to the gradual weakening of the shear strength of the slope soil, thus affecting the slope stability.

Data Availability

The data used to support the findings of this study are available from the corresponding author upon request.

Conflicts of Interest

The authors declare that they have no conflicts of interest.

Acknowledgments

The authors acknowledge the support received from the Key Scientific Research Project Plan of Henan Province Colleges and Universities Program on the Intelligent Identification Method of Railway Subgrade Muddying and Muddying based on Ground Penetrating Radar (Grant no. 22A580007), the Scientific Research and Development Plan of China Railway Zhengzhou Group Co., Ltd. (Grant no. 2022G3), and the Railway Subgrade Safety Emergency Technology Innovation and Demonstration Team of Zhengzhou Railway Vocational and Technical College (Grant no. 21KJCXTD02).

References

[1] X. Liu, X. Zhang, L. Kong, G. Wang, and H. Liu, "Formation mechanism of collapsing gully in southern China and the relationship with granite residual soil: a geotechnical perspective," *Catena*, vol. 210, no. 2, Article ID 105890, 2022.

[2] W. Chen, J. Zhao, L. Fan et al., "The effect of length and content of fiber on glass fiber and basalt fiber-reinforced granite residual soil," *Advances in Civil Engineering*, vol. 2022, Article ID 7803002, 9 pages, 2022.

[3] P. Cai, Y. Xue, Z. Jiang, and X. Li, "3D Large Pore Quantitative Characterization and Flow Simulation of Granite Residual Soil Based on CT Scanning," *Scientia Sinica (Technologica)*, vol. 52, no. 7, pp. 1065–1082, 2022.

[4] L. Tang, H. Wang, and Y. Sun, "Study on the change of tensile strength of granite residual soil during dry and wet process," *Rock and Soil Mechanics*, vol. 43, no. 7, pp. 1749–1760, 2022.

[5] R. Alias, A. Kasa, and M. R. Taha, "Effective shear strength parameters for remolded granite residual soil in direct shear and triaxial tests," *Electronic Journal of Geotechnical Engineering*, vol. 19, pp. 4559–4569, 2014.

[6] F. Ferreira, C. Vieira, and M. de Lurdes Lopes, "Cyclic and post-cyclic shear behaviour of a granite residual soil-geogrid interface," *Procedia Engineering*, vol. 143, pp. 379–386, 2016.

[7] X. Yang, D. Chen, and Y. Liu, "Fracture evolution and slope stability of granite residual soil under dry wet cycle," *Journal of Xiamen University*, vol. 61, no. 4, pp. 591–599, 2022.

[8] Z. Guo, W. Su, W. Zhang, and Z. Zheng, "Study on rainfall infiltration of granite residual soil slope based on improved mein Larson model," *South China of Seismology*, vol. 42, no. 2, pp. 116–123, 2022.

[9] L. Fei and J. Qian, "Measured characteristics of moisture in granite residual soil embankment slope," *Technology of Highway and Transport*, vol. 37, no. 6, pp. 29–35, 2020.

[10] H. Wang, J. Zhang, and F. Chen, "Time varying reliability of granite residual soil slope under heavy rainfall," *Engineering Journal of Wuhan University*, vol. 49, no. 5, pp. 763–767, 2016.

[11] W. Wei, R. Zhao, L. Liao, and Z. Liu, "Analysis of landslide process induced by artificial slope cutting of granite residual soil in Rongxian County, Guangxi," *Mountain Research*, vol. 40, no. 3, pp. 396–410, 2022.

[12] W. R. Gardner, "Some steady state solutions of the unsaturated moisture flow equation with application to evaporation from a water table," *Soil Science*, vol. 85, no. 4, pp. 228–232, 1958.

[13] Y. Li, J. Wu, and K. Li, "Saturated unsaturated seepage analysis based on FLAC3D," *Rock and Soil Mechanics*, vol. 33, no. 2, pp. 617–622, 2012.

[14] X. Deng, Z. He, H. Fu, and L. Zeng, "Influence of rainfall infiltration on stability of high embankment slope with granite residual soil," *Mining and Metallurgical Engineering*, vol. 36, no. 4, pp. 11–15, 2016.

[15] S. R. Zhu, L. Z. Wu, and J. Huang, "Application of an improved P(m)-SOR iteration method for flow in partially saturated soils," *Computational Geosciences*, vol. 26, no. 1, pp. 131–145, 2022.

[16] S. R. Zhu, L. Z. Wu, and X. L. Song, "An improved matrix split-iteration method for analyzing underground water flow," *Engineering with Computers*, 2022.

[17] H. Liao, J. Ji, and J. Zeng, "Stability analysis of soil slope considering saturated unsaturated seepage," *Rock and Soil Mechanics*, vol. 29, no. 12, pp. 3229–3234, 2008.

[18] M. T. Van Genuchten, "A closed-form equation for predicting the hydraulic conductivity of unsaturated soils," *Soil Science Society of America Journal*, vol. 44, no. 5, pp. 892–898, 1980.

[19] D. G. Fredlund and A. Xing, "Equations for the soil-water characteristic curve," *Canadian Geotechnical Journal*, vol. 31, no. 4, pp. 521–532, 1994.

[20] M. Feng and D. G. Fredlund, "Hysteretic influence associated with thermal conductivity sensor measurements," in *Proceedings of the From Theory to the Practice of Unsaturated Soil Mechanics in Association with the 52nd Canadian Geotechnical Conference and Unsaturated Soil Group*, pp. 651–657, Rdgina Sasd, Canada, 1999.

Hindawi
Advances in Civil Engineering
Volume 2022, Article ID 4441705, 16 pages
https://doi.org/10.1155/2022/4441705

Research Article

Impact of Uniaxial Mechanical Perturbation on Structural Properties and Smectite Porosity Features: Ion Exchanger Efficiency and Adsorption Performance Fate

Walid Oueslati, Chadha Mejri, and Abdesslem Ben Haj Amara

Université de Carthage, Faculté des Sciences de Bizerte, LR19ES20, Ressources, Matériaux et Ecosystèmes (RME), Bizerte 7021, Tunisia

Correspondence should be addressed to Walid Oueslati; walidoueslati@ymail.com

Received 2 June 2022; Revised 10 August 2022; Accepted 11 August 2022; Published 3 October 2022

Academic Editor: Zhuo Chen

The use of montmorillonite in the context of engineered barriers makes it possible to minimize the spread of heavy metals from industrial and even radioactive waste. An evaluation of the performance of the mechanisms controlling the clay-environment interaction and predicting the dynamics/configuration of the interlayer space (IS) is required. This work focuses on a quantitative identification of the structural changes and porosity alteration in the case of heavy metal-exchanged montmorillonite samples (Co^{2+} and Cd^{2+} cations) undergoing mechanical stresses (uniaxial oedometric test (loading/unloading)). Relationships between mechanical stress strength, intrinsic structural response, ion exchanger efficiency, and adsorption performance fate are investigated. This goal is achieved through the correlation of in situ quantitative X-ray diffraction (XRD) analysis (under an extremely controlled atmosphere reached by varying relative humidity rate %rh) and porosity investigation (assured by combining outcomes from BET (Brunauer–Emmett–Teller) and BJH- (Barrett, Joyner, and Halenda-) PSD (pore size distribution) analysis). Obtained results show an upsurge in the structural heterogeneities accompanying the theoretical increase in the mixed layer structure (MLS) number and developing an unconventional hydration behaviour after stress relaxation regardless of exchangeable cation nature. Experimental XRD patterns are reproduced using MLS, which suggests the coexistence of more than one "crystallite" specie and more than one exchangeable cation indicating a complex cation exchange capacity (CEC) saturation. For extremely low %rh value, a new homogeneous dehydrated state trend is observed in the case of the Co^{2+} cation. Porosity analysis shows mesopore volume growth for the stressed sample and confirms crystallite exfoliation layer trends, results of the layer cohesion damage, and subsequent constraint strength fluctuations.

1. Introduction

Waste disposal has become one of the most serious modern environmental problems associated with the development of countries. The architecture, design, and operation of the waste disposal sites ensure adequate waste management with respect for human health and the ecosystem. The geological disposal, adopted as a safe solution for the long-term management of radioactive waste, is delivered by a system that (1) isolates waste from the biosphere for extremely prolonged periods of time, (2) ensures that residual radioactive substances reaching the biosphere will be at comparatively insignificant concentrations, and (3) provides reasonable assurance that any risk of inadvertent human intrusion would be extremely low [1–5]. The most common problems of the landfill site are environmental degradation and groundwater contamination [6].

The use of compacted clays, as part of the multibarrier concept, ensures the previously cited requirements [7, 8]. Indeed, the most used materials in landfill disposal are compacted clay liner (CCL) and geosynthetic clay liner (GCL). The main reason for using such materials is their intrinsic properties, such as the large specific surface areas (SSA), the low permeability, the cation exchange capacity (CEC), the high adsorption ability, and the low hydraulic conductivity [6–11]. Compacted clay liners are less

expensive, and it has good attenuation capacity. Clay membranes can be used as toxic gases (originating from the landfill site) eliminator and as a trap for radionuclide migration/diffusion (resulting from a pipeline leak or damage due to various types of stress affecting installation) [12–15]. The clay mineral membranes are exposed to various chemical, biological, and physical stresses, and they are influenced by the subsequent leachate [16–21]. To evaluate the consistency of these membranes, it is important to examine their chemical compatibility with the different fluids or the leachate to which they are subjected [22]. Based on the fine particle size, the homogeneous micropores and the high surface charges, the low hydraulic conductivity, the high adsorption capacity, and the low cost compared with geosynthetic clay (GC), natural bentonites are most prized in this context [23–29]. Indeed, [30] studied the shear strength of compacted clays as affected by the mineral content and wet-dry cycles and demonstrated that the cohesion and frictional strength properties were determined and linked to the proportion of clay minerals and the number of wetting and drying cycles. On the other hand, [31] demonstrated, in the case of compacted clays mixed with a wide range of bentonite for engineered barriers, that compressibility was affected by the bentonite content on geotechnical characteristics.

The use of bentonite, especially as a buffer in the excavated escape galleries between the waste containers and the tunnel walls, achieves important strategic outcomes. Bentonite membrane is usually affected by the surrounding temperature/humidity gradient fluctuation [32, 33]. However, compacted clays present problems with cracking and/or desiccation, especially those containing an appreciable amount of bentonite [34–36]. Numerous studies have shown that compacted clays undergo large physicochemical properties modifications when exposed to a cycle of swelling and/or desiccation-wetting, which constitutes a surrounding variable environmental constraint [28–39]. Montmorillonite fraction, which is a dioctahedral species of the smectite mineral group, can constitute up to 95% of bentonite. These functional materials provide restriction of groundwater access to radioactive waste, promote conditions for mass transfer between waste and groundwater by diffusion, overwhelm the migration of radionuclides in colloidal form into groundwater, ensure effective sorption after possible depressurization of radioactive waste containers, and so on [40–45]. In addition to their presence in the formations housing the storage facilities and their use as backfill material or as sealing material to isolate parts of disposal facility, montmorillonite is also present as a buffer material in the empty space between the package and the host rock [46–48]. The montmorillonite layer structure is constituted by the stacking of two types of sheet: an octahedral sheet O ($MO_4(OH)_2$ with M is a metal cation (Al, Mg)) sandwiched between two tetrahedral sheet T (SiO_4) often labelled T-O-T with an average layer thickness around 10 Å. The layer charge is related to existing isomorphic substitutions in the tetrahedral sheet (Al^{3+}, Si^{4+}) and/or octahedral ones (Mg^{2+}/Li^{+}, Al^{3+}/Mg^{2+}). This charge deficit is compensated by exchangeable cations (Exc.Cat), coming from the soil solution and incorporated in IS. The presence of solvent (water molecule) facilitates exchangeable cations insertion and enables, respectively, layer thickness expansion, mineral dispersion (colloidal properties) in the soil solution, and micro/macroscopic clay swelling. The progressive layer thickness expansion of the basal spacing value d (001) is done by discrete hydration state going from the dehydrated state (0 W, $d_{001} \approx 10$ Å) to the strongly hydrated ones (4 W, $d_{001} \approx 21$ Å) passing, respectively, by 1 W ($d_{001} \approx 12.4$ Å), 2 W ($d_{001} \approx 15.4$ Å), and 3 W ($d_{001} \approx 18.2$ Å) hydration state [49–54].

Montmorillonite fraction interacts physically and chemically with soil and the disposal packages over time, which results in structural changes and alteration of the intrinsic properties [48–60]. Depending on these operating constraints (aggressive variable environment), a thorough predictive study of the behaviour and montmorillonite structural response is required. This response can vary from significant structure transformation and properties to yield affected by the nature of the stress.

The applied constraints (aggressive environment) can be considered individually. In this case, they are divided into three groups: (i) atmospheric (temperature, relative humidity, and pressure) and hydrogeological (soil desiccation/wetting cycles) constraints; (ii) chemical constraints (soil solution composition, water chemistry, and soil solution pH); (iii) mechanical stresses (phenomena of sliding/shearing of soils, tectonics and fracturing, and natural mechanical field) [50–53]. In reality, these constraints are often coupled with combinations up to the third coupling order inducing an enormous disruptive stress potential, which affect necessarily the clay fraction efficiency. The performances of the starting materials, according to the initial objectives, are no longer guaranteed; the main problem in this case becomes the effectiveness of these stressed/disturbed materials.

In this work, structural changes, hydration behaviour evolution, CEC alteration, and porosity fate of dioctahedral smectite (Wyoming montmorillonite) subsequent to the applied mechanical stress (uniaxial load/unload) are explored. An experimental investigation protocol, developed at the laboratory scale, based on three main levels is realized. Indeed, mechanical stress based on the loading/unloading test is done to create material stress. An in situ XRD study, under an extremely controlled atmosphere (variable %rh), is directed. The strength of this structural analysis lies in the use of the theoretical 00l diffraction profiles modelling approach to define the relationship between mechanical constraint and microstructure changes. Finally, the adsorption measurement and the PSD analysis are done by targeting the stress damage to the metal-exchanged montmorillonite porosity features.

2. Materials and Methods

2.1. Baseline Sample. Starting sample is a reference montmorillonite specimen (Swy-2) supplied by the Source Clays Repository of the Clay Minerals Society. The intrinsic characteristic properties of this reference sample can be consulted in the literature data [61, 62]. The structural formula per half unit cell is given by [62]

$$\left(Si_{3.923}Al_{0,077}\right)\left(Al_{1,459}Ti^{4+}_{0,018}Fe^{3+}_{0,039}Fe^{2+}_{0,045}Mg^{2+}_{0,382}\right)O_{10}\,(OH)_2\left(Ca^{2+}_{0,177}Na^{+}_{0,027}\right). \quad (1)$$

2.2. Experimental

2.2.1. Na-Rich Montmorillonite. Raw material requires NaCl pretreatment before application to ensure maximum layer dispersion. This specific treatment is carried out by respecting a classical protocol detailed by [60, 63] to prepare the Na-rich montmorillonite suspension. Indeed, the <2 μm fraction of Wyoming montmorillonite was extracted by allowing larger particles to settle in water and then decanting. The Na-rich montmorillonite was prepared by equilibrating the colloidal fraction with NaCl solution. This step consists of dispersing 40 g of solid in 500 mL of NaCl solution (1 M) and stirring mechanically for 24 h. A SIGMA laboratory centrifuge at 8000 rpm speed is used for the solid fraction separation. To ensure saturation of all exchangeable sites by Na^+ cations, this equilibration was repeated five times. The clay was then washed with distilled water and separated in a high-speed centrifuge until the solution was free of CI^-. Chloride was presumed to be absent when the supernatant liquid gave a negative test with $AgN0_3$.

2.2.2. Metal-Exchanged Montmorillonite. The same ionic exchange procedure (used in the case of Na^+ cation) was followed to prepare, respectively, Co-montmorillonite (SWy-Co) and Cd-montmorillonite (SWy-Cd) suspension. This goal is realized using metal chloride solution (1 M) and Na-rich montmorillonite respecting the following chemical reaction:

$$\mathbf{SWy - Na_x + M^{2+} + xCl^- \longrightarrow SWy - M^{2+} + xNaCl}, \quad (2)$$

where M^{2+} denotes Co^{2+} and Cd^{2+} cations and SWy-M^{2+} denotes SWy-Co and SWy-Cd.

2.2.3. Experiments. Before beginning the study of the compaction/reswelling cycle effect on the stressed samples, a study of the unstressed samples under the same controlled atmosphere is essential. The detailed experimental protocol is summarized in Figure 1.

2.3. Mechanical Tests: Materials Fatigue. The oedometer testing device used is a front-loading oedometer (WF 24251) (Figure 2). The cell diameter is 50 mm. The comparator race extends 12 mm with an accuracy of 2 microns. A predetermined piston pressure can be applied to the metal-exchanged montmorillonite sample, causing fluid expulsion through the filter until the system reaches equilibrium. The Linear Voltage Displacement Transducer (LVDT) measures the displacement of the piston and records the change in the system volume during the test. The measured equilibrium displacement permits the determination of the equilibrium void ratio e, which is defined as the ratio of the fluid volume to that of solid particles. The sample was maintained in contact with an external reservoir of deionized water until the experiment ended. All pressures quoted are gauges; that is, they are pressures relative to atmosphere and hence correspond to the differential pressures causing filtration. Each test consisted of a step-by-step loading and unloading (compaction and swelling) of the clay suspensions. The pressure sequences were 5, 10, 15, 20, 25, and 30 bar for the clay suspension, the same pressures being used during compaction and swelling. At the end of each test, the pressure was totally released, and the sample allowed swelling until equilibrium was reached [64, 65]. Then, the final void ratio e was measured by drying the cake at 140~ overnight. From the known weight of clay fraction M (the amount of suspension introduced in the cell was carefully measured) and the measured piston displacementsΔl, the equilibrium void ratio at each pressure can be calculated from the equation

$$e\,(P) = e_f + \frac{\Delta l \rho_c A}{M}. \quad (3)$$

In this equation, the Δl values are taken relative to the final position of the piston and may be positive or negative. The dry clay density ρ_c was taken as 2.75 g/cm^3 as previously calculated. In both pieces of apparatus, the sample cell is of cross-sectional area $A = 5.07$ cm^2.

2.4. Structural Analysis. Experimental XRD patterns are obtained from a Brucker D8 Advance X-ray diffractometer with the following setting and scanning parameters: (i) 40 kV and 20 mA; (ii) Cu_Kα monochromatic radiation $\lambda = 0.15406$ nm; (iii) 0.04°2θ as step size; (iv) angular range 3, 5–60°2θ; (v) 6 s as counting time per step. Diffractometer installation is equipped with an advanced Ansyco humidity (rh) generator connected to a CHC + Cryo & Humidity Anton Paar Chamber. To decode the structural impact of the applied mechanical constraint on the possible deformations affecting the IS configuration, a study of unstressed and stressed samples under extreme values of %rh is carried out. This appeal targets the understanding of the interstitial water retention and release mechanisms. The environmental rh variation extends from 3% to 97%. The desired rh rates are maintained by equilibrating samples for 0.5 hours with their environment.

2.5. Qualitative XRD Analysis. The qualitative XRD analysis is achieved by QualX 2.0 program [66]. The commercial PDF-2 database associated with the new freely available database POW_COD is used. This analysis targets to identify all present sample phases and provide information, respectively, about the layer thickness (hydrous indication), the 00l reflections positions, and the diffracted profile geometry (based on the symmetry and/or asymmetry peak observations). Additionally, the

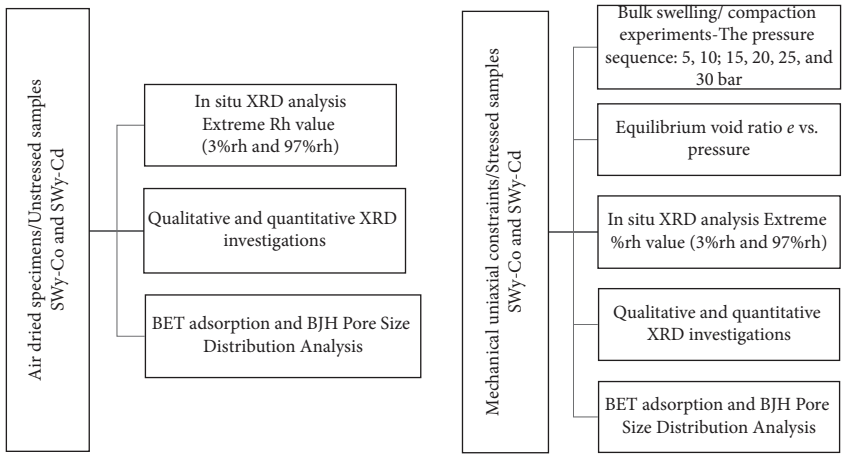

Figure 1: Experimental process of the mechanical constraint details, the in situ XRD analysis, and the porosity characterization.

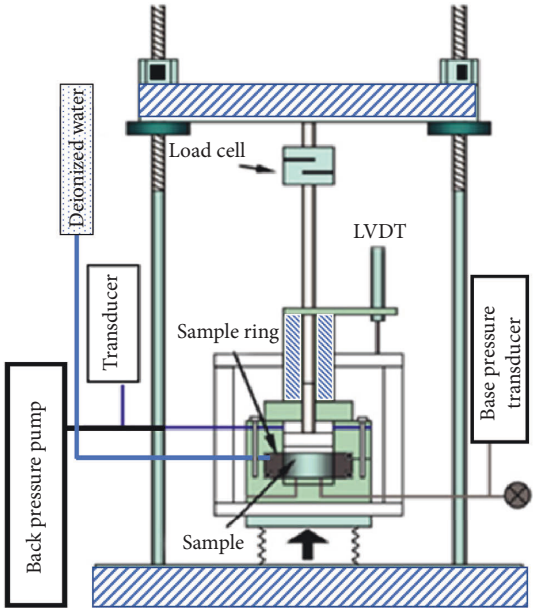

Figure 2: Schematic of oedometer installation used for the bulk swelling/compaction experiments.

calculation of "Full Width at Half Maximum" (FWHM) and the rationality deviation parameters (ξ) related to the 00l reflection (calculated as the standard deviation of the $? \times ?_{00l}$ values for all $?_i$ measurable reflections over the explored $2\theta^{\circ}$ angular range) can provide information on the degree of hydration heterogeneity [66–70]. However, the qualitative interpretation of the XRD profile cannot provide a detailed insight into the coexistence of the different phases with their associated relative proportions as well as their different hydration states, which may coexist in the structure. On the other hand, it does not make it possible to follow the evolution and/or the fluctuations of certain structural parameters along the c^* axis. For these reasons, it is necessary to introduce the quantitative XRD analysis based on the XRD modelling approach.

2.6. Modelling (00l) Reflection Profiles. The theoretical diffracted XRD intensity by a disordered lamellar structure is based on the Drits and Tchoubar [71] algorithm. Based on the expression of the diffracted theoretical intensity, detailed information going from the crystallite size to the elementary tetrahedral or octahedral sheet and its composition can be reached [71]. By optimizing several structural parameters (i.e., Z coordinates of the IS, exchangeable cation position and abundance, and water molecule distribution) during the modelling process, the agreement quality is improved [72–74]. R_{wp} is used as a confidence factor to control this quality [74]. The existing mathematical arsenal behind the modelling approach as well as the details of the fit strategy adopted is exposed in several earlier works [75–77]. It remains to be noted that (per half unit cell) the IS exchangeable cation position respects the provided literature data on similar samples [78, 79].

2.7. Layers Interstratification: Probabilistic Description. The layers stacking within crystallite is defined by the probabilities of succession of the different layer type, which is described according to the Markovian statistics model. The probability of the presence of one layer is only dependent on the types of layers that precede it. The relationship between the presence of a layer and the preceding types of layers corresponds to the degree of order of the interlayer or Reichweite (R). In soils, the most common Reichweite is $R0$ and $R1$; there are also interstratified $R2$ or $R3$ whose probability of occurrence of a layer depends on the two or three previous layers; the latter are not described in the soils but in the diagenetic series. Equations have been developed [70, 78, 79] to respond to clay interstratification problems. We thus find the probabilistic model where we represent (in a simple case) the stacking of two types of layers A and B of proportions W_A and W_B with the probabilities that layer A follows layer B (P_{BA}). The fundamental equations governing this interstratification are as follows:

$$W_A + W_B = 1\, P_{AA} + P_{AB} = 1$$
$$P_{BA} + P_{BB} = 1\, PW_A P_{AB} = W_B P_{BA} \quad (4)$$

Using a combination of the equation, three essential limits for the layers stacking mode appear:

(i) The random stacking $R0$ with $P_{AA} = W_A$ (i.e., no stacking sequence is forbidden; the probability of appearance of a layer in a sequence does not depend on its abundance).

(ii) Stacking with maximum order R1-MPDO prohibiting the succession of two layers in the minority.

(iii) In the case where it is forbidden for two layers of different nature to follow one another ($P_{AB} = P_{BA} = 0$), the probability that two layers of the same nature do so is therefore equal to 1 ($P_{AA} = P_{BB} = 1$), and it is no longer interstratification question but of a physical mixture or total segregation.

It should be noted that the montmorillonite hydration heterogeneities can be treated as layer interstratifications at different hydration states within a clay particle depending on the relative humidity. This can constitute the intermediate hydration state (i.e., 0 W/1 W, 1 W/2 W, and 0 W/1 W/2 W). Hydration heterogeneity is linked to the presence of layer structure heterogeneity (proportion and charge localization of charges) [70, 78, 79].

2.8. Adsorption Measurement and Porosity Investigation. The relationship between mechanical stress and montmorillonite water content affects many geotechnical properties of unsaturated soils, including permeability, volume change, deformation, and shear strength. The main clay properties are mainly controlled by their internal and external surface [80, 81]. The investigation of montmorillonite porosity fate, having undergone structural transformations following the application of mechanical stress, seems essential to confirm quantitative XRD results. Also, the water retention properties are related to the pore structure and the level of external relative humidity experienced. With compaction/reswelling cycles and in situ study by variation of %rh, more layers of water molecules can either be absorbed on the surface of the pores or evacuated by drainage/diffusion by a new transport mechanism.

Adsorption-desorption nitrogen by porous media mainly targets the determination of the surface area (SA) and the pore size distribution (PSD). Montmorillonite powders are obtained by drying each sample. The porosity characteristics are entirely determined by nitrogen sorption [82]. The adsorbed gas amount gives a complete description of the porosity state and even the overall structure [82–86]. Quantachrome NOVA 2000e series volumetric gas adsorption instrument, which is a USA automated gas adsorption system using nitrogen as the adsorptive, is used for the BET-specific surface area and PSD measurement.

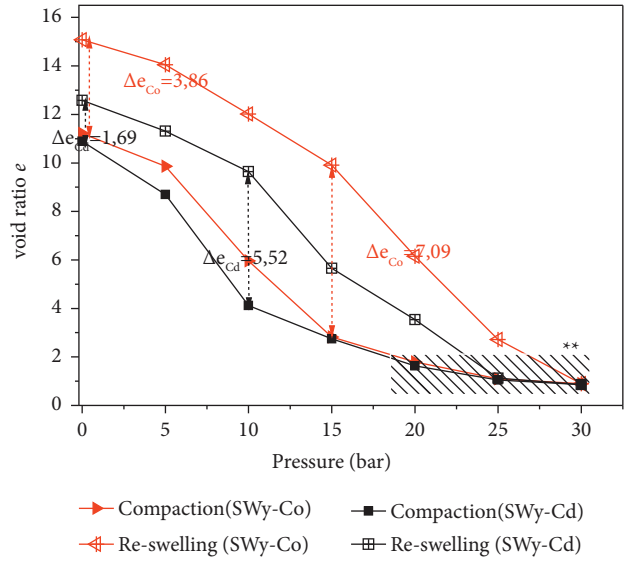

Figure 3: Equilibrium void ratio e for the compaction and reswelling versus applied pressure for SWy-Co and SWy-Cd samples. ∗ ∗ Zone of maximum applied pressure intensity.

Experience setting conditions are as follows: (i) adsorption isotherms are obtained at 77 K and at $P/P0$~0.95 (relative pressure); (ii) the SA and PSD measurements require the removal of adsorbed nitrogen and oxygen. This is carried out under reduced pressure (vacuum) at 100°C for 10 h. The desorption isotherms section, assuming a cylindrical pores model, is the basis of the application of the BJH method to define the PSD [82–91].

3. Results and Discussion

3.1. The Oedometric Test: Compaction and Reswelling. Several parameters control the clay material response to mechanical stress. Montmorillonite fractions are characterized by high porosity and a total volume which essentially depends on the water content, the water saturation, and the water retention mechanisms. Other intrinsic/multiscale parameters ranging from the geological genesis to the individual layer nanometric properties influence the possible deformations [92–95]. This work investigates the response of metal-exchanged montmorillonite specimens (i.e., exchangeable cations are Co^{2+} or Cd^{2+}) to uniaxial mechanical stress ensured by an oedometric test (loading/unloading). The applied stress is confirmed by investigating the void ratio e modification giving the applied pressure (Figure 3). The reswelling curve is obtained following a release of the applied pressure (Table 1). At first sight, the compaction/reswelling curves show the deformation irreversibility process and the nonlinear process, whatever the exchanged cation nature, which agrees with [72, 91] works. This behaviour finds an explanation in [64], which attributes the observed nonlinearity of the consolidation characteristics to the correlation between the consolidation stress (σ_v) and the void ratio (e).

The observed nonlinearity during the loading/unloading process concerns only a single stress cycle which resulted in remarkable fluctuations in the void ratio values. The

Table 1: Equilibrium void ratio e for the compaction and reswelling data for SWy-Co and SWy-Cd samples. Zero bar corresponds to "free" swelling.

Mechanical constraint	P (bar)	0	5	10	15	20	25	30
Compaction	SWy-Co	11.22	9.86	5.96	2.82	1.79	1.10	0.90
Reswelling	SWy-Co	15.08	14.05	12.02	9.91	6.15	2.72	0.90
Compaction	SWy-Cd	10.89	8.69	4.12	2.75	1.63	1.05	0.86
Reswelling	SWy-Cd	12.58	11.31	9.64	5.66	3.54	1.13	0.86

microobjective here is to create material fatigue to examine its hydric behaviour afterwards by varying %rh under a controlled atmosphere. For the two samples, a gap separating the void ratio values Δe in the absence of applied pressure (pressure = 0 bar) is partly explained by the coexistence of two possible scenarios, respectively, irreversible energy losses and interparticle friction, which is an intrinsic phenomenon in lamellar structures and which occurs during the progressive alignment of the particles/crystallites by increasing constraint strength [87, 88].

To understand the obtained void ratio values fluctuations during the reswelling process, the effective stress parameter, the swelling index (Cs), and the compression index (Cc) are introduced. Indeed, [64] uses the constant rate of strain CRS test as a crucial parameter to explore the unloading behaviour of clay minerals. For that, the pore water pressure excess during the unloading sequence is modelled by an assumption based on a cubic polynomial equation. Indeed, the Cc or Cs variations are very sensitive to the consolidation time (at constant load before the unloading) consideration. Along the compaction/reswelling sequence and the global pressure range (0 to 30 bar), in the case of the SWy-Co sample, $\Delta e_{Co} = 3.86$. This value decreases in the case of the SWy-Cd sample to $\Delta e_{Cd} = 1.69$.

On the other hand, a maximum gap is observed for an applied pressure of 15 bar and for which Δe jumps to 7.09 for Co^{2+}. For Cd^{2+} cation, the maximum Cs and Cc fluctuations are observed at 10 bar when Δe jumps to 5.52. For a maximum applied pressure intensity (zone $**$ on Figure 3) and whatever the nature of the exchangeable cation, a similar behaviour of Cs and Cc is observed during the loading sequence from 15 bar. During the unload sequence (reswelling) and from 30 bar applied pressure values, a divergence between the evolution of Cc and Cs is observed.

This noted disparity is explained by the process irreversibility at the nanoscopic scale, where the layer organization inside the crystallite depends essentially on the composition of the interlamellar space (IS). The intrinsic IS configurations are affected by the nature of the exchangeable cation, which afterwards will affect the layer stacking and the crystallite geometry. In fact, the diffuse ion layers around the particles lead to interparticle repulsion ascribed to the osmotic activity of the ions. The existing repulsion force decreases when increasing, respectively, the distance between clay particles, electrolyte concentration, and exchangeable cation valence. It should be noted that the obtained data for the "free" swelling state is realized when the sample is constrained only by the friction of the piston.

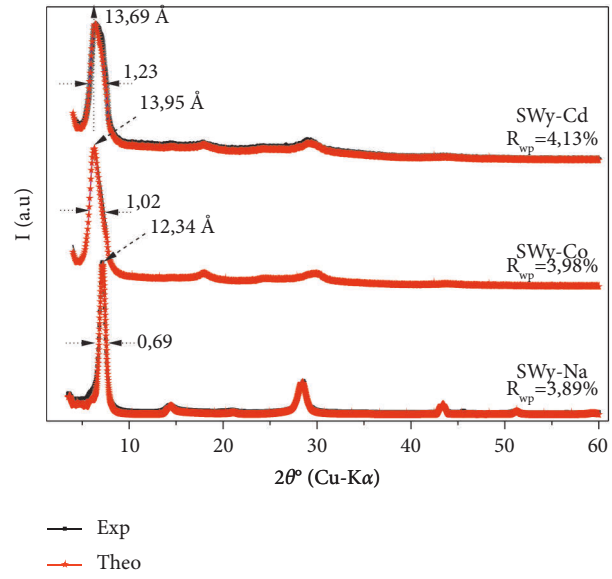

Figure 4: Best agreement obtained between theoretical (red scatter) and experimental (black line) profiles for all studied samples.

3.2. XRD Analysis of Unstressed Samples. The best agreement between the experimental and theoretical XRD profiles for the stressed samples is summarized in Figure 4. Qualitatively, a classical homogeneous 1 W layer phase is observed in the case of SWy-Na [67]. This hydration homogeneity is confirmed by the low values of FWHM and ξ parameter (Table 2) [74]. For the SWy-Co and SWy-Cd samples, an interstratified 1 W/2 W hydration character is observed throughout the entire exploited angular range. The initial d_{001} (Å) value increased (Table 2) towards 13.95 and 13.69, indicating probably the achievement of the cation exchange process and a new IS configuration. For both cases, the XRD profile geometry is characterized by an irrational 00l position (ξ parameter) with a large 001 refection (FWHM ($2\theta^{\circ}$)) = 1.02 and 1.23). The 001 reflection is accompanied by a shoulder towards 7.48 ($2\theta^{\circ}$) attributed to 1 W hydration phases ($d_{001} \approx 12$ Å). Generally, the observed asymmetric 001 reflection reflects the coexistence of several hydration states within the stack and/or an incomplete (partial) cation exchange. Two possible interpretations arise in this case. Either the cation exchange capacity (CEC) is fully saturated by the exchangeable cations, or a minor fraction of the starting Na^{+} cation persists in the IS with partial cation exchange. Compared with the work of [58–60] and considering the ionic potential affinity of the two cations with optimized, verified, and reproducible experimental conditions,

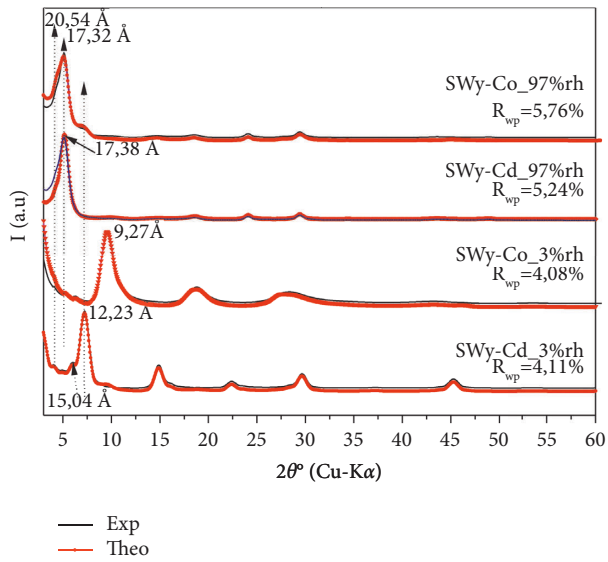

Figure 5: Best agreement obtained between theoretical and experimental profiles for stressed SWy-Cd and SWy-Co studied under extreme %rh value.

Table 2: Qualitative XRD investigation in the case of unstressed and stressed samples.

Samples	$2\theta^\circ$	d_{001} (Å)	FWHM ($2\theta^\circ$)	D (Å)	ξ (Å)	Hydration characters
Unstressed sample						
SWy-Na	7.16	12.34	0.69	25.13	0.086	Homogenous
SWy-Co	6.25	13.95	1.02	16.67	0.428	Interstratified
SWy-Cd	6.45	13.69	1.23	20.62	0.812	Interstratified
Stressed sample						
SWy-Co_3%rh	9.53	9.27	0.64	11.86	0.151	
SWy-Co_97%rh	5.10 4.30	17.32 20.54	1.41	10.67	0.875	Interstratified
SWy-Cd_3%rh	7.22 5.87	12.23 15.04	0.78	12.56	0.127	
SWy-Cd_97%rh	5.08 4.39	17.38 20.11	1.33	11.14	0.788	Interstratified

obtained results in the case of Cd^{2+} and Co^{2+} cation are in concordance. More details can be given later by quantitative XRD analysis. Quantitative XRD investigations are the solution to decide with the predictions of the qualitative analysis [70, 76]. Indeed, in the case of interstratified structures, several hypotheses are necessary, whose resolution requires a more in-depth theoretical approach. In the case of the SWy-Na sample, an agreement between the experimental and theoretical profile is obtained with an $R_{wp} = 3.89\%$ (Table 3). The position of the sodium and its hydration sphere at the medium of the IS respects the literature data [57]. On the other hand, the experimental profile is reproduced theoretically through a randomly distributed two phases, qualitatively inapparent, between a major contribution of the 1 W state (≈75%) and a minor contribution of (≈25%) relative to the 0 W layer.

The 00*l* reflections modelling approach in the case of the SWy-Co sample supposes the coexistence of three mixed layers structure MLS saturated with the Co^{2+} cation. Theoretical models exhibit variable hydration states (e.g., 1 W, 1 W/2 W, and 1 W/2 W). The used MLS (from the best agreement) are decomposed into several layer populations (Table 3) assembled according to a specific succession probability law. The structural parameters released from theoretical models are summarized in Table 3. The MLS are obtained by weighted layer-type populations, which are expected to have, respectively, identical chemical composition, identical layer thickness, and identical Z coordinates of the atoms [67, 96–98].

The best fit of the experimental XRD pattern ($R_{wp} = 4.13\%$) (Figure 4) in the case of the SWy-Cd sample is obtained through theoretical models mainly composed of an interstratified structure using three MLSs including various relative proportions of the hydrated layer (Table 3). The foremost remark in this case is the presence of a reasonable 1 W phase weight (9.04%) attributable to the saturation of the material CEC by starting Na^+ cation. This agrees with the starting assumption concerning the observed experimental 001 reflection shoulder at 7.48 ($2\theta^\circ$). This result calls into question the achievement of the cation exchange process despite compliance with the reproducibility of the experimental cation exchange protocol.

Table 3: Optimal structural parameters taken from quantitative XRD analysis for all studied samples.

Sample	%MLS	xW_Exc.Cat	L.Th (Å)	n_{H2O}	W_A	P_{AA}	M	M_{tot}	$\%R_{wp}$
SWy-Na	74.3	1W_Na	12.2	1.5	1	1	12	9	3.89
	25.7	0W_Na	12.2	0	1	1	5		
SWy-Co unstressed	52.36	1W_Co	12.2	0.8	1	1	11	9	3.98
	33.84	1W_Na	12.2	0.4	0.7	0.59	7		
		2W_Co	15.2	0.3	0.3				
				0.3					
	13.80	1W_Co	12.2	0.4	0.5	0.5	5		
		2W_Co	15.2	0.3	0.5				
				0.3					
SWy-Cd unstressed	51.44	1W_Cd	12.2	0.9	1	1	12	14	4.13
	39.52	1W_Cd	12.2	0.15	0.7	0.71	6		
		2W_Cd	15.2	0.15	0.3				
				0.15					
SWy-Co stressed 3%rh	9.04	1W_Na	10	1.5	1	1	6	10	4.08
	68.61	0W_Co	9.5	0	1	1	12		
	31.39	0W_Co	9.5	0	0.7	0.72	5		
		0W_Na	9.3	0	0.3				
				0					
SWy-Cd stressed 3%rh	65.21	1W_Cd	12.2	0.7	1	1	12	10	4.11
	31.52	1W_Cd	12.2	0.1	0.7	0.6	5		
		1W_Na	12.3	0.1	0.3				
				0.1					
SWy-Co stressed 97%rh	3.27	0W_Cd	9.8	0	1	1	4	7	5.76
	70.20	3W_Co	18.1	1.5	1	1	8		
	23.50	3W_Na	18.2	1.5	0.7	0.7	5		
		4W_Co	21.1	2	0.3				
				2					
SWy-Cd stressed 97%rh	6.30	2W_Na	15.2	1	1	1	4	7	5.24
	70.47	3W_Cd	18.2	1.5	0.3	0.3	8		
		4W_Cd	21.2	2.1	0.7				
				2.1					
	27.57	3W_Cd	18.2	1.5	0.7	0.7	5		
		2W_Na	15.2	1.2	0.3				
				1.2					
	1.96	2W_Na	10	1	1	1	5		

Note. xW_Exc.Cat: layer type and the associated exchangeable cation; L.Th: layer thickness in Å. 2 W, 1 W, and 0 W are attributed to the layer hydration state. n_{H2O}: the number of H_2O molecules per half unit cell. Z_{H2O}: position along $c*$ axis of H_2O molecule is fixed to 10.5 Å, 11.3 Å//13.6 Å, 11.3 Å//13.6 Å//16.6 Å, and 11.3 Å//13.6 Å//16.6 Å//19.3 Å, respectively, for 1 W, 2 W, 3 W, and 4 W hydration state. The position of exchangeable cations per half unit cell calculated along the c$*$ axis is fixed to 8.6 Å, 10.50 Å, 12.4 Å, 14.7 Å, and 16.8 Å, respectively, for 0 W, 1 W, 2 W, 3 W, and 4 W hydration state [78]. $-n_{EXC.CAT}$: the number of exchangeable cations per half unit cell is fixed to 0.33 (for Na^+ cation) and 0.165 for (Co^{2+} and Cd^{2+} cation), indicating full saturation of the cation exchange capacity (CEC).

3.3. XRD Analysis of Mechanically Stressed Samples

3.3.1. Qualitative Investigation. The effect of the applied mechanical stress on the hydration properties of Cd^{2+} and Co^{2+} exchanged montmorillonite is addressed by varying the %rh rate under a controlled atmosphere. The goal is to see the structural evolution of the studied specimens under extreme %rh values (3%rh and 97%rh) (after environment equilibrium), which then allows us to simulate real IS changes affected using clay as a geological membrane. Experimental XRD patterns obtained in the case of SWy-Cd at 3%rh show a $d_{001} = 12.23$ Å indicating probably a 1 W hydration state. An interstratified hydration trend is confirmed by the elevated FWHM and ξ parameter value (Table 2). Indeed, a left-handed profile asymmetry towards the low angles ($2\theta = 5.84°$; $d_{001} = 15.04$ Å), which is ascribed to a minor 2 W hydration state phase, was observed despite the conditioned dry environment. The d_{001} basal spacing value shows conservation of the 1 W hydration state regardless of the experimental equilibrium achieved at 3%rh (one hour of equilibrium with its environment before starting the XRD recording).

For the SWy-Co at 3%rh, the sample seems more sensitive to the %rh level drop, and the $d_{001} = 9.27$ Å indicates a basically dehydrated 0 W state. The observed result is a real manifestation not only of the %rh fluctuations effect but also of the mechanical stress already applied through the compaction and reswelling cycle. The conclusion that can be drawn by qualitative comparison between these two samples (having undergone the same stresses) lies in the modification of the IS organization. Indeed, the basal spacing shift is directly related to the new IS organization, which is very

sensitive to the electrostatic and chemical bonding forces governing the IS equilibrium.

The IS water molecules insertion/release mechanism is interpreted by a hypothesis based on three freedom degree fluctuations, including, respectively, the positions, the abundances of the IS species, and the associated layer stacking probabilities. All cited structural parameters, treated individually or coupled, complicate and/or facilitate the water molecule release process, which can be established when decreasing the %rh rate. This hypothesis is since interpreted in the case of the SWy-Cd sample by the free water transformation (supporting cation exchange process) from the surrounding environment into structural water (intrinsic layer composition), incorporated in the internal and external pore surfaces, which complicates its loss by dehydration [60, 68]. It is noted that, in the case of the SWy-Co sample, an uncomplicated release of an IS water molecule is observed.

At 97%rh, SWy-Cd and SWy-Co are characterized by an asymmetric 00l reflection profile (Figure 5). Both samples present a high hydration state with d_{001} equal, respectively, to 17.38 Å and 17.32 Å, indicating probably a transition to the 3 W hydration state. A shoulder towards the small angles ($d_{001} = 20.54$ Å), which is attributed to a beginning 3 W⟶4 W hydrous transition state, is observed. An interstratified global character is confirmed by the high values of FWHM and the rationality parameter.

3.3.2. XRD Profile Modelling Approach. The best agreement between theoretical and experimental XRD patterns obtained at a variable %rh rate is confirmed by an acceptable R_{wp} that did not exceed 5.71%. Optimum structural parameters used to imitate experimental XRD profile are reported in Table 3.

The theoretical IS water molecule distribution and the compensator cation position follow a discrete distribution consistent with [57, 67, 74] works. For each accepted theoretical model, several layer types with variable stacking modes are used to improve the agreement. The partial segregation ($R1$) is the main MLS distribution adopted for all studied samples. At 3%rh, the experimental profile of the SWy-Cd sample is reproduced by mixing three MLS mainly composed of a major 1 W layer fraction (saturated by Cd^{2+} cation). For the same sample, a minor proportion of the Na^{+} saturated layer is used. Generally, the absence of a monohomogeneous 1 W phase at 3%rh and an $R1$ stacking mode type is the main conclusion. In the case of the SWy-Co sample, which presents a 0 W hydration state at 3%rh, the diffracted intensity is reproduced by two MLS (0 W) mainly saturated by Co^{2+} and Na^{+} cations (Table 3). At 97%rh and regardless of the exchangeable cation nature, the 0 W and 1 W phase contribution in the MLS disappears. The experimental profiles are entirely reproduced by a three-MLS combination characterized by variable weighted layer population. For SWy-Co, a minority bihydrated phase related to Na^{+} cation is introduced, and the major layer fraction saturated by Co^{2+} cation (extremely hydrated 3 W or 4 W water layers) is used to obtain a good fit.

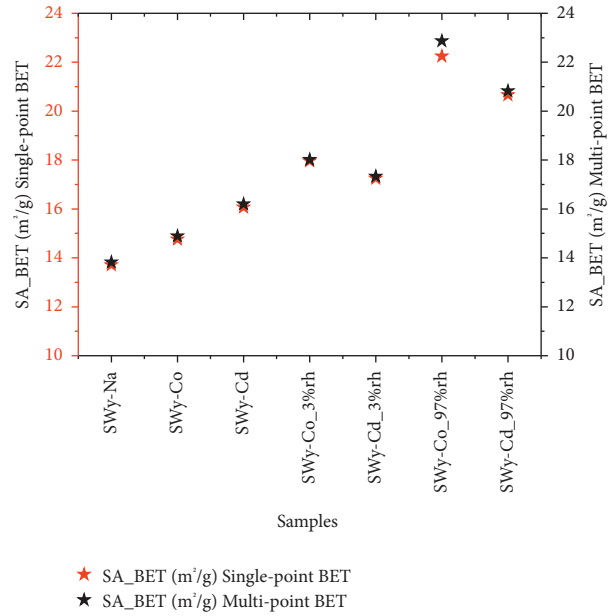

Figure 6: SA_{BET} single and multipoint BET for unstressed and stressed samples.

For SWy-Cd, the structure is completely matched by combining three MLS. Indeed, theoretical models contain a major contribution of 3 W/4 W phase, and the sample retains its interstratified character, which is in accordance with the qualitative description mentioning an interstratified phase. Among the strengths of the modelling approach, the accurate structural heterogeneities identification is related to the coexistence of variable layer populations within the clay particle. Subsequently, it allows us to show the structural changes affecting the IS after applying stresses (Table 3).

3.4. Adsorption and Porosity Features. The clay properties are mainly monitored by their internal and external surface. The total surface includes the external surface, between the clay particles, and the inner surface, relating to the IS. Internal and external layer surfaces are affected during the compaction and reswelling process. The surface modification will probably influence the chemical and physical bonds with the IS content and the adsorption properties. The layer stacking distribution is affected by the applied mechanical constraint (results obtained from XRD analysis), and a possible consequent porosity disturbance may be conducted. In fact, after stress release, the configuration theoretically leans towards a new equilibrium, which differs from the starting configuration [99, 100].

The montmorillonite porosity is still poorly characterized because of the difficulty of visualizing hydrated samples in their original condition. The potential relation between porosity, CEC, crystallite shape/size, and applied mechanical stress is assured by the correlation of BET adsorption measurement and BJH pore size distribution analysis. Single-point and multipoint BET methods (based on the surface area (SA)) are used to assess the possible chemical transformation affecting the external clay layer surface. This

purpose is achieved from nitrogen isotherms [90]. To measure the average pore diameter for each sample, a BJH method is applied. The obtained results from adsorption measurement and porosity for all studied samples are summarized in Figures 4 and 7. Results show an increase in the calculated external surface for samples having undergone mechanical stress, whatever the nature of the exchangeable cation and the constraint type (compaction or reswelling).

By comparing SA value evolution, after applying mechanical stress, a logical values boost is observed for the stressed samples, whatever the applied %rh rate. This is probably interpreted by a crystallite exfoliation tendency which results in a decrease in the average number of layers per crystallite following the layer cohesion damage. Also, it can be interpreted by the diffusion coefficient alteration in relation to the packaging density of the montmorillonite. For saturated CEC by Co^{2+} cations, high SA values are obtained, suggesting the effect of the exchangeable cation nature on the new IS configuration (Figure 6). The average nanopore diameter (Figure 7) respects the same trend with values boost after stress regardless of the cation exchanged.

For all examined samples, an isotherm of nitrogen adsorption- (ads-) desorption (des) was presented (Figure 8). A type II adsorption isotherm [84, 86, 90] is closer to the shape of the obtained curves. This allocation is due to the mesoporous texture described by coexisting of large pores with nanopores, which agrees with the pore sizes distribution for the porous materials. Large pore sizes obtained in the case of stressed SWy-Co sample are justified by the coupling of three essential parameters, respectively, the loading/unloading cycle, the %rh fluctuations (which constitutes a hydrous constraint), and the nature of the exchangeable cation. The Co^{2+} ions exchange promotes the exfoliation process and thereafter increases the porosity degree.

The SA concept does not permit a full textural description extending from 2D to 3D in the case of lamellar structures. The failures and limitations of SA results interpretation involve improvements established on the PSD analysis to access IS information. The PSD analysis is directed based on several approximations summarized in Table 4. The V-r (cumulative pore volume versus pore radius) plots or the mesopore PSD are given in Figure 9. A considerable disparity between SWy-Co and SWy-Cd sample pore size evolution was obtained. For unstressed and stressed samples, the saturated SWy-Co specimen varies in a very close way to the SWy-Cd sample, provided that the diameter of the pores does not exceed 3 nm. For higher values, a divergence appears with a "gap" in favor of Co^{2+} cation, which reaches 0.0068 mL/g (Figure 9). The obtained V-r variation proves, initially, the achievement of the cation exchange process, which is confirmed by specific V-r curve trends yet showing the same appearance. In addition, an increase in the V-r "gap" for stressed samples seems like the direct effect of the application of mechanical stresses. The V-r curve radius derivative for all samples is given in Figure 10.

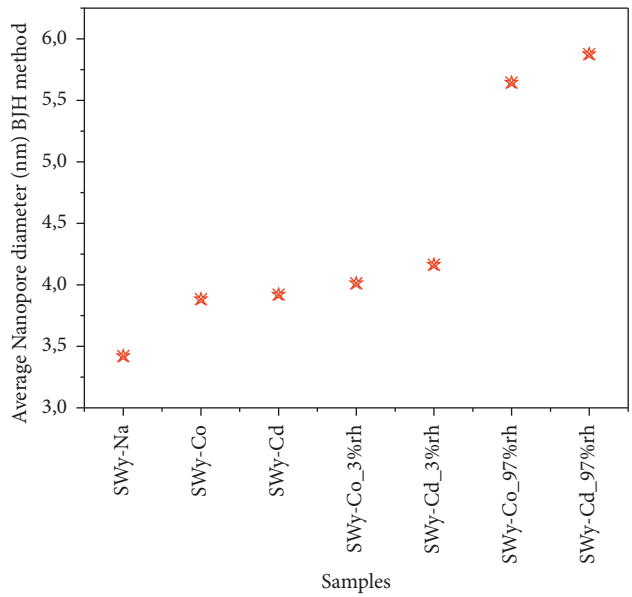

Figure 7: BJH method average pore diameter for unstressed and stressed samples.

The maximum mesopore volume (0.00620 mL/g) reached at 3.99 nm is obtained for the stressed SWy-Co sample. In this case, the determined V-r values are far greater than those relating to SWy-Cd. The gap between the two stressed samples exaggerates until it reaches gap values of 0.0030. This variation is consistent with the XRD modelling profile, which predicts layer exfoliation and presence of a highly hydrated rate (4 W) for both SWy-Co and SWy-Cd. Commonly, the applied mechanical stress affected the volume of the mesopores, which are in any case greater than those determined for the starting sample. For all samples, the mesopore radii varied between 1.598 and 16.828 nm (Figure 10). The porosity investigation using the BET-BJH method confirms obtained results from XRD modelling approach indicating, respectively, high hydration rate layer exfoliation trends and crystallite size fluctuations induced by stress.

The maximum mesopore volume (0.00620 mL/g) is obtained for the stressed SWy-Co sample. The determined V-r values, in the case of SWy-Co, are far greater than those relating to SWy-Cd. For the stressed SWy-Co sample, the maximum mesopore volume is 0.00620 mL/g and obtained at 3.99 nm. The gap between the two stressed samples exaggerates until it reaches gap values of 0.0030. This variation is consistent with the XRD modelling profile, which predicts layer exfoliation and presence of a highly hydrated rate (4 W) for both SWy-Co and SWy-Cd. Commonly, the applied mechanical stress affected the volume of the mesopores, which are in any case greater than those determined for the starting sample. For all samples, the mesopore radii varied between 1.598 and 16.828 nm (Figure 10). The porosity investigation using the BET-BJH method confirms

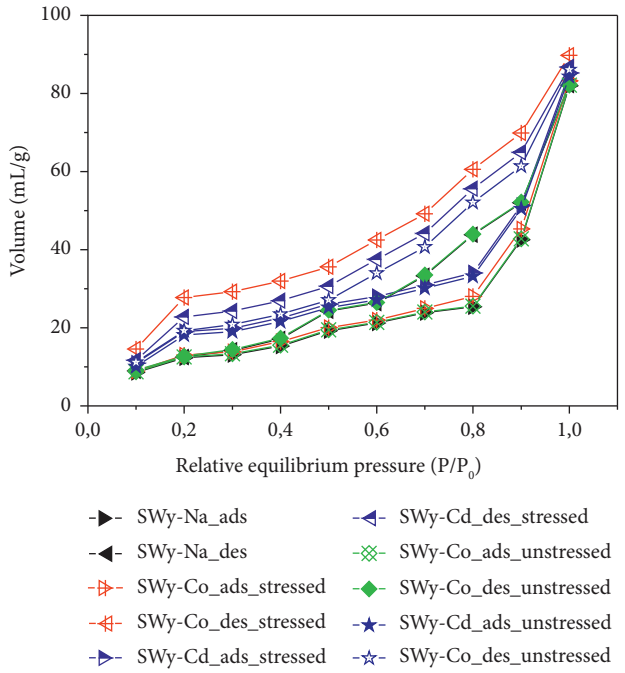

Figure 8: Nitrogen adsorption- (ads-) desorption (des) isotherms.

Table 4: The basic physical approximations adopted for the PSD analysis.

Technical side	Fundamental side
P_0 is the vapor pressure of the bulk liquid nitrogen at the liquid nitrogen temperature (~77 K)	Cylindrical pores shape
P is the equilibrium pressure of desorption at the liquid nitrogen temperature (~77 K)	Cylindrical pores radius (r) approximatively half of its width
The volumes of micropores, mesopores, and macropores, including nanopores in one gram solid, are labelled, respectively, V_{Mi}, V_{Me}, and V_{Ma} (all in mL/g)	Cylindrical mesopores with radii (r) corresponding to V values calculated from the corrected Kelvin equation using P/P_0 values
Specific micromesopore volumes ($V = V_{Mi} + V_{Me}$) is determined using the desorption data (at the relative equilibrium pressure P/P_0)	Macropores do not affect the adsorptive properties [76]

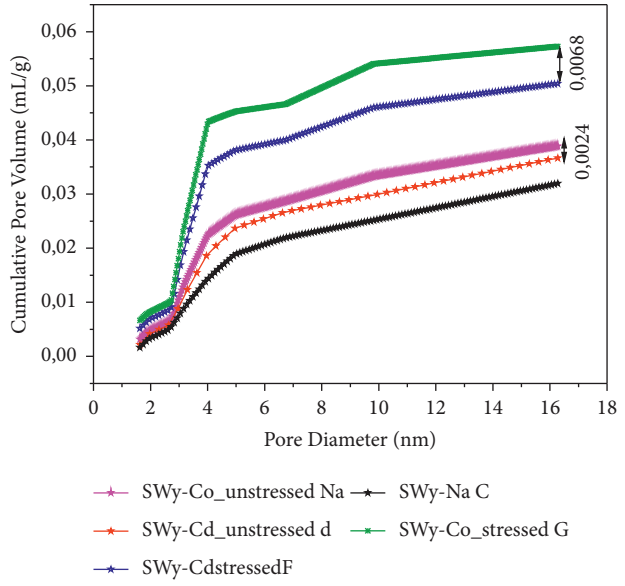

Figure 9: The pore size distribution (PSD) curve for the different studied samples (V-r).

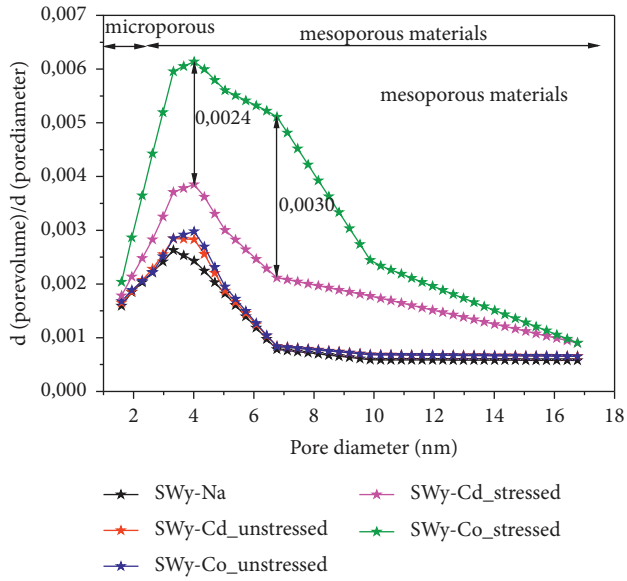

Figure 10: The derivative pore size distribution curve.

obtained results from XRD modelling approach indicating, respectively, high hydration rate layer exfoliation trends and crystallite size fluctuations after stress.

4. Conclusion

This work investigates structural impact, IS response, quantitative CEC instabilities, and porosity alteration of metal-exchanged montmorillonite (Co^{2+} and Cd^{2+}) according to the mechanical constraints created at the laboratory scale. Structures heterogeneities, hydration behaviour, and relationships between macroscopic stresses and microscopic hydration properties have been disclosed through the XRD profile modelling approach and the adsorption measurement. Obtained results demonstrate the following: (i) The void ratio *e* deviation increases along the compaction/reswelling process regardless of the exchangeable cation nature. (ii) At a low extreme %rh rate (3%), a clear and easy 0 W dehydration process is observed for the Co^{2+} cation, which is not obvious for the Cd^{2+} cation, which keeps a 1 W hydration state despite the mechanical disturbance. (iii) A highly 3 W/4 W hydrated state appears for the two studied samples brought to 97%rh, which is explained by a reduction in the average number of layers per crystallite evidence of an exfoliation tendency and the ease of filling of the IS. (iv) At 97%rh, mechanical damage induces, respectively, a clear interstratified character, segregation layer stacking trends, sensitive layer-type junction probabilities, and an increase in the used MLS. (v) The adsorption measurement results confirm the exfoliation layer trends for stressed samples. (vi) The divergence of V-r fluctuations proves the achievement of the cation exchange process, which is confirmed by the specific conduct of the V-r curves despite having the same appearance. (vii) The mechanical stress effect is reflected in the V-r curve by a high "gap" for the stressed samples. (viii) The mesopore V-r shows raised values in the case of Co^{2+} cation, indicating a new IS arrangement (compared with the starting sample) allowing better water profit for the SWy-Co sample [101–103].

Data Availability

The generated and analysed data during the current study are included within the article and can be obtained from the corresponding authors upon reasonable request.

Conflicts of Interest

The authors declare no conflicts of interest.

Authors' Contributions

Walid Oueslati (WO) was responsible for conceptualization, methodology, investigation, validation, formal analysis, visualization, data curation, resources, supervision, writing, editing, reviewing, and project administration. Chadha Mejri (CM) was responsible for investigation, visualization, and resources. Abdesslem Ben Haj Amara (ABHA) was responsible for methodology and resources.

Acknowledgments

The authors acknowledge the assistance provided by the editor.

References

[1] M. Tondel and L. Lindahl, "Intergenerational ethical issues and communication related to high-level nuclear waste repositories," *Current Environmental Health Reports*, vol. 6, no. 4, pp. 338–343, 2019.

[2] S. S. K. AB, "Long-term Safety for the Final Repository for Spent Nuclear Fuel at Forsmark," *Main Report Of the SR-Site Project*, vol. 1, p. 276, 2018.

[3] SELROOS, Jan-Olof et FOLLIN, Sven, "Overview of hydrogeological site-descriptive modeling conducted for the proposed high-level nuclear waste repository site at Forsmark, Sweden," *Hydrogeology Journal*, vol. 22, no. 2, pp. 295–298, 2014.

[4] G. Bernd, "Geological disposal of radioactive waste in clay," *Elements*, vol. 12, no. 4, pp. 239–245, 2016.

[5] R. C. Ewing, "Long-term storage of spent nuclear fuel," *Nature Materials*, vol. 14, no. 3, pp. 252–257, 2015.

[6] P. Landais, "Advances in geochemical research for the underground disposal of high-level, long-lived radioactive waste in a clay formation," *Journal of Geochemical Exploration*, vol. 88, no. 1-3, pp. 32–36, 2006.

[7] T. Manzel, C. Podlech, G. Grathoff, S. Kaufhold, and L.. N. Warr, "In situ measurements of the hydration behavior of compacted Milos (SD80) bentonite by wet-cell X-ray diffraction in an Opalinus clay pore water and a diluted cap rock brine," *Minerals*, vol. 11, no. 10, pp. 1082–1116, 2021.

[8] F. Claret, N. Marty, and C. Tournassat, "Modeling the long-term stability of multi-barrier systems for nuclear waste disposal in geological clay formations," in *Reactive Transport Modeling: Applications in Subsurface Energy, and Environmental Problems*, John Wiley and Sons, Eds., vol. 2018pp. 395–451, Chichester, UK, 2018.

[9] G. Montes-H, B. Fritz, A. Clement, and N. Michau, "Modeling of transport and reaction in an engineered barrier for radioactive waste confinement," *Applied Clay Science*, vol. 29, no. 3-4, pp. 155–171, 2005.

[10] S. Kaufhold and R. Dohrmann, "Distinguishing between more and less suitable bentonites for storage of high-level radioactive waste," *Clay Minerals*, vol. 51, no. 2, pp. 289–302, 2016.

[11] S. Norris, "Multiple roles of clays in radioactive waste confinement–introduction," *Geological Society, London, Special Publications*, vol. 482, no. 1, pp. 1–9, 2019.

[12] Y. Wang, "Leachate Management in the Aftercare Period of Municipal Waste Landfills," *Ph.D. Thesis*, Aalto University, Espoo, Finland, 2013.

[13] Z. Cooper, R. Bringolf, R. Cooper, K. Loftis, A. L. Bryan, and J. A. Martin, "Heavy metal bioaccumulation in two passerines with differing migration strategies," *Science of the Total Environment*, vol. 592, pp. 25–32, 2017.

[14] M. K. Widomski, W. St˛epniewski, and A. Musz-Pomorska, "Clays of different plasticity as materials for landfill liners in RuralSystems of sustainable waste management," *Sustainability*, vol. 10, no. 7, pp. 2489–2505, 2018.

[15] G. Xiao, G. Xu, T Wei, J Zeng, W Liu, and L Zhang, "The effect of Cu (II) on swelling and shrinkage characteristics of sodium bentonite in landfills," *Applied Sciences*, vol. 11, no. 9, pp. 3881–3894, 2021.

[16] P. C. Gomes, M. P. Fontes, A. G. da Silva, E. de S Mendonça, and A. R. Netto, "Selectivity sequence and competitive adsorption of heavy metals by Brazilian soils," *Soil Science Society of America Journal*, vol. 65, no. 4, pp. 1115–1121, 2001.

[17] A. Gupta, R. Zhao, J. T. Novak, and C. D. Goldsmith, "Variation in organic matter characteristics of landfill leachates in different stabilisation stages," *Waste Management & Research: The Journal for a Sustainable Circular Economy*, vol. 32, no. 12, pp. 1192–1199, 2014.

[18] S. Tahervand and M. Jalali, "Sorption and desorption of potentially toxic metals (Cd, Cu, Ni and Zn) by soil amended with bentonite, calcite and zeolite as a function of pH," *Journal of Geochemical Exploration*, vol. 181, pp. 148–159, 2017.

[19] W. Hu, S. Lu, W. Song et al., "Competitive adsorption of U (VI) and Co (II) on montmorillonite: a batch and spectroscopic approach," *Applied Clay Science*, vol. 157, pp. 121–129, 2018.

[20] M. Slaný, L. Jankovič, and J. Madejová, "Structural characterization of organo-montmorillonites prepared from a series of primary alkylamines salts: mid-IR and near-IR study," *Applied Clay Science*, vol. 176, pp. 11–20, 2019.

[21] G. Xiang, W. Ye, F. Yu, Y. Wang, and Y. Fang, "Surface fractal dimension of bentonite affected by long-term corrosion in alkaline solution," *Applied Clay Science*, vol. 175, pp. 94–101, 2019.

[22] H. Lakshmikantha and P. V. Sivapullaiah, "Geotechnical properties of cement treated illite as hydraulic barrier," *Clay Research*, vol. 22, no. 1-2, pp. 29–40, 2004.

[23] J. Bors, S. Dultz, and B. Riebe, "Retention of radionuclides by organophilic bentonite," *Engineering Geology*, vol. 54, no. 1-2, pp. 195–206, 1999.

[24] B Herlin and K. von Maubeuge, "Geosynthetic clay liners (GCLs)," in *Proceedings of the 4th International Pipeline Conference*, vol. 36207, pp. 211–216, 2002.

[25] M. Segad, S. Hanski, U. Olsson, J. Ruokolainen, T. Åkesson, and B. Jönsson, "Microstructural and swelling properties of Ca and Na montmorillonite: (in situ) observations with Cryo-TEM and SAXS," *Journal of Physical Chemistry C*, vol. 116, no. 13, pp. 7596–7601, 2012.

[26] W. Birmili, A. Charron, and R. Harrison, "Treatment of textile wastewater using bentonite clay as a natural coagulant," *Pediatric Transplantation*, vol. 11, pp. 895–900, 2014.

[27] H. Y. Shan and Y. J. Lai, "Effect of hydrating liquid on the hydraulic properties of geosynthetic clay liners," *Geotextiles and Geomembranes*, vol. 20, no. 1, pp. 19–38, 2002.

[28] S. Rosin-Paumier and N. Touze-Foltz, "Hydraulic and chemical evolution of GCLs during filter press and oedo-permeametric tests performed with real leachate," *Geotextiles and Geomembranes*, vol. 33, pp. 15–24, 2012.

[29] B. Wang, J. Xu, B. Chen, X. Dong, and T. Dou, "Hydraulic conductivity of geosynthetic clay liners to inorganic waste leachate," *Applied Clay Science*, vol. 168, pp. 244–248, 2019.

[30] F. N. Charkley, K. Zhang, and G. Mei, "Shear strength of compacted clays as affected by mineral content and wet-dry cycles," *Advances in Civil Engineering*, vol. 2019, pp. 1–8, Article ID 8217029, 2019.

[31] U. Khalid, Z.. u. Rehman, C. Liao, K. Farooq, and H Mujtaba, "Compressibility of compacted clays mixed with a wide range of bentonite for engineered barriers," *Arabian Journal for Science and Engineering*, vol. 44, no. 5, pp. 5027–5042, 2019.

[32] A. Kaya and S. Durukan, "Utilization of bentonite-embedded zeolite as clay liner," *Applied Clay Science*, vol. 25, no. 1-2, pp. 83–91, 2004.

[33] M. Plötze, G. Kahr, R. Dohrmann, and H. Weber, "Hydromechanical, geochemical and mineralogical characteristics of the bentonite buffer in a heater experiment: The HE-B project at the Mont Terri Rock Laboratory," *Physics and Chemistry of the Earth, Parts A/B/C*, vol. 32, no. 8-14, pp. 730–740, 2007.

[34] S. M. Rao and T. Thyagaraj, "Swell–compression behaviour of compacted clays under chemical gradients," *Canadian Geotechnical Journal*, vol. 44, no. 5, pp. 520–532, 2007.

[35] M. Ammar and W. Oueslati, "Crystalline swelling process of Mg-exchanged montmorillonite: effect of external environmental solicitation," *Advances in Civil Engineering*, vol. 2018, pp. 1–18, Article ID 8130932, 2018.

[36] W. Oueslati, "Effect of soil solution pH during the tetracycline intercalation on the structural properties of a dioctahedral smectite: microstructural analysis," *Journal of Nanomaterials*, vol. 201917 pages, Article ID 7414039, 2019.

[37] M. K. Widomski, W. Stępniewski, and A. Musz-Pomorska, "Clays of different plasticity as materials for landfill liners in rural systems of sustainable waste management," *Sustainability*, vol. 10, no. 7, p. 2489, 2018.

[38] Z. Hu, K. Peng, L. Li et al., "Effect of wetting-drying cycles on mechanical behaviour and electrical resistivity of unsaturated subgrade soil," *Advances in Civil Engineering*, vol. 2019, pp. 1–10, Article ID 3465327, 2019.

[39] M. M.. A. Hussein, "Effect of sand compaction piles on the swelling and shrinkage behavior of expansive soil," *Advances in Civil Engineering*, vol. 202110 pages, Article ID 5582197, 2021.

[40] J. Lin, W. Zou, Z. Han, Z. Zhang, and X Wang, "Structural, volumetric and water retention behaviors of a compacted clay upon saline intrusion and freeze-thaw cycles," *Journal of Rock Mechanics and Geotechnical Engineering*, vol. 14, no. 3, pp. 953–966, 2022.

[41] R. Pusch, S. Knutsson, L. Al-Taie, and M. H. Mohammed, "Optimal ways of disposal of highly radioactive waste," *Natural Science*, vol. 04, no. 11, pp. 906–918, 2012.

[42] N. P. Laverov, S. V. Yudintsev, B. T. Kochkin, and V. I. Malkovsky, "The Russian strategy of using crystalline rock as a repository for nuclear waste," *Elements*, vol. 12, no. 4, pp. 253–256, 2016.

[43] Hennig, Theresa, and Michael KÜhn, "Potential Uranium Migration within the Geochemical Gradient of the Opalinus Clay System at the Mont Terri," *Minerals*, vol. 11, no. 10, p. 1087, 2021.

[44] M. Birgersson, O. Karnland, and U. Nilsson, "Freezing in saturated bentonite A thermodynamic approach," *Physics and Chemistry of the Earth, Parts A/B/C*, vol. 33, pp. S527–S530, 2008.

[45] S. D. Baxter, D. Holton, S. Williams, and S. Thompson, "Predictions of the wetting of bentonite emplaced in a crystalline rock based on generic site characterization data," *Geological Society, London, Special Publications*, vol. 482, no. 1, pp. 285–300, 2019.

[46] T. Ishii, M. Kawakubo, H. Asano et al., "A resistivity-based approach to determining the rates of groundwater seepage into buffer materials," in *Geological Society, London, Special Publications*, S Norris, E.A.C. Neeft, and M Van Geet, Eds., vol. 482, no. 1, pp. 205–212, 2019.

[47] E. E. Dagher, T. S. Nguyen, and J. A. Infante Sedano, "Development of a mathematical model for gas migration (two-phase flow) in natural and engineered barriers for radioactive waste disposal," *Geological Society, London, Special Publications*, vol. 482, no. 1, pp. 115–148, 2019.

[48] S. Finsterle, B. Lanyon, M. Åkesson et al., "Conceptual uncertainties in modelling the interaction between engineered and natural barriers of nuclear waste repositories in crystalline rocks," *Geological Society, London, Special Publications*, vol. 482, no. 1, pp. 261–283, 2019.

[49] V. I. Malkovsky, Y. P. Dikov, E. E. Asadulin, and V. V. Krupskaya, "Influence of host rocks on composition of colloid particles in groundwater at the Karachai Lake site," *Clay Minerals*, vol. 47, no. 3, pp. 391–400, 2012.

[50] P. Sellin and O. X. Leupin, "The use of clay as an engineered barrier in radioactive-waste management—a review," *Clays and Clay Minerals*, vol. 61, no. 6, pp. 477–498, 2013.

[51] M. Ammar, W. Oueslati, H. Ben Rhaiem, and A. Ben Haj Amara, "Effect of the hydration sequence orientation on the structural properties of Hg exchanged montmorillonite: quantitative XRD analysis," *Journal of Environmental Chemical Engineering*, vol. 2, no. 3, pp. 1604–1611, 2014.

[52] R. Chalghaf, W. Oueslati, M. Ammar, H.. B. Rhaiem, and A. B.. H. Amara, "Effect of an in situ hydrous strain on the ionic exchange process of dioctahedral smectite: case of solution containing (Cu^{2+}, Co^{2+}) cations," *Applied Surface Science*, vol. 258, no. 22, pp. 9032–9040, 2012.

[53] R. Chalghaf, W. Oueslati, M. Ammar, H.. B. Rhaiem, and ABH Amara, "Effect of temperature and pH value on cation exchange performance of a natural clay for selective (Cu^{2+}, Co^{2+}) removal: Equilibrium sorption and kinetics," *Progress in Natural Science*, vol. 23, no. 1, pp. 23–35, 2013.

[54] P. Delage, Y. J. Cui, and A. M. Tang, "Clays in radioactive waste disposal," *Journal of Rock Mechanics and Geotechnical Engineering*, vol. 2, no. 2, pp. 111–123, 2010.

[55] G. Xiang, W. Ye, Y. Xu, and F. E. Jalal, "Swelling deformation of Na-bentonite in solutions containing different cations," *Engineering Geology*, vol. 277, Article ID 105757, 2020.

[56] N. Güven and S. W. Bailey, "Hydrous Phyllosilicates (exclusive of micas)," *Reviews in Mineralogy*, vol. 19, p. 497, 1988.

[57] T. Sato, T. Watanabe, and R. Otsuka, "Effects of layer charge, charge location, and energy change on expansion properties of dioctahedral smectites," *Clays and Clay Minerals*, vol. 40, no. 1, pp. 103–113, 1992.

[58] I. Bérend, J. M. Cases, M. François et al., "Mechanism of adsorption and desorption of water vapour by homoionic montmorillonites: 2. the Li^+, Na^+, K^+, Rb^+ and Cs^+ exchanged forms," *Clays and Clay Minerals*, vol. 43, no. 3, pp. 324–336, 1995.

[59] J. M. Cases, I. Bérend, M. François, J. P. Uriot, L. J. Michot, and F. Thomas, "Mechanism of adsorption and desorption of water vapour by homoionic montmorillonite: 3. The Mg^{2+}, Ca^{2+}, Sr^{2+} and Ba^{2+} exchanged forms," *Clays and Clay Minerals*, vol. 45, no. 1, pp. 8–22, 1997.

[60] W. Oueslati, H. Ben Rhaiem, and A. Ben Haj Amara, "Effect of relative humidity constraint on the metal exchanged montmorillonite performance: an XRD profile modeling approach," *Applied Surface Science*, vol. 261, pp. 396–404, 2012.

[61] W. F. Moll, "Baseline studies of the Clay Minerals Society Source Clays: Geological Origin," *Clays And Clay Minerals*, vol. 49, no. 5, pp. 374–380, 2001.

[62] A. R. Mermut and A. F. Cano, "Baseline studies of the clay minerals society Source clays: chemical analyses of major elements," *Clays and Clay Minerals*, vol. 49, no. 5, pp. 381–386, 2001.

[63] H. Heller and R. Keren, "Rheology of Na-rich montmorillonite suspension as affected by electrolyte concentration and shear rate," *Clays and Clay Minerals*, vol. 49, no. 4, pp. 286–291, 2001.

[64] H. Tanaka, D. R. Shiwakoti, O. Mishima, Y. Watabe, and M. Tanaka, "Comparison of mechanical behavior of two overconsolidated clays: yamashita and Louiseville clays," *Soils and Foundations*, vol. 41, no. 4, pp. 73–87, 2001.

[65] H. Tanaka, A. Tsutsumi, and T. Ohashi, "Unloading behavior of clays measured by CRS test," *Soils and Foundations*, vol. 54, no. 2, pp. 81–93, 2014.

[66] A. Altomare, N. Corriero, C. Cuocci, A. Falcicchio, A. Moliterni, and R. Rizzi, "QUALX2.0: a qualitative phase analysis software using the freely available database POW_COD," *Journal of Applied Crystallography*, vol. 48, no. 2, pp. 598–603, 2015.

[67] W. Oueslati and M. Meftah, "Discretization of the water uptake process of Na-montmorillonite undergoing atmospheric stress: XRD modeling approach," *Advances in Materials Science and Engineering*, vol. 117 pages, Article ID 5219624, 2018.

[68] M. Ammar, W. Oueslati, N. Chorfi, and A. B.. H. Amara, "The water retention mechanism of a Cs^+ and Na^+ exchanged montmorillonite: effect of relative humidity and ionic radius on the interlayer," *Powder Diffraction*, vol. 30, no. S1, pp. S70–S75, 2015.

[69] W. Oueslati, H. B Rhaiem, and A. B. H Amara, "XRD investigations of hydrated homoionic montmorillonite saturated by several heavy metal cations," *Desalination*, vol. 271, no. 1-3, pp. 139–149, 2011.

[70] B. Lanson, "Modelling of X-ray diffraction profiles: investigation of defective lamellar structure crystal chemistry," *EMU Notes Mineral*, vol. 11, pp. 151–202, 2011.

[71] V. A. Drits, C. Tchoubar, and P. Klimanek, "X ray diffraction by disordered lamellar structures," *Theory and Applications to Microdivided Silicates and Carbons*, Springer-Verlag, 1991.

[72] W. Oueslati, N. Chorfi, and M. Abdelwahed, "Effect of mechanical constraint on the hydration properties of Na-montmorillonite: study under extreme relative humidity conditions," *Powder Diffraction*, vol. 32, no. S1, pp. S160–S167, 2017.

[73] B. A. Sakharov and B. Lanson, "X-ray identification of mixed-layer structures: modelling of diffraction effects," *Developments in Clay Science*, vol. 5, pp. 51–135, 2013.

[74] E. Ferrage, B. Lanson, N. Malikova, A. Plancon, B. A. Sakharov, and V. A. Drits, "New insights on the distribution of interlayer water in Bi-hydrated smectite from X-ray diffraction profile modeling of 00l reflections," *Chemistry of Materials*, vol. 17, no. 13, pp. 3499–3512, 2005.

[75] E. Ferrage, B. Lanson, B. A. Sakharov, N. Geoffroy, E. Jacquot, and V. A. Drits, "Investigation of dioctahedral smectite hydration properties by modeling of X-ray diffraction profiles: influence of layer charge and charge location," *American Mineralogist*, vol. 92, no. 10, pp. 1731–1743, 2007.

[76] M. Ammar, W. Oueslati, H. Ben Rhaiem, and A. Ben Haj Amara, "XRD profile modeling approach tools to investigate the effect of charge location on hydration behavior in the case of metal exchanged smectite," *Powder Diffraction*, vol. 28, no. S2, pp. S284–S300, 2013.

[77] C. Mejri, W. Oueslati, and A. B. H Amara, "How the solid/liquid ratio affects the cation exchange process and porosity in the case of dioctahedral smectite: structural analysis?" *Adsorption Science and Technology*, vol. 2021, pp. 1–24, Article ID 9732092, 2021.

[78] B. A. Sakharov, A. S. Naumov, and V. A. Drits, "X-ray diffraction by mixed-layer structures with a random distribution of stacking faults," *Soviet Physics - Doklady*, vol. 27, p. 523, 1982.

[79] B. A. Sakharov, H. Lindgreen, and V. A. Drits, "Mixed-layer kaolinite-illite-vermiculite in north sea shales," *Clay Minerals*, vol. 34, no. 2, pp. 333–344, 1999.

[80] Z. Sun, Y. G Chen, and W. M Ye, "Adsorption of Eu (III) onto Gaomiaozi bentonite corroded by cement waters: effect of cement solutions on the long-term sorption performance of bentonite in the repository conditions," *Journal of Cleaner Production*, vol. 251, Article ID 119692, 2020.

[81] M. Benzina and A. Bellagi, "Détermination des propriétés du réseau poreux de matériaux argileux par les techniques d'adsorption d'azote et de porosimétrie au mercure en vue de leur utilisation pour la récupération des gaz," *Annales de Chimie*, vol. 15, no. 6, pp. 315–335, 1990.

[82] S. J. Gregg, K. S. W. Sing, and H. W. Salzberg, "Adsorption surface area and porosity," *Journal of the Electrochemical Society*, vol. 114, no. 11, p. 279Ca, 1967.

[83] L. Yu, W. L. Hsu, J. A. Shamim, and H. Daiguji, "Pore network modeling of a solid desiccant for dehumidification applications," *International Journal of Heat and Mass Transfer*, vol. 186, Article ID 122456, 2022.

[84] P. Pang, H. Han, L. Hu, C. Guo, Y. Gao, and Y. Xie, "The calculations of pore structure parameters from gas adsorption experiments of shales: which models are better?" *Journal of Natural Gas Science and Engineering*, vol. 94, Article ID 104060, 2021.

[85] J. C. Groen, L. A. Peffer, and J. Pérez-Ramírez, "Pore size determination in modified micro- and mesoporous materials. Pitfalls and limitations in gas adsorption data analysis," *Microporous and Mesoporous Materials*, vol. 60, no. 1-3, pp. 1–17, 2003.

[86] E. P. Barrett, L. G. Joyner, and P. P. Halenda, "The determination of pore volume and area distributions in porous substances. I. Computations from nitrogen isotherms," *Journal of the American Chemical Society*, vol. 73, no. 1, pp. 373–380, 1951.

[87] T. Liu, L. Ju, Y. Zhou et al., "Effect of pore size distribution (PSD) of Ni-Mo/Al_2O_3 catalysts on the Saudi Arabia vacuum residuum hydrodemetallization (HDM)," *Catalysis Today*, vol. 271, pp. 179–187, 2016.

[88] K. Sing, "The use of nitrogen adsorption for the characterisation of porous materials," *Colloids and Surfaces A: Physicochemical and Engineering Aspects*, vol. 187, pp. 3–9, 2001.

[89] P. Kumar, R. V. Jasra, and T. S. G. Bhat, "Evolution of porosity and surface acidity in montmorillonite clay on acid activation," *Industrial & Engineering Chemistry Research*, vol. 34, no. 4, pp. 1440–1448, 1995.

[90] J. M. Zielinski and L. Kettle, *Physical Characterization: Surface Area and Porosity*, Intertek, London, 2013.

[91] H. Ben Rhaiem, C. H. Pons, and D. Tessier, "Factors affecting the microstructure of smectites. Role of cation and history of applied stresses," *The Clay Minerals Society, Bloomington IN*, vol. 1985, pp. 292–297, 1985.

[92] G. Q. Cai, C. G. Zhao, J. Li, and Y. Liu, "A new triaxial apparatus for testing soil water retention curves of unsaturated soils under different temperatures," *Journal of Zhejiang University - Science*, vol. 15, no. 5, pp. 364–373, 2014.

[93] C. F. Chiu and C. W. Ng, "Coupled water retention and shrinkage properties of a compacted silt under isotropic and deviatoric stress paths," *Canadian Geotechnical Journal*, vol. 49, no. 8, pp. 928–938, 2012.

[94] J. H. Atkinson and P. L. Bransby, *The Mechanics of Soils: An Introduction to Critical State Soil Mechanics*, McGraw-Hill, London, 1978.

[95] N. Saiyouri, D. Tessier, and P. Y. Hicher, "Experimental study of swelling in unsaturated compacted clays," *Clay Minerals*, vol. 39, no. 4, pp. 469–479, 2004.

[96] A. C. Inigo, D. Tessier, and M. Pernes, "Use of X-ray transmission diffractometry for the study of clayparticle orientation at different water contents," *Clays and Clay Minerals*, vol. 48, no. 6, pp. 682–692, 2000.

[97] B. Dazas, B. Lanson, A. Delville et al., "Influence of tetrahedral layer charge on the organization of interlayer water and ions in synthetic Na-saturated smectites," *Journal of Physical Chemistry C*, vol. 119, no. 8, pp. 4158–4172, 2015.

[98] F. Hubert, L. Caner, A. Meunier, and B. Lanson, "Advances in characterization of soil clay mineralogy using X-ray diffraction: from decomposition to profile fitting," *European Journal of Soil Science*, vol. 60, no. 6, pp. 1093–1105, 2009.

[99] S. Charpentier and G. Bourrié, "Deformation of saturated clays under mechanical and osmotic stress and its relation with the arrangement of the clays," *European Journal of Soil Science*, vol. 48, no. 1, pp. 49–57, 1997.

[100] G. R. Rao, I. Srikanth, and K. L. Reddy, "Effect of organo-modified montmorillonite nanoclay on mechanical, thermal and ablation behavior of carbon fiber/phenolic resin composites," *Defence Technology*, vol. 17, no. 3, pp. 812–820, 2021.

[101] K. Yotsuji, Y. Tachi, H. Sakuma, and K. Kawamura, "Effect of interlayer cations on montmorillonite swelling: comparison between molecular dynamic simulations and experiments," *Applied Clay Science*, vol. 204, Article ID 106034, 2021.

[102] G. Wang, L. Ran, J. Xu et al., "Technical development of characterization methods provides insights into clay mineral-water interactions: a comprehensive review," *Applied Clay Science*, vol. 206, Article ID 106088, 2021.

[103] A. Asaad, F. Hubert, E. Ferrage et al., "Role of interlayer porosity and particle organization in the diffusion of water in swelling clays," *Applied Clay Science*, vol. 207, Article ID 106089, 2021.

Hindawi
Advances in Civil Engineering
Volume 2022, Article ID 8762382, 17 pages
https://doi.org/10.1155/2022/8762382

Research Article

Research on Mechanical Model of Canal Lining Plates under the Effect of Frost Heaving Force

Yantao Liang,[1,2] Fuping Zhang,[1,2] Mingming Jing,[1,2] and Pengfei He[1,3]

[1]*State Grid Gansu Electric Power Company Construction Branch, Lanzhou 730050, China*
[2]*State Grid Gansu Electric Power Company, Lanzhou 730030, China*
[3]*Lanzhou University of Technology, Lanzhou 730050, China*

Correspondence should be addressed to Pengfei He; hepf@lut.edu.cn

Received 27 July 2022; Accepted 12 August 2022; Published 20 September 2022

Academic Editor: Zhuo Chen

Frost heaving damage of canal lining in cold and dry areas is one of the important causes of canal leakage. In this paper, based on the bending theory of thin plate, a mechanical model of canal lining under the action of frost heaving force is established and solved. Through parametric and engineering case analysis, the following conclusions are drawn: under the action of frost heaving force, the bending moment, shear force, and internal force of the slope plate show a nonuniform distribution, and the maximum values of bending moment M_x and normal stress σ_x are close to the bottom third of the slope, which is consistent with the existing research and engineering practice. Compared with the theory of beam, the results of the theory of thin plates show that the internal forces and stresses increase at the free boundary (longitudinal expansion joint). The bending moment M_{xy} and stress τ_{xy} are maximum at the four corners of the plate: although the numerical magnitude is lower than that of M_x, it may cause stress concentration to damage the lining plate and thus cause break. The shear force at the longitudinal expansion joint may lead to fracture of the joint material, which needs to be considered in the design process. Due to the uniform distribution of the frost heaving force on the bottom plate lining, its deflection, internal forces, and stresses also show a uniform distribution. The research results can provide scientific reference for the design and operation and maintenance of water transmission canal lining in cold areas.

1. Introduction

China is a large irrigated agricultural production country, and agricultural water consumption accounts for about 63.2% of the total water consumption in the country; meanwhile, more than 50% of China's regions are in arid and semiarid areas, and agricultural water consumption in Gansu, Ningxia, Xinjiang, and Inner Mongolia accounts for more than 75% of the total local water consumption due to factors such as geographical location and climatic conditions [1]. In order to solve the problem of uneven spatiotemporal distribution of water resources, China has constructed a large number of water transmission projects, and more than 800,000 km of trunk and branch canals have been built nationwide, but due to problems such as canal leakage, the average water utilization coefficient of the canal system is only about 0.5, resulting in a large amount of water waste [2]. Canal leakage prevention projects have largely improved the efficiency of water utilization and promoted the development of water conservation projects. China is vast, and the distribution area of multiyear permafrost zone and seasonal permafrost zone accounts for 21.5% and 53.5% of the national land area, respectively [3, 4], and the latitude span of these areas is large, and the climate is complex and diverse, which makes the service life of canal projects vary greatly from place to place. Especially in the vast northern cold regions such as northeast, northwest, and north China, the winter climate is cold and the low temperature lasts for a long time; for example, the winter temperature in Xinjiang is generally −40~−10°C, the annual cumulative average daily negative temperature is −1,000~−1,500°C, and the annual duration of negative temperature is about 130 days [5, 6]. At

the same time, the natural freezing depth in these areas is large, coupled with the repeated freezing and thawing action, resulting in serious frost damage problems in canal projects in general. Canal freezing and thawing disasters not only directly affect the use of the canal, wasting valuable water resources and making the land along the canal have secondary saline-alkalization, but also increase the number of engineering maintenance and operating costs, seriously limiting the efficiency of the project. Therefore, how to prevent and control the freezing and thawing damage of the cold area canal project has become a key problem that settle the development of agricultural production in the national economy of irrigation areas.

The canal lining damage in cold areas is mainly due to the uneven frost heaving of subsoil which makes the lining plate bending moment increase, coupled with the deterioration of lining plate and joint material caused by freezing and thawing action, which causes the fracture and damage to the lining plate. Wang [7] established a mechanical model of trapezoidal canal lining frost heaving damage and analyzed the internal force and dangerous cross section of lining under the action of frost heaving force based on the beam theory. Set et al. [8–11] used similar methods to theoretically analyze the frost heaving damage of lining in different structural forms, such as trapezoidal and U-shaped, and determined the location of the dangerous cross section of lining. Considering that the process of soil frost heaving deformation and the process of canal lining structure deformation in the process of canal frost heaving have an interactive relationship, the frost heaving damage characteristics of lining were analyzed based on the elastic foundation beam theory, which can better reflect the influence of canal subsoil characteristics on lining deformation [12–15].

Based on the beam theory and elastic foundation beam theory to analyze the frost heaving damage on the lining, it is better to predict the internal forces of the canal cross section under different structural forms or conditions, so as to establish the frost heaving damage judgment criterion. However, as a linear project, the size of the lining along the canal line inevitably affects the distribution characteristics of its internal forces and deformations. For small canals, the lining is usually constructed as cast-in-place concrete plates, and for large canals, although precast concrete plates are laid on the surface, a layer of cast-in-place concrete plate is still constructed at the base [16]. Therefore, the use of thin plate theory can better respond to the deformation and internal force characteristics of canal lining plates under the action of frost heaving forces. To this end, this paper takes water transmission canal lining in alpine regions as the research object, based on thin rectangular plate theory, considering the effect of frost heaving force and the boundary conditions of canal lining, combined with typical engineering cases, analyzing the deformation, internal force, and stress of the lining plate. The research results can provide reference for the prevention and control of frost heaving damage of canal lining in alpine regions.

2. Establishment and Solution of the Lining Mechanics Model

2.1. Basic Assumptions and Conventions. Uneven frost heaving of the canal foundation soil makes the liner plate swell, bulge, and fracture, which is the most serious and main form of damage to the liner plate by freezing [7, 16]. The most used precast plates and cast-in-place concrete lining canals are rigid lining, which are susceptible to frost damage for two reasons: on the one hand, because the canal is a groove structure, coupled with the inevitable leakage, water migration during the long-term freeze-thaw cycle process, and the groundwater embedment depth of different parts in canal subsoil, soil moisture content, surface temperature, and different freezing start time, frost heaving deformations of different sizes and directions are bound to be produced. On the other hand, the lining structure is usually an open thin plate structure with small elasticity of concrete material and low tensile strength, and its nonsymmetrical structure makes it less resistant to deformation and prone to have bending damage.

Take the open system trapezoidal concrete lining canal in engineering as an example, as shown in Figure 1. Under certain geological, meteorological, and moisture conditions, moisture recharge is the main factor affecting soil frost heaving. For canal projects, groundwater is the main source of moisture recharge after winter shutdown [9, 12]. However, there are various patterns of frost heaving distribution along the depth direction under different conditions, such as large top with small bottom attenuation type, large middle with small ends type, and small top with large bottom type [3]. Among them, when the soil quality is homogeneous, the soil before freezing is closer to the water table, and the water content of the soil before freezing is higher; thus, the frost heaving is manifested as the large top with small bottom attenuation type. This frost heaving distribution characteristic is also used extensively in the analysis of canal lining frost heaving damage [7, 8, 10, 11]. Both the slope plate and the bottom plate are subjected to frost heaving forces; the top of the slope plate is generally set with a certain width of edge protection in the horizontal direction, having no frost heaving constraint or minor frost heaving constraint, while the bottom of the slope plate and the bottom plate are mutually constrained. Both edges of the bottom plate are constrained by the bottom of the slope plate. According to the characteristics of frost heaving distribution in the depth direction of the canal and the constraint situation of the lining, there is no frost heaving constraint or slight frost heaving constraint at the top of plate, so assuming that the normal frost heaving force on the slope plate is 0 at the top of the slope and maximum at the bottom of the slope, which is linearly distributed [12]. The bottom plate is subjected to a uniformly distributed normal frost heaving force. The canal lining is usually laid at an inclination, and the normal and tangential frost heaving forces are existing between the liner and the soil, and the eccentric press bending of the liner is

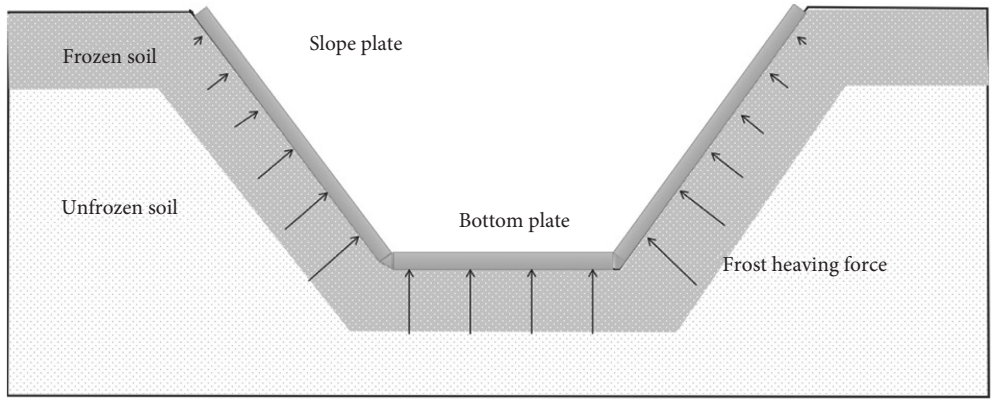

Figure 1: Schematic diagram of canal lining.

caused by the tangential frost heaving force. Corresponding to different engineering requirements, the thickness of the liner plate is usually 10~30 cm. Due to the small force arm, the bending moment caused by tangential frost heave force is smaller compared to that caused by normal frost heave force; therefore, only the effect of normal frost heave force is considered in the paper, which affects the accuracy of stress analysis to some extent, but considering the safety factor in the structural design process, the research results still have important reference value for engineering design. Combining the existing research results and practical engineering experience, the following assumptions and conventions are added to the establishment of the model [7, 13, 14]:

(1) The canal lining mechanics model is simplified to a thin rectangular plate structure.

(2) Due to the slow freezing process in winter, the lining deformation process is regarded as a quasistatic process. The deformation of frozen soil and lining are always coordinated in the process of frost heaving, and the lining is in ultimate equilibrium when the structure is damaged.

(3) The canal lining deformation is in the range of linear elasticity, and only the small deformation of the lining is considered, the rotational effect of the microelements is ignored.

(4) Frost heaving calculation only considers the deformation of frozen soil within the range of freezing depth and does not consider the solidification deformation of frozen soil outside the freezing depth.

(5) After the completion of the canal, the lining self-weight and the foundation reaction force balance each other; the force analysis does not consider the influence of the lining self-weight and only considers the influence of the normal frost heaving force on the internal force of the lining plate.

Figure 2(a) shows the model of slope plate lining structure. The width along the canal line direction is b_1, the height along the canal depth direction is a1, and the thickness of the liner plate is δ. The coordinate system is shown in the figure, the y-direction is the direction of the canal line, the z-direction points to the canal inner slot (that is, the negative z-direction points to the soil body), and the x-direction points from the bottom to the top of the slope. Figure 2(b) shows the schematic diagram of the normal frost heaving force on the slope plate, and because the distance from the water table is different at different locations of the slope plate, the relationship between the amount of frost heaving at different locations and groundwater depth is a power function, which can be approximately regarded as a linear distribution [12]. It is assumed that the frost heaving force is linearly distributed, which is 0 at the top of the slope and maximum q_0 at the bottom of the slope [7].

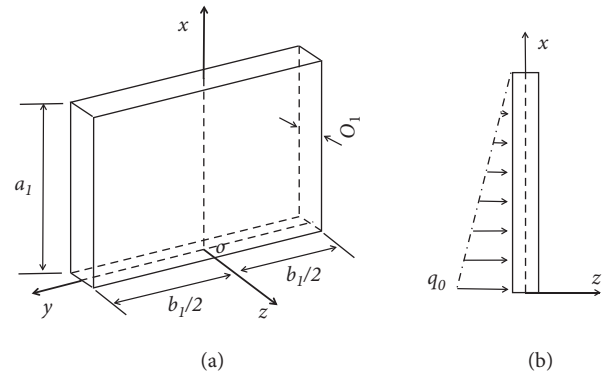

Figure 2: Diagram of force acting on the rectangular slope under frost heaving force.

Figure 3(a) shows the model of the bottom plate lining structure. The width along the canal line direction is b_2, the height along the canal depth direction is a_2, and the thickness of the liner plate remains δ. The coordinate system direction is the same as the slope plate definition. Figure 3(b) shows the schematic diagram of the frost heaving force on the bottom plate lining, and the whole bottom plate is subject to uniform frost heaving force.

When using beam theory to study the force deformation of the lining plate, the two ends of the beam are usually simplified to simply supported constraints (top of slope and bottom of slope) [7, 12, 15–17], so the two ends of the plate are also simplified to simply supported constraints in this paper, where the top of slope ($x = a_1$) and bottom of slope

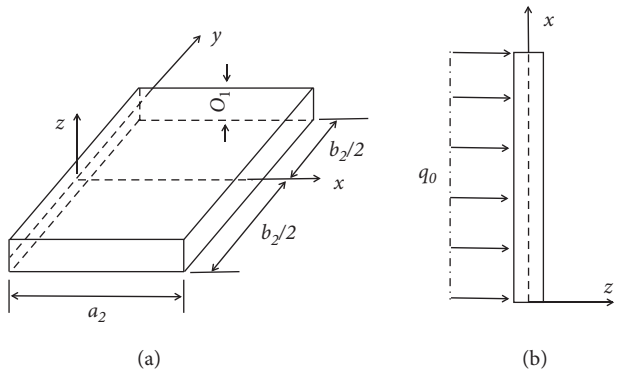

Figure 3: Diagram of force acting on the rectangular bottom plate under frost heaving force.

($x = 0$ or a_2) are regarded as simply supported constraints. Considering that the canal lining will be set up with expansion joints at certain intervals along the longitudinal direction, the material stiffness of the expansion joints is much smaller compared with the concrete lining plate and the deformation allowed to occur is also large, so the boundary is simplified to a free boundary at $y = \pm b_1/2$ and $y = \pm b_2/2$. According to the above simplification, both the slope plate and the bottom plate boundary conditions are thin rectangular plates with two opposite edges simply supported and the remaining edges free. From Figures 2 and 3, the geometric structures and coordinates of the slope plate and the bottom plate are the same; therefore, for the convenience of deriving the equations, a_1 and a_2 are unified as a, and b_1 and b_2 are unified as b in the latter part. Finally, the distinction is made when the results are specifically calculated.

2.2. Model Building and Solution. The differential equation for the elastic deflection surface of the thin rectangular plate is [18]

$$\frac{\partial^4 w}{\partial x^4} + 2\frac{\partial^4 w}{\partial x^2 \partial y^2} + \frac{\partial^4 w}{\partial y^4} = \frac{q}{D}, \tag{1}$$

where D is the flexural stiffness of the lining plate, $D = E\delta^3/12(1-\mu^2)$; E is the elastic modulus of the lining plate; μ is the Poisson's ratio of the lining plate.

The single trigonometric series solution method has been widely used for the solution of thin plate structures, which is suitable for both four-sided simply supported rectangular plates and rectangular plates with one pair of simply supported opposite edges, and the solution function has a simple form and fast convergence [19, 20]. From the model established in the previous section, the model has a boundary case with one pair of opposite edges simply supported and the other two edges free. The corresponding boundary conditions are as follows.

For slope plate and bottom plate lining, when $x = 0$ and $x = a$,

$$w = 0,\ \frac{\partial^2 w}{\partial x^2} = 0. \tag{2}$$

For slope plate and bottom plate lining, when $y = \pm b/2$,

$$\begin{aligned} -D\left(\frac{\partial^2 w}{\partial y^2} + \mu\frac{\partial^2 w}{\partial x^2}\right) &= 0, \\ -D\left[\frac{\partial^3 w}{\partial y^3} + (2-\mu)\frac{\partial^3 w}{\partial y\,\partial x^2}\right] &= 0. \end{aligned} \tag{3}$$

Assuming that the solution of the control equation (1)is a single trigonometric series, the deflection surface function of a rectangular thin plate subjected to frost heaving forces with two simply supported opposite edges and two free opposite edges can be constructed:

$$w = \sum_{m=1}^{\infty} Y_m(y)\sin\frac{m\pi x}{a}, \tag{4}$$

where m is any positive integer and $Y_m(y)$ is independent of the independent variable x. Obviously, the above equation satisfies the simply supported boundary conditions, and the problem is solved if the function $Y_m(y)$, which satisfies the other two boundary conditions, is proved to satisfy the control equation at the same time.

The trigonometric series (4) is substituted into equation (1) to get

$$\begin{aligned} &\sum_{m=1}^{\infty}\left[\frac{d^4 Y_m(y)}{dy^4} - 2\left(\frac{m\pi}{a}\right)^2\frac{d^2 Y_m(y)}{dy^2} + \left(\frac{m\pi}{a}\right)^4 Y_m(y)\right] \\ &\quad\cdot \sin\frac{m\pi x}{a} = \frac{q(x,y)}{D}. \end{aligned} \tag{5}$$

In the above equation, the left end of the equal sign is a trigonometric series with respect to the sine function, and to make the right end correspond to it, the right end of the equal sign is also expanded to a trigonometric series,

$$\frac{q(x,y)}{D} = \sum_{m=1}^{\infty} F_m(y)\sin\frac{m\pi x}{a}, \tag{6}$$

where $F_m(y)$ can be calculated by the following equation [19]:

$$F_m(y) = \frac{2}{Da}\int_0^a q(x,y)\sin\frac{m\pi x}{a}dx, \tag{7}$$

and substituting (6) into (5) yields

$$\begin{aligned} &\sum_{m=1}^{\infty}\left[\frac{d^4 Y_m}{dy^4} - 2\left(\frac{m\pi}{a}\right)^2\frac{d^2 Y_m}{dy^2} + \left(\frac{m\pi}{a}\right)^4 Y_m\right] \\ &\quad\cdot \sin\frac{m\pi x}{a} = \sum_{m=1}^{\infty} F_m(y)\sin\frac{m\pi x}{a}. \end{aligned} \tag{8}$$

Since $\sin m\pi x/a$ is impossible to be constant equal to 0, it follows from the above equation that

$$\frac{d^4Y_m}{dy^4} - 2\left(\frac{m\pi}{a}\right)^2 \frac{d^2Y_m}{dy^2} + \left(\frac{m\pi}{a}\right)^4 Y_m = F_m(y), \tag{9}$$

the above equation is a 4th order ordinary differential equation with constant coefficients and the solution can be expressed as

$$Y_m = Y_m^{(0)} + Y_m^{(*)}, \tag{10}$$

where $Y_m^{(0)}$ is a homogeneous solution and $Y_m^{(*)}$ is a particular solution. The homogeneous solution is

$$Y_m^{(0)} = A_m \cos \mathrm{h} a_m y + B_m \sin \mathrm{h} a_m y + C_m a_m y \cos \mathrm{h} a_m y + D_m a_m y \sin \mathrm{h} a_m y, \tag{11}$$

where $a_m = m\pi/a$, A_m, B_m, C_m, and C_m are undetermined coefficients.

Thus, the general solution of (9) can be expressed as

$$Y_m = A_m \cos \mathrm{h} a_m y + B_m \sin \mathrm{h} a_m y + C_m a_m y \cos \mathrm{h} a_m y + D_m a_m y \sin \mathrm{h} a_m y + Y_m^{(*)}. \tag{12}$$

The particular solution $Y_m^{(*)}$ can be calculated by the form of $F_m(y)$, the undetermined coefficients A_m, B_m, C_m, and D_m can be calculated by the free boundary conditions at both ends.

Substituting (12) into (4) to obtain the expression for the deflection of the lining plate,

$$w = \sum_{m=1}^{\infty} \left(A_m \cos \mathrm{h} a_m y + B_m \sin \mathrm{h} a_m y + C_m a_m y \cos \mathrm{h} a_m y + D_m a_m y \sin \mathrm{h} a_m y + Y_m^*\right) \sin a_m x. \tag{13}$$

The particular solution of the deflection equation of the slope plate $Y_m^{(*)}$ is solved as follows, where the load on the slope plate is

$$q = q_0\left(1 - \frac{x}{a_1}\right). \tag{14}$$

Substituting this into (8) yields

$$F_m(y) = \frac{2}{Da_1} \int_0^{a_1} q \sin \frac{m\pi x}{a_1} dx = \frac{2q_0}{Dm^2\pi^2} (m\pi - \sin m\pi). \tag{15}$$

Assuming that the form of the particular solution is $Y_m^{(*)} = C_0$, substituting it into (9) could yield $C_0 = 2q_0a_1^4/Dm^6\pi^6 (m\pi - \sin m\pi)$; in turn, the particular solution of the slope plate deflection equation is obtained:

$$Y_m^{(*)} = \frac{2q_0a_1^4}{Dm^6\pi^6} (m\pi - \sin m\pi). \tag{16}$$

Substitute the previous equation into equation (13) to obtain the slope plate general solution,

$$w = \sum_{m=1}^{\infty} \left[(A_m + C_m a_m y) \cos h a_m y + (B_m + D_m a_m y) \sin h a_m y + \frac{2q_0a^4}{Dm^6\pi^6} (m\pi - \sin m\pi) \right] \sin a_m x, \tag{17}$$

where the particular solution of the bottom plate deflection equation $Y_m^{(*)}$ is solved such that the load on the bottom plate is $q = q_0$. Substituting it into (8) yields

$$F_m(y) = \frac{2}{Da_2} \int_0^{a_2} q \sin \frac{m\pi x}{a_2} dx = \frac{2q_0}{Dm\pi} (1 - \cos m\pi). \tag{18}$$

Assuming that the particular solution is of the form $Y_m^{(*)} = C_1$, substituting it into (10) yields that $C_1 = 2q_0a_2^4/Dm^5\pi^5 (1 - \cos m\pi)$; in turn, the particular solution of the deflection equation of the bottom plate is obtained:

$$Y_m^{(*)} = \frac{2q_0a_2^4}{Dm^5\pi^5} (1 - \cos m\pi). \tag{19}$$

Substitute the previous equation into equation (13) to obtain the general solution of the bottom plate:

$$w = \sum_{m=1}^{\infty} \left[(A_m + C_m a_m y) \cos h a_m y + (B_m + D_m a_m y) \sin h a_m y + \frac{2q_0a_2^4}{Dm^5\pi^5} (1 - \cos m\pi) \right] \sin a_m x. \tag{20}$$

Since the load, plate geometry, and boundary conditions are symmetric with the x-axis, the deflection w must be an even function of y, which is $w(x, y) = w(x, -y)$. Therefore, the solution to equations (17) and (20) is $B_m = C_m = 0$.

The general solutions for the slope plate and the bottom plate are simplified as

$$w = \sum_{m=1}^{\infty} \left[A_m \cos h a_m y + D_m a_m y \sin h a_m y + \frac{2q_0a_1^4}{Dm^6\pi^6} (m\pi - \sin m\pi) \right] \sin a_m x,$$
$$w = \sum_{m=1}^{\infty} \left[A_m \cos h a_m y + D_m a_m y \sin h a_m y + \frac{2q_0a_2^4}{Dm^5\pi^5} (1 - \cos m\pi) \right] \sin a_m x, \tag{21}$$

where A_m and D_m can be calculated by the boundary conditions when $y = b/2$.

Due to the good convergence of the single triangular series, taking the first 5 terms will obtain good accuracy results. The internal force in the plate can be calculated from the following:

$$M_x = -D\left(\frac{\partial^2 w}{\partial x^2} + \mu\frac{\partial^2 w}{\partial y^2}\right),$$

$$M_y = -D\left(\frac{\partial^2 w}{\partial y^2} + \mu\frac{\partial^2 w}{\partial x^2}\right),$$

$$M_{xy} = -D(1-\mu)\frac{\partial^2 w}{\partial x\,\partial y}, \tag{22}$$

$$Q_x = -D\frac{\partial}{\partial x}\left(\frac{\partial^2 w}{\partial x^2} + \frac{\partial^2 w}{\partial y^2}\right),$$

$$Q_y = -D\frac{\partial}{\partial y}\left(\frac{\partial^2 w}{\partial x^2} + \frac{\partial^2 w}{\partial y^2}\right),$$

where M_x is the cross-sectional moment, M_y is the longitudinal-section moment, M_{xy} is the torque, Q_x is the transverse shear force within the cross section, and Q_y is the transverse shear force within the longitudinal section.

3. Effect of Frost Heaving Forces on the Mechanical Properties of Lining

Figure 4 shows the comparison of the results of slope plate deflection calculated by using beam theory and plate theory, respectively. In Figure 4, the calculation method and parameters (slab thickness 0.2 m, modulus of elasticity 2.2×10^4 Mpa, ultimate tensile strain 0.5×10^{-4}) of the paper by Wang [7] are used for the beam theory calculation method, and the method of this paper is used for the rectangular plate theory calculation. It can be seen that the results obtained from the two calculation methods are in good agreement, and the calculation process in this paper can be considered accurate.

3.1. Mechanical Analysis of the Slope Plate. The canal lining plate is set up with expansion joints at a certain interval in the longitudinal direction to release the deformation caused by temperature and other factors, which is often taken as 3~6 m. The frost heaving force acting on the structure during the freezing of the soil is related to a variety of factors such as the nature of the soil, climatic conditions, and constraints, which makes the frost heaving force take a wide range of values; for example, the maximum frost heaving force of the selected slope plate is as 8 kPa in [7], the simulated value in [15] was 380~560 kPa, the measured frost heaving force in the field was 0.8~32 kPa in [21], and in [22], the frost heaving force in the calculation model was 1.22 kPa. Therefore, the frost heaving forces of 8 kPa, 20 kPa, 50 kPa, and 100 kPa were selected as the maximum values applied to the slope plate in [7], and the width of the slope plate was taken as 5 m and the height as 3 m. Then the variation law of each mechanical variable could be obtained. It can be seen from Figure 5 that the change of deflection of the lining plate under the effect of frost heaving force is basically uniform, and the value of deflection increases and then decreases from the bottom to the top of the plate and reaches the maximum near the midline of the plate. The deflection equivalent curve is symmetrically distributed up and down with respect to the middle line of the plate, which is the same as the lining deflection variation law in the existing studies [12, 13]. With the gradual increase of the frost heaving force, the deflection value increases significantly, and the deflection at the midpoint of both edges of the plate (expansion joints) is greater than that at the center of the plate. From Figure 6(e), it can be observed that the maximum value of deflection is 0.3 mm when the maximum frost heaving force is 8 kPa; the maximum value of deflection is 0.7 mm when the maximum frost heaving force is 20 kPa; the maximum value of deflection is 1.9 mm when the maximum frost heaving force is 50 kPa; and the maximum value of deflection is 3.7 mm when the maximum frost heaving force is 100 kPa. The change in the size of the frost heaving force has a large effect on the deflection value.

The cross-sectional bending moment is the main internal force causing the damage of the lining plate. Figure 7 shows the effect of different frost heaving forces on the cross-sectional bending moment. It can be seen that the bending moment M_x has a similar variation trend as deflection when the lining plate is under the effect of frost heaving force, where the value of bending moment increases and then decreases from the bottom to the top of the plate. Unlike the deflection distribution, the bending moment is asymmetrically distributed along the height direction of the plate, which is caused by the nonuniformly distributed frost heaving force. The bending moment is the second order derivative of the deflection, which can further reflect the concavity of the deflection. The deflection at the midpoint of both edges of the plate (expansion joints) is greater than that at the center of the plate, which is the danger point. From Figure 7(e), it can be seen that when the value of bending moment M_x reaches the maximum at the height of 1.2 m of the plate and the maximum frost heaving force increases from 8 kPa to 20 kPa, the maximum value of bending moment M_x increases by 1.5 times; when the maximum frost heaving force increases to 50 kPa, the maximum value of bending moment M_x increases by 5.24 times; when the maximum frost heaving force increases to 100 kPa, the maximum value of bending moment M_x increases by 11.49 times. It can be seen that the change in the magnitude of the frost heaving force has a large effect on the value of bending moment M_x.

From Figure 8, it can be seen that the lining plate has a circular distribution of bending moment M_y under the effect of frost heaving force, and the value of bending moment M_y is higher as it goes to the center and reaches the maximum value at the height of 1.2 m. With the gradual increase of frost heaving force, the value of bending moment M_y also increases gradually, and the equivalent curves of bending moment M_y are arranged more and more closely. From Figure 8(e), when the maximum frost heaving force is 8 kPa, the maximum value of bending moment is 0.7 kN m; when the maximum frost heaving force increases from 8 kPa to 20 kPa, the maximum value of bending moment M_y increases 1.3 times; when the maximum frost heaving force increases to 50 kPa, the maximum value of bending moment M_y increases 5.3 times; and when the maximum frost

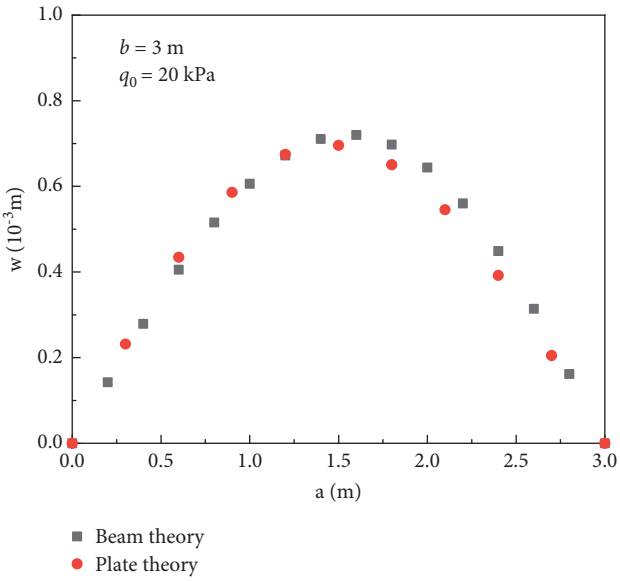

Figure 4: Deflection comparison between beam theory and plate theory.

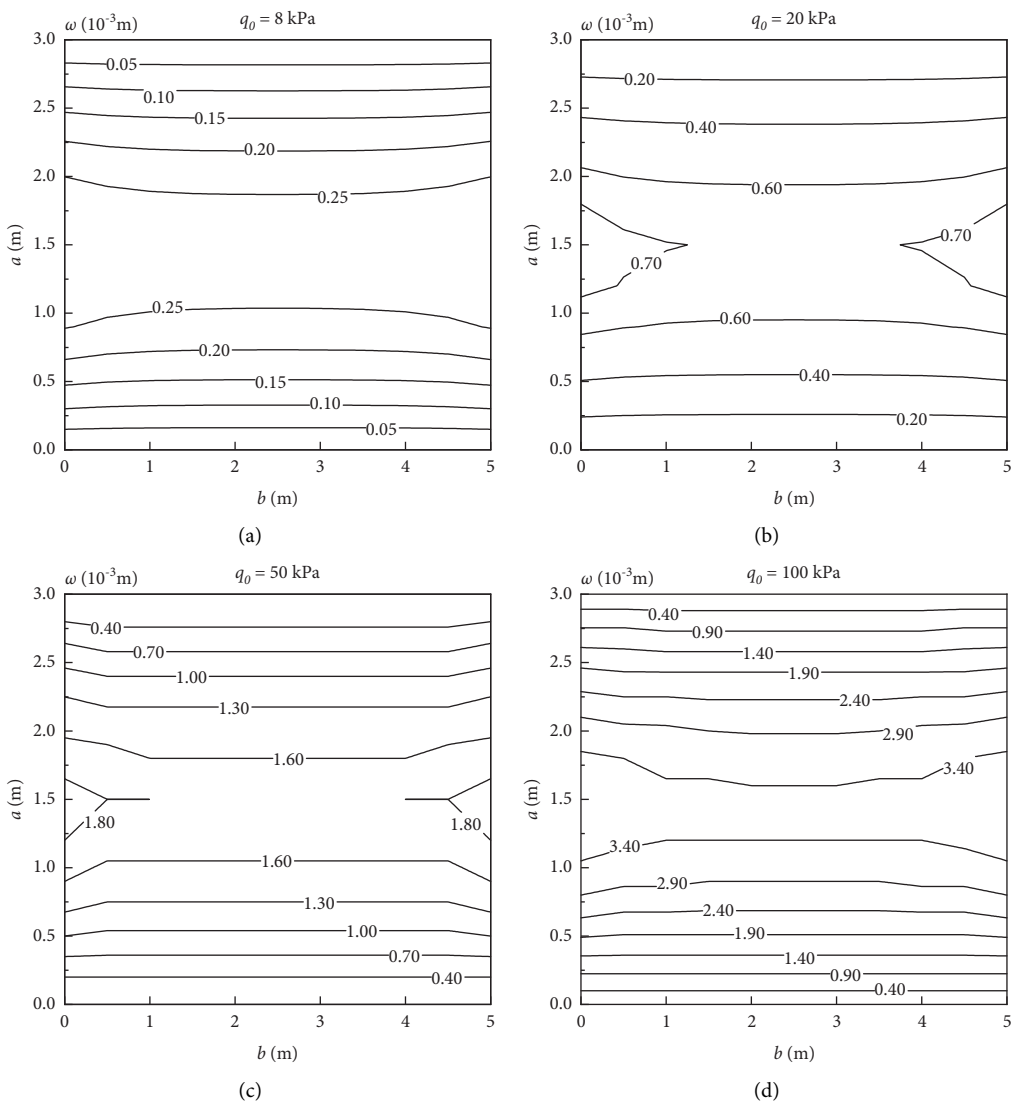

Figure 5: Continued.

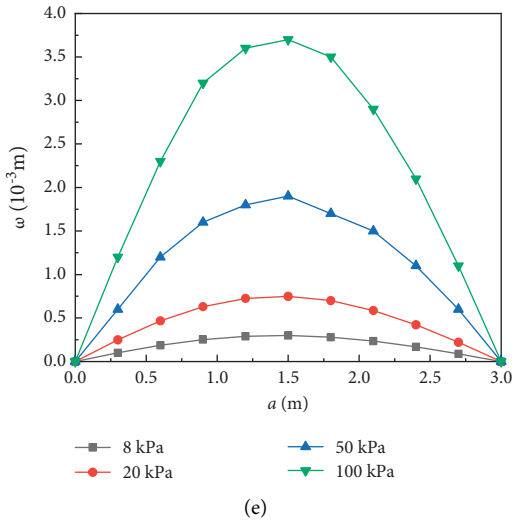

Figure 5: Effect of frost heaving force on deflection (w).

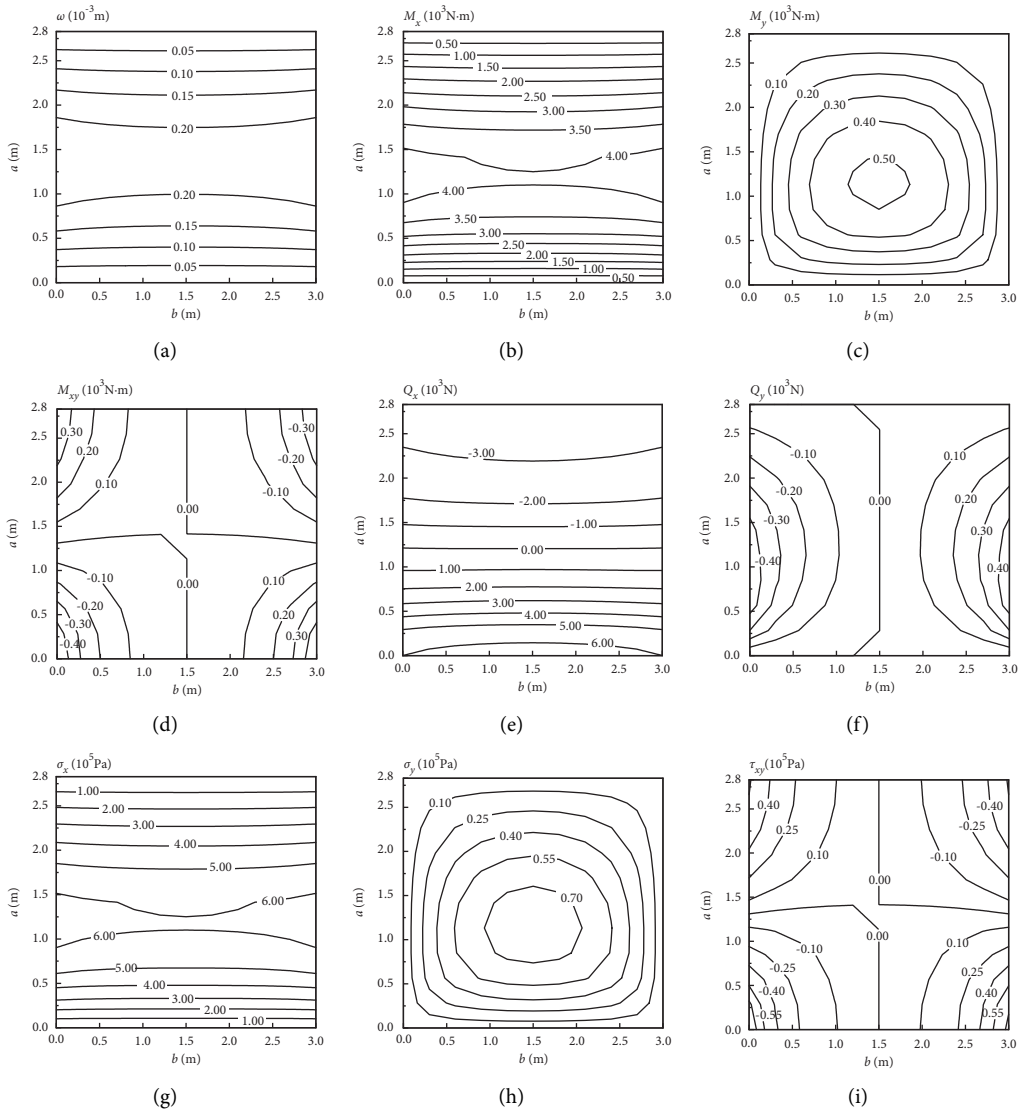

Figure 6: Distribution of deflection, internal force, and stress of slope plate.

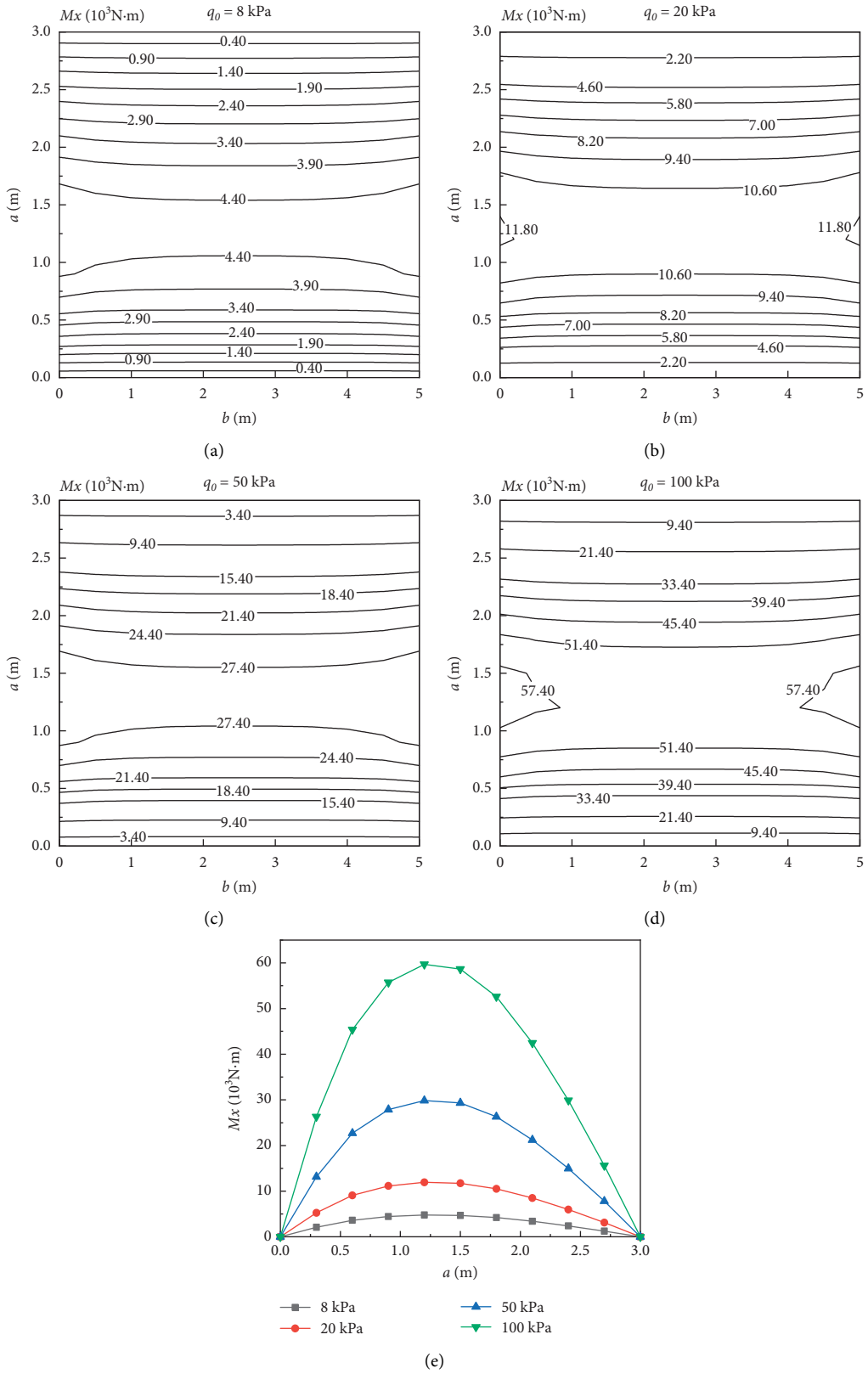

Figure 7: Effect of frost heaving force on bending moment M_x.

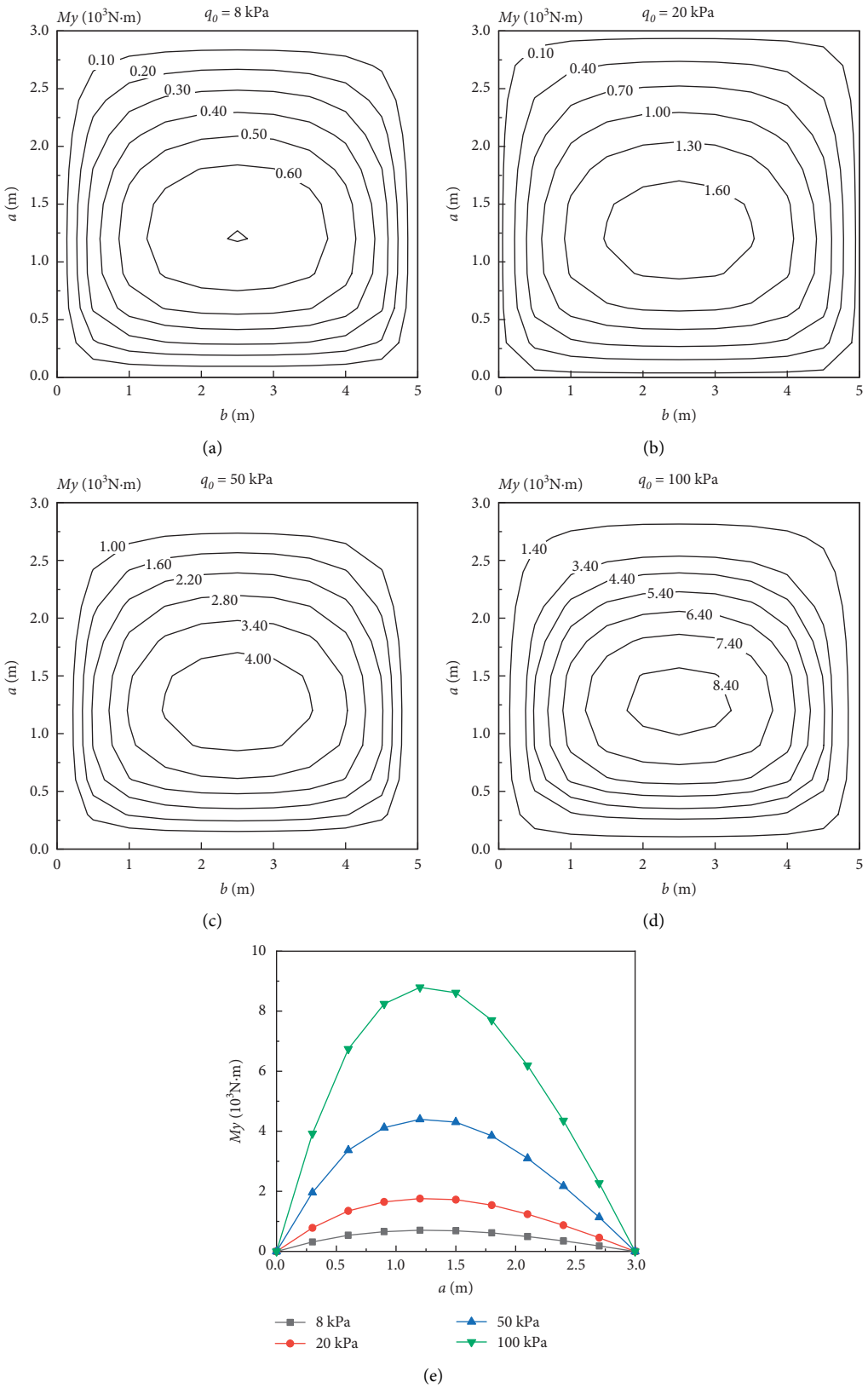

Figure 8: Effect of frost heaving force on bending moment M_y.

heaving force increases to 100 kPa, the maximum value of bending moment M_y increases 11.3 times. The increase multiplier is comparable to the bending moment M_y, which shows that the change in the magnitude of the frost heaving force also has a large effect on the value of the bending moment M_y.

From Figure 9, it can be seen that the equivalent curve of torque M_{xy} is symmetrically distributed with respect to the center of the lining plate, and the maximum values are at the four corners of the plate. If the horizontal axis is shifted upward, the first and third quadrants have negative torque, and the second and fourth quadrants have positive torque. Their maximum values are distributed at the corners of the lining plate, and the overlapping of torque on two adjacent sides is likely to cause stress concentration at the corners. From Figure 9(e), it can be seen that the increase in frost heaving force increases the value of torque M_{xy}.

Figure 10 shows the variation law of cross-sectional shear force. The figure shows that the shear force Q_x is negative on the upper side of the lining plate and positive on the lower side, reaching its maximum value at the position of the upper and lower edges of the plate, and is nonuniformly distributed up and down. The shear force at the upper and lower edges (simply supported restraints) is slightly larger in the middle than at the sides, and the shear force at the top of the slope is smaller than that at the bottom. From Figure 10(e), it can be seen that similar to the torque M_{xy}, the slope of the curve increases significantly by increasing the magnitude of the frost heaving force, indicating that increasing the frost heaving force will increase the value of the shear force Q_x.

As can be seen from Figure 11, the equivalent curve of the longitudinal interface shear force Q_y is symmetrically distributed with respect to the midline of the thin plate on the left and right, and the shear value decreases and then increases from the left to the right side of the plate. Although the shear forces at the left and right edges (joints) are not as large as the cross-sectional shear force, it may lead to fracture of the joint material and needs to be considered in the design process. The shear force Q_y is still nonuniformly distributed along the top to bottom of the plate. From Figure 11(e), it can be seen that the shear force Q_y reaches the maximum at the height of 0.9 m. The shear force Q_y gradually increases as the frost heaving force gradually increases. The maximum value of shear force increases from 0.5 kN to 6.2 kN when the frost heaving force increases from 8 kPa to 100 kPa.

Since the stress change of the lining plate corresponds to its internal force change, only the graph of the stress change in the plate at different frost heaving forces is given. From Figure 12(a), it can be seen that the value of stress x increases and then decreases from the bottom to the top of the plate and reaches the maximum at the height of 1.2 m of the plate. When the frost heaving force is 8 kPa, the maximum value of stress x is 7.2×10^5 Pa; when the frost heaving force is 100 kPa, the maximum value of stress x is 89.5×10^5 Pa, indicating that the change of the frost heaving force has a large effect on the value of stress x. From Figure 12(b), it can be seen that when the frost heaving force increases from 8 kPa to 100 kPa, the maximum value of stress y increases from 1.1×10^5 Pa to 13.2×10^5 Pa. From Figure 12(c), it can be seen that the value of stress τ_{xy} increases significantly with the increase of the frost heaving force.

3.2. Mechanical Analysis of the Bottom Plate. The bottom plate can also be regarded as a thin rectangular plate subjected to the uniform frost heaving force. Take the width of the bottom plate as 5 m and the height as 3 m, applying the frost heaving forces of 8 kPa, 20 kPa, 50 kPa, and 100 kPa to the bottom plate in turn. Due to space limitations, only the data of the internal force and stress along the height direction of the plate are given. The bottom plate is subjected to uniform frost heaving forces, so the internal forces and stresses are also uniformly distributed along the height direction of the plate, but slightly larger at the free boundary than at other locations. From Figure 13(a), it can be seen that when the bottom plate lining is subjected to the action of frost heaving forces, the deflection value increases and then decreases from the bottom to the top of the plate and reaches the maximum at the midline position of the plate. The maximum value of deflection increases from 0.6 mm to 7.5 mm when the frost heaving force increases from 8 kPa to 100 kPa. It can be seen from Figure 12(b) that the variation trend of the bending moment M_x is similar to that of the deflection, and the value of bending moment increases first and then decreases from the bottom to the top of the plate. The maximum value of the bending moment M_x increases 11.48 times when the frost heaving force increased from 8 kPa to 100 kPa. From Figure 12(c), it can be seen that the maximum value of bending moment M_y increases by 11.3 times when the frost heaving force increases from 8 kPa to 100 kPa. From Figures 12(d)–12(f), it can be seen that increasing the magnitude of the frost heaving force will increase the values of bending moment M_{xy}, shear force Q_x, and shear force Q_y, and they are symmetrically distributed along the height of the plate. Figures 12(g)–12(i) show that when the frost heaving force increases from 8 kPa to 100 kPa, the stress σ_x increases by 12.6 times, the stress σ_y increases by 12.3 times, and the stress τ_{xy} increases by 12.3 times.

4. Engineering Case Analysis

Wang [7] calculated the frost heaving deformation and damage location of a plain concrete lined trapezoidal canal, and the following calculation was carried out using the parameters of the engineering case used by Wang, and the dimensional loading parameters of the canal are as follows. The height of bottom plate is 2 m, and the width is 3 m; the height of slope plate is 2.83 m, and the width is 3 m; the thickness of plates is 0.2 m, the frost heaving force of bottom plate is 7.3 kPa, and the maximum frost heaving force of slope plate is 8 kPa. The elastic modulus of the concrete is 2.2×10^4 MPa and Poisson's ratio is 0.16.

Figure 13 shows the deflection, internal force, and stress distribution of the slope plate. Figure 13(a) shows that the deflection is basically symmetrical along the height of the plate, and the maximum deflection value is 0.22 mm, which meets the deformation requirements of the lining plate.

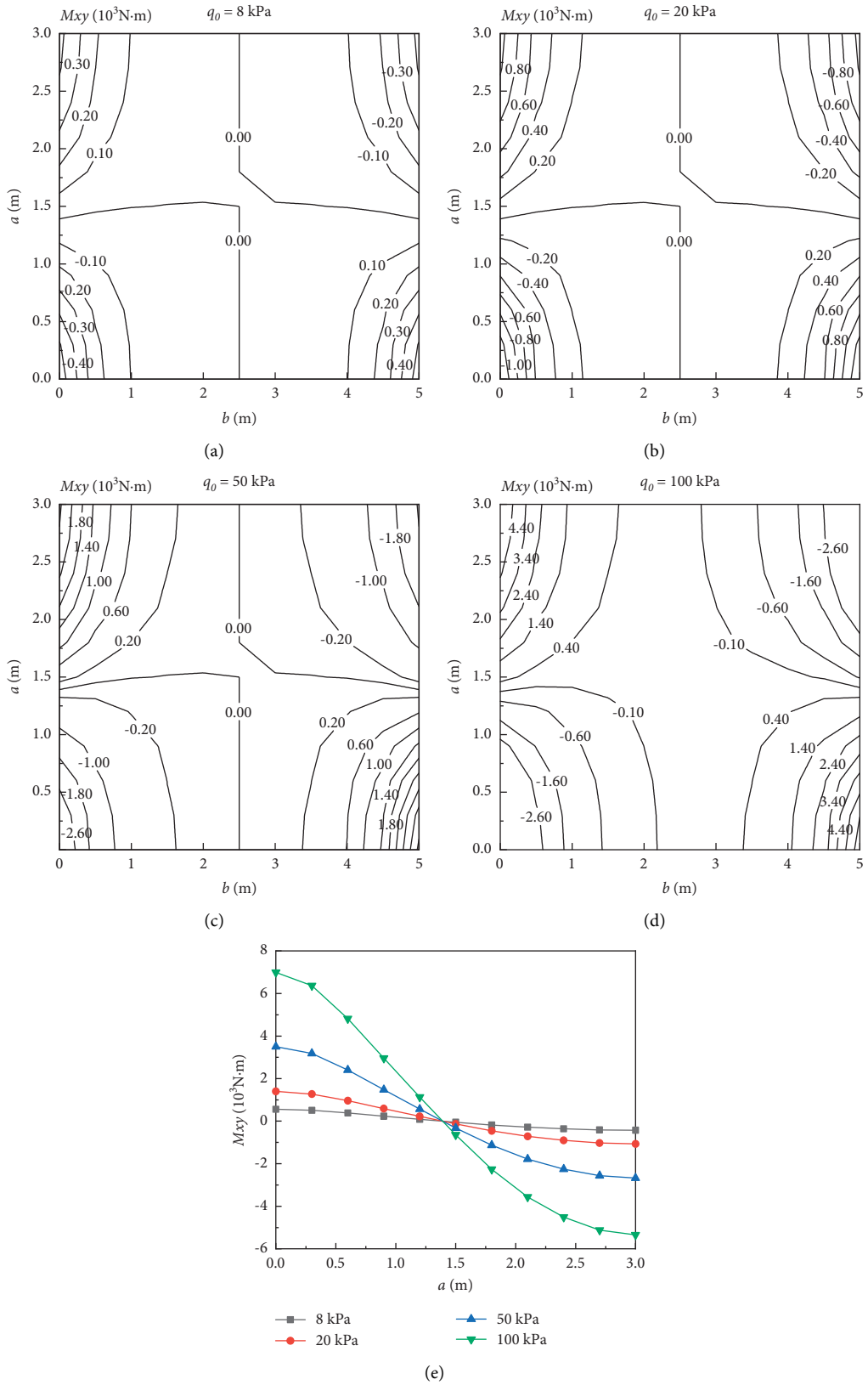

FIGURE 9: Effect of frost heaving force on bending moment M_{xy}.

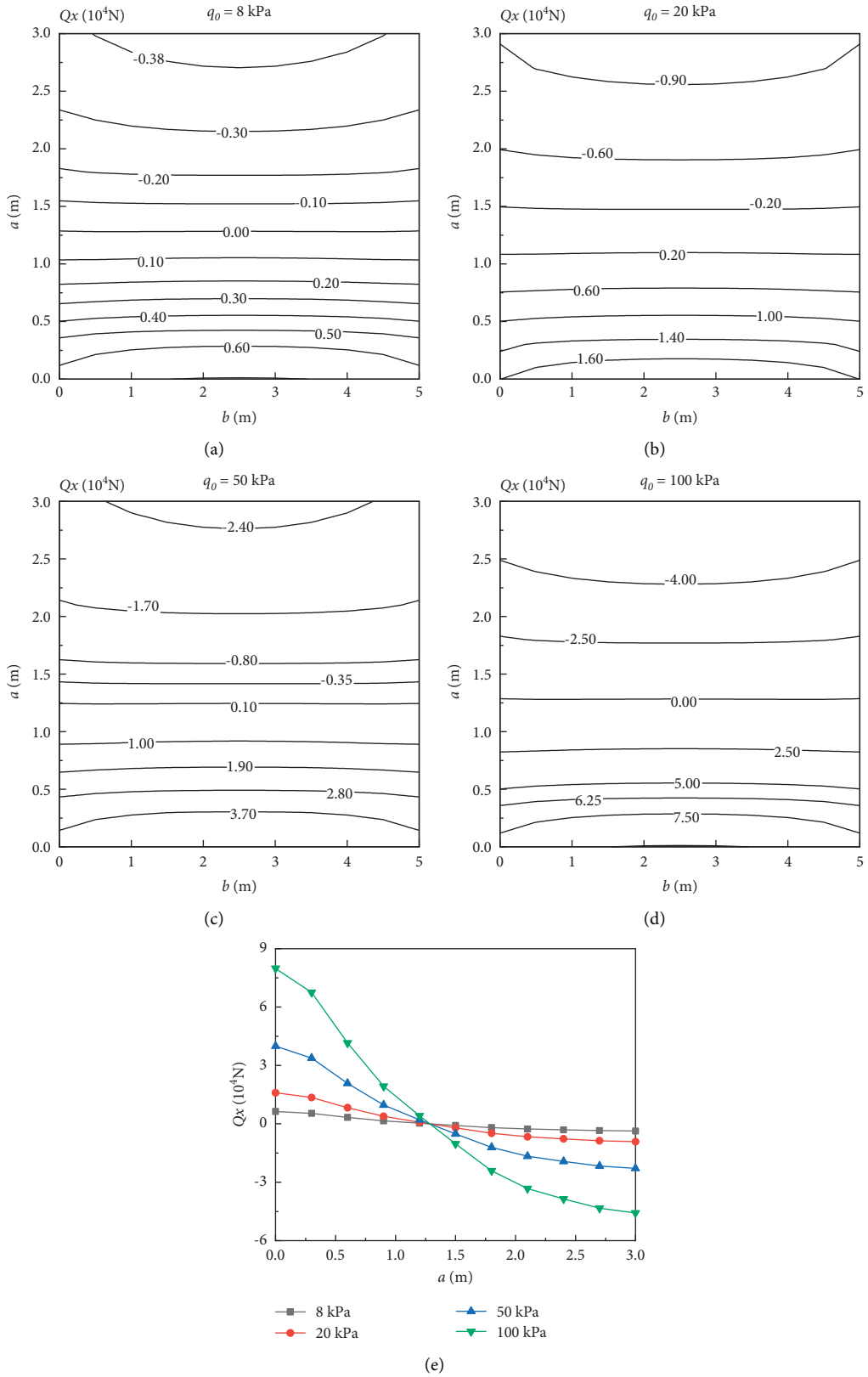

Figure 10: Effect of frost heaving force on shear force Q_x.

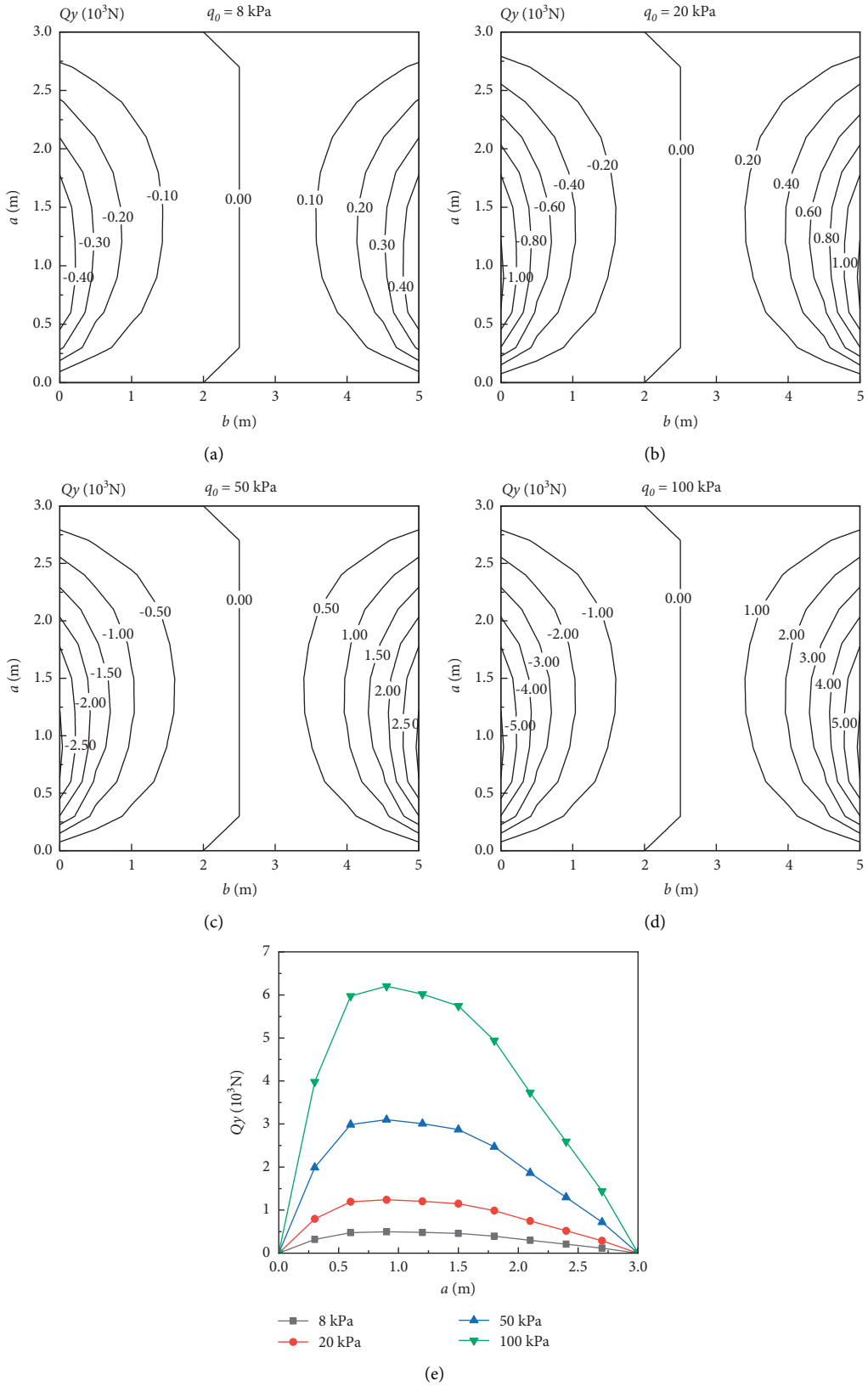

Figure 11: Effect of frost heaving force on shear force Q_y.

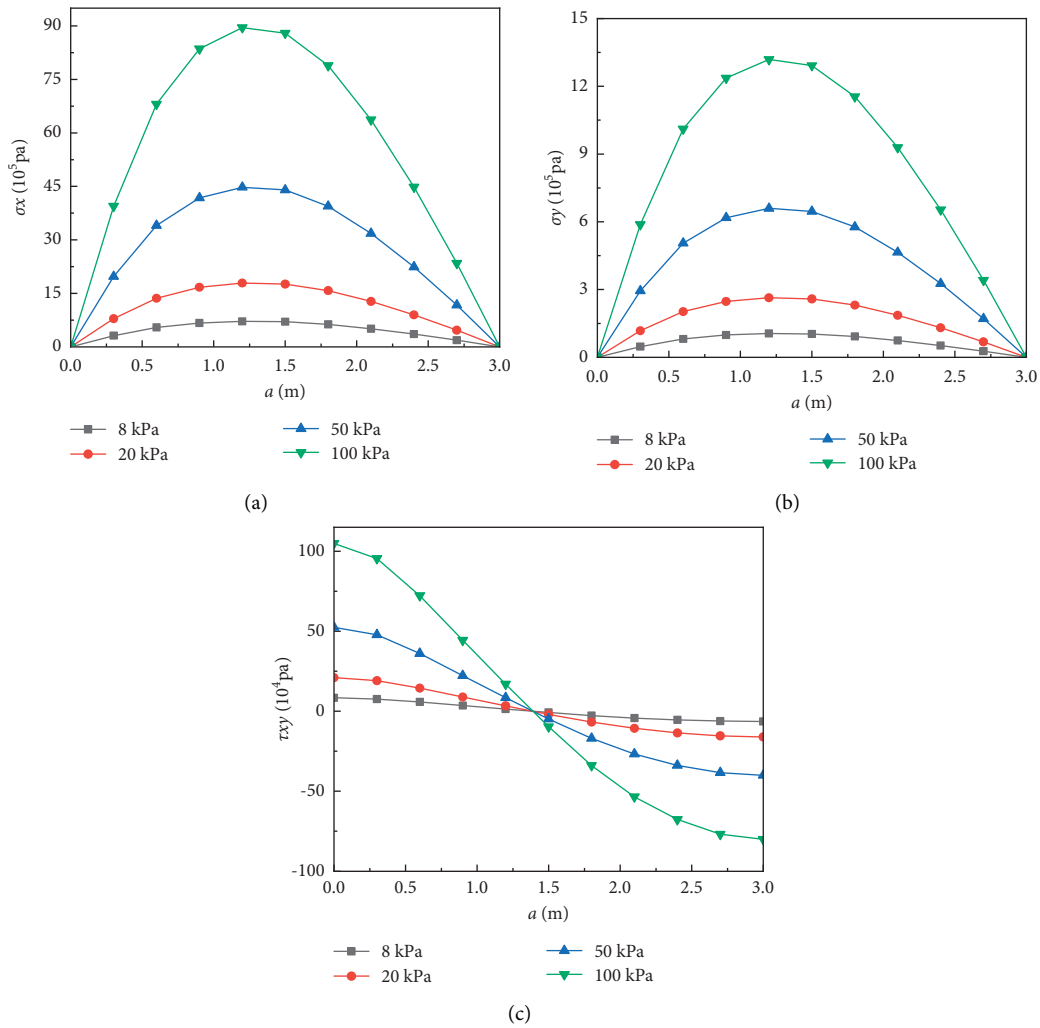

Figure 12: Effect of frost heaving force on stress.

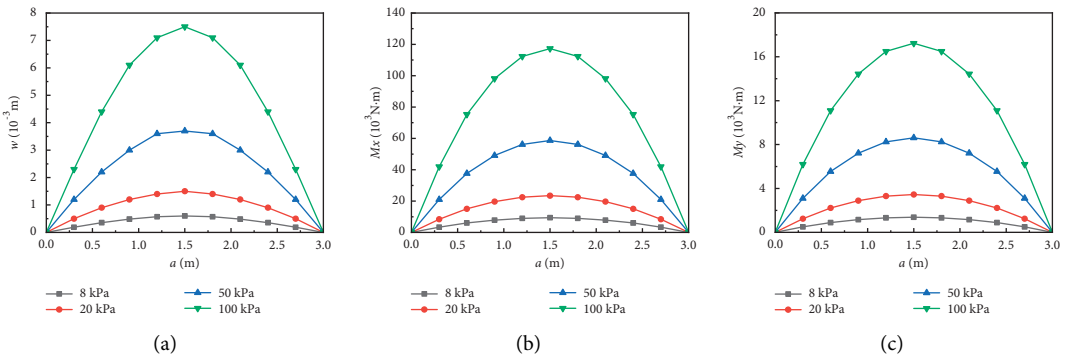

Figure 13: Continued.

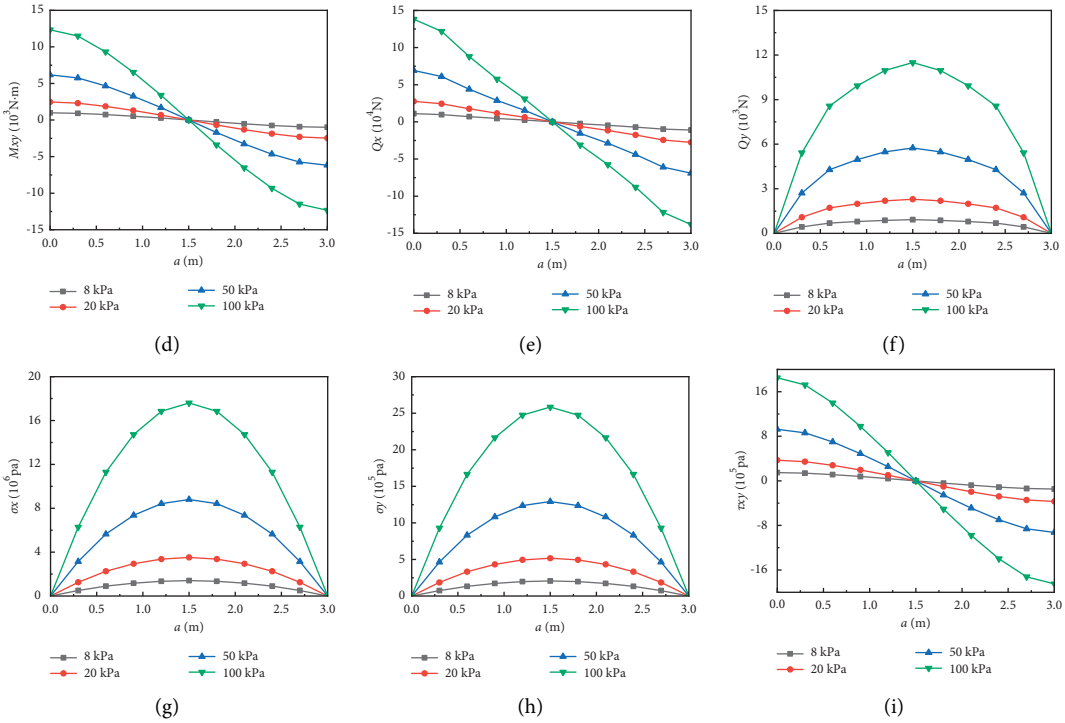

Figure 13: Effect of frost heaving force on deflection, internal force, and stress of the bottom plate.

Figure 13(b) shows that the bending moment M_x is asymmetrically distributed along the height direction of the plate. The bending moment M_x is the main internal force causing the longitudinal crack, and the maximum bending moment is near the location of the slope bottom, which is consistent with the references and the damage location in engineering practice [12, 23, 24]. The bending moment M_y (Figure 13(c)) is small at the edge and large at the center of the plate. The torque M_{xy} (Figure 13(d)) is maximum at the four corners of the plate and coincides with the geometric inflection points of the plate; although its numerical magnitude is lower than the value of the bending moment M_x, it may also cause stress concentration to damage the lining plate and thus cause leakage. The maximum values of shear forces Q_x and Q_y (Figures 13(e), (f)) are at the upper and lower edges and left and right edges, respectively, and are asymmetrically distributed along the height direction of the slope plate. The distribution laws of stresses σ_x, σ_y, τ_{xy} (Figures 13(g), (h), (i)) are the same as their corresponding internal force distribution laws.

5. Conclusion

(1) A mechanical model for deformation analysis of canal lining plates under the action of frost heaving force is established based on the theory of rectangular thin plate, the boundaries of rectangular thin plate are simplified to two pairs of simply supported opposite edges and the other two pairs of opposite edges are free (longitudinal expansion joints), and the solution process of the model is given.

(2) Under the action of nonuniformly distributed frost heaving force, the slope plate has no obvious nonuniform distribution of deflection along the depth of the canal; the bending moment, shear force, and internal force show nonuniform distribution; and the maximum values of bending moment Mx and positive stress σ_x are biased to the bottom plate position. Compared with the beam theory, the calculation results of the plate theory show that the internal forces and stresses increase at the free boundary.

(3) The bending moment M_{xy} and stress τ_{xy} are maximum at the four corners of the plate and geometrically coincide with the corners of the plate, although their numerical magnitudes are lower than that of the bending moment M_x, and they may also cause stress concentration to damage the lining plate and thus cause leakage. Although the shear forces at the left and right joint locations are not as large as the cross-sectional shear force, they may lead to fracture of the joint material, which needs to be considered in the design process.

(4) Due to the uniform distribution of the frost heaving force on the bottom plate lining, its deflection, internal force, and stress also show uniform distribution.

Data Availability

Data can be obtained from the article and corresponding author upon request.

Conflicts of Interest

The authors declare that they have no conflicts of interest.

Authors' Contributions

Yangtao Liang was responsible for project administration. Fuping Zhang carried out formal analysis and wrote the original draft. Mingming Jing did data curation and formal analysis. Pengfei He carried out writing (original draft preparation) and formal analysis.

Acknowledgments

This work was supported by the State Grid Gansu Electric Power Company Science and Technology (project no. SGGSJS00XMYBJS2100062).

References

[1] Ministry of water resources of the People's Republic of China, *China Water Resources Bulletin*, China Water&Power Press, Beijing, 2017.

[2] J. Li, *Study on Mechanical Model and Anti-frost Heaving Structure of Canal Lining*, Northwest A&F University, 2008.

[3] X. Chen, J. Liu, and H. Liu, *Frost Action of Soil and Foundation Engineering*, Science Press, Beijing, 2006.

[4] Y. Zhou, D. Guo, and G. Qiu, *Geocryology in China*, Science Press, Beijing, 2000.

[5] A. Li, "Anti-seepage engineering techniques for irrigation canals," *Water Saving Irrigation*, vol. 4, pp. 6–8, 1998.

[6] H. Adalat and S. Yu, "Study and prospect of ice damage prevention and control in Xinjiang's water conveyance projects," *Journal of Water Resources and Architectural Engineering*, vol. 8, no. 3, pp. 46–49, 2010.

[7] Z. Wang, "Establishment and application of mechanics models of frost heaving damage of concrete lining trapezoidal open canal," *Transactions of the Chinese Society ofAgricultural Engineering*, vol. 20, no. 3, pp. 24–29, 2004.

[8] G. Sun, Z. Wang, and W. Wang, "Frostheave fracture mechanical model for concrete lining trapezoidal canal and its application," *Transactions of the Chinese Society of Agricultural Engineering*, vol. 29, no. 8, pp. 108–114, 2013.

[9] M. Xiao, Z. Wang, and Q. Liu, "Mechanical analysis on frost heave damage of cast-in-place concrete trapezoidal canal considering influence of groundwater table," *Transactions of the Chinese Society of Agricultural Engineering*, vol. 33, no. 11, pp. 91–97, 2017.

[10] J. Shi, Z. Wang, and F. Zhang, "Development and application of frost-heaving fracture damage mechanical model for concrete lining canal with arc-bottom trapezoidal at high groundwater level," *Journal of Northwest A&F University*, vol. 43, no. 1, pp. 213–219, 2015.

[11] Y. Wang, L. Wang, and S. Cheng, "Study on frost heave resistance of different section structures of U-Shaped canal," *Journal of Northeastern University*, vol. 41, no. 9, pp. 1341–1347, 2020.

[12] M. Xiao, Z. Wang, and Q. Liu, "Elastic foundation beam model of frost heave damage of trapezoidal canal considering interaction between frozen soil and lining structure," *Journal of Hydraulic Engineering*, vol. 48, no. 10, pp. 1229–1239, 2017.

[13] P. He, W. Ma, and Y. Mu, "Elastic foundation beam model for frost heave damage of trapezoidal canal lining considering frost heave force and adfreeze force," *Journal of Central South University*, vol. 52, no. 11, pp. 4148–4157, 2021.

[14] J. Ge, Y. Niu, and Z. Wang, "Elastic foundation beam model of canal considering ice cover formation decaying and coupling effect between ice-structure-frozen soil," *Journal of Hydraulic Engineering*, vol. 52, no. 2, pp. 215–228, 2021.

[15] Z. Li, X. Yao, and L. Yang, "Frost heavemechanical model of concrete lining trapezoidal canal basedon elastic foundation beam theory," *Transactions of the Chinese Society of Agricultural Engineering*, vol. 35, no. 15, pp. 110–118, 2019.

[16] Z. Wang, H. Jiang, and Y. Wang, "Research progresses and frontiers in anti-seepage and anti-frost heave of canals in cold-arid regions," *Transactions of the Chinese Society of Agricultural Engineering*, vol. 36, no. 22, pp. 120–132, 2020.

[17] Z. Li, X. Yao, and R. Zhang, "Frost heave mechanical model of concrete lining trapezoidal canal considering nonuniform frost heave of foundation soil based on elastic foundation beam theory," *Transactions of the Chinese Society of Agricultural Engineering*, vol. 36, no. 21, pp. 114–121, 2020.

[18] Y. Huang and F. He, *Beam, Plate, Shell on Elasticfoundation*, Science Press, Beijing, 2005.

[19] Z. Xu, *Elasticity Mechanics*, Higher Education Press, Beijing, 5th edition, 2016.

[20] S. Timoshenko and S. Woinowsky-Krieger, *Theory of Plates and Shells*, McGraw-Hill, New York, 1959.

[21] X. Pan, H. Wang, and S. Tang, "Monitoring of the effect of slab structure on frost heaving of U-shaped concrete lining canal," *Yellow River*, vol. 41, no. 4, pp. 153–158, 2019.

[22] S. Tang and H. Wang, "Mechanical model of small U-shaped concrete lining canal with three arc-plates under frost heaving," *Transactions of the Chinese Society of Agricultural Engineering*, vol. 32, no. 11, pp. 159–166, 2016.

[23] Z. Zhou, W. Ma, S. Zhang, Y. Mu, and G. Li, "Effect of freeze-thaw cycles in mechanical behaviors of frozen loess," *Cold Regions Science and Technology*, vol. 146, 2018.

[24] Z. Zhou, W. Ma, S. Zhang, Y. Mu, and G. Li, "Experimental investigation of the path-dependent strength and deformation behaviours of frozen loess," *Engineering Geology*, vol. 265, Article ID 105449, 2020.

Hindawi
Advances in Civil Engineering
Volume 2022, Article ID 7803002, 9 pages
https://doi.org/10.1155/2022/7803002

Research Article

The Effect of Length and Content of Fiber on Glass Fiber and Basalt Fiber-Reinforced Granite Residual Soil

Weijie Chen,[1] Jin Zhao,[1] Litao Fan,[1] Jia Li,[2] Bingxiang Yuan,[1] Hongzhong Li,[1] Guoping Jiang,[3] Hanbo Li,[4] and Tianying Chen[1]

[1]*School of Civil and Transportation Engineering, Guangdong University of Technology, Guangzhou 510006, China*
[2]*Company: Jiangmen Yinzhouhu Highway Co LTD, Transportation and Civil Engineering, Changsha University of Science and Technology, Changsha, China*
[3]*Fujian Jiangxia University, Fuzhou 350108, China*
[4]*Company: CCCC Fourth Navigation Bureau Second Engineering Co Ltd, Wuhan, China*

Correspondence should be addressed to Bingxiang Yuan; yuanbx@gdut.edu.cn

Received 30 May 2022; Accepted 20 June 2022; Published 15 July 2022

Academic Editor: Zhuo Chen

Fiber-reinforced soil boasts fewer cracks, higher energy absorption, and higher residual strength. With the well-established concept of carbon neutralization, it is necessary to reduce the dependence on high carbon-emitting reinforcement materials such as cement and concrete. The need for resource recycling has led to the development of reusing construction waste as the raw material for slope and embankment reinforcement. The purpose of this study is to analyze the reinforcement performance and environmental feasibility of glass and basalt fiber on granite residual soil with the content of 3%, 4%, and 5% and the length of 6 mm, 9 mm, and 12 mm. The reinforced samples were subjected to static impact load tests and SEM analysis to study its mechanical properties, microcharacteristics, and structure before and after reinforcement. Results show that the incorporation of 3% glass fibers of 6 mm has the best reinforcement effect on GRS, while the incorporation of 4% basalt fibers of 6 mm also has a good reinforcement ability. Glass fiber performs better than basalt fiber under the optimal content and length. SEM results indicate that glass fibers bind the soil particles more closely, thereby increasing their friction and leading to higher compressive strength. When the length and content of fiber exceed a certain range, the fibers are prone to cross and knot and fail to fill between soil particles, so the fiber and soil particles are separated, which lowers the strength of the soil. It is concluded that both glass fiber and basalt fiber can be well used for reinforcing GRS for higher bearing capacity and fewer cracks at the given proportion and length. Fiber length and content were considered when reinforcing GRS with different fibers in this study.

1. Introduction

With a skyrocketing population, the necessity of relieving traffic in urban areas and bolstering infrastructure construction has grown. Subway and infrastructure construction significantly alleviated traffic and satisfied people's demands, but it also inevitably generated a mass of waste soil, the treatment of which has become a matter of concern. It is predicted that China produced about 2 million tons of construction waste in 2019 alone [1]. Typically, the waste is removed by transportation and landfill. However, this traditional method is not sustainable, eco-friendly, or land-efficient; thus, the recycling of construction waste soil has become an important area of study.

In South China, the majority of construction waste consists of granite residual soil (GRS), which is produced under certain geographical conditions, climate, and geological environments. It is also known as a regionally distinctive soil due to its unique composition and structure [2–4]. Physical and chemical weathering crafted its distinctive structure with heterogeneity and anisotropy and its unique engineering geomechanical characteristics. Granite residual soil has good compressive properties in dry environment and unique structural properties, which include

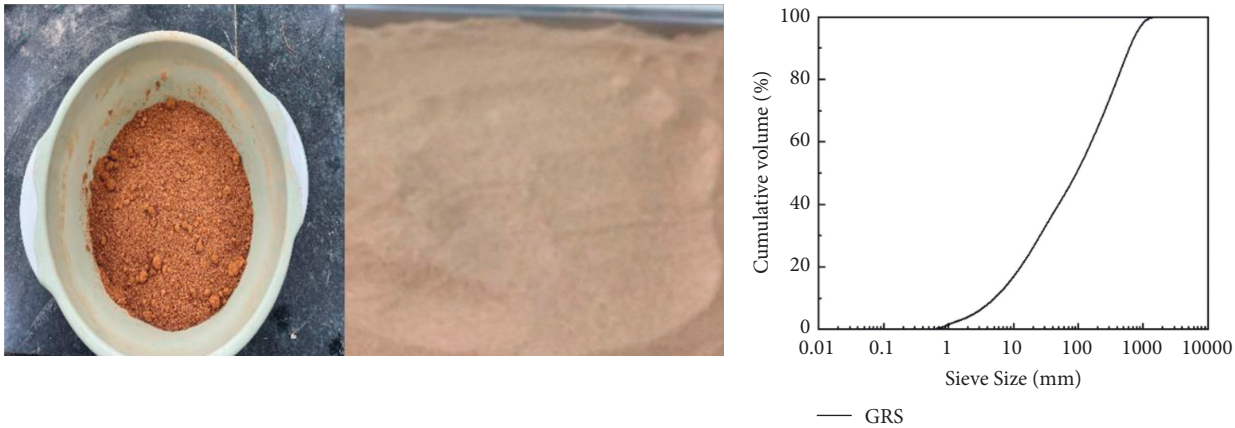

Figure 1: Material diagram. (a) Granite residual soil. (b) GRS particle size.

high void ratio, high strength, low density, and medium and low compressibility [5–9], rendering it a poor compressive material. This easily leads to a significant decrease reduction in bearing capacity after being saturated in water and a particularly sharp decline under dry-wet cycles, which in actual projects triggers natural disasters such as slope landslides and soil collapse. In reality, the majority of GRS is therefore treated as construction waste soil. For the recycling of GRS, the issue of its high porosity must be resolved, as it suggests restricted contact between soil particles [10–15]. Under external impact, bearing capacity tends to decline, resulting in incidents such as dislocation and sliding. Recycling GRS requires addressing its porosity.

Fibers, such as steel fiber, polyethylene fiber, and basalt fiber, are frequently employed in concrete engineering since it has been demonstrated that they effectively reduce the cracking of concrete and increase its tensile resistance under external load [16–19]. Therefore, some researchers utilized fibers to reinforce GRS. For instance, waste rubber fibers were mixed with swelling soil, and the mixture properties were studied by laboratory compaction test [20–24]. Results indicate that waste rubber fibers can considerably limit soil expansion and increase its resistance to cracking [25–27]. The modified swelling soil mixture is ideally suited for utilization as impervious liners and covers for urban solid waste landfills. Sisal fibers were incorporated into the soil, and the tensile properties of reinforced soils were investigated by indoor strength testing. Additionally, cement and cactus pulp were added to boost the strength [28–30]. The results demonstrated that cactus pulp, an environmentally benign natural ecological material, outperformed sisal fibers in reinforcing capacity. Apus bamboo root fibers were utilized to reinforce soil, and the shear strength behavior of the reinforced soil was analyzed using a direct shear test with a large box sample. The ratio of soil volume to root volume is proposed to quantify root density in soil mass [31]. The peak shear strength of reinforced soil was shown to improve as the soil-root volume ratio increased. Previous studies indicated that the impact resistance of GRS under dynamic load can be significantly improved by introducing SH solution and glass fiber. After reinforcing, the microscopic investigation revealed that the porosity was reduced and hydrophilic groups were replaced with hydrophobic groups, hence removing the hydrophilicity of GRS [32, 33].

Many authors have reported on fiber-reinforced GRS, with the majority focusing on fiber comparison. Little study has been conducted on the effect of fiber length and content. This study focuses on reinforcing GRS in an effective and economically viable manner, with environmental protection and sustainability as its central goals. The static load test was used to explore the reinforcing effect of glass and basalt fibers of varying lengths and contents, and SEM was used to analyze the reinforcement mechanism of GRS and the effect of fiber length and content from a microscopic perspective.

2. Experimental Study

2.1. Materials

2.1.1. Granite Residual Soil. Widely distributed in South China, granite residual soil is produced under specific geographical conditions, climates, and geological environments. Since it has special composition and structure, it is also called a regional special soil. The physical and chemical weathering made its distinctive structure with heterogeneity and anisotropy, and its unique engineering geomechanical characteristics. GRS often comprises yellowish-brown colors and mainly consists of cohesive soil, partly cobbly cohesive soil (Figure 1). This study adopted GRS from the Guangzhou area. The main geomechanical properties are given in Table 1.

2.1.2. Glass Fibers. As shown in Figure 2, the glass fiber used in the experiment is an inorganic nonmetallic transparent material with excellent performance. Glass fibers boast excellent performances, i.e., good insulation, heat resistance, corrosion resistance, and high mechanical strength. Glass fibers of 6 mm, 9 mm, and 12 mm in length were used as the reinforcer. The specific parameters of the glass fibers are shown in Table 2.

Table 1: Properties of granite residual soil samples.

Specific gravity, d_s	Water content, ω (%)	Density (g/cm^3)	Liquid limit, ω_l	Plastic limit, ω_p
2.67	13	16.5	48.3	27

(a) (b)

Figure 2: Material diagram. (a) Glass fiber. (b) Basalt fiber.

Table 2: Basalt fiber parameters.

Density (g/cm^3)	Linear density (dtex)	Elastic modulus (MPa)	Tensile strength (MPa)	Melting point (°C)	Elongation (%)
2.65	8.21	4500	330	958	3.0

Table 3: Glass fiber parameters.

Density (g/cm^3)	Linear density (dtex)	Elastic modulus (MPa)	Tensile strength (MPa)	Melting point (°C)	Elongation (%)
0.91	8.21	4286	346	169	36.4

2.1.3. Basalt Fiber. As shown in Figure 2, the basalt fiber used in this experiment is a continuous fiber made from natural basalt rock, composed of oxides including silicon dioxide, aluminum oxide, calcium oxide, magnesium oxide, ferric oxide, and titanium dioxide. Basalt continuous fiber is a new type of inorganic and green material with high performance including electrical insulation, corrosion resistance, and high-temperature resistance. Basalt fibers of 6 mm, 9 mm, and 12 mm in length were used as the reinforcer. The diameter of glass fiber is 14 μm, and the diameter of basalt fiber is 14–20 μm. The fiber data of this test are all provided by Taishan Fiber Co., Ltd. The specific parameters of the basalt fibers are given in Table 3.

2.2. Sample Preparation and Curing. The soil samples were baked in an oven at about 105°C for 6–8 h. The samples were removed out of the oven after they dropped to room temperature and then crushed and sieved (1.18 mm). The two fibers of different lengths and content were mixed with the soil samples evenly. According to the geotechnical specification [34], the GRS and fibers were prepared by layered sample preparation. First, the fibers and GRS were stirred evenly with a small electric mixer, then a small compactor was used for layered compaction, and the number of layers was 3 layers. A small compaction instrument was used to compact the samples into a cylinder with a diameter of 100 mm and a height of 50 mm (Figure 3) by adding the soils three times. The samples were air-dried in a ventilated and dry indoor place for 14 days. The sample weight is 1600 g.

2.3. Test Plan

2.3.1. Static Load Test. The optimal water content adopted in this study is 13% of existing research [32].

Fibers of different types, lengths, and contents were included in soil samples under the optimal water content, and the effects of different groups were studied through a static load test. The test plan is shown in Table 4.

The fiber content was kept at 3%, the optimal data from previous research, so only the effect of the length change of fiber is considered in this test.

Groups A, B, and C contain 3% glass fiber with a length of 6 mm, 9 mm, and 12 mm, respectively. As the reference, group 0 is GRS with no fiber. Other groups of the different mixtures are given in Table 4, and three samples were made for each variable.

2.4. Test Methods

2.4.1. Static Load Test. The uniaxial compressive strength of the samples was measured by a 4 W uniaxial compression

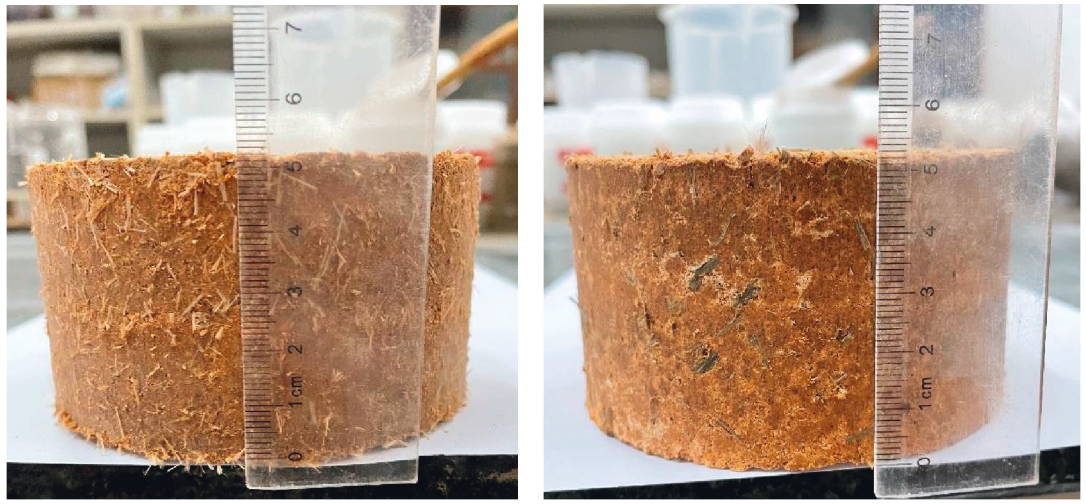

Figure 3: Reinforced glass fiber soil sample and reinforced basalt fiber soil sample.

Table 4: Static load test plan.

	Group	Sample name	Glass fiber (%)	Basalt fiber (%)	Length (mm)
Static load test	A	Glass fiber, 3%–6 mm	3	0	6
	B	Glass fiber, 3%–9 mm	3	0	9
	C	Glass fiber, 3%–12 mm	3	0	12
	D	Basalt fiber, 3%–6 mm	0	3	6
	E	Basalt fiber, 4%–6 mm	0	4	6
	F	Basalt fiber, 5%-6 mm	0	5	6
	G	Basalt fiber, 4%–9 mm	0	4	9
	H	Basalt fiber, 4%–12 mm	0	4	12
	O	0	0	0	0

test instrument (Figure 4). The samples were placed in the center of the bearing plate of the press to ensure that no eccentric loading occurs in loading. The loading rate was 0.5 MPa/s. The loading axial force when the sample failed was recorded to calculate the uniaxial compressive strength of each sample with the following formula [34]:

$$R = \frac{P}{A}. \quad (1)$$

R is the ultimate compressive strength of the sample, P is the maximum load when the sample failed, and A is the cross-sectional area of the sample.

The strength of the three samples under the same concentration was recorded. The strength values were averaged following the principle that the limit load does not exceed 10%. The reinforcement effect of fiber type, length, and content to GRS was investigated by a static load test. Aiming at achieving the optimal effect at a reasonable cost, the desired content and length of the two types of fiber were obtained in this study.

Figure 4: Uniaxial compression test instrument.

3. Results and Discussion

3.1. Static Load Test. The maximum stress of the soil sample without fiber was 850 kPa, and the corresponding strain value was 0.04% under static load as illustrated in Figure 5(a). From the data of groups A, B, and C as illustrated in Figure 5(b), the sample reinforced with glass fiber of 3% in content and 6 mm in length exhibited the best reinforcement performance of a maximum stress value of 1650 kPa, a corresponding strain value of 0.06% and a 94% increase of strength compared to fiberless samples. This finding signified that glass fiber can improve the compressive

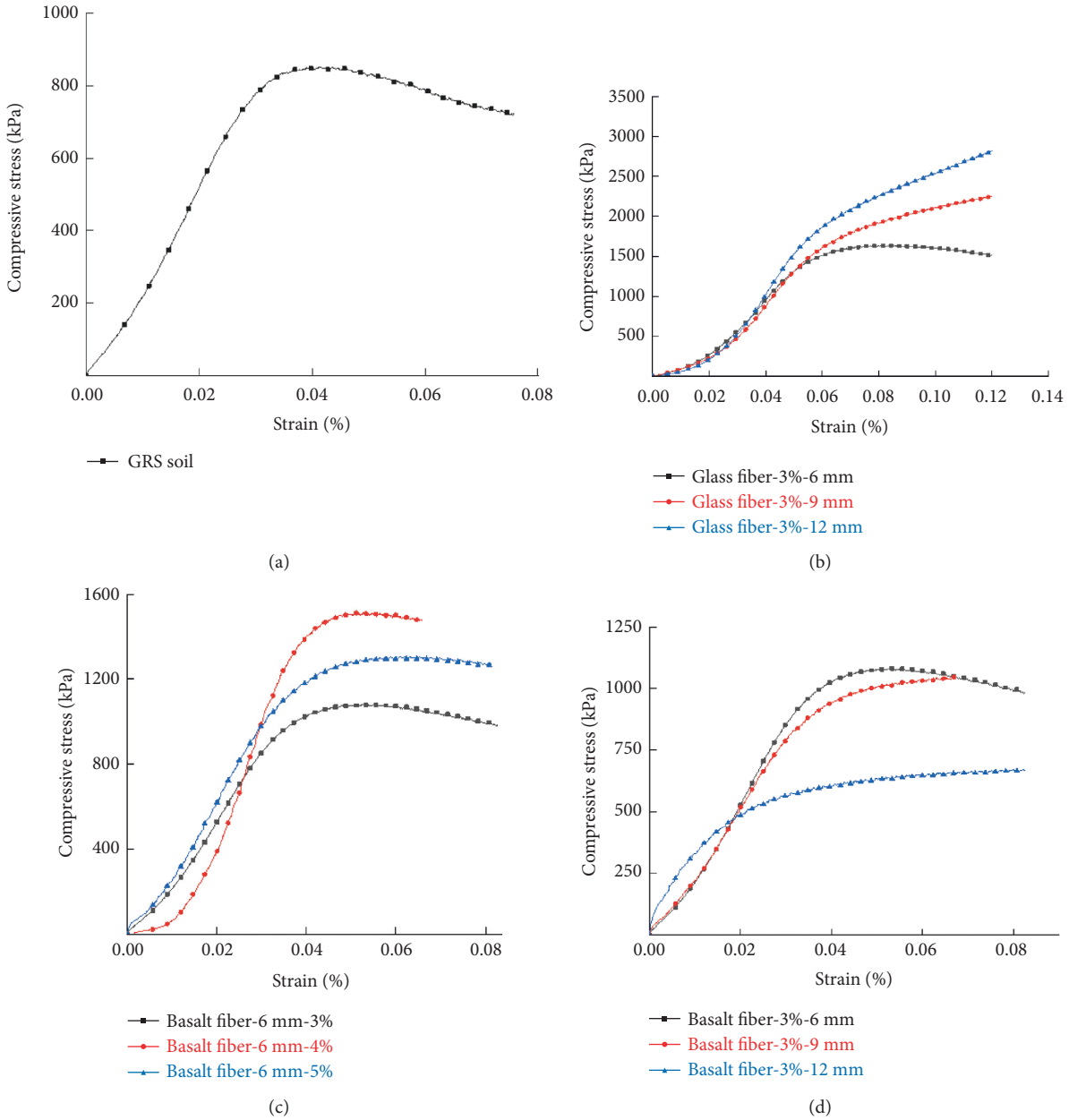

Figure 5: Continued.

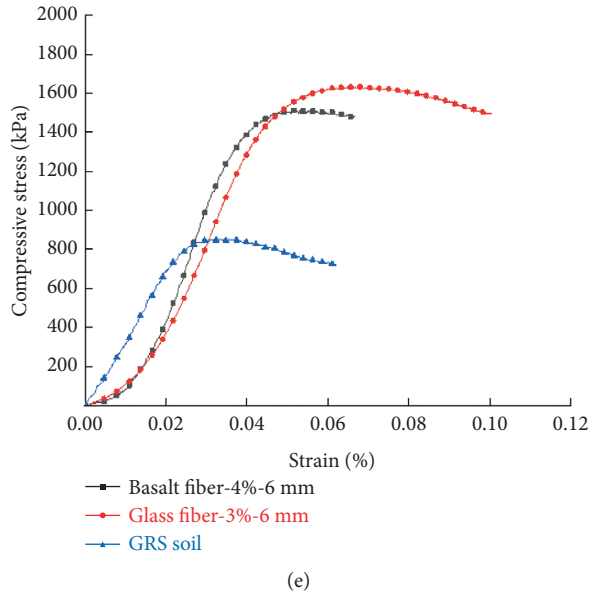

(e)

Figure 5: Compressive strength curve.

capacity of the sample. For samples of all three kinds of lengths, they went upward before the strain reached 0.05% and showed varied trends after that but before the strain reached 0.05%. An obvious trend of increase, peak, and decrease was observed in samples with 6 mm glass fibers, which peaked at 1650 kPa. However, samples with 9 mm and 12 mm glass fibers only showed a continuous upward trend. This result reveals that the incorporation of 6 mm glass fibers has a better reinforcement effect on GRS than 9 mm and 12 mm at the content of 3%. The reason behind this is that 6 mm glass fiber contacts with soil particles better and creates higher friction, enabling the sample to be more integrated and bear force together with fibers. The samples with 6 mm fiber had relatively reasonable deformation under the stress, and there is a corresponding relationship between strain and stress. By contrast, the stress of 9 mm and 12 mm samples increased with the strain continuously without peak or decline, indicating that the sample can be compressed and deformed infinitely and the stress can also increase infinitely, which is unreasonable. Therefore, it was concluded from the data that the reinforcement ability of the 6 mm glass fiber reinforcement effect was better than 9 mm and 12 mm under the same content of 3%.

From Figure 5(c), it is noticed that the samples with 6 mm basalt fibers at 3%, 4%, and 5% presented the maximum stress value of 900 kPa, 1500 kPa, and1300 kPa, respectively, 5%, 76%, and 53% higher than the fiberless sample. Thus, the inclusion of basalt fiber in GRS can improve its bearing capacity. In addition, the three curves all showed three stages: rise, peak, and fall. The strain value corresponding to the maximum stress value of the three was 0.05%. At a fixed length of 6 mm, the bearing capacity of the reinforced soil can be improved under the three content as proved in their curves and maximum stress values. To obtain a rather economical result, 3% basalt fibers showed a better reinforcement effect compared to 4% and 5% under the same length of 6 mm based on their maximum stress value and the corresponding strain value.

At a fixed basalt fiber proportion of 3%, the effect varied with lengths as illustrated in Figure 5(d), wherein the 6 mm sample performed the best as they reached a maximum stress value of 1100 kPa and a corresponding strain value of 0.05%, and the curve could be also divided into three stages of rising, peak, and fall. The curves of 9 mm and 12 mm length basalt fibers had a similar trend but only rose continuously.

The reason may be that a lower length of fiber means a larger quantity for the two kinds of fibers under the same content, so the fiber is distributed more evenly in the soil sample during preparation. At the initial stage of compression, the air and water in soil pores were expelled, and fiber processes higher elastic modulus compared to soil particles. Thus, the incorporation of fibers with lower length means more short fibers are distributed between soil particles, leading to higher friction and closer integration between soil and fiber, which is attributed to the higher compressive performance of the reinforced soil. However, long fiber in the soil is inclined to cross knot and overlap with each other, so the separation between the soil particles and fiber would occur under external load. Consequently, the fiber takes the force in place of the soil particles' stress, so the stress continued to increase with the strain without peak or downturn as shown in the figure. Thus, the optimum content and length of glass fiber are 3% and 6 mm and those of basalt fiber are 4% and 6 mm from the above data.

At the above optimal formula, the basalt and glass fiber reached a maximum stress of 1550 kPa and 1650 kPa and a corresponding strain of 0.05% and 0.06%, respectively, in Figure 5(e). The two kinds of fibers displayed an excellent effect on reinforcing GRS as an enhancement of the bearing capacity of GRS was achieved. GRS reinforced with 3% 6 mm glass fiber and 82% 6 mm basalt fiber witnessed a 94% and 82% strength increase, respectively. The results evidence that

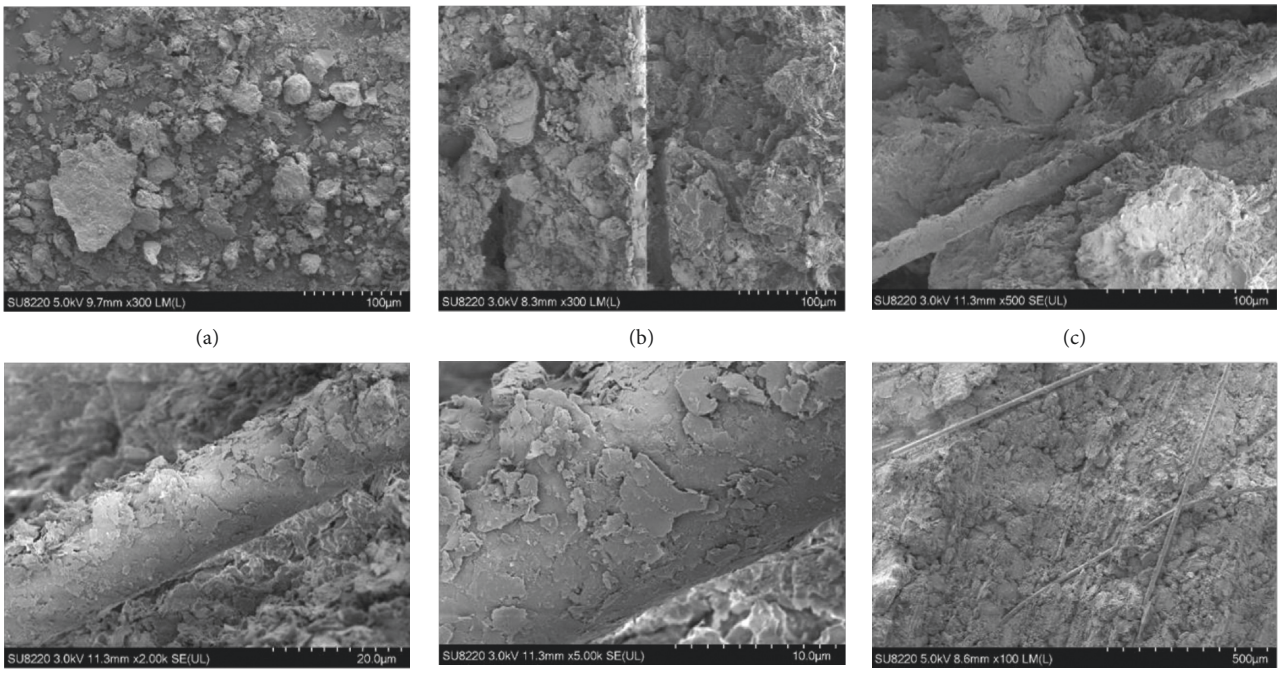

(a) (b) (c)

(d) (e) (f)

Figure 6: SEM of test soil.

glass fiber exhibited a better reinforcement effect than basalt fiber. The reason may be that glass fiber is finer than basalt fiber. As shown in Figure 2, glass fiber, a relatively fine cylinder as opposed to the flat basalt fiber, would find itself more easily filling in the pores of soil particles under the same length. The increased friction help enhance the integrity of the samples, which results in higher bearing capacity.

From the static load test analysis, it can be concluded that the reinforcement effect of glass fiber on granite residual soil is better than that of basalt fiber under the condition of optimal fiber content and length.

3.2. SEM. Given that the reinforcing ability of glass fiber is better than basalt fiber from the above mechanical analysis, the glass fiber samples were studied by SEM. The SEM images of samples taken from group O, group A, and group C after the static load test are given in Figure 6. At the magnification of 500x, the soil of control group O (Figure 6(a)) was granular particles with weak particle connection, so the sample failed under the impact of excessive static load. Compared with group O, the figures of group A (Figures 6(b)–6(e)) and group C (Figure 6(f)) show that the samples remained relatively intact under the impact load with glass fiber binding the soil into integration and jointly bearing the load. The glass fiber added to the soil acted as the reinforcer, which enhanced the integrity of the sample and its limit bearing capacity. It was noticed in Figures 6(d) and 6(e) that a considerable amount of soil particles were attached to the fiber, indicating that the inclusion of glass fiber into GRS can improve the friction and effective stress between soil particles and thus strengthen the soil. Based on the Mohr–Coulomb criterion of rock failure, when the failure occurs in the soil as a shear failure, the shear bearing capacity of soil fails to bear the shear stress produced by an external load. The shear stress-bearing capacity of soil lies in the friction force produced by the relative replacement of soil particles when sliding after compaction. Thus, the incorporation of glass fiber and basalt fiber increases the surface friction.

From Figure 6(f), it was revealed that fibers of excess length and content might cross and knot with each other and fail to contact the soil particles. Consequently, the soil particles and fibers were separated and failed to work together under the action of external load, so the effective stress of soil particles cannot be improved. Meanwhile, due to the separation of fibers and soil particles, the pores between soil particles are not filled with fibers. Therefore, adding fibers of excess length and amount cannot exhibit an excellent reinforcement effect, but may easily lead to a decline in bearing capacity.

SEM results show that, at appropriate length and content, fiber will be able to distribute well in the pores between soil particles, increase the internal friction force between soil particles, and attach to the surface of more soil particles. Fibers play a role alike to bridging and in connecting the soil particles around them, thus enhancing the integrity of the soil particles and helping maintain the intactness of the sample under external load.

4. Conclusion

In this study, a static load test was conducted on reinforced GRS to compare the reinforcing effect of glass and basalt fibers of different lengths and contents through group experiments. The influence of fiber's length and content and

the reinforcement mechanism were identified using the SEM technique:

(1) In static load tests, an enhancement in compressive strength is witnessed with the inclusion of the glass fiber and basalt fiber compared to fiberless samples, which proves the improvement effect of glass fiber and basalt fiber on the bearing capacity of GRS.

(2) The results of the static load test show that the incorporation of 6 mm basalt fiber exhibited the best reinforcement effect with a maximum stress of 1100 kPa among samples containing 3% basalt fiber. Moreover, the incorporation of 4% basalt fiber exhibited the best reinforcement effect with a maximum stress of 1550 kPa among samples containing 6 mm basalt fiber. Hence, the optimal length and content of basalt fiber are 6 mm and 4%. The optimal length and content of glass fiber are 6 mm and 3% based on the data.

(3) At the above optimal formula, the basalt and glass fiber reached a maximum stress of 1550 kPa and 1650 kPa and a corresponding strain of 0.05% and 0.06%. Re-SEM analysis indicates that fibers are prone to cross and knot and fail to fill between soil particles when the length and content of the fiber exceed a certain range, which lowers the integration between them and lowers the bearing capacity of the soil.

(4) SEM analysis indicates that fibers are prone to cross and knot and fail to fill between soil particles when the length and content of fiber exceed a certain range, which lowers the integration between them and lowers the bearing capacity of the soil.

Data Availability

Data can be obtained from the corresponding author upon request.

Conflicts of Interest

The authors declare that they have no conflicts of interest.

Acknowledgments

The authors would gratefully like to acknowledge the support provided by the National Natural Science Foundation of China (nos. 51978177 and 41902288).

References

[1] S. Nanda and F. Berruti, "Municipal solid waste management and landfilling technologies: a review," *Environmental Chemistry Letters*, vol. 19, pp. 1433–1456, 2020.

[2] Y. He, F. Gu, C. Xu, and Y. Wang, "Assessing of the influence of organic and inorganic amendments on the physical-chemical properties of a red soil (Ultisol) quality," *Catena*, vol. 183, Article ID 104231, 2019.

[3] Y. Deng, X. Duan, S. Ding, C. Cai, and J. Chen, "Suction stress characteristics in granite red soils and their relationship with the collapsing gully in south China," *Catena*, vol. 171, pp. 505–522, 2018.

[4] J. Xia, C. Cai, Y. Wei, and X. Wu, "Granite residual soil properties in collapsing gullies of south China: spatial variations and effects on collapsing gully erosion," *Catena*, vol. 174, pp. 469–477, 2019.

[5] W. Chen, Z. Chen, and S. Liu, "EXPERIMENTAL RESEARCH ON STRESS PATHS OF GRANITE RESIDUAL SOIL," *Industrial Construction*, vol. 47, pp. 11–16, 2017.

[6] B. Bai, Y. Wang, D. Rao, and B. Fan, "The effective thermal conductivity of unsaturated porous media deduced by pore-scale SPH simulation," *Frontiers of Earth Science*, 2022.

[7] B. Bai, Q. Nie, ZhangYike, X. Wang, and W. Hu, "Cotransport of heavy metals and SiO2 particles at different temperatures by seepage," *Journal of Hydrology*, vol. 597, Article ID 125771, 2021.

[8] B. Bai, R. Zhou, G. Cai, W. Hu, and G. Yang, "Coupled thermo-hydro-mechanical mechanism in view of the soil particle rearrangement of granular thermodynamics," *Computers and Geotechnics*, vol. 137, no. 8, Article ID 104272, 2021.

[9] B. X. Yuan, M. J. Chen, W. J. Chen, Q. Luo, and H. z. Li, "Effect of pile-soil relative stiffness on deformation characteristics of the laterally loaded pile," *Advances in Materials Science and Engineering*, 2022.

[10] X. Liu, X. Zhang, L. Kong, G. Wang, and H. Li, "Formation mechanism of collapsing gully in southern China and the relationship with granite residual soil: a geotechnical perspective," *Catena*, vol. 210, Article ID 105890, 2022.

[11] H. Mei, X. Jian, W. Zhang, H. Fu, and S. Zhang, "Behavioral differences between weathering and pedogenesis in a subtropical humid granitic terrain: implications for chemical weathering intensity evaluation," *Catena*, vol. 203, Article ID 105368, 2021.

[12] F. Ferreira, C. Vieira, and M. De, "Cyclic and post-cyclic shear behaviour of a granite residual soil -geogrid interface," *ADVANCES IN TRANSPORTATION GEOTECHNICS III*, pp. 379–386, 2016.

[13] Y. Peng, S. Tang, J. Huang, C. Tang, L. Wang, and Y. Liu, "Fractal analysis on pore structure and modeling of hydration of magnesium phosphate cement paste," *Fractal Fract*, vol. 6, p. 337, 2022.

[14] L. Wang, Z. Yu, B. Liu, F. Zhao, S. Tang, and M. Jin, "Effects of fly ash dosage on shrinkage, crack resistance and fractal characteristics of face slab concrete," *Fractal Fract*, vol. 6, p. 335, 2022.

[15] L. Wang, G. Li, X. Li et al., "Influence of reactivity and dosage of MgO expansive agent on shrinkage and crack resistance of face slab concrete," *Cement and Concrete Composites*, vol. 126, Article ID 104333, 2022.

[16] D. Kar, "Properties, Applications: Slurry Infiltrated Fiber Concrete (SIFCON)," *Concrete International*, 1984.

[17] H. Y. Yang, J. Li, Q. Z. Ye, and X. C. Zhang, "Research on absorbing EMW properties of steel-fiber concrete," *Journal of Functional Materials*, 2002.

[18] S. Acostacalderon, P. Gordillosilva, V. B. Dan, and J. F. Rada, "Comparative Evaluation of Sisal and Polypropylene Fiber Reinforced Concrete Properties," *FIBERS*, 2022.

[19] A. Tibebu, E. Mekonnen, L. Kumar, J. Chimdi, H. Hailu, and N. Fikadu, "Compression and workability behavior of chopped glass fiber reinforced concrete," *Materials Today Proceedings*, 2022.

[20] S. S. Narani, M. Abbaspour, S. M. M. M. Hosseini, E. Aflaki, and F. M. Nejad, "Sustainable reuse of Waste Tire Textile

Fibers (WTTFs) as reinforcement materials for expansive soils: with a special focus on landfill liners/covers," *Journal of Cleaner Production*, vol. 247, no. C, Article ID 119151, 2020.

[21] B. Yuan, Z. Li, Z. Zhao, H. Ni, Z. Su, and Z. Li, "Experimental study of displacement field of layered soils surrounding laterally loaded pile based on Transparent Soil," *Journal of Soils and Sediments*, vol. 21, pp. 3072–3083, 2021.

[22] B. Yuan, S. Meng, X. Lei, Q. Luo, P. S. Prasad, and H. z. Li, "Investigation of 3D deformation of transparent soil around a laterally loaded pile based on a hydraulic gradient model test," *Journal of Building Engineering*, vol. 28, no. 3, Article ID 1010124, 2020.

[23] B. Yuan, M. Sun, Y. Wang, L. Zhai, Q. Luo, and X. Zhang, "Full 3D displacement measuring system for 3D displacement field of soil around a laterally loaded pile in transparent soil," *ASCE International Journal of Geomechanics* no. 5, Article ID 04019028.

[24] B. Yuan, Z. Li, Z. Su, Q. Luo, M. Chen, and Z. Zhao, "Sensitivity of multistage fill slope based on finite element model," *Advances in Civil Engineering*, Article ID 6622936, 2021.

[25] P. S. Narayanan, "Study on Shear Parameters of Waste Tire Rubber Fiber Mixed Cohesionless Soil by Series of Triaxial Tests," *International Journal of Advanced Scientific and Technical Research*, 2015.

[26] B. Yuan, L. Zihao, W. Chen et al., "Xudong. Influence of groundwater depth on pile–soil mechanical properties and fractal characteristics under cyclic loading," *Fractal and Fractional*, vol. 6, no. 4, p. 198, 2022.

[27] B. Yuan, L. Xiong, L. Zhai et al., "Transparent synthetic soil and its application in modeling of soil-structure interaction using optical system," *Frontiers of Earth Science*, vol. 7, p. 276, 2019.

[28] R. Mattone, "Sisal fibre reinforced soil with cement or cactus pulp in bahareque technique [J]," *Cement and Concrete Composites*, vol. 27, no. 5, pp. 611–616, 2004.

[29] P. V. Joseph, K. Joseph, and S. Thomas, "Effect of processing variables on the mechanical properties of sisal-fiber-reinforced polypropylene composites," *Composites Science and Technology*, vol. 59, no. 11, pp. 1625–1640, 1999.

[30] G. Xiang, D. Song, and Z. Chen, "Investigated stress-strain relationships of municipal solid waste incineration bottom ash," *Geomatics, Natural Hazards and Risk*, vol. 11, no. 1, pp. 2431–2448, 2020.

[31] M. F. Ma'Ruf, "Shear strength of Apus bamboo root reinforced soil," *Ecological Engineering*, vol. 41, pp. 84–86, 2012.

[32] B. Yuan, L. Zihao, C. Yiming et al., "Mechanical and microstructural properties of recycling granite residual soil reinforced with glass fiber and liquid-modified polyvinyl alcohol polymer," *Chemosphere*, vol. 286, no. P1, Article ID 131652, 2022.

[33] B. X. Yuan, W. J. Chen, J. Zhao, F. Yang, Q. Luo, and T. Chen, "The effect of organic and inorganic modifiers on the physical properties of granite residual soil," *Advances in Materials Science and Engineering*, 2022.

[34] "GB/T 50123-2019," *Standard for Geotechnical Testing Method*, 2019.